

DISS. ETH. NO. 28203

---

**Lamb Shift of Exotic Atoms:  
Precision Measurement in Muonium and  
Progress Towards the First Direct  
Determination in Antihydrogen**

---

*A thesis submitted to attain the degree of  
Doctor of Sciences of ETH Zurich*

*(Dr. sc. ETH Zurich)*

*presented by*

Gianluca JANKA

MSc in Interdisciplinary Sciences ETH, Zurich

born on 29.11.1992

citizen of Switzerland

*Accepted on the recommendation of*

Prof. Paolo Crivelli, examiner

Prof. Klaus Kirch, co-examiner

Dr. Thomas Prokscha, co-examiner

2022





## Declaration of Authorship

I, Gianluca JANKA, declare that this thesis titled, “Lamb Shift of Exotic Atoms: Precision Measurement in Muonium and Progress Towards the First Direct Determination in Antihydrogen” and the work presented in it are my own. I confirm that:

- This work was done wholly or mainly while in candidature for a research degree at this University.
- Where any part of this thesis has previously been submitted for a degree or any other qualification at this University or any other institution, this has been clearly stated.
- Where I have consulted the published work of others, this is always clearly attributed.
- Where I have quoted from the work of others, the source is always given. With the exception of such quotations, this thesis is entirely my own work.
- I have acknowledged all main sources of help.
- Where the thesis is based on work done by myself jointly with others, I have made clear exactly what was done by others and what I have contributed myself.

Signed:

---

Date:

---



*“If I have seen further, it is by standing on the shoulders of giants.”*

Sir Isaac Newton



EIDGENÖSSISCHE TECHNISCHE HOCHSCHULE ZÜRICH

*Abstract*

Institute of Particle Physics and Astrophysics

Doctor of Sciences of ETH Zurich

**Lamb Shift of Exotic Atoms:  
Precision Measurement in Muonium and Progress Towards the First Direct  
Determination in Antihydrogen**

by Gianluca JANKA

Due to its lack of internal structure, muonium is an excellent candidate to provide stringent tests for bound state QED. This work presents the design and the measurement of the muonium Lamb shift performed at the PSI low energy muon (LEM) beamline in the Mu-MASS (MUonium IASer Spectroscopy) experiment. The analysis of the data showed the  $n = 2$  muonium Lamb shift to be 1047.2(25) MHz, which agrees well with theory and is an improvement of an order of magnitude upon the last measurements. Additionally, the  $2S_{1/2,F=0} \rightarrow 2P_{1/2,F=1}$  transition was measured for the first time in muonium at 580.6(68) MHz. From the two measurements, the  $2S$  hyperfine splitting was extracted to be 559.6(72) MHz. Furthermore, muonium in the excited  $n = 3$  state was detected for the first time.

In preparation of these measurements, this thesis includes as well the characterization of the intensity of the metastable flux of muonium at LEM by commissioning the antihydrogen Lamb shift setup designed for GBAR.

Physics with antihydrogen is a blossoming field of research which studies aim to shed light on the observed matter-antimatter asymmetry in the Universe. The GBAR project at CERN primarily aims to measure the free fall acceleration of ultracold neutral antihydrogen atoms in the terrestrial gravitational field. The work performed within this dissertation on the Micromegas GBAR tracker is required for the efficient reconstruction of the antihydrogen annihilation vertex and thus essential for the measurement of its free fall. As a parasitic measurement, the Lamb shift of antihydrogen will be measured with the setup presented in this work with a targeted precision of 100 ppm, which would lead to its first direct determination and allow the extraction of the antiproton charge radius to a level of 10 %.



EIDGENÖSSISCHE TECHNISCHE HOCHSCHULE ZÜRICH

## *Abstract*

Institute of Particle Physics and Astrophysics

Doctor of Sciences of ETH Zurich

**Lamb Shift of Exotic Atoms:  
Precision Measurement in Muonium and Progress Towards the First Direct  
Determination in Antihydrogen**

by Gianluca JANKA

Weil Myonium keine Substruktur besitzt, ist es ein hervorragender Kandidat, um die Theorie der Quantumelektrodynamik für gebundene Zustände strikt zu testen. Diese Arbeit präsentiert die Vorbereitung und Messung der Lamb-Verschiebung in Myonium, ausgeführt an der Low Energy Muon (LEM) Strahlline am PSI mit dem Mu-MASS (MUonium LASer Spectroscopy) Experiment. Die Analyse der Daten hat gezeigt, dass die  $n = 2$  Myonium-Lamb-Verschiebung bei 1047.2(25) MHz liegt, was gut mit dem theoretischen Wert übereinstimmt und einer Verbesserung der bisherigen Messungen von einer Größenordnung entspricht. Zusätzlich wurde zum ersten Mal der  $2S_{1/2,F=0} \rightarrow 2P_{1/2,F=1}$  Übergang in Myonium bei 580.6(68) MHz gemessen. Von diesen zwei Messungen konnte die  $2S$  Hyperfeinstruktur-Aufspaltung von 559.6(72) MHz extrahiert werden. Ausserdem wurde mit dieser Messung zum ersten Mal Myonium im angeregten  $n = 3$  Zustand nachgewiesen.

Als Vorbereitung zu diesen Messungen enthält diese Arbeit auch die Charakterisierung der Intensität des metastabilen Flusses von Myonium am LEM, bei dem gleichzeitig auch das System für die Messung der Antiwasserstoff Lamb-Verschiebung für GBAR kommissioniert wurde.

Physik mit Antiwasserstoff ist ein blühendes Forschungsfeld, welches versucht Aufschluss über die im Universum beobachtete Asymmetrie zwischen Materie und Antimaterie zu geben. Das GBAR Projekt am CERN versucht hauptsächlich den freien Fall von ultra-kalten Antiwasserstoffatomen im Erdgravitationsfeld zu messen. Die in dieser Dissertation präsentierte Arbeit zum Micromegas-GBAR-Tracker ermöglicht eine effiziente Rekonstruktion des Annihilationsvertex des Antiwasserstoffes und ist essentiell für eine erfolgreiche Messung des freien Falls. Mit dem in der Arbeit präsentierten Versuchsaufbau soll die Lamb-Verschiebung in Antiwasserstoff mit einer anvisierten Präzision von 100 ppm gemessen werden. Dies wäre die erste direkte Bestimmung und würde es erlauben, den Antiprotonradius mit einer Präzision von etwa 10 % zu extrahieren.





## Acknowledgements

At the end of my time as PhD student, I look back at the years spent at ETH and realize how many amazing people I met and was allowed to work with during this journey. First and foremost, I want to thank my supervisor Prof. Paolo Crivelli for giving me this incredible opportunity. Pol became my mentor already in my early Master's degree studies, being a constant source of good advice, suggestions and endless motivation to keep me going in more challenging times. Thanks to him, I turned into the physicist I am today, which I am very grateful for. I also want to express my gratitude to Prof. Klaus Kirch for being a co-examiner of my thesis. I'm also thankful to him for his teaching efforts during my Bachelor's studies. While I initially had trouble to decide which branch of physics to focus on, his lectures made me fall in love with (low energy) particle physics, which I will never regret. Next I would also like to thank Dr. Thomas Prokscha for being a co-examiner, but also for supporting me throughout the years and patiently answering all questions I had about muons and the LEM.

At the start of my PhD, I could always count on Dr. Dave Cooke when one of the detectors or other equipment was behaving strangely and some magic had to happen. The same kind of magic Dr. Balint Radics performed for me when some code did not want to compile. I want to thank them for letting me profit from their vast experience and turning magic into skills. I'm also grateful to Dr. Lars Gerchow, with whom I shared an office for the major part of my time. He had the «joy» of listening to many of my problems, and often had a hands-on solution and a helping hand ready. I enjoy remembering the times when we were staying late in the evening in the lab, enthusiastically trying to fix one of my problems. In a later stage of my PhD, I had the luck to work with Dr. Ben Ohayon, who helped me vastly improve my skills in data analysis and thinking not only about the experimental, but also theoretical aspects of the measurement. Thanks to him, «if someone wakes me up in the middle of the night, asking a question about particle physics», I will have an answer ready.

I would also like to thank the RD51 collaboration, in particular Eraldo Olivieri and Givi Sekhniaidze for teaching me the about Micromegas. Thanks as well to Sebastien Procureur for letting me benefit from his experience with Micromegas. I also want to thank the entire GBAR collaboration for letting me be a part of an amazing project and supporting me whenever I was in Geneva.

Special thanks to Mr. Dr. Emilio Depero and Dr. Michael Heiss, who lived through their PhDs at a similar time as I did. Allowing each other to laugh at our mistakes, but also celebrating our success together created a strong bond, which I hope will last beyond our scientific careers. Another special thanks to Irene Cortinovia, Philipp Blumer and Lucas de Sousa Borges, with whom I was working with closely in my last year. The fresh wind you brought in the group made me feel old, but in a good way. I am excited to see where your journey is leading you. In general, I want to thank all colleagues I worked with during my years, creating a fantastic work environment and having great conversations (accompanied by good beer) with: Carlos, Dipanwita, Laura, Henri, Benjamin, Alex, Johannes, Botao, Artem, Zak, Jesse, Paul, Mark, Amit, Pierre, Mirald, Nikola, Ryoma, Devesh, Clement, Finn, and many others.

I am also thankful for all the other friends I made during my time so far in Zurich. The group of the PC-N students and wider circle, especially Stephi, Raphi, Gian-Marco, Fadri, Christian and Holger for honouring the Call of Duty. My former flat-mates, especially Julian, Michelle and Marko, who never failed to convince me to play a good game or watch a series, letting me detach from work. The entire HPK E-Floor of biologists and their gang, especially Rafal, Mateusz, Matt and Barry, who I could always count on for beers after work or on a heck of a party. Only thing I had to promise was not to talk about physics - and not to make biology jokes. Thank you all for being amazing!

Last but not least, I'm grateful for my extended family.

I bi dankbar fir mini Familia. Pappa Christian, Mamma Berta, zamma mit miner Schwester Melanie. Iahr hait mi immer unterstützt, was au immer i ha macha wella. I bi mr sicher, as isch ned immer eifach gsi mit miar, speziell woni am Larna gsi bi. Oder ned aso gsprächig am Telefon wenni spat am Schaffa gsi bi. Aber iahr hait's albig verstanda, und hait mi albig wieder motiviert. D Wuchaend mit auch in Obersaxa sind albig dr best Wag gsi um min Chopf z'lüfta und mi mental chenna vorbereita fir dia nächsta Wucha. I bi so wiani bi, dank auch. Und fir das, und no viel meh, bini auch extrem dankbar. Au wenn iahr immer no da Lit saged, dass ich «Irgendappis mit Physik» am schaffa bi, hoffi doch, dass iahr stolz uf mini Leistig sid. Viela Dank Mamma! Viela Dank Pappa! Viela Dank Meli!

Sono anche grato per la mia seconda famiglia a Cantù. Quando vengo da voi, mi sento come se venissi nella mia seconda casa. Anche quando lavoro come un pazzo, voi siete sempre pieni di comprensione, e mi aiutate in ogni modo possibile. Non dimenticherò mai le numerose volte in cui la Laura è venuta su per le scale, col vassoio pieno di goccioline e un caffè, chiedendomi se volessi anche un gelato. E delle costine del Sergio non ne voglio parlare. Mi fate sentire come un principino. Laura, Sergio, Chiara e Ali, grazie mille per essere nella mia vita.

And now to you, my Quokkettina. Words cannot describe what I feel for you. We met right at the beginning of my start exploring the world of particle physics. You saw all my ups and downs from the front row. You stayed always patient, always supportive, always yourself. And this constantly throughout the last 5 years. When I was feeling down, one of your babbate cheered me up in no time. You turned our apartment into our home, one of the best places to recharge my batteries. We were locked in there together for a few months during the first COVID wave and we did not even fight once. I have no idea how you managed to endure me for that long, but I am happy you did. I'm quite certain nobody else would have been able to. I don't want to imagine how much more difficult my journey would have been without you. This thesis is not only my achievement, we are a team. I consider it our achievement. I liaba di, Sissi!

# Contents

<b>Declaration of Authorship</b>	<b>iii</b>
<b>Abstract</b>	<b>vii</b>
<b>Abstract</b>	<b>ix</b>
<b>Acknowledgements</b>	<b>xi</b>
<b>Preface</b>	<b>1</b>
<b>1 Introduction</b>	<b>3</b>
1.1 The Standard Model . . . . .	3
1.2 Searches for Physics Beyond . . . . .	5
1.2.1 Antihydrogen . . . . .	5
1.2.2 Muonium . . . . .	6
1.3 The GBAR experiment . . . . .	6
1.4 The Mu-MASS experiment . . . . .	10
<b>2 GBAR: Annihilation Vertex Detector</b>	<b>13</b>
2.1 Micromegas Detectors . . . . .	14
2.1.1 Working Principle . . . . .	14
2.1.2 Choice of Gas . . . . .	14
2.1.3 Genetic Multiplexing . . . . .	15
2.2 Free Fall Simulation . . . . .	17
2.3 The GBAR Micromegas . . . . .	18
2.4 Hit Reconstruction . . . . .	21
2.4.1 Pre-Processing of Signal . . . . .	21
2.4.2 Unfolding Algorithm . . . . .	21
2.4.3 Cluster Finder Algorithm . . . . .	23
2.5 Comparison of different MMD . . . . .	23
2.5.1 Tracking Algorithm . . . . .	24
2.5.2 Extraction of Double Hits . . . . .	25
<b>3 The Lamb Shift</b>	<b>27</b>
3.1 History . . . . .	27
3.1.1 Lamb shift in hydrogen . . . . .	28
3.1.2 The Proton Radius Puzzle . . . . .	31
3.1.3 Lamb shift in muonium . . . . .	32
3.2 Beamfoil Technique and Contamination . . . . .	33
3.2.1 Working Principle . . . . .	33
3.2.2 2S Formation & Contamination . . . . .	34
3.3 Lamb Shift theory . . . . .	36
3.4 New Physics . . . . .	41
3.4.1 Lorentz- & CPT-Violation . . . . .	41

3.4.2	Muonic Forces . . . . .	41
3.5	Optical Bloch equations for a two-level system . . . . .	43
3.5.1	Approximate Solution . . . . .	46
<b>4</b>	<b>GBAR: Design and Commissioning of the Lamb Shift Setup</b>	<b>47</b>
4.1	Ly-a Setup . . . . .	47
4.1.1	Microchannel Plates . . . . .	47
	Working Principle . . . . .	48
	Design . . . . .	48
	Coatings . . . . .	49
	HV dividers . . . . .	50
4.1.2	Quenching Setup . . . . .	51
4.1.3	Vacuum Chamber . . . . .	51
4.2	First test at PSI with Muonium . . . . .	53
4.2.1	Determining Time Offset . . . . .	54
4.2.2	Energy Calibration . . . . .	55
4.2.3	M formation fraction at different energies . . . . .	56
4.2.4	M(2S) formation fraction . . . . .	57
4.2.5	Summary . . . . .	58
4.3	Microwave . . . . .	59
4.3.1	Design of Transmission Line . . . . .	59
4.3.2	Microwave Setup . . . . .	60
	Scanner TL . . . . .	60
	HFS TL . . . . .	61
4.3.3	Characterization . . . . .	61
4.3.4	Power Determination inside TL . . . . .	62
4.4	Installation and commissioning at CERN . . . . .	64
<b>5</b>	<b>Mu-MASS: Muonium Lamb Shift</b>	<b>65</b>
5.1	Simulation . . . . .	65
5.1.1	Simulating TL Fields . . . . .	66
5.1.2	Simulating Lamb Shift Transitions . . . . .	67
5.2	Experimental Setup . . . . .	68
5.3	DAQ and Trigger Logic . . . . .	69
5.4	Optimization and Data Taking . . . . .	70
5.5	Data Analysis . . . . .	72
5.5.1	Data Extraction . . . . .	72
5.5.2	Power Corrections . . . . .	73
5.5.3	Fitting Procedure . . . . .	74
5.6	Results . . . . .	74
5.6.1	Fitting Results for Hydrogen . . . . .	75
5.6.2	Fitting Results for Muonium . . . . .	76
5.6.3	Systematics . . . . .	77
	Doppler Shift . . . . .	77
	Stark Shift . . . . .	77
	Higher States Contamination . . . . .	78
	MW Field Intensity . . . . .	78
	Velocity Distribution . . . . .	79
	Earth's Magnetic Field . . . . .	79
	Quantum Interference . . . . .	79
5.6.4	Summary & Constraints on New Physics . . . . .	79

<b>6</b>	<b>Conclusions and Future Prospects</b>	<b>83</b>
6.1	GBAR . . . . .	83
6.1.1	Micromegas Detectors . . . . .	83
6.1.2	Multiple Hit Reconstruction . . . . .	83
	Data Preparation . . . . .	84
	Setting up the NN . . . . .	84
	Multiple Hits Identification . . . . .	85
	Hit reconstruction . . . . .	86
6.1.3	Antihydrogen Lamb Shift . . . . .	88
6.2	Muonium Lamb Shift . . . . .	89
6.2.1	Statistics . . . . .	89
6.2.2	Beam Contamination . . . . .	90
	Increasing Length of Beamline . . . . .	90
	Adding Transmission Line . . . . .	90
	Adding Electrical Field . . . . .	92
6.2.3	Beamtime Estimations . . . . .	94
6.2.4	Doppler Shift & Monitoring Power . . . . .	95
6.2.5	Summary . . . . .	96
<b>A</b>	<b>Additional Figures</b>	<b>97</b>
A.1	Updated Sensitivity Plot for CPT-violation . . . . .	97
A.2	Complete Efficiency Scan for all MMD . . . . .	98
<b>B</b>	<b>Algorithms for Micromegas</b>	<b>99</b>
B.1	Creating Multiplexing Map . . . . .	99
B.2	Building Minimization Function . . . . .	100
B.3	Unfolding Algorithm . . . . .	100
<b>C</b>	<b>Mathematica Code for Lamb Shift Theory</b>	<b>103</b>
C.1	Calculating Transition Elements . . . . .	103
C.2	Calculating Theoretical 2S Lamb Shift Contributions . . . . .	103



# List of Figures

1.1	Sensitivity plot for CPT tests with antihydrogen and muonium . . . . .	7
1.2	Schematic view of the GBAR experiment . . . . .	8
1.3	Schematic view of the GBAR Free Fall experiment . . . . .	9
1.4	Schematic view of the GBAR Lamb shift setup . . . . .	10
1.5	Schematic view of the Mu-MASS experiment including the LEM beam-line . . . . .	12
2.1	Sketch of the working principle of a Micromegas . . . . .	15
2.2	Multiplexing maps for factor 12 and 17 . . . . .	16
2.3	Example of signal extraction of one MM plane . . . . .	16
2.4	The cylindrical free fall chamber with MMD trackers implemented in Geant4 . . . . .	17
2.5	Cosmic testbench to characterize MMD . . . . .	18
2.6	Scans of the resolution and signal-to-noise depending on the multiplexing factor . . . . .	19
2.7	Scan of the tough event fraction in MMDs depending on the multiplexing factor . . . . .	19
2.8	Picture of a GBAR MMD assembled . . . . .	20
2.9	Example of typical waveforms collected with a MMD . . . . .	21
2.10	Example of signal extraction of one MM plane with the unfolding algorithm . . . . .	22
2.11	Example of a typical cluster size and cluster area distribution in a MMD . . . . .	23
2.12	Example of a reconstructed single track through four MMDs . . . . .	24
2.13	Example of track properties reconstructed with the unfolding algorithm . . . . .	24
2.14	Example of a MMD plane residuals analyzed for double hits . . . . .	26
2.15	Example of a reconstructed double track . . . . .	26
3.1	Schematic of the history of atomic models . . . . .	28
3.2	Schematic of the Lamb experiment . . . . .	29
3.3	Schematic of the hydrogen energy levels . . . . .	30
3.4	Schematic of the Lamb shift energy levels of muonium and hydrogen . . . . .	30
3.5	Sketch of a particle interacting with a carbon foil . . . . .	33
3.6	Grotrian diagram for hydrogen and muonium . . . . .	34
3.7	Example of muonium Lamb shift line-shape . . . . .	35
3.8	Feynman diagrams of self-energy and vacuum polarization . . . . .	36
4.1	Schematic of the working principle of a Chevron-type MCP . . . . .	48
4.2	CAD drawing of the GBAR CsI-MCP . . . . .	49
4.3	Picture of a CsI- and a KBr-coated MCP . . . . .	50
4.4	Schematics of the high voltage divider used for operating MCPs . . . . .	51
4.5	CAD drawing of the GBAR Ly- $\alpha$ detection setup . . . . .	52
4.6	Picture of assembled GBAR Lamb shift setup . . . . .	52
4.7	Sketch of experimental setup for testing the GBAR Ly- $\alpha$ detection setup . . . . .	53

4.8	TOF distributions of muonium . . . . .	54
4.9	Energy distributions of muonium . . . . .	55
4.10	Histogram showing muonium formation . . . . .	56
4.11	Graph for muonium formation efficiency with the beamfoil technique . . . . .	57
4.12	Histogram showing M(2S) detection . . . . .	58
4.13	Picture of MW transmission line for GBAR Lamb shift setup . . . . .	60
4.14	Sketch of MW Scanner setup . . . . .	61
4.15	Sketch of MW HFS setup . . . . .	61
4.16	Characterization curves of MW amplifiers and splitters . . . . .	62
4.17	Characterization curves of MW TLs and attenuators . . . . .	63
4.18	Sketch of how to determine power inside Scanner TL . . . . .	63
4.19	Sketch of how to determine power inside HFS TL . . . . .	64
4.20	The GBAR Lamb shift setup installed in the GBAR beamline at CERN . . . . .	64
5.1	Simulated fields for scanner TL on- and off-axis . . . . .	66
5.2	Experimental setup used in the muonium Lamb shift measurement . . . . .	68
5.3	Diagram of DAQ and communication pathways . . . . .	69
5.4	Muonium and hydrogen selection cut . . . . .	72
5.5	Ly- $\alpha$ selection cut for muonium and hydrogen . . . . .	73
5.6	Hydrogen Lamb shift line-shape and fitting results . . . . .	75
5.7	Muonium Lamb shift line-shape and fitting results . . . . .	76
5.8	Systematic scans for the Doppler and Stark shift . . . . .	78
5.9	Muonium Lamb shift values measured including theoretical expectation . . . . .	81
5.10	Plot showing constraints from muonium Lamb shift on new muonic forces . . . . .	81
6.1	Training Curve of the Multiple Hits Neural Network . . . . .	86
6.2	Training curve and residuals for a multiple hit reconstruction with a Neural Network . . . . .	87
6.3	Example of the input image of a 2D hit for a convolutional neural network . . . . .	88
6.4	Scan of depopulating 3S and 4S states by extending the beamline . . . . .	91
6.5	Example of reducing 3S states for a more precise muonium Lamb shift scan . . . . .	92
6.6	Quenching probability scan for muonium atoms in 2S, 3S and 4S states . . . . .	93
6.7	Line-shape scans with and without additional electrical quenching field for both 583 MHz and 1140 MHz transitions . . . . .	93
6.8	Statistical uncertainty estimation for future muonium Lamb shift experiments . . . . .	94
6.9	Sketch of proposed MW setup for a future muonium Lamb shift measurement . . . . .	95
A.1	Update on sensitivity plot for CPT tests with antihydrogen and muonium . . . . .	97
A.2	Detailed summary of the results for double hit reconstruction with different MMDs, analysed with the unfolding algorithm. . . . .	98



# List of Tables

2.1	The specifications for the GBAR MMD tracker . . . . .	20
2.2	Summary of the double hit reconstruction with different MMD . . . . .	25
3.2	Calculated transition elements . . . . .	45
4.1	Values extracted to characterize intense metastable muonium beam . . . . .	59
4.2	List of available MW elements . . . . .	62
5.1	Summary of resonance frequencies of interest for hydrogen and muonium . . . . .	67
5.2	Statistics gathered during the beamtime June 2021 . . . . .	71
5.3	Results of the muonium Lamb shift . . . . .	80
6.1	Design of simple one-dimensional Neural Network . . . . .	85
6.2	Summary of possible upgrades to the Mu-MASS setup and which contributions of the M LS could be probed . . . . .	96



# Preface

When I was young, I was interested in almost every school subject. Learning was never considered an obligation, just fun. I tried to soak up all the knowledge like a sponge, so I could become as smart as the people I looked up to. At least that was my hope. When finishing my Matura, I never had any doubts as to where to go. ETH was the logical next step to me. But what topic to study was a difficult choice. There was just such a huge selection, and I wanted to do it all. Fortunately, I found the Bachelor's programme of Interdisciplinary Sciences, where I could still learn about a broad range of topics. What I immediately liked about the field of particle physics was that learning by heart is not as helpful as truly understanding the concepts with some physics intuition gained through experience. This motivated me to start my first experimental works, and that's when I fell in love with particle physics. I realized that experimental particle physics embodies exactly what I always enjoyed most - the interplay of many different fields. Mathematics is used to describe physics, informatics to simulate physics, engineering to build devices to measure physics. There was always so much more to discover. In my Master's degree, I was lucky enough to stumble upon a semester project which I had the chance to join in its first stage. I was allowed to be a part of many of the steps, gaining experience in a wide range of topics. The semester project, together with my Master's thesis, ended up being the groundwork to this thesis.

My thesis is about the journey of two detector setups. In Chapter 1, we will see our motivation as to why it was interesting to us to build these. In Chapter 2, we will cover the journey of the Micromegas detectors for the GBAR experiment. It will take us from an early prototype stage, over simulation and experimental studies on how to optimize them, to the final design. The next chapters are about the journey of the Ly- $\alpha$  detection setup to measure the Lamb shift. In Chapter 3, we will first read about the history of the Lamb shift. In the second part, we will dig into the theoretical background necessary to perform such an experiment. The beginning of the Ly- $\alpha$  setup's journey starts in Chapter 4, where we will explore the design of the setup. It continues with its commissioning with the first measurements performed at PSI and ends with the final installation in the GBAR beamline, ready to take data to measure the antihydrogen Lamb shift. In Chapter 5, we will then use what we have learned before, and apply it to measure the Lamb shift in muonium. We will see the design of an adapted version of the GBAR Ly- $\alpha$  setup, followed by data collection at the LEM at PSI and their analysis with the aid of a detailed simulation. The results we found are discussed and put into context for the search for physics beyond the Standard Model. However, we are not at the final destination yet. In Chapter 6, we draw our conclusions and give an outlook on the ideas floating around in our heads on how to improve the setups, opening up the possibility to measure even more accurately.

As you can see, my thesis contains a lot of fields. From engineering, over mathematically describing and simulating the measurement, to actually measuring physics and evaluating data. The little boy in me could not be happier.



## Chapter 1

# Introduction

In this first chapter, I will give a brief introduction to the motivation of my thesis. It will start with a short summary of the Standard Model, the theory describing most of the interactions governing our Universe. We will explore its success, but also its limits, especially the puzzling matter-antimatter asymmetry. The answer to this puzzle is yet to be found, but a lot of experimental and theoretical efforts have been done and are ongoing to come closer to a solution. We will focus in Sec. 1.2 on experiments performed on antihydrogen and muonium.

Antihydrogen ( $\bar{\text{H}}$ ) consists of a negatively charged antiproton  $\bar{p}$  as the nucleus with a positively charged positron  $e^+$  orbiting around it. It makes an excellent candidate for testing the Lorentz- and CPT-symmetry by comparing it to its matter counterpart, the hydrogen atom. With the GBAR experiment, we attempt to study its gravitational behaviour as well as perform microwave spectroscopy to measure the Lamb shift. A more detailed description is given in Sec. 1.3.

Muonium (M), on the other hand, is a bound system composed of a positively charged muon  $\mu^+$  as the nucleus and an orbiting electron  $e^-$ . Since both do not have any substructure, muonium is free from finite size effects and can be almost purely described via bound state QED (b-QED), making it a great system to probe new physics or extract fundamental constants such as the muon mass or the magnetic moment. Our aim with the Mu-MASS experiment described in Sec. 1.4 is to push the limits in muonium spectroscopy.

## 1.1 The Standard Model

The Standard Model is a theory successfully describing the properties of the building blocks of our Universe, the elementary particles, and how they interact via electromagnetic, strong or weak force with each other. Only gravity, the fourth fundamental force, could not be included.

With their historic publications, S. Weinberg (1), A. Salam (2) and S. L. Glashow (3) built the core of the Standard Model. At this time, not only the rather recently discovered quarks could be described, but also specific predictions could be made for other particles still to be detected. For example the W and Z gauge bosons (4; 5), the top-quark (6) or the tau neutrino (7) were all experimentally confirmed afterwards and cemented the acceptance of the Standard Model. Its success culminated with the experimental observation of the Higgs boson in 2012 (8).

Although it is a very successful and elegant theory, not everything observed to this day can be explained. One of the shortcomings of the theory is, besides not including gravity, the necessity of 18 experimentally determined input parameters (9), such as masses of the elementary particles or coupling constants. It also does not contain any explanation of the dark sector such as dark matter (10) or dark energy

(11), and wrongly assumes neutrinos to be massless and therefore not to oscillate in flavour (12).

Another problem with the Standard Model arises from the fact that matter and antimatter can only be produced together in pairs due to charge, lepton and baryon number conservation. At the beginning of the Universe, the Big Bang (13), an unimaginable amount of energy was released, first forming particles, cooling down over time to slowly form atoms, molecules and eventually life. However, these two concepts appear to be mutually exclusive. If the same amount of matter and antimatter was always produced, they would eventually annihilate again, leaving just an empty Universe filled only with radiation. However, looking around us, everything we see is built almost entirely by matter. Even further afield, outside of our solar system, we observe that there is always much more matter than antimatter (see (14) as summary). For the overproduction of baryons over antibaryons, called the baryogenesis, to happen, A. Sakharov formulated three conditions (15):

1. Violation of Baryon Number B
2. Violation of C- and CP-symmetry
3. Interactions out of thermal equilibrium

The C- and CP-symmetry was found experimentally to be broken, e.g. in Kaons (16; 17; 18) or later also in other mesons (19; 20), and can be included in the Standard Model. However, the effect of CP violation within the Standard Model is too small to account for such a large asymmetry (14). The matter-antimatter asymmetry is still to this day one of the biggest puzzles in physics waiting to be solved.

Without the third Sakharov condition, the CPT symmetry, one of the most fundamental properties of the Standard Model, would take care of balancing the baryons and antibaryons and no matter-antimatter asymmetry would be visible (21). But what if CPT and subsequently also Lorentz-invariance (22; 23) would be broken? In 1997, D. Colladay and A. Kostelecky proposed an effective field theory based on the Standard Model, but including CPT-violation (24), extending it later with full Lorentz-violation (25) and eventually including gravity (26). The framework of the Standard Model Extension (SME) was created. It certainly became less elegant compared to the Standard Model, introducing many more coefficients (27), but it might be able to help solving the puzzle of the matter-antimatter asymmetry.

Another puzzle arises from the theoretical calculation and measurements of the anomalous magnetic moments. For the electron, the experimental (28) and theoretical value (29) agree well up to 10 significant digits, making it the most accurately verified prediction of the Standard Model. The current limitation is coming from the uncertainty in the fine-structure constant  $\alpha$ , whose measurement by LKB (30) and Berkley (31) are disagreeing by  $5.4\sigma$ . In contrast, the experimental value of the anomalous magnetic moment for the muon (CERN (32; 33), BNL (34)) deviated  $3.5\sigma$  from the theoretical value, and was even increased to  $4.2\sigma$  by a recent measurement at Fermilab (35). These results are a strong indicator of new physics beyond the Standard Model in the muonic sector. One of many possible explanations could be a so far undiscovered dark fundamental force (36; 37).

## 1.2 Searches for Physics Beyond

### 1.2.1 Antihydrogen

The first demonstration of antihydrogen production was shown at the Low Energy Antiproton Ring (LEAR) at CERN in 1996 (38). Shortly afterwards in 1997, antihydrogen formation was shown as well at Fermilab (39). Driven by the first antihydrogen detections, the Antiproton Decelerator (AD) (40) was built and commissioned at CERN in 2000 to deliver low-energy antiprotons (5.3 MeV) for precision experiments. This allowed the ATHENA (41) and ATRAP (42) collaborations to produce for the first time cold antihydrogen inside nested Penning traps. ALPHA managed in 2010 for the first time to trap antihydrogen in a Ioffe-Pritchard trap (43). Only a year later, ALPHA was able to trap the atoms for 1000 s (44), ensuring that the atoms relaxed to the ground state and therefore opening up the possibility to start performing precision spectroscopy experiments.

Motivated by that success, the ELENA storage ring (45) was designed and went into the implementation phase in 2014. The idea of ELENA was to further slow down the antiprotons coming from the AD, from 5.3 MeV to 0.1 MeV. This enables the collaborations to reduce the thickness of degrader foils to slow down the antiprotons and therefore increase the antiproton capture efficiency significantly.

Being able to trap antihydrogen for a sufficiently long time, the ALPHA collaboration managed to successfully measure the  $1S - 2S$  transition (46), the hyperfine spectrum (47) and the  $1S - 2P$  transition (48) of antihydrogen. From these measurements, they were able to also indirectly extract for a first time the Lamb shift frequency of antihydrogen to 1046(35) MHz (49). So far, all their measurements agree well with the hydrogen counterpart and are therefore consistent with CPT invariance.

The ALPHA collaboration also demonstrated for the first time laser cooling of antihydrogen (50), opening up the possibility to further improve upon the uncertainty of their previously measured transitions. Additionally, the ASACUSA collaboration aims at improving the measurement of the hyperfine structure (HFS) of antihydrogen, but with an antihydrogen beam instead of a trap (51). During the Long Shutdown 2 (from December 2018 to July 2021), ELENA was commissioned (52) and all the collaborations in the AD hall connected to benefit from low-energy antiprotons.

When comparing antihydrogen to hydrogen, not only spectroscopic quantities are of interest, but also the gravitational behaviour. The Weak Equivalence Principle (WEP), an important part of Einstein's theory of General Relativity (53), states that the trajectory a particle would follow in a gravitational field is independent of its mass or internal structure. This principle has been tested for antimatter only indirectly (see summary (54)) or directly with a very large range ( $-65g < \bar{g} < 150g$ ) by ALPHA (55), but several collaborations are currently working towards a more precise determination of the anti- $g$  to a precision of 1%. The AEGIS collaboration is attempting to extract the gravitational constant from a beam experiment with a Moire deflectometer (56), where they just recently reached a first milestone by producing the first antihydrogen atoms (57). The ALPHA- $g$  experiment (58) as well as GBAR (59) are attempting to measure  $\bar{g}$  with a classical free-fall experiment.

Within GBAR, a parasitic measurement was proposed by P. Crivelli et al. (60) to measure the antihydrogen Lamb shift directly for the first time. This would improve upon the indirectly measured value from ALPHA (49) by more than two orders of magnitude. The design and commissioning of the GBAR Lamb shift experiment is a

large part of my thesis and is explained in greater detail in the sections and chapters to come.

### 1.2.2 Muonium

Muonium has first been observed by Hughes et al. (61) in 1960 by stopping muons in pure argon gas and measuring its characteristic Larmor frequency. Over the years, many other production methods of muonium have been shown, for example through interaction with a foil to produce a beam in vacuum (62) or by interaction with a silica powder (63) or aerogel (64) to form the atoms at room temperature velocity.

Using the method of producing muonium in a gas, Liu et al. (65) at LAMPF measured the currently most precise ground state hyperfine structure of muonium. The MuSEUM collaboration at J-PARC aims to improve the measurement of the ground state hyperfine structure and is showing promising results already with the best determination of the HFS at zero magnetic field (66), and the potential to further improve upon this by around two orders of magnitude (67).

The Lamb shift of muonium was observed for the first time in 1984 by A. Badertscher et al. (68) at LAMPF and around the same time measured by C. J. Oram et al. (69) at TRIUMF. Later in 1990, K. A. Woodle et al. (70) also measured the muonium Lamb shift at LAMPF. Furthermore, the fine structure interval  $2^2S_{1/2} \rightarrow 2^2P_{3/2}$  of muonium was measured by S. H. Kettell (71) in 1990, from which the Lamb shift transition was extracted. All these measurements were statistically limited due to massive losses in the degrader foils slowing down the beam, and therefore no precision measurement was yet possible.

The  $1S - 2S$  transition in muonium was first measured by Chu et al. in 1988 at KEK (72) and improved over the years by Maas et al. (73). The current best determination of the  $1S - 2S$  transition was measured by Meyer et al. in 1999 (74) at RAL. In 2018, P. Crivelli proposed the Mu-MASS experiment, which aims to improve upon the  $1S - 2S$  transition (75). Within Mu-MASS, an improvement on the Lamb shift measurement was also possible. This experiment is the main part of this thesis and discussed in detail in the next chapters.

The current best measurements as well as the proposed uncertainties for upcoming measurements are summarized in Fig. 1.1, for both muonium and antihydrogen. Within the SME framework, muonium depends on different Lorentz-violating coefficients than hydrogen and therefore these tests are complementary.

## 1.3 The GBAR experiment

The idea for the GBAR experiment originated from J. Walz and T. Hänsch in 2004 (80) and was proposed to the SPSC at CERN in 2011 (59). The goal is to measure the  $\bar{H}$  free fall and extract the gravitational constant  $\bar{g}$ . The central part of the experiment is to produce positively charged antihydrogen ions ( $\bar{H}^+$ ), which will be trapped and cooled down to  $10 \mu\text{K}$  to minimize the uncertainty coming from the initial velocity. A laser pulse with a wavelength of  $1640 \text{ nm}$  will photo-ionize the trapped  $\bar{H}^+$  and gives the start time of the free fall. The  $\bar{H}$  eventually will annihilate at the chamber wall, producing on average 3 charged pions. These pions will be detected with tracking detectors, leading to the annihilation position and time, from which the gravitational constant  $\bar{g}$  can be determined. The installation of the



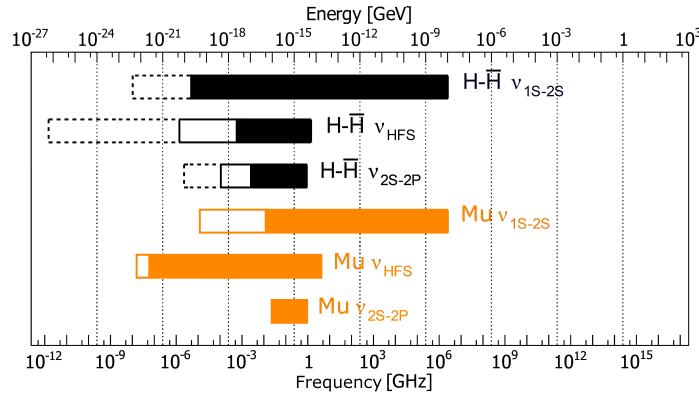


FIGURE 1.1: Comparison of CPT tests in antihydrogen and muonium. The right edge represents the absolute value, whereas the left edge is the absolute accuracy of the measurement. The length of the bar is corresponding to the relative precision of the CPT test. Filled bars are the to-date most precise determination and the solid empty bars the expected accuracies of ongoing measurements, the references given in the text. The dashed bars indicate the most precise measurement of the hydrogen equivalent (76; 77; 78). Adapted from Ref. (79).

experiment started in December 2016 in the AD hall at CERN. The schematic view of the GBAR experiment is shown in Fig. 1.2.

The  $\bar{H}^+$  is produced in a two charge-exchange process:



where the  $\bar{p}$  are produced by the AD at an energy of 5.3 MeV and further slowed by the ELENA storage ring to 100 keV. Around  $10^7$   $\bar{p}$  are ejected every 110 s towards the GBAR zone. The  $\bar{p}$  are further decelerated to a few keV by a pulsed high-voltage decelerator (81) before reaching the reaction chamber. In the meantime, the GBAR LINAC generates 9 MeV electrons, hitting a tungsten target to produce positrons  $e^+$ . The  $e^+$  are moderated and the eV positrons extracted. The goal in the proposal is to have at least  $3 \times 10^7 \text{ s}^{-1}$  moderated  $e^+$ . The system was successfully commissioned and a flux of  $5.0(6) \times 10^7 \text{ s}^{-1} e^+$  demonstrated. These are guided into first a buffer gas trap, and eventually stacked up in a high field trap. Within an AD-cycle of 110 s, the goal is to accumulate  $10^{10} e^+$  ready to be ejected into the reaction chamber. Recently, the trapping of  $3.8(4) \times 10^8 e^+$  within 560 s was demonstrated (82). In the reaction chamber, the  $e^+$  will hit a  $\text{SiO}_2$  target to form a cloud of positronium (Ps) in vacuum. The  $\bar{p}$  are timed to fly through the cloud, ideally collecting through the two-step process described in Eq. 1.1 two  $e^+$ , forming  $\bar{H}^+$ .

In optimal running conditions, on average every third pulse will produce a  $\bar{H}^+$ . The beam of  $\bar{H}^+$ ,  $\bar{H}$  and  $\bar{p}$  leaves the reaction chamber, passing through the Lamb shift setup explained later, and is separated in the switchyard with an electrostatic field. The  $\bar{p}$  are led to a beam dump far away, the  $\bar{H}$  are detected by an MCP, and the  $\bar{H}^+$  are guided into the free fall chamber. Within the free fall chamber, the  $\bar{H}^+$  are first trapped in a Paul trap, preloaded with  $\text{Be}^+$  ions. Through sympathetic cooling, the  $\bar{H}^+$  is cooled down to around 1 mK, while the  $\text{Be}^+$  ions are kept cool with laser-cooling. In a second step, the  $\bar{H}^+$  are transferred into a precision trap, where with

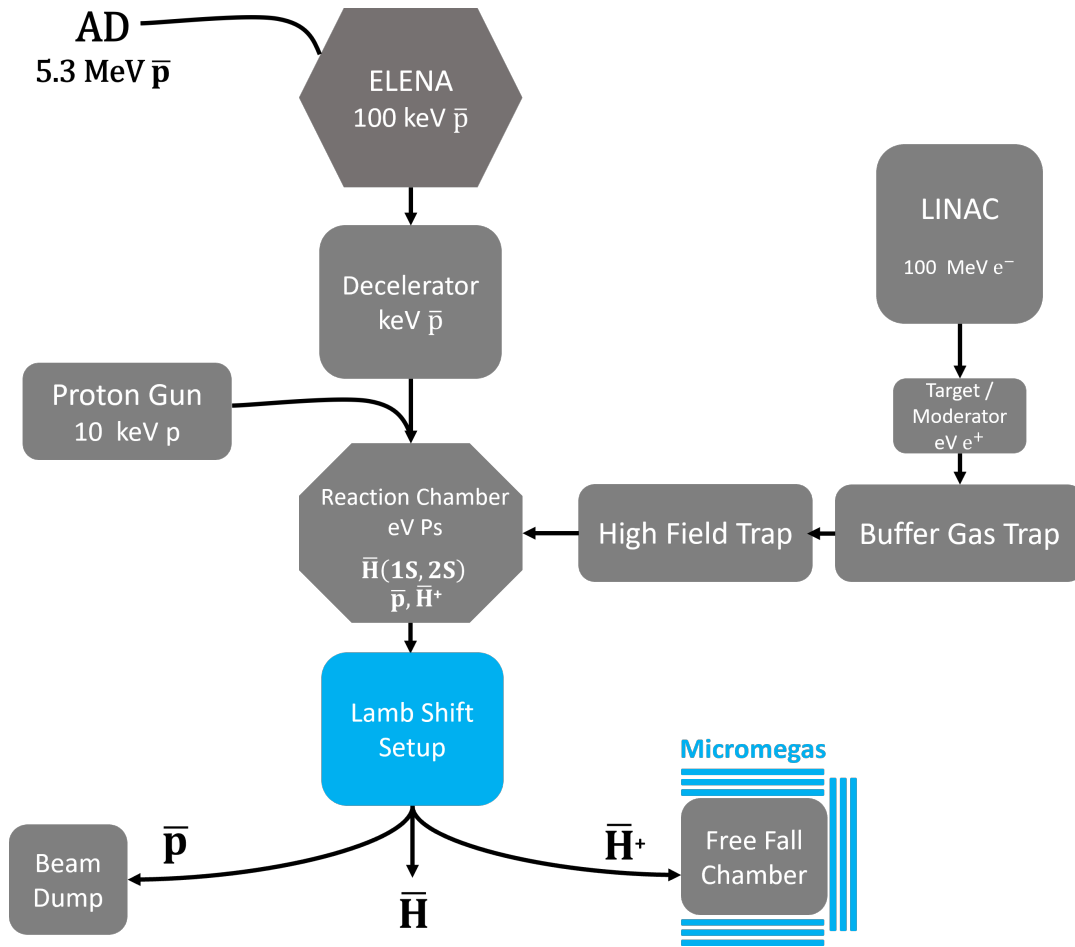


FIGURE 1.2: A schematic view of the GBAR experiment. The Micromegas tracking detectors as well as the Lamb shift setup marked in blue are central topics of the thesis and discussed more in detail in Chap. 2 and Chap. 4, respectively.

Raman sideband cooling the ion will be cooled further down to  $10\ \mu\text{K}$ .

The next processes happening in the free fall chamber are shown in Fig. 1.3. Once cooled, the  $\bar{\text{H}}^+$  is ionized by a  $1640\ \text{nm}$  laser, giving the start time  $t_0$  for the free fall experiment. The now  $\bar{\text{H}}$  is not trapped anymore and will start its fall. Inevitably, the anti-atom will come into contact with matter and annihilate, producing on average 3 charged pions  $\pi^\pm$ . The free fall chamber is surrounded by Micromegas detectors, arranged in triplets, whose purpose is to detect pions passing through them and record the hit position. When the pion passes at least two out of three detectors in the triplet, its track can be reconstructed. Having multiple tracks, the vertex position of the  $\bar{\text{H}}$  annihilation can be determined, providing information on how far the anti-atom fell.

In the example of Fig. 1.3, the vertex can be reconstructed by three tracks, two of them even reconstructed by the same Micromegas triplet. Preparing the Micromegas detectors for GBAR as well as providing a method to reconstruct hit position and tracking was a central part of my work and will be presented in Chap. 2.

The outer layer of the detection system is built by TOF scintillator bars (83). This

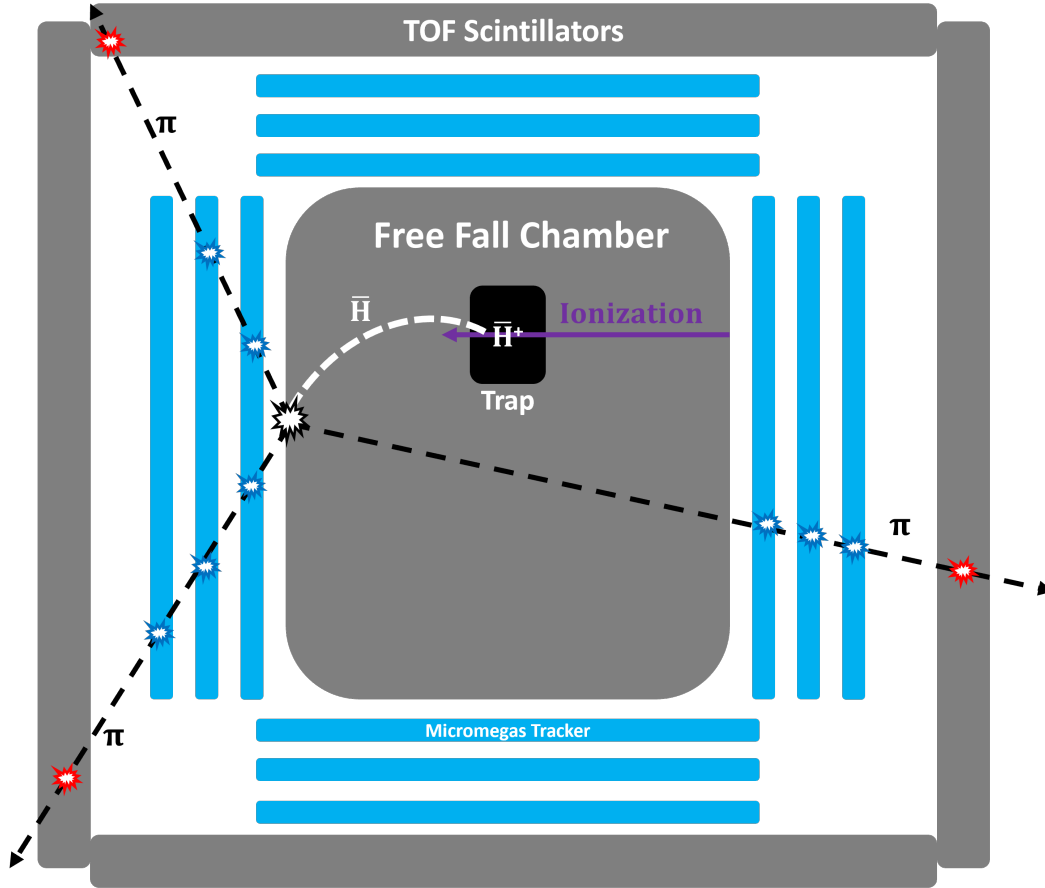


FIGURE 1.3: A schematic view of the GBAR Free Fall experiment. The Micromegas tracker detectors marked in blue are part of the thesis and will be discussed more in detail in Chap. 2.

additional system helps the experiment obtain more precise information on the annihilation time  $t_{\text{an}}$ , as well as to discriminate between true annihilation and background (cosmic radiation) events.

The  $\bar{g}$  can then be extracted via:

$$h = v_z^0 (t_{\text{an}} - t_0) + \frac{1}{2} \bar{g} (t_{\text{an}} - t_0)^2 \quad (1.2)$$

Since  $v_z^0$  is not a priori known, and the annihilation height is a complicated distribution as well, a more advanced analysis based on a realistic free fall simulation done by our group at ETHZ (84) in collaboration with S. Reynaud et al. (85; 86) is under construction. The goal is to determine  $\bar{g}$  in a first step to a precision of 1%. An improvement of three orders of magnitude could be achieved by studying quantum interference (87; 88).

As shown in Eq. 1.1 and indicated in Fig. 1.2, a greater amount of  $\bar{\text{H}}$  is produced in the process than the actual ions. In the GBAR proposal (59), around 400  $\bar{\text{H}}$  per pulse would be expected. Roughly 10% of the atoms are expected to be in the 2S state. In 2016, P. Crivelli et al. (60) proposed to utilize the beam to measure the Lamb shift in antihydrogen. The proposed schematic of the experiment is shown in Fig. 1.4.

The setup has to be installed just after the reaction chamber and before the switchyard, so the  $\bar{\text{H}}$  (2S) are not accidentally quenched by electrical fields to the ground

state and therefore lost. The setup consists of two microwave regions; the first acting as hyperfine state selector, the second to drive the transition of interest. The  $\bar{\text{H}}$  ( $2S$ ) passes through these microwaves, potentially being driven to the  $2P$  state. The  $2P$  state is unstable and the atom relaxes back to the ground state with a lifetime of 1.6 ns. The third stage of the experiment is the Lyman-alpha detection. In case the  $\bar{\text{H}}$  atom is still in the  $2S$  state, it will experience a strong electric field of the order of  $100 \text{ V cm}^{-1}$ . This field mixes the metastable  $2S$  and unstable  $2P$  states, eventually depopulating the  $2S$  completely. While the  $2P$  states relax to the ground state, a Lyman-alpha photon ( $\text{Ly-}\alpha$ ) of 122 nm is emitted. These photons are detected by the  $\text{Ly-}\alpha$  detectors surrounding that area. The closer the microwave frequency is to resonance, i.e. it is driving the Lamb shift transition more efficiently, the fewer  $2S$  states manage to enter the  $\text{Ly-}\alpha$  detection region and therefore less signal coming from  $\text{Ly-}\alpha$  photons is observed. To normalize on beam variations and reduce background through time coincidence, the  $\bar{\text{H}}$  are eventually detected with an MCP at the end of the beamline.

Through a simple counting experiment while scanning the microwave frequency, the transition frequency can eventually be determined. The objective of this measurement is to determine the antihydrogen Lamb shift to an uncertainty of around 100 kHz and for the first time extract the antiproton charge radius at a level of 10%. The Lamb shift measurement of antihydrogen, including the construction of the setup and its commissioning, is one of the main parts of my thesis and are described in more detail in Chap. 3 and Chap. 4.

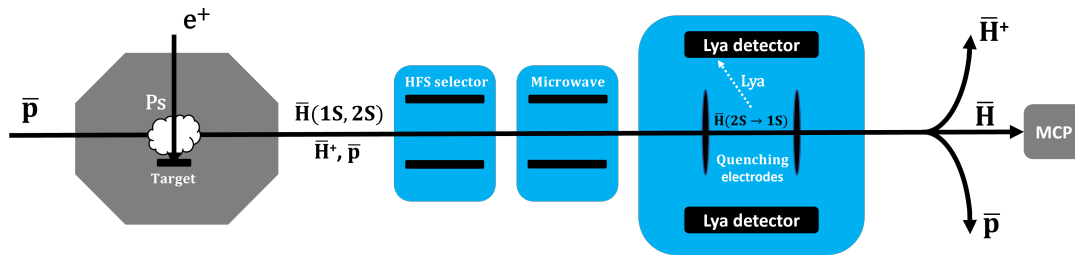


FIGURE 1.4: A schematic view of the GBAR Lamb shift experiment. The elements marked in blue are part of the thesis and will be discussed more in detail later in Chap. 4.

## 1.4 The Mu-MASS experiment

The Mu-MASS experiment was proposed by P. Crivelli in 2018 (75). The goal is to improve upon the  $1S - 2S$  transition frequency of muonium by three orders of magnitude. This result would lead to the best determination of the muon mass, which is relevant in the context of the anomalous magnetic moment puzzle of the muon mentioned in Sec. 1.1 (89). Combining the results of Mu-MASS with the hyperfine results from MuSEUM would probe b-QED to a new level. The Rydberg constant could be determined independent of finite-size effects, which would be helpful in resolving the proton radius puzzle (see Sec. 3.1.2). Using the currently accepted CODATA Rydberg constant value would lead to a new determination of  $\alpha$ , which can help understanding the discrepancy in  $\alpha$  described in Sec. 1.1.

The schematic view of the experiment is shown in Fig. 1.5. The main difference over the previous measurements in muonium is the change from a pulsed to a high-power CW UV-laser for the excitation, eliminating systematic effects such as chirp and residual 1<sup>st</sup>-order doppler shift.

Another big change is the unique Low-Energy Muon (LEM) beamline (90) at the Paul Scherrer Institute (PSI), which provides a continuous, intense  $\mu^+$  beam at around 10 keV energy. 590 MeV protons from the proton cyclotron at PSI are impinging on a graphite target, producing amongst other things pions, some of them stopping close to the target surface. The pions decay to  $\mu^+$  which are extracted at an energy of 4 MeV. These muons reach the solid gas moderator (91), where they are in a first step slowed down to around 15 eV and eventually are re-accelerated, continuing their path with an adjustable energy in the range between 1 to 20 keV. A first einzel lens (L1) focuses and an electrostatic mirror bends the beam by 90 deg, separating particles generated in the moderator from the actual  $\mu^+$ . The  $E \times B$  spin rotator rejects other particles, such as protons, with similar energy as the muons. Another einzel lens (L2) ensures the further continuation as a collimated beam. The  $\mu^+$  eventually reach a chamber, where for the  $\mu$ SR experiments at LEM a carbon foil and a tagging MCP are installed. For the purposes of Mu-MASS, this foil and detector are retracted. The last element of the LEM beamline is a conical lens to focus the beam on the target inside the Mu-MASS chamber.

The  $\mu^+$  beam enters the chamber, passing a carbon foil and releasing secondary electrons. These electrons are detected by an MCP, giving the start signal. Then, the  $\mu^+$  hits the cryogenic SiO<sub>2</sub> target, forming M(1S) and emitting it into vacuum. Two options of the Mu-MASS setup are then discussed:

- **Option A: Ionization of M(2S)**

The M(1S) goes first through the 1S – 2S laser, getting excited to the 2S state. It will then pass a second laser, which is used to ionize M(2S) (and not affecting M(1S)), releasing a free muon. This muon is then detected with an MCP. Alternatively, the second laser can excite the M(2S) to the 20P Rydberg state and the atom then gets field-ionized. This option would have the advantage of allowing to reconstruct the time-of-flight (TOF) and trajectory of the atom and therefore correct the 2<sup>nd</sup>-order Doppler shift. Both options were successfully set up in our laboratory at ETH and tested with positronium (92).

- **Option B: Quenching of M(2S)**

The M(1S) goes first through the 1S – 2S laser, getting excited to the 2S state. It will then leave the field-free zone, suddenly experiencing a strong electrical field. The field causes the M(2S) to get quenched into the 2P state, relaxing to the ground state while emitting a Ly- $\alpha$  photon at 122 nm. This photon is detected with dedicated MCPs, coated with either CsI or KBr. Additionally, the decay positron can be detected with scintillators. By using a parabolic quenching grid, the 2<sup>nd</sup>-order Doppler shift could be corrected as well by reconstructing the TOF.

The 1S – 2S CW UV-laser at 243 nm was built and shown to be stable for several hours at an intercavity power of 20 W (93). Other key elements such as the electrical quenching and detection of single Ly- $\alpha$  photons with MCPs of option B were tested and are explained in Chap. 4.

With a similar setup, but without the target, utilizing the muonium in the 2S state formed already at the carbon foil, and adding microwave regions in between

muonium formation and  $2S$  detection, a similar experiment as in Fig. 1.4 explained in Sec. 1.3 can be performed. The experiment to measure the Lamb shift of muonium, the culmination of this thesis work, is described and summarized in Chap. 5.

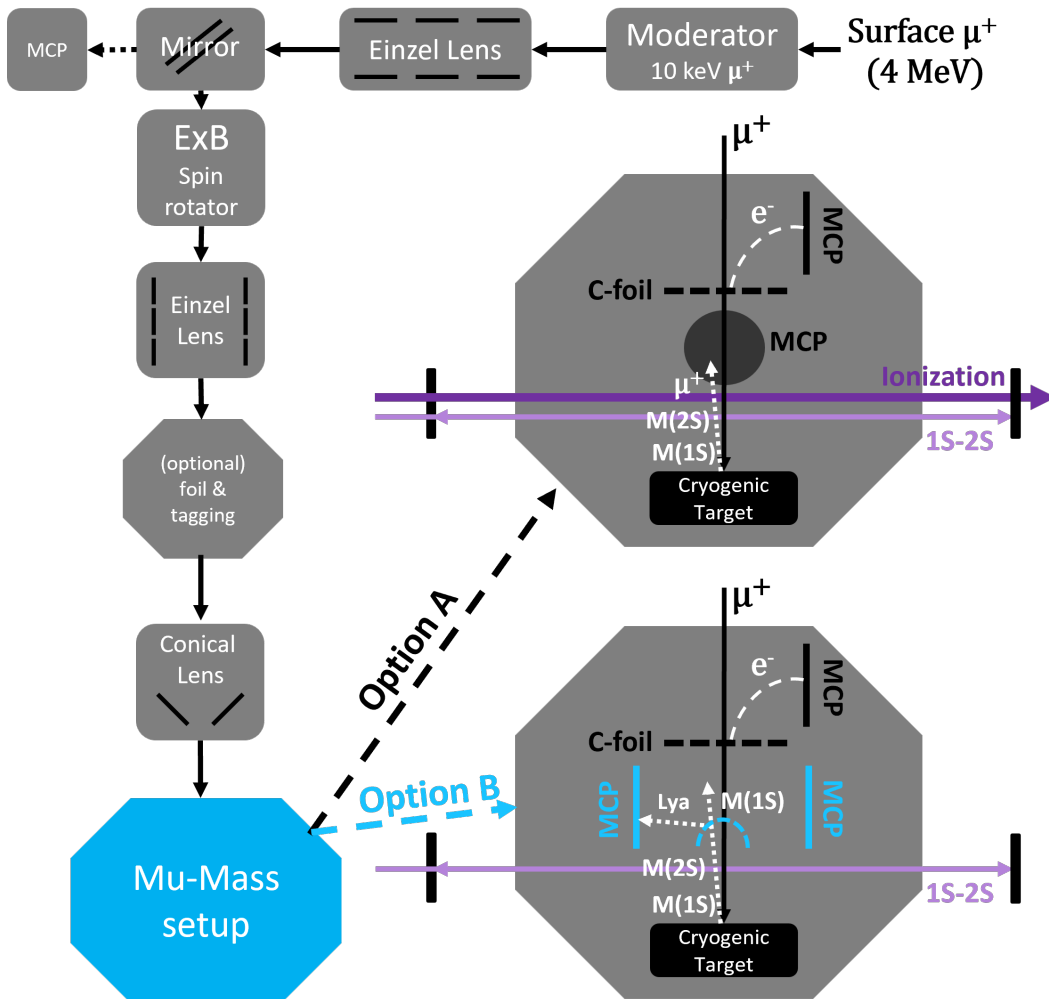


FIGURE 1.5: A schematic view of the Mu-MASS experiment including the LEM beamline. The Mu-MASS setup, marked in blue, was enlarged and two proposed detection methods shown. Option A shows the method with two lasers, one for the  $2S$  excitation and the other for the ionization of the muonium atom, eventually detecting the free muon with an MCP. Option B shows the method with a single laser for  $2S$  excitation and a quenching field to eventually detect the emitted  $\text{Ly-}\alpha$  photon. Option B, specifically studying the quenching of M(2S) and detection of the  $\text{Ly-}\alpha$  photon (marked in blue) is part of this thesis' work (Chap. 4) and culminated eventually in the measurement of the muonium Lamb shift described in Chap. 5.

## Chapter 2

# GBAR: Annihilation Vertex Detector

In the first section 2.1 of this chapter, I will give a general introduction about multiplexed Micromegas detectors. The requirements such Micromegas detectors have to fulfill to achieve the goal of GBAR were studied with the GBAR free fall simulation developed by D. Banerjee and improved by P. Blumer, described in Sec. 2.2.

Several ways to optimize the detectors, such as different multiplexing factors, to meet the requirements were tested and the results summarized in Sec. 2.3. These studies motivated a reduction of the multiplexing factor from 17 to 12, increasing the signal-to-noise ratio and reducing ambiguities caused by the multiplexing while keeping a good spatial resolution.

From the simulation it was also seen that in a large fraction of annihilation events, more than just one pion track will be detected by the same Micromegas triplet. With a multiplexed readout as described in Sec. 2.1.3, the hit position is often not easily visible. Due to multiple strips being connected to the same readout channel some positional information is lost, and while reversing the mapping several artificial hits will appear. In the general case with only one charged particle in the detector, it is often a very good assumption that the largest cluster in charge and width is the true hit. This can not be applied anymore in the case with multiple hits since the second true hit might be smaller than the fake hits created by the first one. Therefore, we developed a novel algorithm to unfold particle hit positions based on numerical minimization with the addition of a penalization term to prefer smooth, continuous solutions. The details of the method are published in (94). The general algorithm is explained with the help of an example step-by-step in Sec. 2.4.

We validated the algorithm for single as well as double hit reconstruction on data taken with Micromegas detectors similar to the GBAR prototype with multiplexing factor 17, as well as the final design for GBAR with a multiplexing factor 12. The results are presented in Sec. 2.5, showing a single hit reconstruction efficiency of around 83%, which is comparable to efficiencies obtained with methods by S. Procureur et al. on the same dataset. For double hits,  $\geq 80\%$  of the prior identified single hits could both be accurately extracted again.



## 2.1 Micromegas Detectors

Micromegas (MICRO Mesh Gaseous Structure) is a type of micropattern gaseous detector, invented by I. Giomataris and G. Charpak in 1995 (95). The typical spatial resolution of a Micromegas detector (MMD) is of the order of 10  $\mu\text{m}$  to 100  $\mu\text{m}$  and time resolution of 10 ns. In the last 20 years, the MMD has gained more and more popularity, for example being used to detect antihydrogen annihilations (ASACUSA, (96)), probe dark sectors (NA64, (97)), scan pyramids with muonic tomography (ScanPyramids, (98)), for the ATLAS New Small Wheels upgrade (99) and even for detecting nuclear material for Homeland Security (M-Cube, (100)).

### 2.1.1 Working Principle

A MMD consists of a gas-filled volume, separated into two gaps; the drift and the amplification gap. A sketch of a MMD is shown in Fig. 2.1.

In the drift gap, typically a few millimeters long, the incoming particle ionizes the gas atoms causing the release of primary electrons. These electrons are guided by a field of the order of 500  $\text{V cm}^{-1}$  to the micro-mesh, the starting point of the amplification gap. An optimal ratio between the field in drift and amplification gap ensures a high mesh transparency for the primary electrons to pass through (101). The field in the amplification gap is of the order of 50  $\text{kV cm}^{-1}$  to accelerate the primary electrons to an energy where they efficiently ionize the gas atoms again, releasing more electrons and kicking off an avalanche process. The amplification gap is typically only 128  $\mu\text{m}$  wide, to avoid having a large spatial spread of the avalanche as well as to be able to use still a moderate high voltage. The avalanche eventually reaches the end of the amplification gap and impinges onto anode strips, which collect the signal to be read out.

In the case of GBAR, resistive XY MMDs are used. The word resistive refers to the layer of resistive strips, acting as the anode. The combination of a narrow amplification gap and necessity for high detection efficiency and hence a high amplification field bears a risk of voltage breakdowns and sparks. The layer of resistive strips smears out the charge more and thus reduces the chance of sparking. This in turn allows for applying a higher voltage and hence achieving a higher gain (102). Additionally, sparks neutralize by flowing from the resistive strips through a resistor to ground, avoiding a long detector dead time. The readout strips lie below the resistive strips, separated by a thin insulating layer. They are capacitatively coupled to the resistive strips, so the induced signal can be read out. The XY in the name refers to the two differently oriented planes of readout strips. The first plane of strips (Y) is rotated by 90 deg, the second plane (X) is parallel relative to the resistive strips, making it possible to reconstruct the hit in 2D. The entire circuit including strips is printed on a circuit board (PCB), where the pillars are also attached to hold the micro-mesh in place.

### 2.1.2 Choice of Gas

The gas mixture flowing through the MMD is a crucial element to ensure high detection efficiency, stable over a long time. Typically, the gas mixture consists of a noble gas and a quencher. The noble gas, such as argon or neon, is chosen as the main source of primary electrons due to it being inert while still providing a high ionization yield.



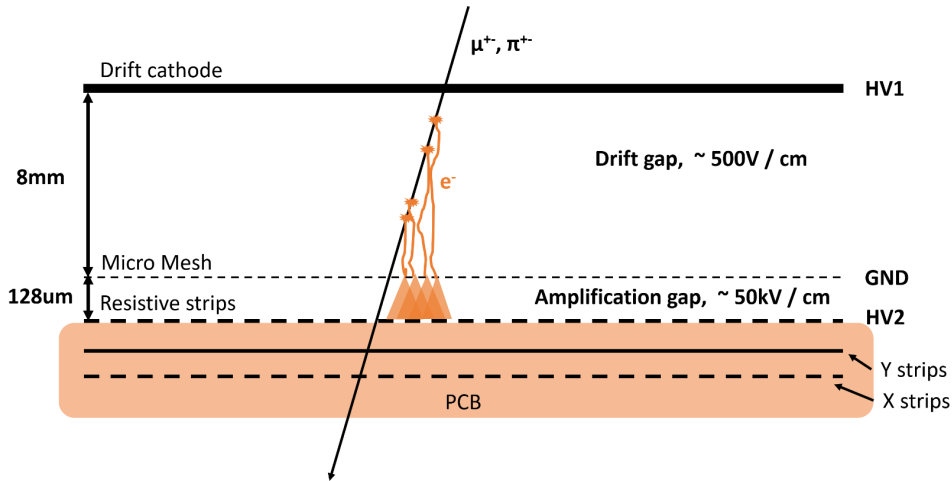


FIGURE 2.1: The sketch of the working principle of a Micromegas detector.

When accelerated electrons interact with the gas, there is also a chance of excitation. When the excited atoms relax back to the ground state, they emit UV photons. These photons have a rather long mean free path ( $> \text{mm}$ ) in a noble gas and can excite gas atoms much further away. These excited atoms are very reactive and can through the Penning effect (103; 104) ionize other atoms as well, potentially starting off a new avalanche. This would lead to a spreading out of the original avalanche and increase the chance of sparks. The quencher is added to the mixture to absorb the UV, mediating the avalanche process. Efficient quenchers are for example  $\text{CO}_2$ ,  $\text{CF}_4$ , DME or isobutane ( $\text{iC}_4\text{H}_{10}$ ). Preferentially, gas mixtures such as Ar- $\text{CO}_2$  (93%-7%) or the T2K gas Ar- $\text{CF}_4$ - $\text{iC}_4\text{H}_{10}$  (95%-3%-2%) are used since they are non-flammable and have full efficiency for most of the MMDs. In the case of large and highly multiplexed MMDs, the high input capacitance might force consideration of flammable mixtures such as Ar- $\text{iC}_4\text{H}_{10}$  (95%-5%), which has a higher gain (mainly due to its better ionization potential (105)), but is more difficult to handle.

Studies on the specific gain of different percentages of the quencher fraction have been made, for example for  $\text{CO}_2$  (106) and  $\text{iC}_4\text{H}_{10}$  (107), or in general as a comparison between different gas-mixtures (108).

### 2.1.3 Genetic Multiplexing

The larger the active area of a XY MMD, the more electronics are needed to read out the signal and thus the costlier it gets. A way to reduce readout channels is to use a method called genetic multiplexing, proposed by S. Procureur et al. (109).

A particle usually leaves a signal spread out over multiple strips in the detector, leading to more information than is actually needed to extract the hit position. With genetic multiplexing, a map is created which links a specific group of strips to a single readout channel. How many strips these groups contain corresponds to the multiplexing factor  $m$ . To keep the level of ambiguity introduced by the multiplexing (i.e. the amount of valid artificial clusters) as low as possible, an optimal map needs to be calculated. For a MMD with  $p$  readout channels, where  $p$  is supposed to be a prime number, one generates  $(p-1)/2$  sub-lists for the ordering of  $p \cdot m$  strips. The ordering is given by

$$\mathcal{O} = 1 + [(i \times s) \bmod p] \quad (2.1)$$

where  $i$  ranges from 0 to  $p-1$  and  $s$  is the number of the sub-list. Examples of these maps are shown in Fig. 2.2 for a multiplexing factor of 12 and 17. These maps were generated with the code attached in the Appendix B.1.

From the detectors response, which will be a certain amount of charge collected on every channel, the map needs to be eventually reversed to see the clusters in strip space. In general, the true cluster can then be distinguished from the artificial clusters in terms of largest total charge and width. An example for a signal extraction of a MMD with multiplexing factor 12 is shown in Fig. 2.3, where the black signals are artificial clusters created by the multiplexing and the orange the true cluster. The reduction of electronic channels through multiplexing comes at the cost of a larger input capacitance per strip, leading to a degradation of the signal-to-noise ratio S/N.

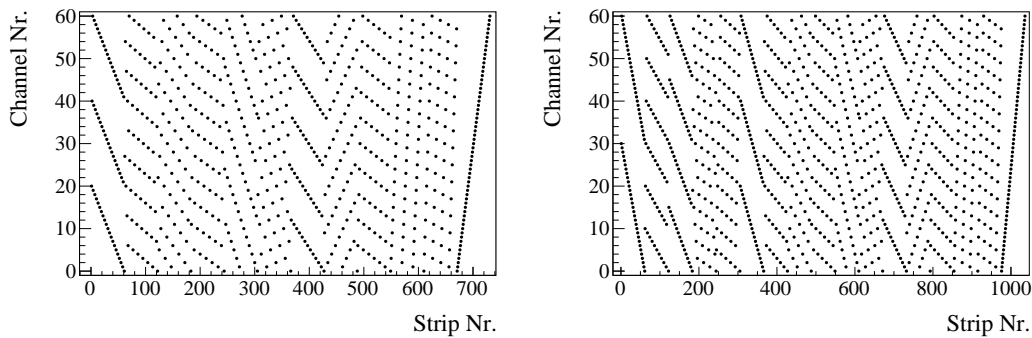


FIGURE 2.2: The multiplexing pattern generated by the algorithm for multiplexing factors of 12 (left) and 17 (right).

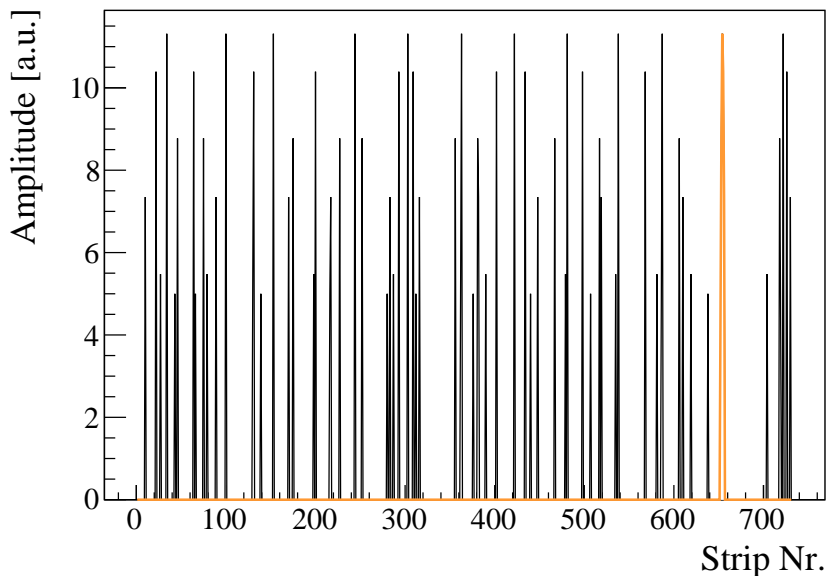


FIGURE 2.3: The example of a signal extraction of one MMD with multiplexing factor 12. The black lines correspond to the raw multiplexed data, whereas the orange line is the true hit.

## 2.2 Free Fall Simulation

The free fall simulation was developed by D. Banerjee (84) and further improved by P. Blumer. It is based on the Geant4 toolkit for simulating particle passages through matter (110). In the center of the free fall chamber, the antihydrogen atoms are released and their free fall in a gravitational field simulated. An example of such an implementation is shown in Fig. 2.4. Once it comes into contact with matter, the antihydrogen atom annihilates and releases on average 3 charged pions. In the simulation, the annihilation vertex position as well as the pion hits in each MMD are recorded. With a tracking algorithm, these individual hits are used to study how accurately the vertex position can be determined. From this study, the requirements on the MMDs about resolution, minimum efficiency as well as positioning around the chamber can be extracted.

It was shown that primarily the multiple scattering at the chamber walls is adding to the uncertainty of the vertex reconstruction, and thus the MMDs need to be placed as close as possible to the chamber itself to reduce its leverage effect. This would mean to find a compromise between reducing the drift gap of the MMD, while still maintaining a high detection efficiency for the incoming pions.

Further important information was found about the multiplicity of pion hits in a single MMD. For a single annihilation event, it was seen that in 39.4% of the cases, a single MMD needs to be able to resolve two hits and in 6.6% even three at the same time. With a highly multiplexed readout, a multiple hit reconstruction is non-trivial due to the charge sharing between multiple strips. Since such an annihilation event can be considered a rare event, only happening in the best case every 110 s due to the AD cycle, one of the objectives must be to have a large solid angle covered with the MMDs, but also maintain a high reconstruction efficiency. Therefore, a combination of a robust method to reconstruct multiple hits as well as optimized MMD characteristics such as continuity and narrowness of the clusters to simplify a hit reconstruction needed to be found.

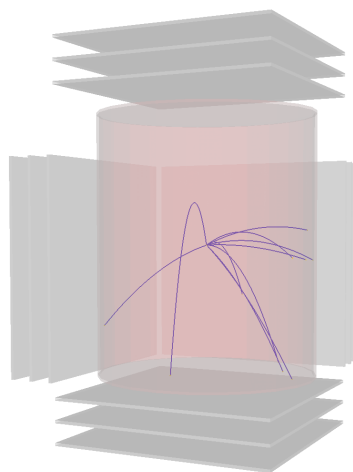


FIGURE 2.4: The cylindrical free fall chamber (red) surrounded by MMD triplets (gray) as implemented in Geant4. In the center of the chamber, antihydrogen atoms are released and their free fall simulated until coming in contact with matter (blue tracks). From there, the MMDs detect pion tracks coming from the annihilation (not shown).

### 2.3 The GBAR Micromegas

The conditions coming from the free fall simulation described in Sec. 2.2 would require a MMD with a drift gap as short as possible, with continuous but narrow clusters, while still keeping full detection efficiency and as little as possible ambiguities introduced by the multiplexing. With a multiplexing factor of 5 and an active area of  $64 \text{ cm}^2$ , an efficiency  $\geq 95\%$  can be reached with an electronic readout based on APV chips and an Ar-CO<sub>2</sub> mixture as shown by the NA64 collaboration (97). For highly-multiplexed MMDs with an active area of  $50 \times 50 \text{ cm}^2$ , first tests with a design proposed in (84), called the GBAR prototype, showed that a different gas mixture as well as another readout for large input capacitance detectors needed to be identified.

To further optimize such a design, we collaborated with S. Procureur to study the MGv0 prototype with multiplexing factor 17 and an active area of  $50 \times 50 \text{ cm}^2$ , characterized already in (111). The findings were summarized in (112), a manuscript is currently in preparation.

The advantage of this prototype is that the multiplexing bus is located outside the active area, on top of the PCB. It was therefore possible to cut strips, reducing in a destructive way the multiplexing factor one by one. To characterize the signal-to-noise ratio as well as the resolution for each multiplexing factor, a cosmic testbench was set up, shown in Fig. 2.5, consisting of four well characterized MMDs as reference and in the center the modified prototype. The gas mixture used was Ar-iC<sub>4</sub>H<sub>10</sub> (95%-5%), circulating with a flow of  $3 \text{ L h}^{-1}$ . As readout electronics, the DREAM Asic (113), developed for high input capacitance detectors, was used.

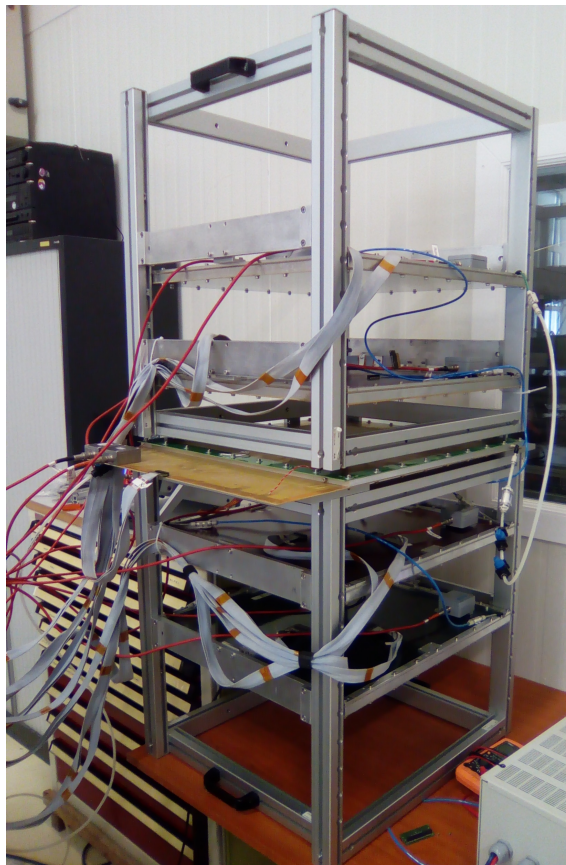


FIGURE 2.5: The cosmic testbench in Saclay to study the impact of the multiplexing factors on signal reconstruction of an MMD

The results are shown in Fig. 2.6 for the resolution and for the signal and noise levels depending on multiplexing. The resolution stayed throughout the measurements constant, independent of the multiplexing factor. The dominant property determining the resolution of a MMD is its pitch, which remained unchanged in the tests. The theoretical resolution  $\sigma_{\text{Res}}$  can be estimated via:

$$\sigma_{\text{Res}} = \frac{\text{pitch}}{\sqrt{12}} \quad (2.2)$$

The noise level did increase slightly for increasing multiplexing factors, but eventually reached a plateau at around a multiplexing factor of 8. The signal amplitude is shown to go linearly down with increasing multiplexing factor.

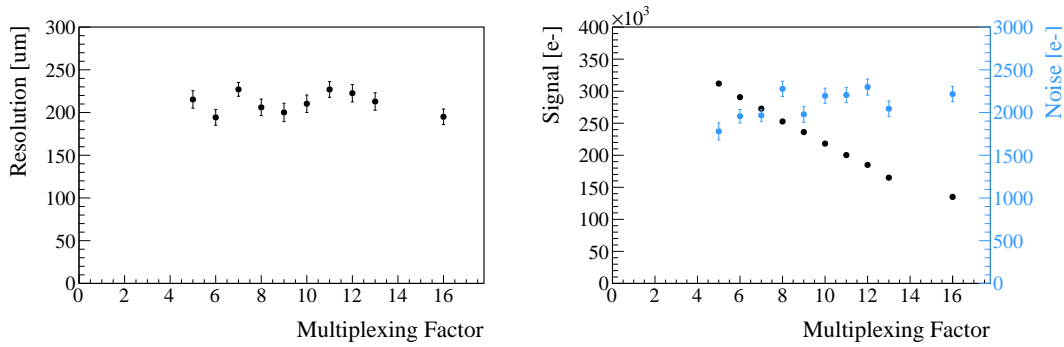


FIGURE 2.6: The scans of a MMDs resolution (left) and signal-to-noise (right) depending on the multiplexing factor.

A simulation was written to study the double cluster reconstruction depending on the multiplexing factor. As input, the cluster size distribution for a m17 MMD was used, allowing tracks up to 40 deg, comparable to the scenario in GBAR. The active area was kept constant at  $50 \times 50 \text{ cm}^2$  as well as the maximally used readout channels  $p$  of 61. The amount of strips ( $p \cdot m$ ) and the pitch ( $\frac{50 \text{ cm}}{p \cdot m}$ ) had to be adjusted accordingly for each multiplexing factor  $m$ . A *tough event* was defined to be a hit sharing more than 25% of the channels with the second hit. The results of the simulation is shown in Fig. 2.7.

By combining the information obtained about the S/N and the tough events, one would chose a small multiplexing factor to achieve a high S/N as well as a high

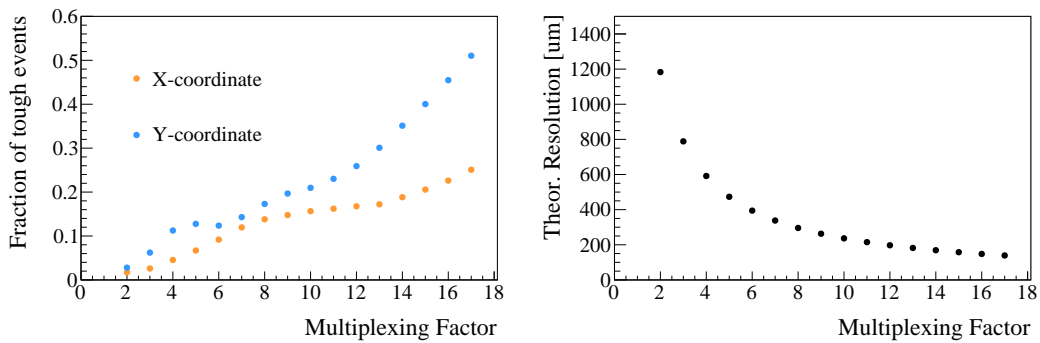


FIGURE 2.7: The simulation scan of a MMDs probability to have tough events to be reconstructed in the case of double hits (left) and the theoretical resolution (right), depending on the multiplexing factor.

chance of being able to reconstruct multiple hits events. This would lead to a large resolution, making it difficult to get a precise vertex position for GBAR. Moreover, with a large pitch, the chance of a pion firing only a single strip is much higher, making it impossible to extract a hit position. Taking everything into consideration, a compromise was found to reduce the multiplexing factor from 17 to 12 and increase the pitch from  $482\ \mu\text{m}$  to  $683\ \mu\text{m}$ . All the specifications are summarized in Tab. 2.1.

21 of such Micromegas have been given into production in 2019 and the first ones arrived at GBAR assembled in October 2021, being currently tested and characterized. A picture of an assembled GBAR MMD is shown in Fig. 2.8.

TABLE 2.1: The specifications for the GBAR MMD as obtained by the studies from S. Procureur and the GBAR Prototype as suggested by (84).

	GBAR MMD	GBAR Prototype
Active Area	$50 \times 50\ \text{cm}^2$	$50 \times 50\ \text{cm}^2$
Multiplexing Factor	12	17
Number of Strips	732	1037
Pitch	$683\ \mu\text{m}$	$482\ \mu\text{m}$
Resolution	$197\ \mu\text{m}$	$140\ \mu\text{m}$
Y-Strip Width	$200\ \mu\text{m}$	$100\ \mu\text{m}$
X-Strip Width	$583\ \mu\text{m}$	$380\ \mu\text{m}$
Gas mixture	Ar-C <sub>4</sub> H <sub>10</sub> (95%-5%) or T2K	Ar-CO <sub>2</sub> (93%-7%)
Readout Electronic	DREAM Asic	SRS & APV25 Asic
Drift Gap	6 - 10 mm*	8 mm

\* The drift gap was not decided on yet and will be tested with different frames during the characterization.

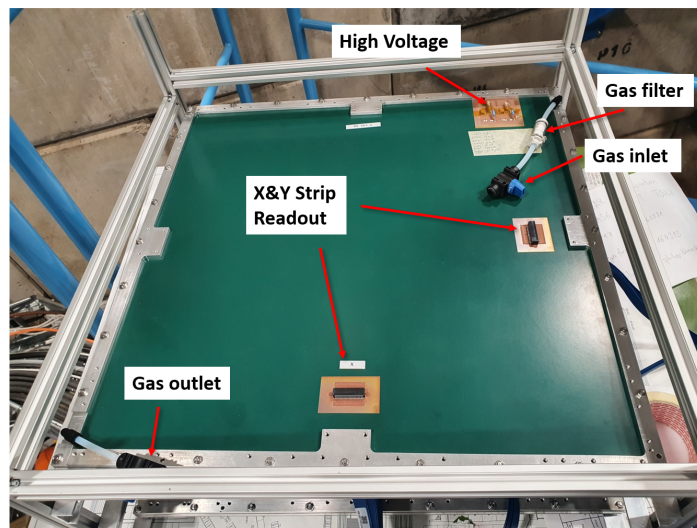


FIGURE 2.8: A MMD for the GBAR trackers assembled, currently located in the GBAR zone at CERN.



## 2.4 Hit Reconstruction

### 2.4.1 Pre-Processing of Signal

Due to the multiplexed readout, the raw signal consists of 61 waveforms, one per each channel. The waveform recorded with the DREAM electronics is 50 time samples long, each time sample corresponds to 25 ns. An example of all 61 waveforms overlaid is shown in Fig. 2.9. The waveforms colored in orange correspond to a common-mode signal that is eventually subtracted from the raw data.

For the further analysis, a typical approach is to either continue with the maximal amplitude of each waveform or its maximal slope. For the unfolding algorithm, a better performance was achieved by choosing the square-root of the maximal slope. The data is corrected for the common-mode signal by subtracting the median response over all channels and an additional 10 % to account for larger oscillations. As an example in Fig. 2.9, the median response is at roughly 4.3 and therefore a value of 4.8 is subtracted from each channel. As a last step, the data is transformed from channel to strip space by reversing the multiplexing map, shown in Fig. 2.10 in black.

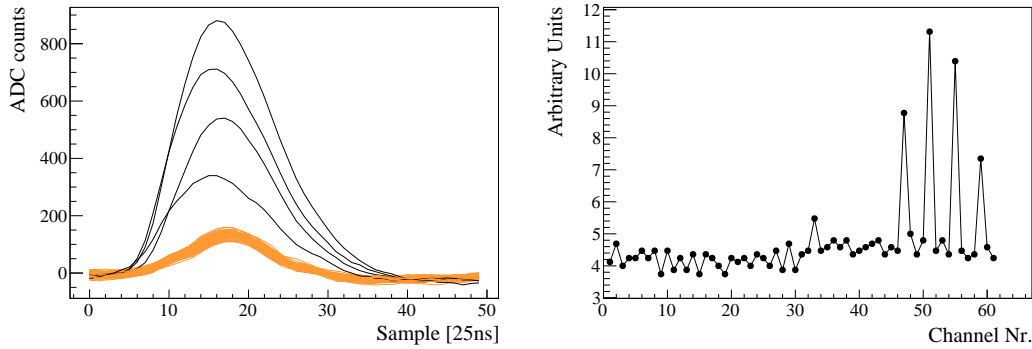


FIGURE 2.9: Example of typical waveforms collected with a MMD over all channels (left) and its representation in channel space (right)

### 2.4.2 Unfolding Algorithm

In a classical problem, where the vector  $\vec{b}$  is measured and the transformation matrix  $A_{p \times n}$  known, the solution can be found by solving the set of linear equations of:

$$A\vec{x} = \vec{b} \quad (2.3)$$

where  $\vec{x}$  is the underlying solution. In most of the cases, the dimensions of the matrix  $A$  are the same ( $n=p$ ), meaning that there is only one unique solution. In the multiplexed case,  $n$  is a multiple of  $p$  and therefore there are more unknown parameters than equations. A popular choice to deal with such kind of problems is the Tikhonov regularization (114; 115). By changing the problem from an under determined linear equation system to a minimization problem and introducing a penalizing term to highlight special properties of the data, a numerical solution can be found. The equation to be minimized is:

$$\min_{\vec{x} \in \mathbb{R}^n} \{ \|A\vec{x} - \vec{b}\|^2 + \lambda^2 \|L\vec{x}\|^2 \} \quad (2.4)$$

where  $L\vec{x}$  is the regularization term and  $\lambda$  is a tuning factor that decides how strongly the penalization is applied. The best results with multiplexed Micromegas were obtained by choosing  $L$  to be the second-order finite difference matrix. In this case, the regularization term is penalizing highly oscillating clusters, where smooth and continuous clusters are highlighted.

$$L = \begin{pmatrix} 2 & -1 & 0 & \cdots & 0 \\ -1 & 2 & -1 & \cdots & 0 \\ 0 & -1 & 2 & \cdots & 0 \\ \vdots & \vdots & & \ddots & \vdots \\ 0 & 0 & \cdots & -1 & 2 \end{pmatrix} \quad (2.5)$$

As a numerical minimization program, Minuit in combination with ROOT is used (116). To speed up the minimization, the matrices are defined within the Eigen C++ library for linear algebra (117). Furthermore, the degree of the problem is reduced by fixing the strips not fired to 0, which are afterwards not considered in the minimization.

The result of such a minimization is shown in Fig. 2.10, where the black data is corresponding to the dataset before minimization and the orange one after. In average, such a minimization takes around 20 s on a single 2.2 GHz CPU core.

The code snippets to build the minimization function is show in the Appendix B.2, the actual unfolding in Appendix B.3. The minimized solution is fed to a cluster finder algorithm to extract information about total charge and position.

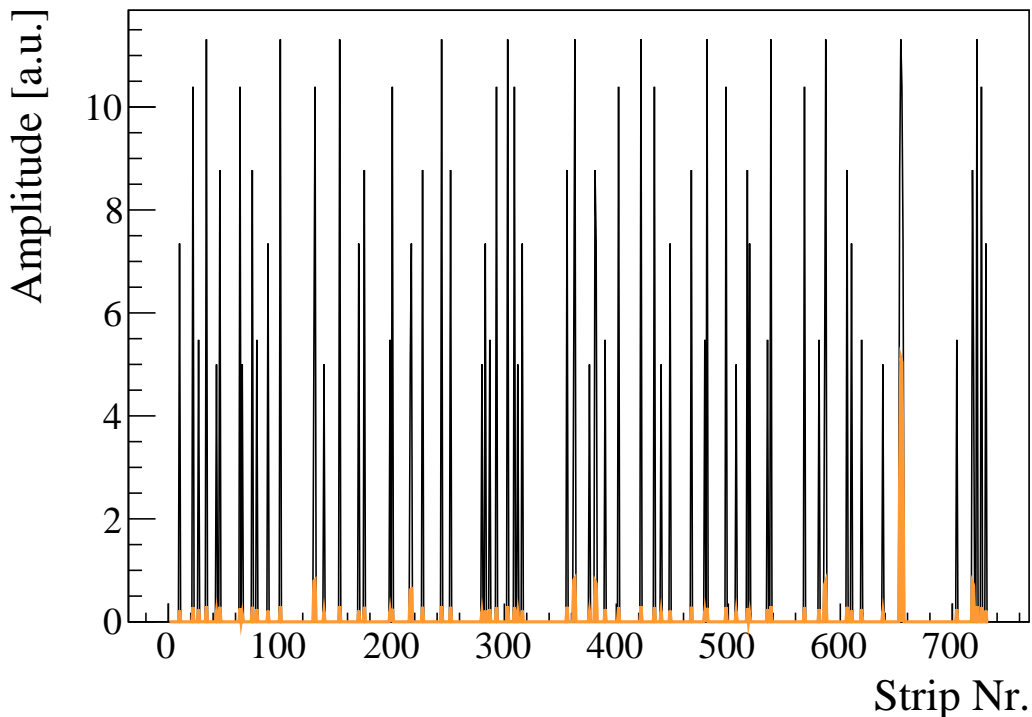


FIGURE 2.10: An example of signal extraction of one MMD plane with the unfolding algorithm. In black the raw multiplexed data is shown, whereas the orange area represents the solution returned by the unfolding algorithm.



### 2.4.3 Cluster Finder Algorithm

The cluster finder loops over all the ordered strips starting from strip number 0, checking the amplitude value. Since the minimized solution still contains residual oscillations, the cluster finder algorithm only considers strips that are above a pre-set amplitude threshold to suppress noise. It is typically set on a low level, since afterwards the clusters stemming from residual oscillations can be rejected with total cluster charge and cluster width cuts. Examples of typical cluster size and area distributions are shown in Fig. 2.11. These distributions are created beforehand by assuming the largest cluster found in total accumulated charge is representing the hit cluster, ignoring the chance of having multiple hits.

Once a strip above noise level is found, the cluster finder starts integrating the charge over the next strips and calculates the weighted mean position until the threshold condition does not hold anymore. After passing all the minimal requirements of a cluster, its information is stored and the algorithm continues to look for a next one.

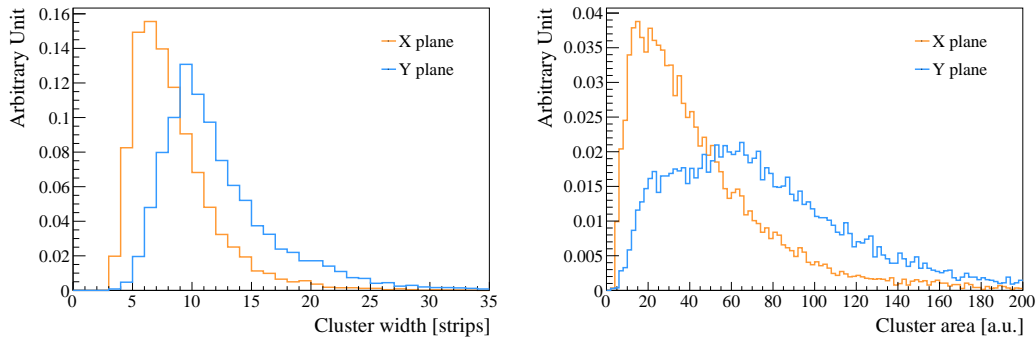


FIGURE 2.11: An example of a typical cluster size (left) and cluster area distribution (right). The orange lines correspond to distributions from the X-plane, whereas the blue to the Y-plane of a MMD.

## 2.5 Comparison of different MMD

A similar telescope arrangement as described in Sec. 2.3 was used to collect data to be analysed with the unfolding algorithm. A first analysis was done on four MMDs with multiplexing factor 17 used for muography projects (98), which were placed in a telescope at  $z=(0, 100, 450, 550)$  mm and operated with an Ar- $i$ C<sub>4</sub>H<sub>10</sub>(95%-5%) gas mixture. Another telescope arrangement with  $z=(0, 70, 200, 270)$  mm was used to measure cosmic tracks with MMDs similar to the GBAR MMD in Tab. 2.1 with multiplexing factor 12 and the T2K gas mixture.

For a single cosmic event, both the X and Y plane of all the four MMDs were analysed and the hit positions extracted by using the unfolding algorithm presented in Sec. 2.4. An example is shown in Fig. 2.12. The colors correspond to the hit position in  $z$ ; 0mm (orange), 70mm (blue), 200mm (gray), 270mm (black). Since the tracks are not as clear in every case as in the example, a tracking algorithm was written to determine the actual hit positions.

### 2.5.1 Tracking Algorithm

For every possible track made with three MMD firing, the most outer two hits were chosen and a line drawn. The third hit, being in the middle of the other two, was used to calculate its distance from that line. This distance corresponds to the residual of the reconstruction and is taken as a figure of merit for the track. In the case of all four MMD firing, all the possible combinations with only three MMD involved are considered and the one with best residual chosen. Once the best track with smallest residuals was identified, all the artificial hits linked with the optimal ones were deleted. The residuals both in X- and Y-coordinate need to be both smaller than 5 mm to be accepted. Afterwards, the tracking algorithm starts again to find a next track fulfilling the cut requirements.

In the example of Fig. 2.12, the orange MM1 showed three possible hit positions in the y-plane. With the tracking, two could be eliminated; the same happened for the artificial hit for MM2 in blue and MM4 in black. MM2 and MM4 were taken as the outer two hits and the distance from their line to MM3 gave the residuals. In the end, MM1 was not required for this event reconstruction.

Through analysing all events taken with the telescope, the angle distribution and a residual distribution can be built, as shown in Fig. 2.13. A total of around 82 % single and 1 % double tracks were found with the unfolding algorithm, independent of the telescope arrangement.

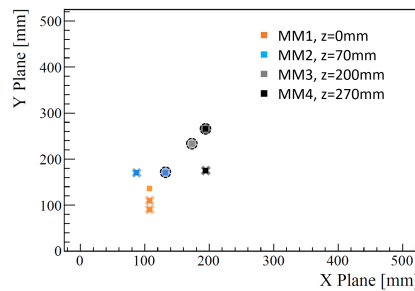


FIGURE 2.12: An example of a reconstructed single track going through four MMD. The different MMDs are marked with the colors orange (MM1), blue (MM2), gray (MM3) and black (MM4). The ghost hits marked with crosses were rejected by the tracking algorithm, the circled hits were accepted.

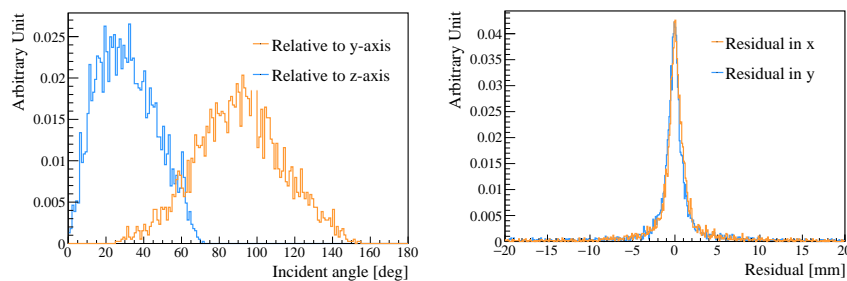


FIGURE 2.13: An example of the angle distribution of the incoming particles (left). The orange distribution corresponds to the incoming angle relative to the y- and the blue relative to the z-axis. On the right side, the distributions of residuals in x (orange) and y (blue) coordinate from a perfectly straight line are shown.

### 2.5.2 Extraction of Double Hits

Knowing from the single track reconstruction the actual hit positions of the cosmic particles, two separate events were merged into one by adding their measured vectors  $\vec{b}_{\text{merged}} = \vec{b}_i + \vec{b}_{i+1}$ . The merged dataset was afterwards analysed in the exact same way as the single hits with the unfolding algorithm.

To determine the fraction of events where both single hits can be retrieved again, the residual distribution from the position difference of known hit and extracted hit, both in X and Y coordinate, was built. An example is shown in Fig. 2.14. An acceptable residual of 1 mm was chosen, with a range of  $\pm 0.5$  mm.

The performance of the different MMD is summarized in Tab. 2.2. The results are given for the three different residual cuts; the value quoted is for 1 mm, the ones in super- and subscript are for 1.5 mm and 0.5 mm, respectively. For MMD with multiplexing factor 12, a high efficiency in both X- and Y-coordinate is achieved with a residual cut of 1 mm of 95 % and 92 %, respectively, leading to a 2D hit reconstruction efficiency of 87 %. The dataset for the GBAR prototype was taken with the Ar- $i$ C<sub>4</sub>H<sub>10</sub> gas, which has a higher gain than the T2K mixture used for the GBAR MMD, leading to an efficiency of 81 %.

The improvements due to reducing the multiplexing factor as well as significantly increasing the resistivity of the resistive strips clearly outweigh the choice of the gas mixture. This allows us to still use the non-flammable and easy to handle T2K gas, while having a better overall detector performance. A more detailed scan of every separate detector in the telescope is shown in the Appendix A.2.

TABLE 2.2: Summary of the results for double hit reconstruction with different MMDs, analysed with the unfolding algorithm.

MMD	Gas	Resistivity (M $\Omega$ /sq)	Double Hit Efficiency [%]		
			X-Plane	Y-Plane	XY-Plane
GBAR (m12)	T2K	$\geq 2$	95 <sup>+1</sup> <sub>-3</sub>	92 <sup>+1</sup> <sub>-5</sub>	87 <sup>+3</sup> <sub>-6</sub>
Prototype* (m17)	5 % $i$ C <sub>4</sub> H <sub>10</sub>	$\sim 0.4$	91 <sup>+0</sup> <sub>-4</sub>	89 <sup>+1</sup> <sub>-5</sub>	81 <sup>+1</sup> <sub>-8</sub>

\* The data were from the MMD used for the muography (98), but are of same type as the GBAR prototype.

With each MMD plane having two hits, it is not straightforward to know which X- and Y-coordinate should be paired to build a track. Therefore, always four possible track solutions are visible, where only two are true and two are fake. Additionally, artificial clusters that passed the cuts increase the possibilities of tracks and make the hit map more crowded, which in turn makes it more difficult to identify the true solution by eye. An example is shown in Fig. 2.15. The true solution is colored and circled with a dashed line, the symmetric fake solution is only colored. The artificial hits were crossed and rejected by the tracking algorithm.

To get rid of symmetric fake solutions, additional information needs to be looked at in the algorithm. One way could be to correlate the cluster area in X and Y plane to reject the artificial hit. In the case of GBAR, the knowledge of a common origin of the tracks, the annihilation vertex, will be useful to find the true tracks.

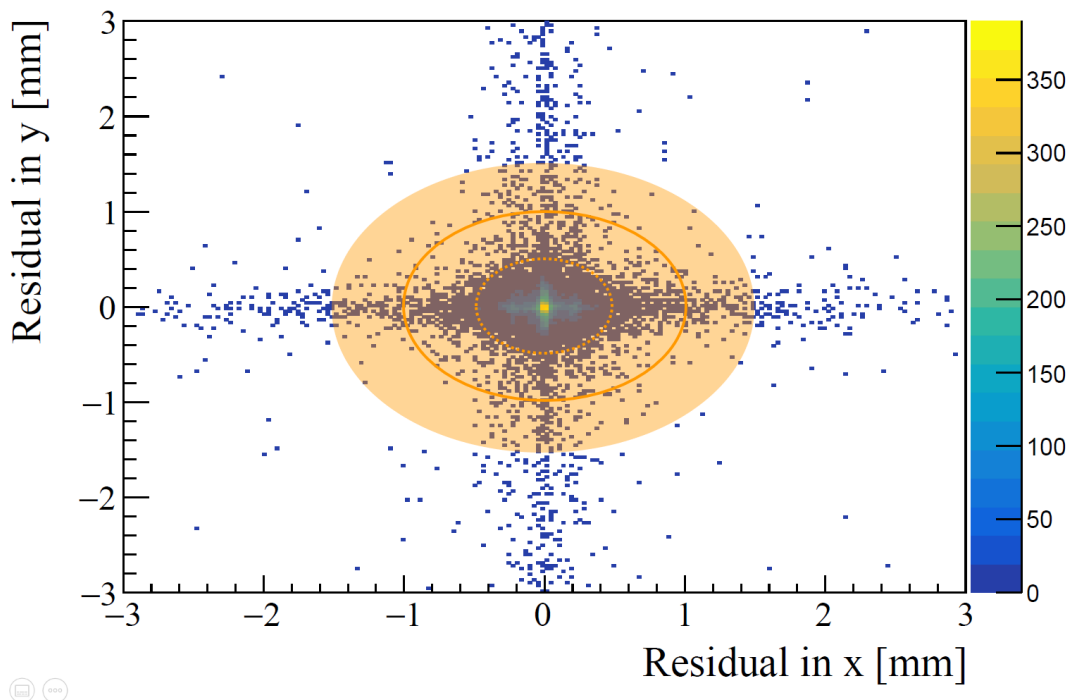


FIGURE 2.14: An example of a MMD plane residuals for double hits, analyzed with the unfolding algorithm. The three zones show the residual cuts for 0.5, 1 and 1.5 mm.

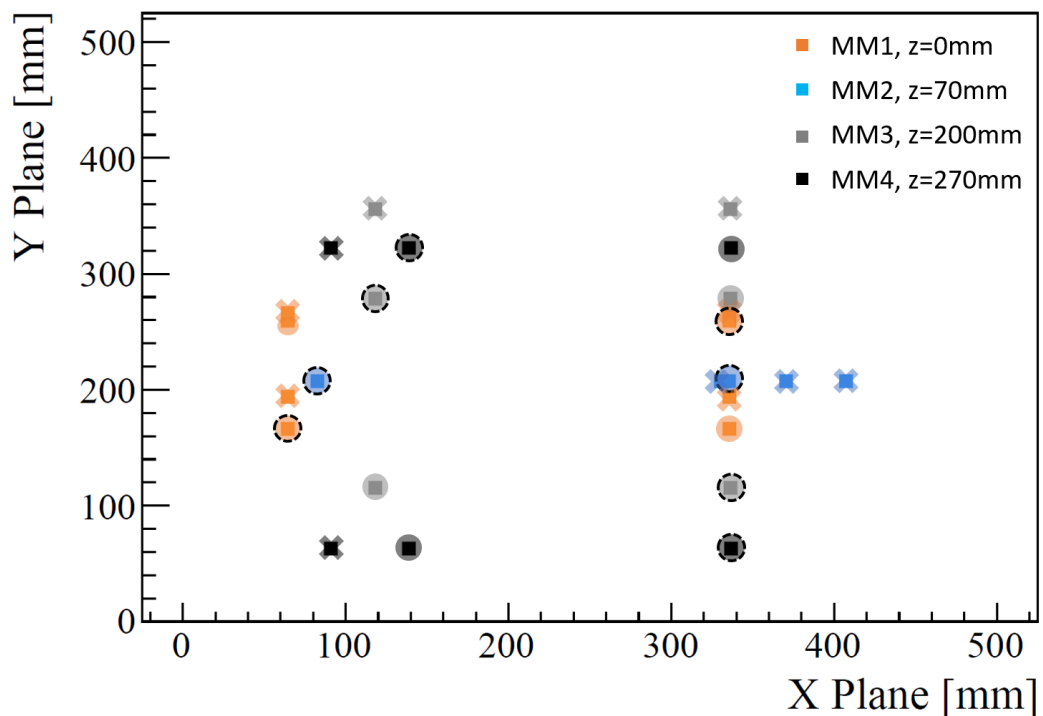


FIGURE 2.15: An example of a reconstructed double track going through four MMD. The different MMDs are marked with the colors orange (MM1), blue (MM2), gray (MM3) and black (MM4). The artificial hits marked with crosses were rejected by the tracking algorithm, the colored and dashed circled hits were accepted. The hits only colored are part of the symmetric fake solution.

## Chapter 3

# The Lamb Shift

In this chapter, we review the history and the theory of the Lamb shift. We start in Sec. 3.1 with a historical flashback of the atomic model and the first measurement of the Lamb shift in hydrogen, motivating the pursuit of developing the field theory of Quantum Electrodynamics (QED).

In Sec. 3.1.1, the advances in lowering the experimental uncertainty of the hydrogen Lamb shift are summarized. The first attempts of precision measurements of the muonium Lamb shift are covered in Sec. 3.1.3. Due to the lack of low-energy muons of the order of 10 keV necessary for an efficient muonium production via beamfoil technique, the muonium Lamb shift measurements were limited by statistics. The technique, including the possibility of forming excited states higher than  $M(2S)$ , is explained in Sec. 3.2.2.

With the measurements in hydrogen, the correctness of QED was tested repeatedly with improved uncertainties, which drove theoretical physicists to also improve upon the uncertainty of the QED calculations. However, the last update on the theoretical value for muonium was given by J. R. Sapirstein and D. R. Yennie in 1990 (118). In Sec. 3.3 we review the QED corrections concerning the Lamb shift known to this day, evaluate them for muonium and compare them to hydrogen. The comparison between the two atoms helped to identify the effects of the Barker-Glover correction as well as the nucleus self-energy to be more dominant in muonium due to its smaller nuclear mass. We set the levels of 160 kHz (Barker-Glover, higher-order recoil) and 40 kHz (nucleus self-energy) as goals for future muonium Lamb shift measurements, since these effects are below the level of the latest measurement in hydrogen and thus could not be tested yet.

In Sec. 3.4, the possibility of probing new physics beyond the Standard Model such as Lorentz and CPT violation or new muonic forces is described. In order to study the line-shape of the Lamb shift transition, in Sec. 3.5 the optical Bloch equations for a two-level system are derived and approximately solved to obtain a Lorentzian model for the transition and quenching rate.

### 3.1 History

The discovery of the electron by J. J. Thomson in 1897 (119), awarded with a Nobel prize in 1906, was the start of describing the atom composed of multiple particles. In Thomson's model called the "plum pudding", the atom was imagined to be a spherical cloud of positive charge, which also contains negatively charged electrons scattered throughout. When E. Rutherford and co-workers in 1911 shot alpha particles on a thin gold foil and looked at their scattering angle, he found that most of the particles went almost straight through, but a few were scattered at an unusually large angle (120). The only explanation for his findings was that the atom actually consists mostly of empty space, and the mass is concentrated in a positively charged

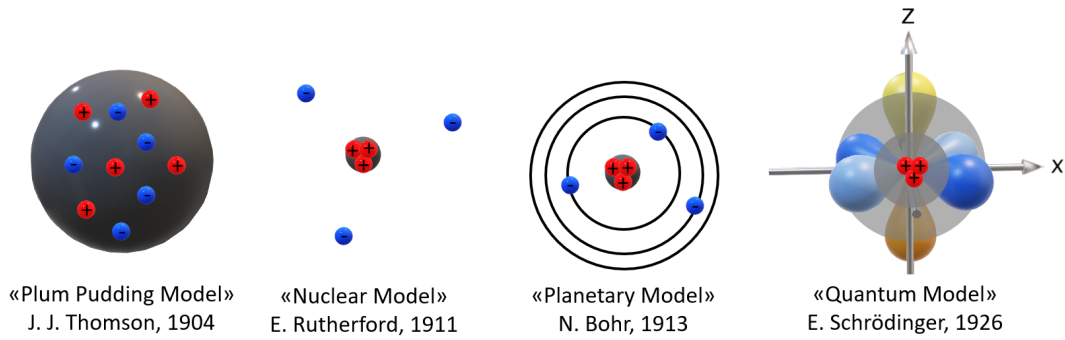


FIGURE 3.1: Simplified schematics of the atomic models in history.

nucleus in the center. Bohr picked up Rutherford's model in 1913 and added the electrons spinning around the nucleus in fixed orbits, introducing the quantization of the electron energy (121). With this model, the empirically found equation by J. Balmer and J. Rydberg (122) to calculate the hydrogen spectral lines was finally explained:

$$E_n = \frac{E_R Z^2}{n^2} \quad (3.1)$$

where  $E_R$  describes the Rydberg energy of  $-13.6\text{eV}$ ,  $Z$  the atomic number and  $n$  the principal quantum number. The atomic model by Bohr was extended until 1917 by A. Sommerfeld, introducing additional quantum numbers such as the azimuthal quantum number  $l$  and the magnetic quantum number  $m_l$ , being able to explain the observed fine structure in hydrogen(123). The Stern-Gerlach experiment (124) was thought to test the Bohr-Sommerfeld model and the results seemed to confirm it (125). Only later in 1926 G. E. Uhlenbeck and S. Goudsmit found the actual reason for the observed splitting by discovering the electron spin (126). Bohr was awarded the Nobel prize for his model in 1922. One of the main issues of his model was though that it could not explain why the electrons stayed on their fixed orbit and would not lose energy radiatively, eventually collapsing into the nucleus.

With the rise of quantum mechanics and the formulation of the Schrödinger equation by E. Schrödinger in 1926 (127), this problem was solved. The orbits were replaced with clouds which have a certain probability to have an electron inside, called orbitals. The bound electron does not have an identifiable position or a fixed path to follow as in the classical interpretation. Therefore, it also has no acceleration assigned, no resulting emission of radiation and no energy loss due to its movement. The evolution of the picture of the atom is shown in Fig. 3.1. P. Dirac expanded the formulation, including the conditions of special relativity, to arrive to his famous Dirac equation (128). With the framework at hand, the energy spectrum of the hydrogen atom could be explained very accurately. Dirac and Schrödinger got the Nobel prize for their atomic theory in 1933, together with W. Heisenberg for the creation of quantum mechanics.

### 3.1.1 Lamb shift in hydrogen

According to the Dirac equation, the  $2S_{1/2}$  and  $2P_{1/2}$  states are degenerate and thus have the same energy. Already in the 1930s, first evidence was found from absorption spectroscopy for a difference in energy of these levels (129; 130), although not conclusive yet. The World War 2 delayed further efforts, but also allowed for rapid development of radar and microwaves. In 1947, W. E. Lamb and R. C. Retherford

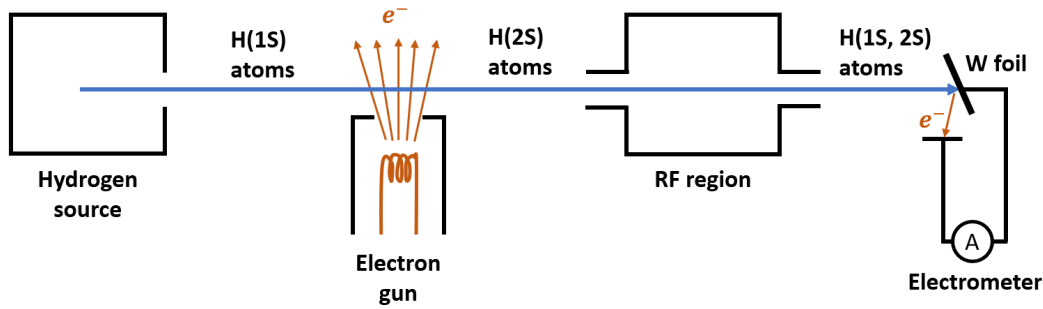


FIGURE 3.2: Simplified schematic of the experiment conducted by Lamb and Retherford.

profited from the improved microwave technology and set up an experiment trying to resolve the shift in energy (131; 132). The experimental sketch is shown in Fig. 3.2. In their experiment, they had an oven emitting hydrogen atoms in their ground state. To excite the atoms from 1S to 2S, the atoms were bombarded by low energy electrons. These excited atoms then travelled onto a tungsten foil, releasing electrons, which were detected by an electrometer. This process would not occur with 1S hydrogen. In between the electron gun to excite the beam and the detection setup, the atoms were exposed to radio-waves and a magnetic field. The magnetic field was varied, shifting the resonance frequency of the atoms, while the frequency of the radio-waves was fixed. When close to resonance, i.e. when driving the  $2S-2P_{1/2}$  transition efficiently, the atoms would get excited to the  $2P$  state. In contrast to the metastable  $2S$  state (around 100 ms lifetime), the  $2P$  is short-lived and relaxes back to the ground state with a lifetime of 1.6 ns. With this technique, the population of  $2S$  hydrogen was reduced and therefore also the current measured by the electrometer. The closer the RF was to resonance, the less signal was observed and therefore the existence of an energy splitting between the  $2S$  and  $2P_{1/2}$  demonstrated.

Lamb and Retherford found a shift of roughly 1000 MHz. Their measurement was awarded with the Nobel prize in 1955. This important discovery was fundamental for the development of Quantum Electrodynamics (QED) (133), which to this day is one of the most stringently probed theories in physics. A sketch of the evolution of the energy levels of hydrogen is shown in Fig. 3.3.

From the schematic it is visible that after applying the QED corrections, the states can be split up further by including the interactions with the nucleus and its spin, called the hyperfine structure. For the Lamb shift, as later calculated in Sec. 3.5, in total three transitions would be allowed by selection rules in the dipole approximation. The three allowed transitions are:

$$2^2S_{1/2}(F = 0, m_F = 0) \rightarrow 2^2P_{1/2}(F = 1, m_F = 0) \quad (3.2)$$

$$2^2S_{1/2}(F = 1, m_F = 0) \rightarrow 2^2P_{1/2}(F = 0, m_F = 0) \quad (3.3)$$

$$2^2S_{1/2}(F = 1, m_F = \pm 1) \rightarrow 2^2P_{1/2}(F = 1, m_F = \pm 1) \quad (3.4)$$

where the term symbols are defined as  $n^{2S+1}L_J(F, m_F)$  with  $n$  the principal quantum number,  $S$  the total spin,  $L$  the orbital quantum number,  $J$  the total angular quantum number and  $F$  the quantum number describing the coupling of orbital angular momentum and nuclear spin.



The Lamb shift transition frequency  $\nu_{Lamb}$  is defined as:

$$\nu_{Lamb} = \nu_{(3,4)} - \frac{1}{4} \left[ \nu_{(3,4)} - \nu_{(3,2)} \right] + \frac{1}{4} \left[ \nu_{(3,3)} - \nu_{(3,4)} \right] \quad (3.5)$$

where the subscripts are referring to the transitions in equations 3.2, 3.3 and 3.4. The transitions and characteristic frequencies are summarized in Fig. 3.4 for both hydrogen and muonium.

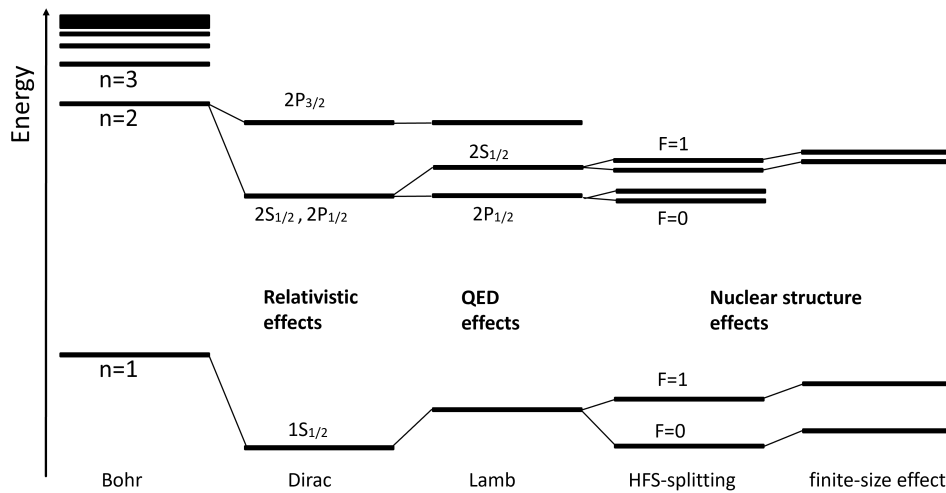


FIGURE 3.3: Schematic of the hydrogen energy levels.

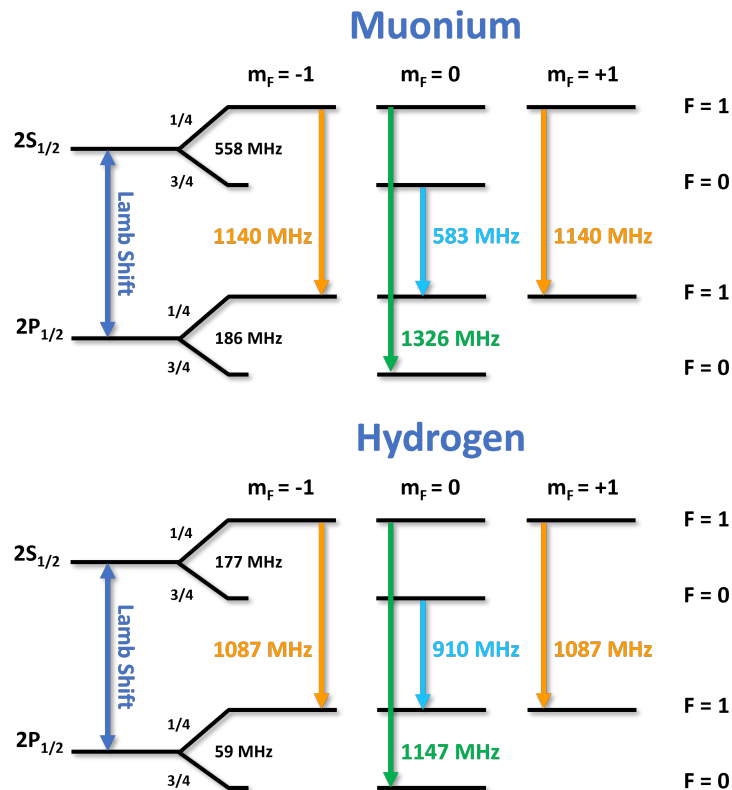


FIGURE 3.4: Schematic of the  $2S_{1/2}$ – $2P_{1/2}$  energy levels for muonium (top) and hydrogen (bottom).



The Lamb shift was remeasured several times over the years, applying new approaches to lower the experimental uncertainty and challenge theorists to improve the uncertainty of QED calculations. In 1966, R. T. Robiscoe and B. L. Cosens used the technique of level-crossing and electrical quenching (134), reaching the mark of 0.1 MHz uncertainty. In the following years, G. Newton reached in 1979 the result of 1057.826(20) MHz (135) with transmission lines used for driving the transition and the technique of electrical quenching to eventually detect Ly- $\alpha$  photons emitted from the H(2S) with a photomultiplier tube. Two years later in 1981, S. R. Lundeen and F. M. Pipkin used separatory oscillating fields (SOF) (136) instead of simple transmission lines to narrow the linewidth and thus improve the result to 1057.845(9) MHz (137).

This result was considered the most precise determination of the hydrogen Lamb shift for the next 40 years to come. At this point, the experiment had caught up and surpassed the theoretical uncertainty. To this level, uncertainties in the effects of the nucleus itself, especially the fact that the proton is not a point-like particle but has a substructure, started to become important. The input parameter to the theory, the proton charge radius, was typically measured via electron-proton scattering experiments. A summary of the results is for example given by (138). The experiments yielded a large spread of values for the radius, demanding for a different method to extract the proton charge radius. Since QED was already calculable to this level, the charge radius was also extracted from spectroscopic measurements such as the Lamb shift of hydrogen (see Eq. 3.31). These additional measurements yielded similar results and uncertainties as the data from the scattering experiments. A jump in precision on determining the proton charge radius was needed to further probe upon QED.

### 3.1.2 The Proton Radius Puzzle

In 2010, the proton charge radius was extracted from the Lamb shift experiment of muonic hydrogen (139), which triggered the proton radius puzzle. The measured charge radius from the muonic hydrogen experiment had a much smaller uncertainty, but was  $5\sigma$  off from the average of prior measurements. This in turn triggered more experiments using electron scattering (see (138)), as well as a muonic hydrogen experiment from  $2S_{1/2}^{F=0} \rightarrow 2P_{3/2}^{F=1}$  and re-evaluation of the  $2S_{1/2}^{F=1} \rightarrow 2P_{3/2}^{F=2}$  transition (140). The puzzle only got deepened as the disagreement increased to  $7\sigma$ .

With a modification of the SOF technique to a frequency-offset SOF (SOSOF) (141) and using an acetone-filled gas-ionization detector to count the Ly- $\alpha$  photons, E. A. Hessels and co-workers measured in 2019 the hydrogen Lamb shift to be 1057.8298(32) MHz (78). The SOSOF technique allowed to control and resolve systematic effects more cleanly and is insensitive to the experimental frequency response and low-frequency noise. Additionally, the resonance frequency could be extracted by a simple linear fit of the phase of the detection signal. Their result not only holds the record for the most precise determination of the Lamb shift value in hydrogen, but also contributed to resolve the proton radius puzzle to a great degree, as their extraction of the proton charge radius agrees well with the previous determinations from muonic hydrogen experiments. Their value of the hydrogen Lamb shift was  $1.5\sigma$  away from the one of Lundeen and Pipkin, though. A reanalysis of Lundeen and Pipkins work by Hessels et al. led to a smaller radius and increased uncertainty, eventually in good agreement with Hessels work (142).

The most recent determinations of the radius from e-p scattering (143) and the  $2S - 4P$  transition in hydrogen (144) are also in agreement with the value from muonic hydrogen, while the most recent measurement of the  $2S_{1/2} - 8D_{5/2}$  transition in hydrogen is disagreeing (145). Measurements of the  $1S - 3S$  transition in hydrogen support both the smaller radius (146) as well as the originally accepted value (147). The discrepancy between the experiments is yet to be understood (148).

### 3.1.3 Lamb shift in muonium

With the theory of the hydrogen Lamb shift being sensitive to finite-size corrections and therefore having the proton charge radius with its rather large uncertainty as input, it got more and more difficult to further probe QED.

In contrast to hydrogen, muonium has a point-like nucleus and is therefore free from finite size effects. With its nucleus also having a much smaller mass it makes a good candidate to test higher recoil corrections. Since the nuclear mass of the system changes, so does also the value of the Lamb shift itself. A comparison between hydrogen and muonium is shown in Fig. 3.4.

The first to measure the muonium Lamb shift were C. J. Oram et al. (69) at TRIUMF in 1984 with a value of  $1070^{+12}_{-15}$  MHz. Later, in 1990, K. A. Woodle et al. measured at LAMPF a value of  $1042^{+21}_{-23}$  MHz (70). Both experiments were similar; a  $\mu^+$  beam was used, impinging on a foil and creating muonium. As detection setup, the electrical quenching technique and CsI-coated photomultiplier tubes or MCPs were used, the process already established with hydrogen experiments. At the same time in 1990 at LAMPF, S. H. Kettell et al. (71) extracted the muonium Lamb shift value, but from measuring the  $2S_{1/2} \rightarrow 2P_{3/2}$  transition instead. The value was found to be  $1027^{+30}_{-35}$  MHz. In all cases, the experiments were limited by statistics. Utilizing the beamfoil technique to form muonium required low-energy  $\mu^+$  of around 10 keV. To get the  $\mu^+$  slowed down, they had to use degrader foils, which created a diffuse beam and a lot of  $\mu^+$  were lost. To advance in improving the Lamb shift uncertainty in muonium, a directional low energetic  $\mu^+$  beam was needed. However, that only recently became available through the LEM beamline at PSI (90).

## 3.2 Beamfoil Technique and Contamination

### 3.2.1 Working Principle

An efficient method to produce a beam of muonium is the beamfoil technique. By guiding  $\mu^+$  onto a carbon foil, the muon will interact with the material and lose energy. In this process electrons are freed and are, if freed close to the surface, released into vacuum. These low-energy electrons can be detected to tag the incident  $\mu^+$  and give the start signal of a time-of-flight measurement. The muon itself, under the condition of having a high enough incident energy, will eventually exit the carbon foil. Just before exiting, it has a probability to pick up an electron at the surface and form muonium. A sketch is shown in Fig. 3.5.

The process of low-energy electron emission into vacuum as well as the electron pick-up to form muonium is heavily dependent on the incident energy, angles, foil properties, and the incident particle type itself. For muonium not much data was available, but for hydrogen it is well tested. A summary is available from Allegrini et al. (149) on thin carbon foils.

Even at low incident energies of a few keV with thin ( $\approx 10$  nm) carbon foils, several electrons will be emitted into vacuum with a peak energy of 1-5 eV (149; 150), allowing for an efficient tagging of the incident particle. The angular scattering of the beam after the foil (straggling) is connected to the energy loss throughout the foil. The more energy loss (e.g. the thicker the foil or the less energetic the incident beam), the more diffuse the beam will become (151). The formation efficiency of hydrogen is for example summarized in Gonin et al. (152), showing that with incident 10 keV protons beams, a hydrogen formation efficiency up to 80 % was achieved.

At the LEM beamline at PSI, the beamfoil technique is routinely used with an incident beam of around 5-15 keV  $\mu^+$ . Both good tagging efficiency as well as muonium formation was shown and the energy loss studied on a 10 nm carbon foil by Khaw et al. (153). Mass-scaling the hydrogen formation efficiencies to the muon mass, at around 10 keV residual energy after the foil, a roughly 30 % muonium

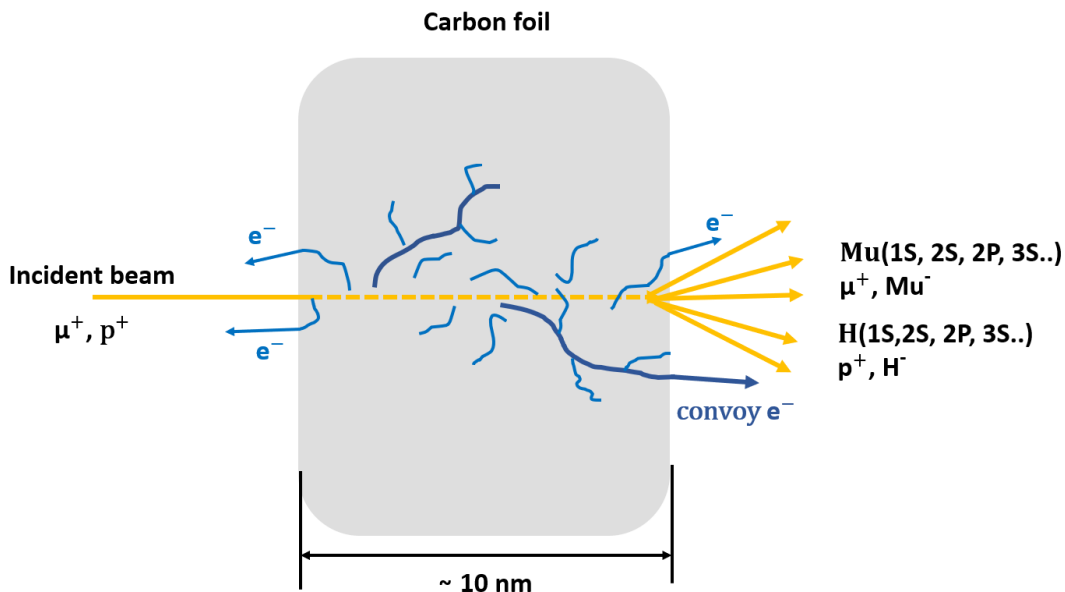


FIGURE 3.5: A simplified sketch showing the interaction between an incident beam of  $\mu^+$  or  $p^+$  with a thin carbon foil.

formation efficiency and at 5 keV even 50% would be expected. Summarized, a very thin carbon foil in combination with low-energy incident particles of around 5-10 keV would be optimal to produce an intense, directed muonium beam, while still keeping a high electron yield for an efficient tagging.

### 3.2.2 2S Formation & Contamination

Utilizing the beamfoil technique, the captured electron does not necessarily need to be in the 1S orbital. Measurements with protons on a carbon foil showed that a lot of possible levels can be populated ( $n=2$  (154; 155; 156; 157; 158),  $n=3$  (154; 159; 157; 158),  $n=4$  (159; 160; 157)) with non-negligible probabilities.

A rough rule of thumb is to assume that the initial populations are scaling with  $\frac{1}{n^3}$ , i.e.  $P(n=2,3,4) \approx (0.125, 0.037, 0.015)$  (135). The distribution over the  $l$  states is non-trivial. The relative population ratios of  $(2s, 2p, 3s, 3p, 3d, 4s, 4p, 4d) = (0.75, 1, 0.34(2), 0.21(1), 0.15(1), 0.07, 0.08, 0.02)$  are extracted from the measurements mentioned above. Taking the probability to form  $n = 2$  of 0.125 from the rule of thumb would result in a probability to form  $nS$  states  $P(nS)$  of  $P(2S, 3S, 4S) = (0.054, 0.024(2), 0.005)$ . A result of simulating the Coulomb recombination of a moving muon with a stationary electron by C. Fry (161) shows a  $P(2S)$  of  $\approx 0.11$  and  $P(3S)$  of  $\approx 0.04$ , which both are disagreeing with the measurements.

These probabilities would correspond to the formation efficiency right after the foil. Most of these states are not stable though, and will relax to a lower energy level. A summary of the possibilities including lifetimes are shown in the Grotrian diagram in Fig. 3.6, which was adapted from (162).

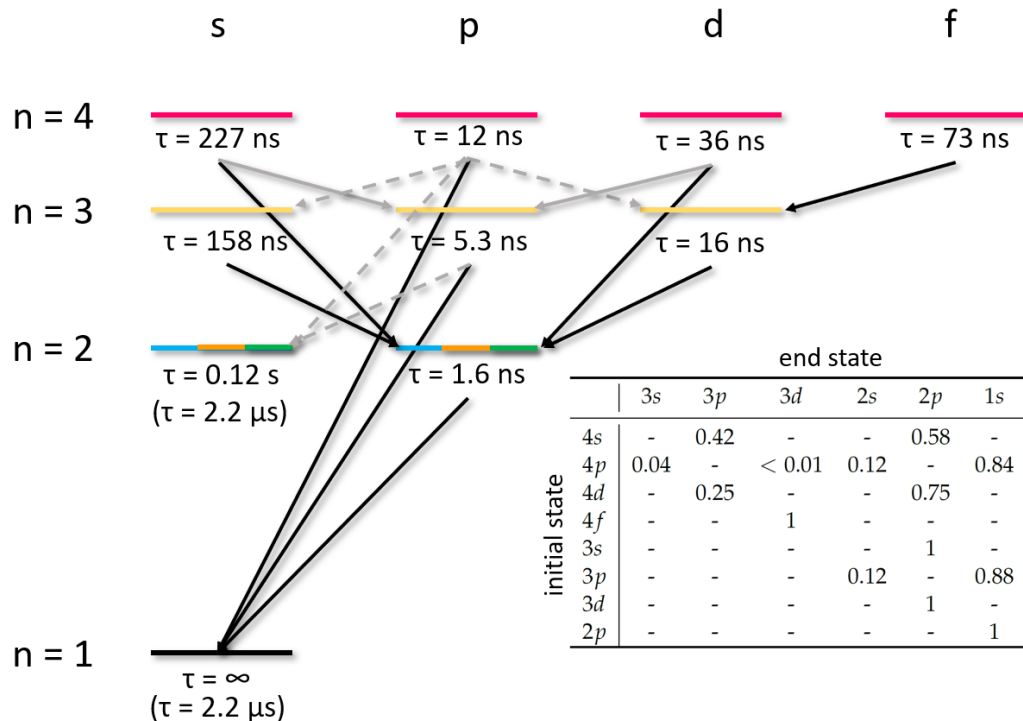


FIGURE 3.6: The Grotrian diagram including ratios and lifetimes for hydrogen as well as muonium. The lifetimes for the 2S and 1S state for muonium is written in parenthesis. The figure was adapted from (162).

How much of the population  $P_0$  would survive until the detection area can be calculated via:

$$P(t) = P_0 \exp \left[ -\frac{t}{\tau} \right] \quad (3.6)$$

$$t = \frac{L}{\sqrt{2E_{\text{kin}}/m}}$$

where  $t$  is the time,  $\tau$  the lifetime of the state,  $L$  the distance between foil and detection setup,  $E_{\text{kin}}$  the kinetic energy after the foil and  $m$  the mass of the particle.

Since the  $2S$  state is metastable, i.e. its relaxation to the  $1S$  state forbidden in the dipole approximation, its lifetime is much longer than compared to all the other states. Hence, with the beamfoil technique, a large fraction will be formed as  $2S$  and available for experiments. Higher states such as  $3S$  and  $4S$  would not survive in large quantities if the time to reach the detection setup is much longer than their lifetime.

In hydrogen experiments, where statistics is not an issue, the beamline can just be extended. In the case of muonium, where the losses of muonium along the beamline need to be minimized, a significant contamination of  $3S$  and  $4S$  might be present in the beam. An example of how a line-shape could look like with a short distance between foil and detection setup of around 20 cm and an incident beam energy  $E_{\text{kin}}$  of 7.5 keV  $\mu^+$  is shown in Fig. 3.7.

Another type of beam contamination could come from convoy electrons created at the foil. In Fig. 3.5, the process of the muon ionizing the material and freeing electrons is shown. In this process, electrons can be released with a velocity close to the one of the passing proton or muon (163; 164; 165). This would mean that, depending on what electrical field configuration is applied in the detecting area, the electron could get detected and fake a Ly- $\alpha$  signal, in the worst case passing the time cuts and contributing to the background.

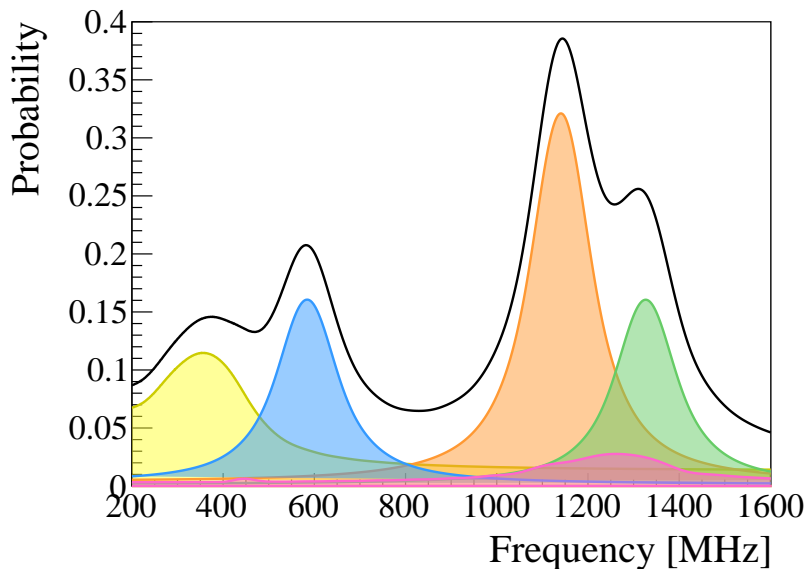


FIGURE 3.7: A possible Lamb shift line-shape for muonium showing the three hyperfine transitions from the  $2S$  level: 583 MHz (blue), 1140 MHz (orange), 1326 MHz (green). The contributions from beam contamination from  $3S$  states (yellow) and  $4S$  (pink) are shown as well.

### 3.3 Lamb Shift theory

QED is a quantum field theory describing the interaction of charged particles with an electromagnetic field. For every interaction the charged particle emits a virtual photon, the force carrier of the electromagnetic field, which will in turn interact with another particle. This describes the most direct way of an interaction. For an accurate description of the process, all possible ways have to be included. A first order correction in  $\alpha$  comes from one-loop processes as shown in Fig. 3.8, where  $\alpha$  corresponds to the fine-structure constant of roughly  $\frac{1}{137}$ . Evaluating such Feynman diagrams involves the construction of the process operators and propagators and dealing with infrared and ultraviolet divergences via renormalization, which is outside the scope of this thesis and can be found in literature (166; 167; 168).

In the following, we focus on a summary of the QED corrections for hydrogen and muonium. If not mentioned otherwise, the corrections are adapted from the CODATA 2018 recommended values (169) for the hydrogen Lamb shift. For additional corrections important to muonium, the reference is given. The following review was prepared as a manuscript and can be found in Ref. (170).

We use  $m_e$  for the electron,  $m_n$  for the nuclear and  $m_r$  for the reduced mass. The reduced mass is defined as:

$$m_r = \frac{m_e m_n}{m_e + m_n} \quad (3.7)$$

When calculating the energy difference between the  $2S_{1/2}$  and  $2P_{1/2}$  states both in hydrogen as well as muonium, the main contribution is coming from the self-energy  $E_{SE}$ , shown in Fig. 3.8A. The self energy is the process of the bound electron emitting and re-absorbing a virtual photon. A similar effect comes from the vacuum polarization (Fig. 3.8B), which can be looked at as an effect from the self-energy of the exchange photon. It produces a virtual  $e^+e^-$  pair ( $E_{VP}$ ), or in more suppressed cases a  $\mu^+\mu^-$  ( $E_{VP\mu}$ ) or a hadronic ( $E_{VP, had}$ ) pair, which eventually annihilate again.

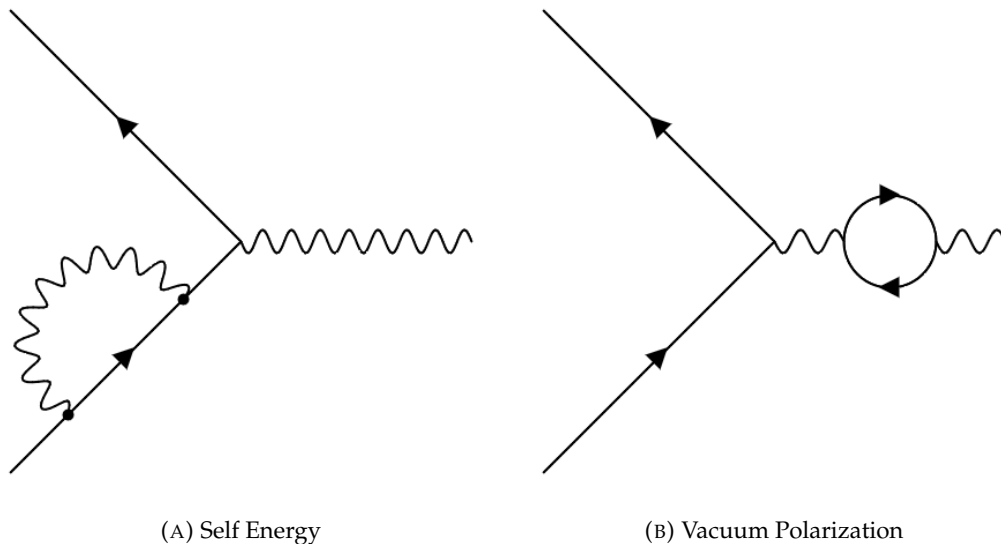


FIGURE 3.8: The Feynman diagrams showing the major contributions to the Lamb shift.

The contributions can be calculated as:

$$E_{\text{SE}} = \frac{\alpha}{\pi} \frac{(Z\alpha)^4}{n^3} \left(\frac{m_r}{m_e}\right)^3 F(Z\alpha) m_e c^2 \quad (3.8)$$

$$E_{\text{VP}} = \frac{\alpha}{\pi} \frac{(Z\alpha)^4}{n^3} \left(\frac{m_r}{m_e}\right)^3 H(Z\alpha) m_e c^2 \quad (3.9)$$

$$E_{\text{VP}\mu} = \frac{\alpha}{\pi} \frac{(Z\alpha)^4}{n^3} \left(\frac{m_r}{m_e}\right)^3 \left(\frac{m_e}{m_\mu}\right)^2 \left[-\frac{4}{15}\right] \delta_{l0} m_e c^2 \quad (3.10)$$

$$E_{\text{VP, had}} = 0.671(15) E_{\text{VP}\mu} \quad (3.11)$$

$$F(Z\alpha) = L A_{41} + A_{40} + (Z\alpha) A_{50} + (Z\alpha)^2 [L^2 A_{62} + L A_{61} + G_{\text{SE}}(Z\alpha)] \quad (3.12)$$

$$H(Z\alpha) = V_{40} + (Z\alpha) V_{50} + (Z\alpha)^2 [L V_{61} + G_{\text{VP}}(Z\alpha) + G_{\text{VP}}^{(R)}(Z\alpha)], \quad (3.13)$$

where we use  $L = \ln\left(\frac{m_e}{m_r} \frac{1}{(Z\alpha)^2}\right)$  and  $\delta_{ij}$  as the Kronecker delta. The functions  $F(Z\alpha)$  and  $H(Z\alpha)$  are expanded through perturbation theory, the remainder of higher orders summarized in the  $G$  functions. These  $G$  functions are carrying an estimate of the uncertainty with them.

Higher-order non-recoil contributions come from two- and three-photon corrections  $E_{2\text{ph}}$  and  $E_{3\text{ph}}$ :

$$E_{2\text{ph}} = \left(\frac{\alpha}{\pi}\right)^2 \frac{(Z\alpha)^4}{n^3} \left(\frac{m_r}{m_e}\right)^3 F_{2\text{ph}}(Z\alpha) m_e c^2 \quad (3.14)$$

$$E_{3\text{ph}} = \left(\frac{\alpha}{\pi}\right)^3 \frac{(Z\alpha)^4}{n^3} \left(\frac{m_r}{m_e}\right)^3 F_{3\text{ph}}(Z\alpha) m_e c^2 \quad (3.15)$$

$$F_{2\text{ph}}(Z\alpha) = B_{40} + (Z\alpha) B_{50} + (Z\alpha)^2 [L^3 B_{63} + L^2 B_{62} + L B_{61} + B_{60}] \\ + (Z\alpha)^3 [L^2 B_{72} + L B_{71} + \dots] \quad (3.16)$$

$$F_{3\text{ph}}(Z\alpha) = C_{40} + (Z\alpha) C_{50} + (Z\alpha)^2 [L^3 C_{63} + L^2 C_{62} + L C_{61} + C_{60} + \dots]. \quad (3.17)$$

Compared to hydrogen, the nucleus of muonium is approximately nine times lighter, making it more sensitive to recoil corrections. The recoil corrections appearing in CODATA 2018 are the Barker-Glover correction  $E_{\text{BKG}}$ , the relativistic recoil  $E_{\text{rec,S}} + E_{\text{rec,R}}$ , the radiative recoil  $E_{\text{RR}}$  and the nucleus self-energy  $E_{\text{SEN}}$ :

$$E_{\text{BKG}} = \frac{(Z\alpha)^4}{2n^3} \left(\frac{m_r}{m_e}\right)^3 \left(\frac{m_e}{m_n}\right)^2 \frac{1 - \delta_{l0}}{\kappa (2l + 1)} m_e c^2 \quad (3.18)$$

$$E_{\text{rec,S}} = \frac{(Z\alpha)^5}{\pi n^3} \left(\frac{m_r}{m_e}\right)^3 \left(\frac{m_e}{m_n}\right) S(Z\alpha) m_e c^2 \quad (3.19)$$

$$E_{\text{rec,R}} = \frac{(Z\alpha)^6}{n^3} \left(\frac{m_r}{m_e}\right)^3 \left(\frac{m_e}{m_n}\right) R(Z\alpha) m_e c^2 \quad (3.20)$$

$$E_{\text{RR}} = \frac{\alpha}{\pi} \frac{(Z\alpha)^5}{\pi n^3} \left(\frac{m_r}{m_e}\right)^3 \left(\frac{m_e}{m_n}\right) Q(Z\alpha) \delta_{l0} m_e c^2 \quad (3.21)$$



$$E_{\text{SEN}} = \frac{Z^2\alpha}{\pi} \frac{(Z\alpha)^4}{n^3} \left(\frac{m_r}{m_e}\right)^3 \left(\frac{m_e}{m_n}\right)^2 \left[ \left(\frac{10}{9} + \frac{4}{3} \ln \left[ \frac{m_n}{m_r(Z\alpha)^2} \right] \right) \delta_{l0} - \frac{4}{3} \text{lnk}_0 \right] m_e c^2 \quad (3.22)$$

$$S(Z\alpha) = L D_{51} + D_{50} - \frac{2\delta_{l0}}{m_n^2 - m_e^2} \left[ m_n^2 \ln \left( \frac{m_e}{m_r} \right) - m_e^2 \ln \left( \frac{m_n}{m_r} \right) \right] \quad (3.23)$$

$$R(Z\alpha) = D_{60} + (Z\alpha) G_{\text{REC}}(Z\alpha) \quad (3.24)$$

$$Q(Z\alpha) = 6\zeta[3] - 2\pi^2 \ln(2) + \frac{35\pi^2}{36} - \frac{448}{27} + (Z\alpha) \left[ \frac{2}{3} \pi \ln((Z\alpha)^{-2})^2 \right] + \dots \quad (3.25)$$

where  $\kappa$  is the angular momentum parity quantum number,  $\zeta$  is the Riemann zeta function and  $\text{lnk}_0$  is the relevant Bethe logarithm.

In atoms with a nuclear size such as hydrogen, the  $\frac{10}{9}$  term in  $E_{\text{SEN}}$  (Eq. 3.22) would be absorbed in the finite size contributions. Since muonium has no substructure, it is free from finite size effects and therefore the finite nuclear size contributions could be omitted and  $E_{\text{SEN}}$  needed to be extended. See also the discussion in Ref. (171).

In addition to the above, higher-orders recoil contributions are added. These are completely negligible for hydrogen, but are up to two orders of magnitude larger for M and therefore potentially of importance. Czarnecki and Melnikov (172) calculated higher-order mass contributions to the radiative recoil insertions in the electron line, of which the 2<sup>nd</sup> order is

$$E_{\text{RR2e}} = \frac{\alpha}{\pi} \frac{(Z\alpha)^5}{n^3} \left(\frac{m_r}{m_e}\right)^3 \left(\frac{m_e}{m_n}\right)^2 \left[ \pi 8 \ln(2) - \pi \frac{127}{32} \right] \delta_{l0} m_e c^2, \quad (3.26)$$

which returns a negligible 80 Hz for the muonium LS. Another radiative recoil contribution comes from polarization insertions calculated in (173), whose 2<sup>nd</sup> order in mass correction is given in (174)

$$E_{\text{RR2p}} = \frac{\alpha}{\pi} \frac{(Z\alpha)^5}{n^3} \left(\frac{m_r}{m_e}\right)^3 \left(\frac{m_e}{m_n}\right)^2 \left[ -\frac{3\pi}{16} \right] \delta_{l0} m_e c^2, \quad (3.27)$$

returning a negligible  $-10$  Hz for the muonium LS. Very recently, spin-independent three-loop radiative corrections have been calculated for positronium and muonium (174), giving

$$E_{\text{RR3}} = \left(\frac{\alpha}{\pi}\right)^2 \frac{(Z\alpha)^5}{\pi n^3} \left(\frac{m_r}{m_e}\right)^3 \left(\frac{m_e}{m_n}\right) [-11.4\dots] \delta_{l0} m_e c^2, \quad (3.28)$$

which returns a negligible  $-30$  Hz contribution to the M LS.

For pure recoil contributions, equations 3.19 and 3.23 account for recoil terms up to order  $(Z\alpha)^5 (m_e/m_n)^3 \ln(m_e/m_n)$ . The expansion in mass ratio of the pure recoil term of order  $(Z\alpha)^6$  is calculated partially in (172), which to 2<sup>nd</sup> order gives

$$E_{\text{rec,R2}} = \frac{(Z\alpha)^6}{n^3} \left(\frac{m_r}{m_e}\right)^3 \left(\frac{m_e}{m_n}\right)^2 \left[ \frac{4}{\pi^2} \ln \frac{m_n}{m_e} - \frac{8}{3} \ln \frac{m_n}{m_e} - \frac{12\zeta_3}{\pi^2} + \frac{3}{\pi^2} + \frac{8}{3} \right] \delta_{l0} m_e c^2, \quad (3.29)$$

returning  $-575$  Hz for the M LS. This contribution is not negligible compared with the 0.8 kHz uncertainty attached to equation 3.21. To account for it being partial, the



full contribution of 1.0 kHz is taken as its uncertainty.

As another addition to CODATA 2018, the off-diagonal hyperfine-structure contribution  $E_{\text{HFS}}$  was included. This additional recoil contribution arises from the mixing of the fine structure sublevels due to the hyperfine interaction as given by for example V. Yerokhin et al. (175):

$$E_{\text{HFS}} = m_e c^2 \frac{m_e^2}{m_p^2} \frac{\alpha^2 (Z\alpha)^2}{n^3} \frac{\mu^2}{\mu_N^2} \frac{2I(I+1)}{81} (-1)^{j+1/2} \delta_{l1}. \quad (3.30)$$

The  $I$  is the nuclear spin quantum number,  $\mu$  the nuclear magnetic moment and  $\mu_N$  the nuclear magneton.

For completeness, the finite-size and nuclear polarizability effects contributing to the hydrogen Lamb shift  $E_{\text{nucl}}$  are included as given by CODATA 2018:

$$E_{\text{nucl}} = \frac{2}{3} \frac{(Z\alpha)^4}{n^3} \left( \frac{m_r}{m_e} \right)^3 \left( \frac{r_n}{\lambda_C} \right)^2 m_e c^2 \times \left[ N_S(Z\alpha) \delta_{l,0} + \left( \frac{n^2-1}{4n^2} \right) N_P(Z\alpha) \delta_{l,1} \right] + \frac{h \cdot 0.393}{n^3} \quad (3.31)$$

$$N_S(Z\alpha) = 1 - \frac{1}{2} (Z\alpha) \left( \frac{r_{pF}^3}{\lambda_C r_n^2} \right) - (Z\alpha)^2 \left( \frac{9}{4n^2} - 3 - \frac{1}{n} + 2\gamma - \ln\left[\frac{n}{2}\right] + \psi[n] + \ln\left[\frac{m_r r_{n2}}{m_e \lambda_C} (Z\alpha)\right] \right) + \alpha (Z\alpha) (4\ln[2] - 5) + \frac{\alpha}{\pi} (Z\alpha)^2 \left( -\frac{2}{3} \ln[(Z\alpha)^{-2}]^2 + \ln\left[\frac{m_r r_n}{m_e \lambda_C}\right]^2 \right) \quad (3.32)$$

$$N_P(Z\alpha) = (Z\alpha)^2 \delta_{\kappa l} + \frac{\alpha}{\pi} (Z\alpha)^2 \left( \frac{8}{9} \ln[(Z\alpha)^{-2}] - \frac{8}{9} \ln[2] + \frac{11}{27} + \delta_{\kappa l} + \frac{4n^2}{n^2-1} G_N \right)$$

In these corrections,  $r_n$  is the proton charge radius,  $r_{pF}$  the effective radius for the proton (1.947(75) fm, also known as Friar radius),  $r_{n2}$  the effective radius for high-energy contributions ( $1.068497r_n$ ) and  $\lambda_C$  the reduced Compton length of the electron  $\lambda_C = \hbar/(m_e c)$ . The  $\gamma$  corresponds to Euler's constant,  $\psi$  to the Digamma function and  $h$  to Planck's constant. The additional third term in Eq. 3.31 corresponds to a nuclear polarization contribution for hydrogen, where the first two terms are a combination of finite nuclear size and radiative finite nuclear size contributions.

All the coefficients  $A$ ,  $B$ ,  $C$ ,  $D$  and  $V$ , the remainder functions  $G$  as well as the uncertainties of each contribution are tabulated in Ref. (169; 175) and are summarized in Appendix C.2 in the form of a Mathematica notebook. These quantities typically depend on the quantum numbers  $n$  (principal),  $l$  (azimuthal) and  $j$  (total angular momentum), but were here not specifically mentioned for better visualization.

For both hydrogen and muonium, these contributions were evaluated for the  $2S_{1/2}$  and  $2P_{1/2}$  levels. Their difference in frequency are summarized in Tab. 3.1. We calculate an updated LS frequency for muonium of 1047.498(1) MHz, while validating our result with the values summarized by Yerokhin for hydrogen (175). Only uncertainties  $\geq 500$  Hz were included. Our value of the hydrogen Lamb shift agrees well with the one obtained by Yerokhin et al. In the case of the muonium Lamb shift,

the result agrees with the one from Sapirstein and Yennie (118). There is though a significant discrepancy of more than 200 kHz with the most recent value calculated from effective field theories by C. Frugiuele et al. (176), which deserves further scrutiny.

Comparing our results for hydrogen and muonium, we identify the Barker-Glover correction as well as the nucleus self-energy as the two contributions most dependent on the nuclear mass. As mentioned before, the current best determination of the hydrogen Lamb shift has an uncertainty of around 3 kHz (78), hence these two contributions could not be resolved so far. In muonium, they are enhanced and can be probed by achieving Lamb shift uncertainties of 160 kHz and 40 kHz, respectively. These uncertainty levels will be set as goals for future muonium Lamb shift measurements (see Sec. 6.2).

TABLE 3.1: Summary of the calculated contributions to the hydrogen and muonium Lamb shift transition. The theoretical calculations from Sapirstein & Yennie (118) and from Frugiuele et al. (176) are included for comparison. Uncertainties smaller than 0.5 kHz are not tabulated.

	Largest Order	Hydrogen (MHz)	Muonium (MHz)
$E_{SE}$	$\alpha (Z\alpha)^4 L$	1084.128	1070.940
$E_{VP}$	$\alpha (Z\alpha)^4$	-26.853	-26.510
$E_{VP\mu+had}$	$\alpha (Z\alpha)^4 (m_e/m_\mu)^2$	-0.001	-0.001
$E_{2ph}$	$\alpha^2 (Z\alpha)^4$	0.065	0.065
$E_{3ph}$	$\alpha^3 (Z\alpha)^4$	0.000	0.000
$E_{BKG}$	$(Z\alpha)^4 (m_e/m_n)^2$	-0.002	-0.168
$E_{rec,S}$	$(Z\alpha)^5 L (m_e/m_n)$	0.358	3.138
$E_{rec,R}$	$(Z\alpha)^6 (m_e/m_n)$	-0.001	-0.012
$E_{rec,R2}$	$(Z\alpha)^6 (m_e/m_n)^2$	-0.000	-0.001(1)
$E_{RR}$	$\alpha (Z\alpha)^5 (m_e/m_n)$	-0.002	-0.014(1)
$E_{RR2e+p}$	$\alpha (Z\alpha)^5 (m_e/m_n)^2$	0.000	0.000
$E_{RR3}$	$\alpha^2 (Z\alpha)^5 (m_e/m_n)$	-0.000	-0.000
$E_{SEN}$	$Z^2 \alpha (Z\alpha)^4 (m_e/m_\mu)^2$	0.001	0.041
$E_{HFS}$	$\alpha^2 (Z\alpha)^2 \mu^2$	0.002	0.019
$E_{nucl}$	$(Z\alpha)^4 r_n^2$	0.139(1)	0.000
Sum		1057.834(1)	1047.498(1)
Ref. (175)		1057.8341(2)	
Ref. (118)			1047.49(9)
Ref. (176)			1047.284(2)

## 3.4 New Physics

As history has taught us, theoretical prediction and experimental measurement do not always agree with each other. As soon as the disagreement becomes significant, new physics might explain what the established physics fails to. In the following, we will explore two attempts that go beyond the Standard Model. By evaluating the experimental results within the framework of the Standard Model Extension (Sec. 3.4.1) or by adding new, dark forces to the interaction picture (Sec. 3.4.2), their theoretical coefficients can be probed and constrained.

### 3.4.1 Lorentz- & CPT-Violation

Within the Standard Model Extension (SME) framework, the Lagrange density  $\mathcal{L}$  is, amongst other things, extended with Lorentz- and CPT-violating terms. For the further calculations and explanations of using the SME framework on the muonium Lamb shift, the studies of A. Gomes et al. (177) were used as guidance.

As an example for the muonic sector, the Lagrange density is

$$\mathcal{L} \supset \frac{1}{2} \bar{\psi} (\gamma^\mu i \delta_\mu - m_\mu + \hat{\mathcal{Q}}) \psi + \text{H.c.} \quad (3.33)$$

where  $\psi(x)$  is the muon quantum field,  $m_\mu$  the muon mass and  $\hat{\mathcal{Q}}$  the spinor-matrix operator which includes the Lorentz- and CPT-violating kinetic effects. The SME-coefficients within the spinor-matrix describe the size of the violations. An effective non-relativistic Hamiltonian was built and decomposed with Pauli matrices in spin-dependent and independent components. In the following, we were only interested in the spin-independent term. The energy levels of  $2S_{1/2}$  and  $2P_{1/2}$  were obtained with the simplified Hamiltonian and the appropriate expectation values calculated, which lead to the SME shift  $\delta\nu_{\text{Lamb}}$  relative to the Lamb frequency:

$$2\pi\delta\nu_{\text{Lamb}} = -\frac{2}{3} (\alpha m_r)^4 \left( \overset{\circ}{a}_4^{\text{NR}} + \overset{\circ}{c}_4^{\text{NR}} \right) \quad (3.34)$$

where  $\alpha$  is the fine structure constant, and both  $\overset{\circ}{a}_4^{\text{NR}}$  and  $\overset{\circ}{c}_4^{\text{NR}}$  isotropic non-relativistic SME coefficients. The  $\overset{\circ}{a}$  coefficient describes how strongly the Lorentz- and CPT-symmetry would be broken, whereas  $\overset{\circ}{c}$  would only account for Lorentz-violation.

With the best experimental value of the muonium Lamb shift before this work at  $1042_{-23}^{+21}$  MHz (70), the bounds were set at

$$\left| \overset{\circ}{a}_4^{\text{NR}} + \overset{\circ}{c}_4^{\text{NR}} \right| < 1 \times 10^6 \text{ GeV}^{-3} \quad (3.35)$$

### 3.4.2 Muonic Forces

Precision spectroscopy with muonium also opens up the possibility to look for new light bosons coupling to muons and electrons. Considering a new scalar boson, its non-relativistic potential of the Yukawa-type is given by:

$$V_{ss}(\vec{r}) = -g_e^s g_\mu^s \frac{e^{-Mr}}{4\pi r}, \quad (3.36)$$

where  $M$  is the mass of the scalar, and  $g_e^s$  and  $g_\mu^s$  the coupling strengths to electrons and anti-muons, respectively. Calculations on how to derive such a potential can be

found in (178). The energy shift caused by such a potential is given to first order by:

$$\langle V_{SS} \rangle = -\frac{g_e^S g_\mu^S}{4\pi} \left\langle \frac{e^{-Mr}}{r} \right\rangle_{n,l} \quad (3.37)$$

Evaluating the expectation value in Eq. 3.37 for a hydrogen-like system, the energy shift caused for the Lamb shift can be found to be:

$$\Delta E_{SS}(2S \rightarrow 2P) = \frac{g_e^S g_\mu^S}{4\pi} \left( \frac{1}{4a_0(Ma_0 + 1)^4} - \frac{2M^2 a_0^2 + 1}{4a_0(Ma_0 + 1)^4} \right) \quad (3.38)$$

with  $a_0$  the bohr radius. The sensitivity plot can be drawn by:

$$g_e^S g_\mu^S > \frac{h \cdot \max(|v_{\text{exp}} - v_{\text{theo}}| \pm 2\rho)}{\Delta E_{SS} \setminus (g_e^S g_\mu^S)} \quad (3.39)$$

where  $\rho = \sqrt{\rho_{\text{exp}}^2 + \rho_{\text{theo}}^2}$  is the standard error and  $h$  Planck's constant.

A currently exciting example for a hint of new muonic physics is coming from the muon  $g-2$  puzzle, mentioned in Chap. 1. To make a comparison to the constraints from Eq. 3.39, the favoured region in the constraint space for a new scalar boson coupling to the muon coming from the muon  $g-2$  anomaly needs to be computed. For a boson with mass  $M$  much larger than the lepton mass  $m_l$ , the one-loop contribution to the  $g-2$  can be calculated to be (179):

$$\Delta a_S = \frac{g_S^2}{4\pi^2} \left( \frac{m_l}{M} \right)^2 \left[ \frac{M}{m_l} - \frac{7}{12} \right] \quad (3.40)$$

where  $l$  stands for either the electron or muon. In the case for the Lamb shift or the  $1S - 2S$  transition, one is becoming sensitive to boson masses below the electron mass and therefore the above approximation does not hold anymore. The contribution needs to be computed numerically (180):

$$\Delta a_S = \frac{g_S^2}{8\pi^2} \int_0^1 \frac{(1-x)^2(1+x)}{(1-x)^2 + x\left(\frac{M}{m_l}\right)^2} dx \quad (3.41)$$

The upper and lower limit  $\text{lim}_l^\pm$  is calculated via:

$$\text{lim}_l^\pm = \sqrt{\frac{\Delta a_l^\pm}{\Delta a_S}} \quad (3.42)$$

where  $\Delta a_l^\pm$  is the disagreement between theory and experiment  $a_l^{\text{exp}} - a_l^{\text{theo}}$  for the lepton  $l$ . The  $\pm$  corresponds to whether the uncertainty on  $\Delta a$  is added or subtracted. For the experimental electron magnetic moment we take the value from Gabrielse et al. (181) and for the muon the combined results from BNL and Fermilab (35). Both the results for the fine-structure constant  $\alpha$  from Berkley (31) and from LKB (30) are used to calculate the theoretical Standard Model prediction and is compatible within  $2\sigma$ , which is used as theoretical bound. The final computations of  $\Delta a_l^\pm$  are:

$$\Delta a_e^\pm = (-8.8 \pm 3.6) \times 10^{-13} \quad (3.43)$$

$$\Delta a_\mu^\pm = (251 \pm 59) \times 10^{-11} \quad (3.44)$$

The favoured region can then be obtained by plotting  $\lim_e^\pm \cdot \lim_\mu^\pm$  versus the boson mass  $M$ . An example of such a comparison is shown later in Fig. 5.10.

### 3.5 Optical Bloch equations for a two-level system

To derive the Maxwell-Bloch equations for a two-level system, our starting point is the von-Neumann equation:

$$\frac{\partial \hat{\rho}}{\partial t} = -\frac{i}{\hbar} [\hat{H}, \hat{\rho}] \quad (3.45)$$

where  $\hat{\rho}$  is the density operator and  $\hat{H}$  the Hamiltonian of the system. The following steps were done after studying the works (182; 183). The Hamiltonian can be split up into an energy and interaction part:

$$\hat{H} = \hat{H}_E + \hat{H}_{Int} = \hat{H}_E + \hat{D} \cdot \hat{V} = \hat{H}_E - q\hat{r} \cdot \hat{V} \quad (3.46)$$

where the interaction is described by the dipole moment operator  $\hat{D}$  and the electromagnetic field operator  $\hat{V}$ . For a two-level system, each operator can be described in a 2x2 matrix form:

$$\hat{\rho} = \begin{bmatrix} \rho_{gg} & \rho_{ge} \\ \rho_{eg} & \rho_{ee} \end{bmatrix} \quad (3.47)$$

$$\hat{D} \cdot \hat{V} = \begin{bmatrix} 0 & V_{ge} \\ V_{eg} & 0 \end{bmatrix} \quad (3.48)$$

$$\hat{H}_E = \begin{bmatrix} E_g & 0 \\ 0 & E_e \end{bmatrix} \quad (3.49)$$

where we used the notation  $g$  for the ground state and  $e$  for the excited state of the two-level system. By solving the von-Neumann equation, we end up with a set of four equations:

$$\frac{d\rho_{gg}}{dt} = i \left( V_{ge}^* \rho_{ge} - V_{ge} \rho_{eg} \right) \quad (3.50)$$

$$\frac{d\rho_{ee}}{dt} = i \left( V_{ge} \rho_{eg} - V_{ge}^* \rho_{ge} \right) \quad (3.51)$$

$$\frac{d\rho_{ge}}{dt} = \frac{d\rho_{eg}}{dt} = \frac{i(E_g - E_e)}{\hbar} \rho_{ge} + iV_{ge}^* (\rho_{ee} - \rho_{gg}) \quad (3.52)$$

The spontaneous decays of both original and excited state, in our case for the muonium in the 2S as original state and as 2P in the excited state, can be included by adding their phenomenological decay terms:

$$\frac{d\rho_{gg}}{dt} = i \left( V_{ge}^* \rho_{ge} - V_{ge} \rho_{eg} \right) - \gamma_{2S} \rho_{gg} \quad (3.53)$$

$$\frac{d\rho_{ee}}{dt} = i \left( V_{ge} \rho_{eg} - V_{ge}^* \rho_{ge} \right) - (\gamma_{2S} + \gamma_{2P}) \rho_{ee} \quad (3.54)$$

$$\frac{d\rho_{ge}}{dt} = \frac{d\rho_{eg}}{dt} = \frac{i(E_{2S} - E_{2P})}{\hbar} \rho_{ge} + iV_{ge}^* (\rho_{ee} - \rho_{gg}) - \left( \frac{\gamma_{2S}}{2} + \frac{\gamma_{2P}}{2} \right) \rho_{ge} \quad (3.55)$$

where the  $\gamma$ -factors are the inverse lifetime and describe the decay rate of either the 2S or the 2P state.

The electrical dipole matrix element  $V_{ge}$  is defined as:

$$V_{ge} = \langle e | \frac{q}{\hbar} \vec{r} \vec{V}(t) | g \rangle = \frac{q \vec{V}(t)}{\hbar} \langle e | \vec{r} | g \rangle = \frac{q V_0}{\hbar} \cos(\omega t + \delta) \cdot D_{ge} \quad (3.56)$$

where  $D_{ge}$  stands for the transition dipole moment. Taking the splittings into account up to hyperfine level, the formula for  $D_{ge}$  was taken from (183):

$$D_{ge} = D_{J' l' F' m', J I F M} = R_{n' l', n l} \cdot A_{J' l' F' M', J I F M}^{l' l s} \quad (3.57)$$

$$R_{n' l', n l} = \int_0^\infty R_{n' l'} r^3 R_{n l} dr \quad (3.58)$$

$$A_{J' l' F' M', J I F M}^{l' l s} = (-1)^{1+l'+s+J+J'+I-M'} \sqrt{\max(l, l')} \quad (3.59)$$

$$\cdot \sqrt{(2J+1)(2J'+1)(2F+1)(2F'+1)} \quad (3.60)$$

$$\cdot \begin{Bmatrix} l' & J' & s \\ J & l & 1 \end{Bmatrix} \begin{Bmatrix} J' & F' & I \\ F & J & 1 \end{Bmatrix} \begin{pmatrix} F & 1 & F' \\ M & (M' - M) & -M' \end{pmatrix} \quad (3.61)$$

where  $R_{n' l', n l}$  is the contribution from the radial wavefunctions and  $A_{J' l' F' M', J I F M}^{l' l s}$  the normalization stemming from the angular contribution. The terms in round brackets are  $3j$ - and in curly brackets are  $6j$ -Wigner symbols, whereas the terms in the square root are Clebsch-Gordan coefficients. The transition elements calculated for hydrogen transitions of  $2S_{1/2} \rightarrow 2P_{1/2}$ ,  $3S_{1/2} \rightarrow 3P_{1/2}$ ,  $4S_{1/2} \rightarrow 4P_{1/2}$  and  $4S_{1/2} \rightarrow 4P_{3/2}$  can be found in Tab. 3.2. A code snippet in Mathematica to compute the transition elements can be found in Appendix C.1.

To get transitions for hydrogen-like atoms with different mass or nuclear charge number  $Z$ , the transition elements should be multiplied with a factor of (184):

$$\frac{1}{Z^4} \left( \frac{m_e}{m_r} \right)^3 = \frac{1}{Z^4} \left( \frac{m_e(m_N + m_S)}{m_N m_S} \right)^3 \quad (3.62)$$

where  $m_r$  is the reduced,  $m_e$  the electron,  $m_N$  the nuclear and  $m_S$  the orbiting particle's mass. In case of the muonium atom, the factor would be 1.015 and is therefore negligible. For another system like positronium, though, this factor would be 8 and needs to be considered.

TABLE 3.2: Computed values for  $D_{ge}$  from Eq. 3.57 including splittings down to hyperfine level. A general state is described as  $|n^{2s}L_j, F, M_F\rangle$

	$ 2^2S_{1/2}, 0, 0\rangle$	$ 2^2S_{1/2}, 1, 0\rangle$	$ 2^2S_{1/2}, 1, \pm 1\rangle$
$\langle 2^2P_{1/2}, 0, 0 $	0	$-\sqrt{3}ea_0$	0
$\langle 2^2P_{1/2}, 1, 0 $	$-\sqrt{3}ea_0$	0	0
$\langle 2^2P_{1/2}, 1, \pm 1 $	0	0	$-\sqrt{3}ea_0$
	$ 3^2S_{1/2}, 0, 0\rangle$	$ 3^2S_{1/2}, 1, 0\rangle$	$ 3^2S_{1/2}, 1, \pm 1\rangle$
$\langle 3^2P_{1/2}, 0, 0 $	0	$-3\sqrt{2}ea_0$	0
$\langle 3^2P_{1/2}, 1, 0 $	$-3\sqrt{2}ea_0$	0	0
$\langle 3^2P_{1/2}, 1, \pm 1 $	0	0	$\pm 3\sqrt{2}ea_0$
	$ 4^2S_{1/2}, 0, 0\rangle$	$ 4^2S_{1/2}, 1, 0\rangle$	$ 4^2S_{1/2}, 1, \pm 1\rangle$
$\langle 4^2P_{1/2}, 0, 0 $	0	$-2\sqrt{15}ea_0$	0
$\langle 4^2P_{1/2}, 1, 0 $	$-2\sqrt{15}ea_0$	0	0
$\langle 4^2P_{1/2}, 1, \pm 1 $	0	0	$\pm 2\sqrt{15}ea_0$
	$ 4^2S_{1/2}, 0, 0\rangle$	$ 4^2S_{1/2}, 1, 0\rangle$	$ 4^2S_{1/2}, 1, \pm 1\rangle$
$\langle 4^2P_{3/2}, 1, 0 $	$2\sqrt{30}ea_0$	0	0
$\langle 4^2P_{3/2}, 1, \pm 1 $	0	0	$\pm\sqrt{30}ea_0$
$\langle 4^2P_{3/2}, 2, 0 $	0	$2\sqrt{30}ea_0$	0
$\langle 4^2P_{3/2}, 2, \pm 1 $	0	0	$\mp 3\sqrt{10}ea_0$
$\langle 4^2P_{3/2}, 2, \pm 2 $	0	0	0

### 3.5.1 Approximate Solution

To be able to estimate the fields necessary to electrically quench 2S states, an approximate solution of the Bloch equations mentioned in 3.55 is sufficient. They can be rewritten by changing the basis to  $\begin{pmatrix} |s\rangle \\ |p\rangle \end{pmatrix}$  instead of taking the density matrix, where  $|s\rangle$  and  $|p\rangle$  represent the original and final state. In this derivation, we follow closely the one made by C. Fry (161). The equations will be:

$$i \frac{d}{dt} \begin{pmatrix} |s\rangle \\ |p\rangle \end{pmatrix} = \begin{bmatrix} (\frac{E_{2S}}{\hbar} - i\frac{\gamma_{2S}}{2}) & V_{ge} \\ V_{eg} & (\frac{E_{2P}}{\hbar} - i\frac{\gamma_{2P}}{2}) \end{bmatrix} \begin{pmatrix} |s\rangle \\ |p\rangle \end{pmatrix} \quad (3.63)$$

These equations can be simplified by defining a unitary transformation  $A$  to be able to redefine the Hamiltonian to  $H_A$ :

$$A = \begin{bmatrix} e^{i\omega t/2} & 0 \\ 0 & e^{-i\omega t/2} \end{bmatrix}, H_A = A H A^\dagger + i\hbar \frac{dA}{dt} A^\dagger \quad (3.64)$$

$$H_A = \begin{bmatrix} (\omega_{2S} - \frac{\omega}{2} - i\frac{\gamma_{2S}}{2}) & D_{ge} \cdot V_0 e^{i\delta} \\ D_{ge} \cdot V_0 e^{i\delta} & (\omega_{2P} + \frac{\omega}{2} - i\frac{\gamma_{2P}}{2}) \end{bmatrix} + \begin{bmatrix} 0 & V_0 e^{i\delta t} \\ V_0 e^{-i\delta t} & 0 \end{bmatrix} \quad (3.65)$$

Only the second term of  $H_A$  is time-dependent. This term varies rapidly and can be omitted by applying the rotating wave approximation (RWA). The solution of the time evolution operator can be described by:

$$U(t) = e^{-iH_A t/\hbar} \quad (3.66)$$

When solving the system by finding the eigenvalues of  $H_A$ , from the imaginary part of the eigenvalue for the  $|s\rangle$  one can extract:

$$\frac{1}{\tau} = \gamma_{2S} + \frac{V_0^2 \cdot D_{ge}^2 (\gamma_{2P} - \gamma_{2S})}{(\omega_{2S} - \omega_{2P} - \omega)^2 + \frac{(\gamma_{2S} - \gamma_{2P})^2}{4}} \quad (3.67)$$

To obtain this result, a low power assumption was also made. Hence, an approximated solution with a Lorentzian model is only valid at low powers and will not be sufficient at high powers anymore. This equation can even be more simplified, since  $\gamma_{2P} \gg \gamma_{2S}$  and  $\omega_{2S} - \omega_{2P} = \omega_{Lamb}$  to:

$$\frac{1}{\tau_{2S}} = \frac{V_0^2 \cdot D_{ge}^2 \cdot \gamma_{2P}}{(\omega_{Lamb} - \omega)^2 + \frac{\gamma_{2P}^2}{4}} \quad (3.68)$$

For the quenching of 2S states with a static electrical field, the  $\omega$  goes to 0. By plugging in the transition elements for  $2S \rightarrow 2P$  calculated up to the fine-structure (3ea<sub>0</sub>), the final equation for the quenching would be:

$$\frac{1}{\tau_{2S}} = \frac{9e^2 a_0^2 V_0^2}{\hbar^2} \frac{\gamma_{2P}}{\omega_{Lamb}^2 + \frac{\gamma_{2P}^2}{4}} \quad (3.69)$$

which agrees with the derived equation for electrical quenching for example done in (185). By using Eq. 3.68 and summing the rates for every hyperfine state, with  $\omega \rightarrow 0$  and approximating that all transition frequencies  $\omega_{Lamb}$  are the same, one would also reproduce Eq. 3.69 (186).



## Chapter 4

# GBAR: Design and Commissioning of the Lamb Shift Setup

In this chapter, we will examine the Lamb shift setup prepared for the GBAR experiment in greater detail. In Sec. 4.1, we will discuss all parts involved in the detection of the Ly- $\alpha$  photons, from the design to the final assembly. Once being familiar with the detection setup, in Sec. 4.2 we will see it for the first time in action, characterizing the muonium beam at the LEM beamline at PSI. The results, published in (187), not only showed that we can form an intense beam of M(2S), opening up the possibility to improve the Lamb shift measurement of muonium, but also that the setup is operational and well-tested for the upcoming measurements with  $\bar{\text{H}}$  in GBAR.

In Sec. 4.3.1, we will see the design and assembly of the microwave setup. Knowing accurately the frequency-dependent power inside the microwave setup is a crucial element of the experiment. Therefore, our methods of operating the microwave setup are explained. For each element, the power loss characterization is presented, which will help to choose the right equipment for the Lamb shift measurement.

We conclude this chapter with Sec. 4.4, where we will see the Lamb shift setup installed in GBAR, ready to take first data.

### 4.1 Ly- $\alpha$ Setup

Since the measurement of the  $\bar{\text{H}}$  Lamb shift is planned to be a parasitic experiment of GBAR, the setup needed to be designed to have as little impact on the beam quality as possible. On the other hand, we were interested to utilize the  $\bar{\text{H}}(2\text{S})$  beam efficiently, which meant to find a solution that has a large solid angle covered with an efficient single Ly- $\alpha$  photon detector. Furthermore, an electrical field needed to be integrated that quenches all the remaining  $\bar{\text{H}}(2\text{S})$  but does not deflect the charged part of the beam. In addition, the setup needed to be able to reach vacuum levels of  $10^{-10}$  mbar and all parts to be non-magnetic.

#### 4.1.1 Microchannel Plates

As a detector, Microchannel Plates (MCPs) were chosen. In this section, first the working principle of such a detector is explained and our 3D design shown. A subsection is dedicated to the discussion about special plate coatings to increase the detection efficiency of Ly- $\alpha$ . Furthermore, the electronics involved to operate an MCP, such as different types of high voltage dividers, are discussed by showing the electrical circuit sketches.

### Working Principle

The MCP is a detector type similar to an electron multiplier, but can also offer spatial information. The MCP is a thin (usually around 1 mm) plate with a lot of channels, similar to a sieve. The channels are all under a certain angle relative to the plate. Across the plate, an accelerating potential difference is applied. When an incoming particle hits the MCP and interacts with the material, secondary electrons will be released. Within the channel, the electrons will be accelerated and gain enough energy to knock out more electrons, creating an avalanche. Eventually, the electrons will end up on the readout anode, where the signal will be read off as an electronic pulse.

To increase the gain, multiple plates can be combined; two plates together are called Chevron, three are a Z-stack. For a single stage, the gain will be  $>10^4$ , for a Chevron  $>10^7$  and for a Z-stack  $>10^8$  (188). It is advantageous to have the plates rotated relative to each other, optimally 180 deg, to have the channels maximally misaligned and thereby making it more difficult for the electrons to pass through without any interaction with the walls. With a Chevron setup, even single particles can be detected and counting experiments performed. A sketch of the working principle of a Chevron MCP is shown in Fig. 4.1.

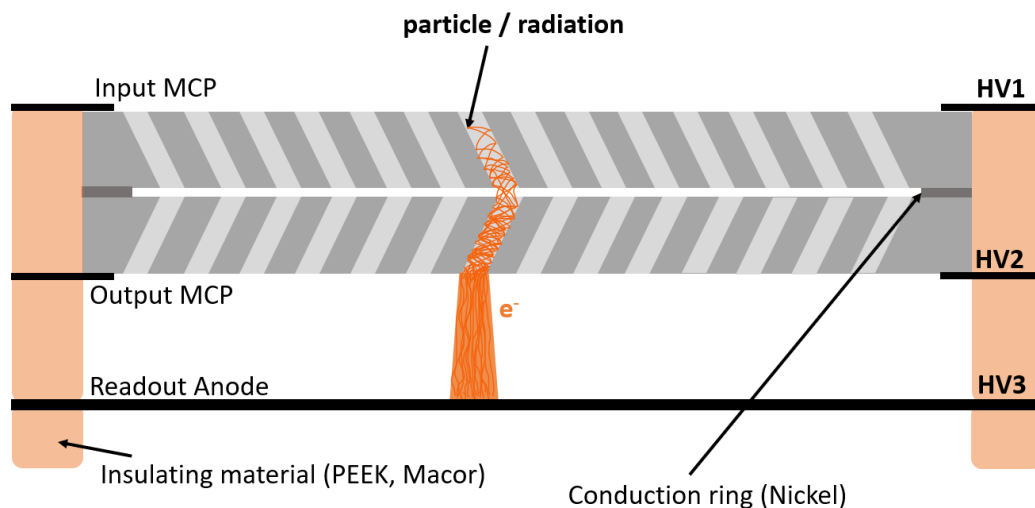


FIGURE 4.1: A schematic of a Chevron-type MCP and its working principle shown.

### Design

Our custom design is based on a standard MCP that can be bought commercially. The entire setup is mounted on a grounded stainless steel base plate. Through the plate, several PEEK pillars are screwed through. The pillars have a certain height to accommodate either the readout anode, the back frame or the front frame of the MCP. The back frame is used to have the output MCP plate resting on. In between output plate and back frame, a nickel spacer with a thickness of 100  $\mu\text{m}$  is placed to improve the electrical contact. Between the output and input plate, another nickel spacer is sandwiched. The input plate is eventually pressed down by another nickel spacer and the front frame. All the screws have to be hand tight, since with over tightening one might risk cracking the thin MCP plates. All screws are enclosed by

PEEK pillars and are fastened either by some tapped hole in the frames or by nuts close to the base plate. The electrical connections to apply HV on each of the plates as well as on the anode are done by fastening cable lugs at one of the base plate connections. The cable lugs are crimped to UHV compatible coax cables, which are eventually connected to vacuum feedthroughs. A picture of the assembly is shown in Fig. 4.2, where all important parts are described. To avoid having virtual leaks due to trapped air, all holes have an additional tiny venting hole drilled. Since the detectors will be under high voltage, all edges needed to be smoothed to minimize the risk of electrical discharges and sparks.

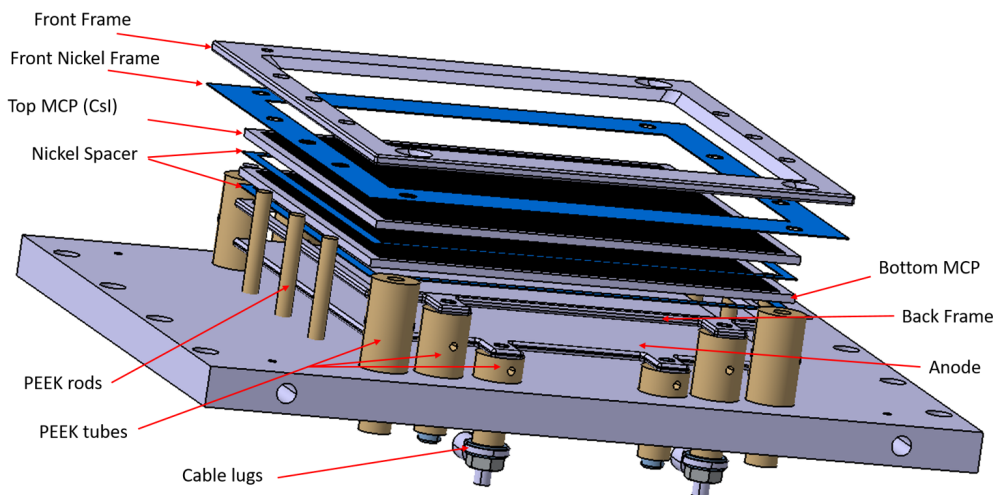


FIGURE 4.2: The 3D design of an MCP for the GBAR Lamb shift setup. The layers are in "exploding mode" to see, layer by layer, how the sandwich-assembly looks like.

## Coatings

MCPs are usually used for efficient detection of low-energy charged particles. For visible, UV or X-ray radiation, the detection efficiency is non-negligible, but maximally around a few % (189). In the case of detecting single Ly- $\alpha$  photons at 122 nm wavelength, such a low detection efficiency would not be sufficient. To enhance the efficiency, the input plate in the detector setup is coated with a material such as caesium iodide (CsI) or potassium bromide (KBr). These coatings act as a converter from UV photon to a single electron with a quantum efficiency of around 50 % (CsI) (190) and 30 % (KBr) (191).

The electrons created at the surface of the MCP are backscattered, whereas the electrons created inside the first layers of the channel will stay there. Electrons at eV energy can be efficiently detected with a Chevron setup. The disadvantage of such coatings are that both CsI and KBr are hygroscopic materials and will degrade when exposed to humidity. In the case of CsI, this will happen already when exposed to air for a few hours, whereas the order for KBr is rather days (192). This makes not only the assembly and installation of the CsI detectors more challenging, but also the storage and transportation should always be in a vacuum better than  $10^{-2}$  mbar (193). The main reason a CsI coating was chosen over KBr is its better quantum efficiency, increasing the single Ly- $\alpha$  photon detection by a factor of roughly 1.66.

The CsI-MCPs for the GBAR setup were assembled in nitrogen atmosphere, since an open assembly within minutes was not possible. In Fig. 4.3, two fully assembled MCPs with a CsI (left) and KBr coating (right) are shown. If the coating degraded, the colors would turn from a shiny to a milky appearance.

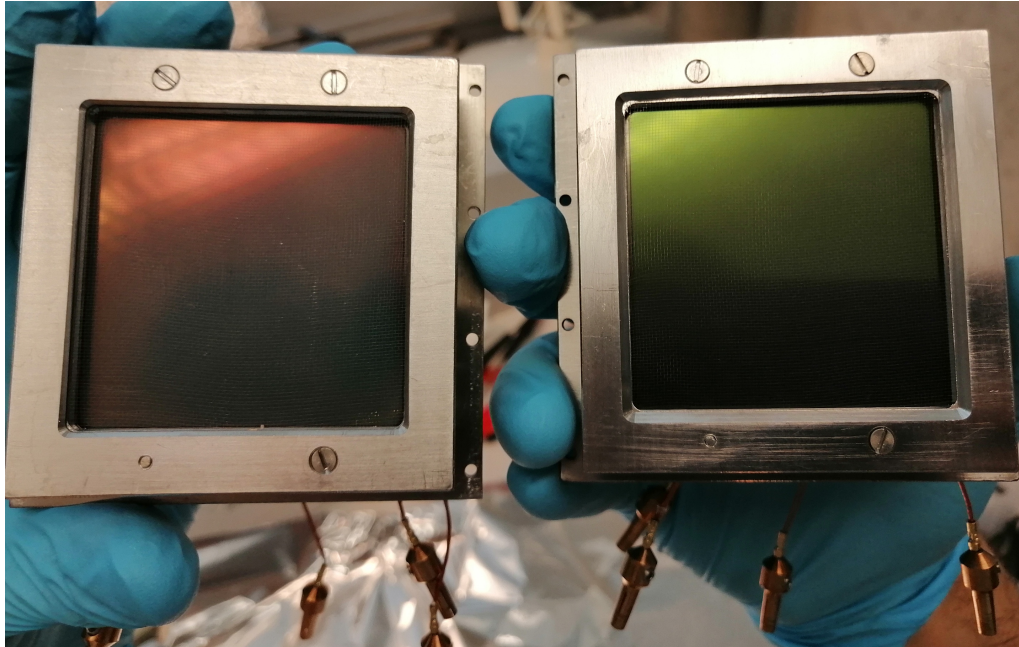


FIGURE 4.3: An MCP setup with CsI (left) and a second one with KBr coating (right).

### HV dividers

The plates have a resistance of around  $100\text{ M}\Omega$ . Therefore, when trying to bias front and back frame with separate HV channels of a regular supply, an assembled MCP is behaving as a closed circuit. One channel will limit the other and no sufficient field can be applied. By using supplies that allow high voltage as well as high current, this problem could be overcome, introducing though another risk. If one of the supplies fails or by ramping up the supplies wrongly, too large voltages could be applied across the plates and would damage them. A safer way around is to bias the MCP with a single HV channel through a voltage divider, whose total resistance is much smaller than the internal one of the MCP. We typically chose a total resistance of around  $10\text{ M}\Omega$ , so currents of the order of hundreds of  $\mu\text{A}$  are drawn from the supply.

An MCP can be operated in two different modes to detect photons. Usually the first mode to be used is to have the front frame highly negatively biased and the anode grounded. This way, only positively charged ions will make it to the MCP and the floating anode can be read out by directly hooking it up to the readout devices. An example is shown in Fig. 4.4 on the right side. The maximum (safe) voltage across two plates is around  $2\text{ kV}$ . As described in the coating section, the electrons generated on the surface by the UV-photons are backscattered and would therefore be rejected in this mode, though. With an additional, negatively biased grid in front of the MCP, the background electrons can be still rejected, while the surface electrons generated by UV will be pushed into the MCP itself. If no additional biasable grid can be integrated, the divider can be switched to an electron-accepting mode.

The front frame can be biased positively, so that negatively charged particles are being attracted. In this case, to have the generated secondary electrons travelling towards the anode, the back frame needs to be more positively biased and the anode even slightly (typically around +200 V) more. A sketch of such a circuit is shown in Fig. 4.4 on the left side. In this mode, electrons are accepted and thus usually a larger background will be seen. Additionally, the signal on the anode cannot be read off directly; it has to be capacitatively coupled to avoid having 2.6 kV on the readout channel afterwards. To avoid attracting very low energy electrons, the sketch can be altered by having the front frame on ground.

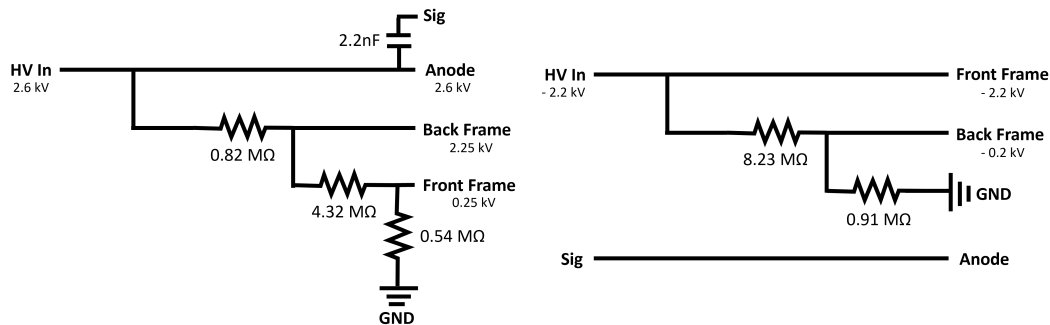


FIGURE 4.4: The high voltage divider options for a positively biased anode (left) and grounded anode (right).

### 4.1.2 Quenching Setup

Since the Lamb shift measurement is parasitic and the main goal is to efficiently transport  $\bar{\text{H}}^+$  through the setup, one crucial condition for the design of the quenching area is to not interfere with the path of the ions. The setup with two ring anodes was found to be optimal to create the electrical field. The entire quenching region is surrounded by a grounded grid made of tungsten (92 % transparency), to avoid the MCPs influencing the quenching area and vice versa. The quenching rings are designed to be biased with opposite voltages. A SIMION simulation showed that  $\pm 1.5$  kV is sufficient to create a field of the order of  $100 \text{ V cm}^{-1}$  which efficiently quenches a 6 keV  $\bar{\text{H}}(2\text{S})$  beam. It also maximizes the solid angle covered by the MCPs for Ly- $\alpha$  detection (total of  $\sim 41.5\%$ ). The entire setup is shielded by copper plates to minimize the interference coming from the microwave region, but also to be able to fix all components. In this way, the detection setup can be guided as a single piece into the vacuum chamber. Fig. 4.5 shows the complete setup, except that three CsI-MCPs are missing for easier visualization. Four CsI-MCPs would in fact enclose the entire area.

### 4.1.3 Vacuum Chamber

The entire setup was eventually put into the vacuum chamber and fixed with the clamps on the copper plates. The HV connections for the ring electrodes as well as the MCPs were guided through the arms of the chamber and connected to SHV feedthroughs. The system was closed with three gate valves, two on each side of the CF160 openings and one on top of the turbo pump, which is connected to the free CF40 port at the vacuum chamber. In this way, the chamber can be comfortably transported in vacuum, without risking the CsI-MCPs to degrade. The assembled



setup is shown in Fig. 4.6. The chamber has a pressure meter connected so the pressure inside can be monitored at all times. The setup was pumped down to vacuum levels of  $10^{-9}$  mbar. In the GBAR beamline, with help from additional pumping, the pressure went down to the goal of a few  $10^{-10}$  mbar.

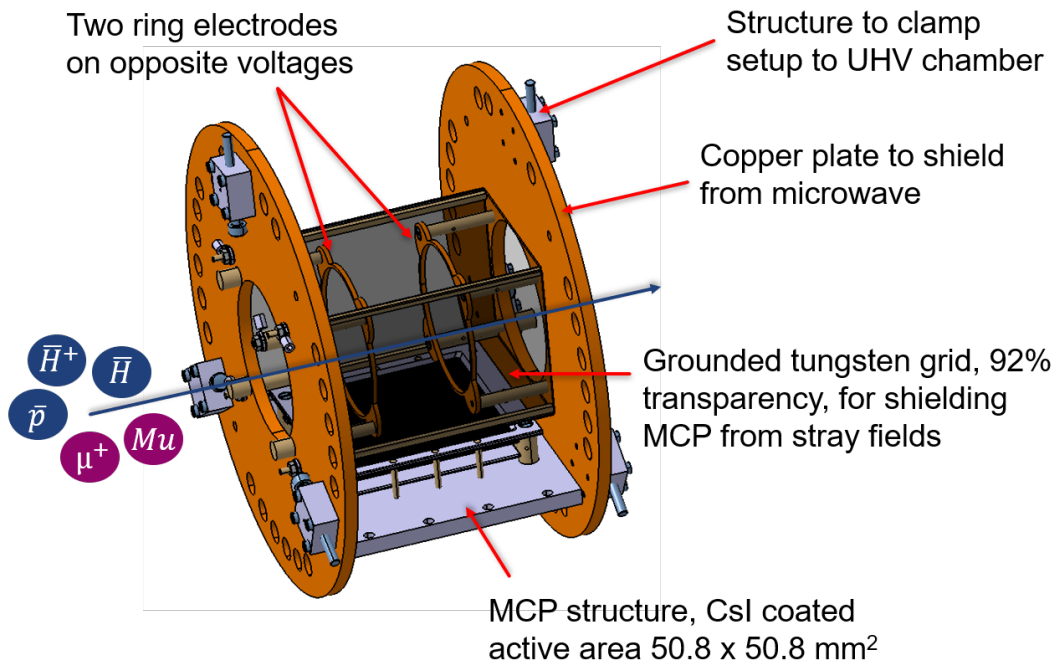


FIGURE 4.5: The 3D drawing of the  $\text{Ly-}\alpha$  detection setup for GBAR.

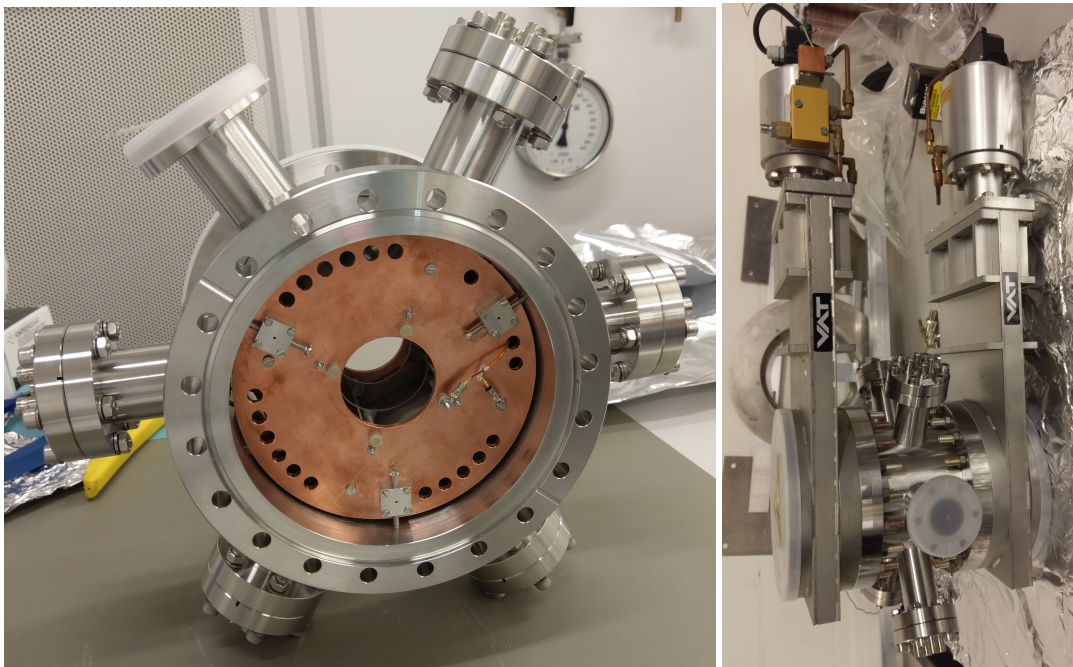


FIGURE 4.6: The vacuum chamber with the  $\text{Ly-}\alpha$  detection setup inside for the GBAR Lamb shift experiment. On the left side, the vacuum chamber is open and the  $\text{Ly-}\alpha$  detection visible, whereas on the right side, both gate valves are mounted.

## 4.2 First test at PSI with Muonium

To commission the setup meant for measuring the Lamb shift of  $\bar{H}$  at GBAR, the Low-Energy Muon Beamline (LEM) at PSI was used. The goal was to study the possibility of forming an intense beam of metastable muonium  $M(2S)$  to demonstrate our ability to detect  $M(2S)$  for Mu-MASS. The following sections will follow closely the findings published in (187). The setup used in these measurements is shown in Fig. 4.7.

The LEM beamline can provide a slow, monoenergetic beam of positive muons ( $\mu^+$ ) in the energy range of 2 to 20 keV. In this energy range, referring to proton data, a non-negligible amount of  $M(2S)$  is expected to be formed when using the beamfoil technique described in Sec. 3.2.

The 10 nm thin carbon foil not only acts as converter to produce muonium, but also to give us the ability to tag incoming  $\mu^+$ . Upon impact, the muon releases secondary electrons from the foil, which are detected with the Tag-MCP to give the start trigger signal. The beam passes then through the Ly- $\alpha$  setup shown in Sec. 4.1.1, where the metastable fraction is quenched by the electrical field created by the two ring electrodes. Due to the electrical field, the  $2S$  atoms are continuously pushed into the  $2P$  state, where they relax to the ground state within a few nanoseconds, under the emission of a Ly- $\alpha$  photon. This area is surrounded by four CsI-coated MCPs, which are used to count these photons. To separate eventually the  $M$  from the  $\mu^+$  beam, a rejection electrode is put on high voltage to let only the  $M$  pass. After the rejection electrode, a Stop-MCP detects the  $M$  and gives the stop signal.

In Fig. 4.10, a time-of-flight example of an incident 10 keV  $\mu^+$  beam is shown, once with rejection electrode turned off and once on, showing the clear formation of muonium. These measurements were done at three different incident  $\mu^+$  energies (5.0, 7.5 and 10.0 keV) to identify the optimal energy to produce an intense  $M(2S)$  beam.

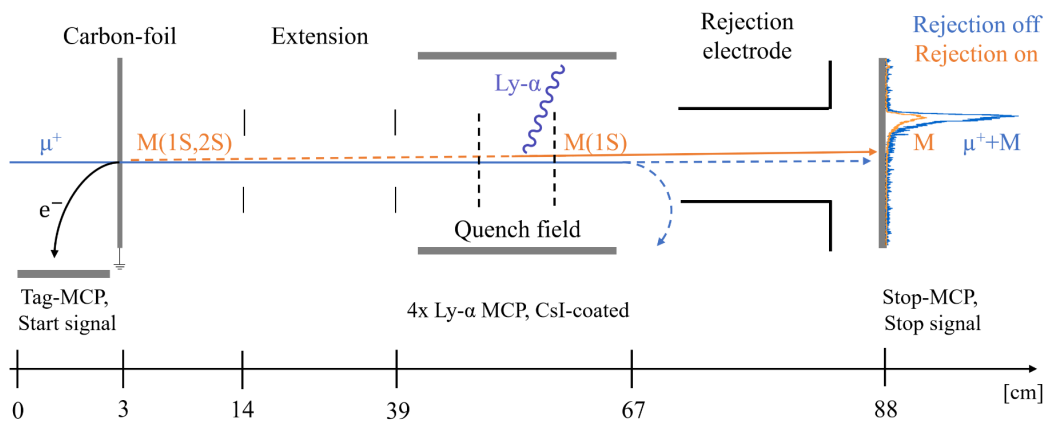


FIGURE 4.7: The experimental setup installed at the end of the LEM beamline. The lengths at the bottom are not to scale. The GBAR Ly- $\alpha$  setup is located in the middle of the entire setup.

### 4.2.1 Determining Time Offset

By measuring the time-of-flight (TOF) of the particles from the Tag-MCP to the Stop-MCP, a lot of information such as energy loss in the foil or the energy-dependent M formation fraction can be extracted. This requires to know the delays along the beamline (e.g. time-of-flight of secondary electrons from foil to Tag-MCP, different cable lengths for detectors etc.).

A reliable way to extract the time offset  $t_0$  of the detection system is to measure a TOF spectrum with the beam length  $L_1$ , introduce afterwards an extension with well-known length  $\Delta L$  to the beamline and then re-measure the TOF spectrum. An example of such two TOFs at an incident  $\mu^+$  energy of 10 keV is shown in Fig. 4.8. A Landau distribution was used to fit the TOF spectra and extract the most-probable times  $t_1$  and  $t_2$ . The  $t_0$  can be calculated with:

$$t_0 = \frac{[(L_1 + \Delta L) \cdot t_1 - L_1 \cdot t_2]}{\Delta L} \quad (4.1)$$

Evaluating all our data taken, we calculated the  $t_0$  to be 51(4) ns. From all the measured TOF spectra this value had to be subtracted to obtain the true time-of-flight.

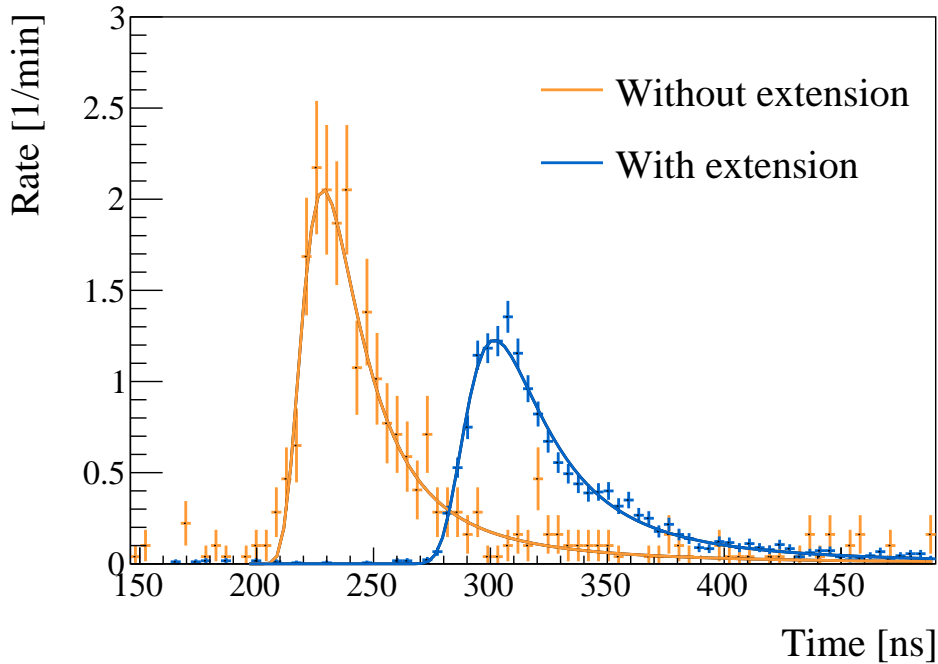


FIGURE 4.8: TOF distributions of M for 10 keV  $\mu^+$  incident on foil, with (blue) and without (orange) extension stage. A Landau distribution was used for fitting the spectra.



### 4.2.2 Energy Calibration

After time correcting the TOF spectra, the energy loss in the carbon foil can be studied. This was done by converting the TOF spectra collected at 5.0, 7.5 and 10 keV to energy spectra via:

$$E = \frac{1}{2} \cdot m_{\mu} \cdot \left( \frac{L_{\text{tot}}}{t_{\text{corr}}} \right)^2 \quad (4.2)$$

where  $m_{\mu}$  is the muon mass,  $L_{\text{tot}}$  the total length of the system and  $t_{\text{corr}}$  the corrected TOF. The three energy distributions are shown in Fig.4.9.

It was found that the most probable energy loss in the foil is in the range of 2.5 - 3.0 keV, which does not agree with the values of around 1.5 to 2.0 keV found by other measurements performed with 10 nm-thick carbon foils at LEM. The musrSIM Geant4 simulation, in which the effective interaction of  $\mu^+$  with the carbon foil is integrated (153), finds that the energy loss distributions fits better to a thicker foil of around 15 nm. The quality of the foil installed was not optimal, a few holes were present. Additionally, the foil was not stored in vacuum before installing it in the LEM beamline, which could result in some additional layers of water deposited on its surface. In any case, these defects do not limit us in detecting M and 2S formation.

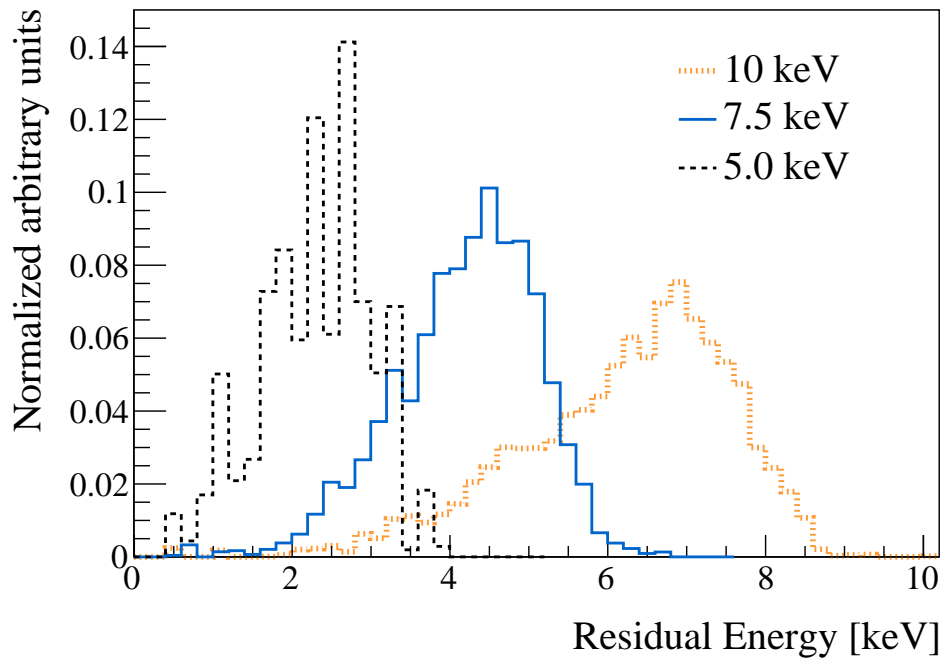


FIGURE 4.9: Energy distributions of muons measured at three different  $\mu^+$  incident energies. The histograms are normalized to an area of 1. The orange belongs to the 10 keV, blue 7.5 keV and black 5 keV incident  $\mu^+$  energy datasets.

### 4.2.3 M formation fraction at different energies

By knowing the energy distributions, the M formation fraction at different energies can be determined. By gathering a dataset with rejection electrode on, only M is detected by the Stop-MCP. From all the TOF a flat background of around 0.1 counts/min was subtracted. Normalizing the TOF histograms with the measuring time and integrating their area in the region of interest yields the M rate  $R_M$ . Turning the rejection electrode off, the rate for M and  $\mu^+$  reaching the Stop-MCP is measured. By integrating the same area, the normalization factor  $R_{M+\mu^+}$  is obtained. The M formation fraction  $f_M$  is then defined as:

$$f_M = \frac{R_M}{R_{M+\mu^+}} \quad (4.3)$$

To obtain M formation fractions at additional energies than just the three measured, the TOF was split in multiple time bins. Calculating the ratio mentioned in Eq. 4.3 for only a specific bin and thus specific energy range, the amount of fractions is increased. The example of the 10 keV dataset is shown in Fig. 4.10. From this specific dataset, a total of six fractions at different energies was obtained.

All the M formation fraction results are summarized in Fig. 4.11, where the fractions were plotted together with mass-scaled hydrogen data (194; 195; 196; 197; 198; 199; 200; 149). Despite the systematically lower formation fraction compared to hydrogen, the yield is large enough to detect metastable M(2S).

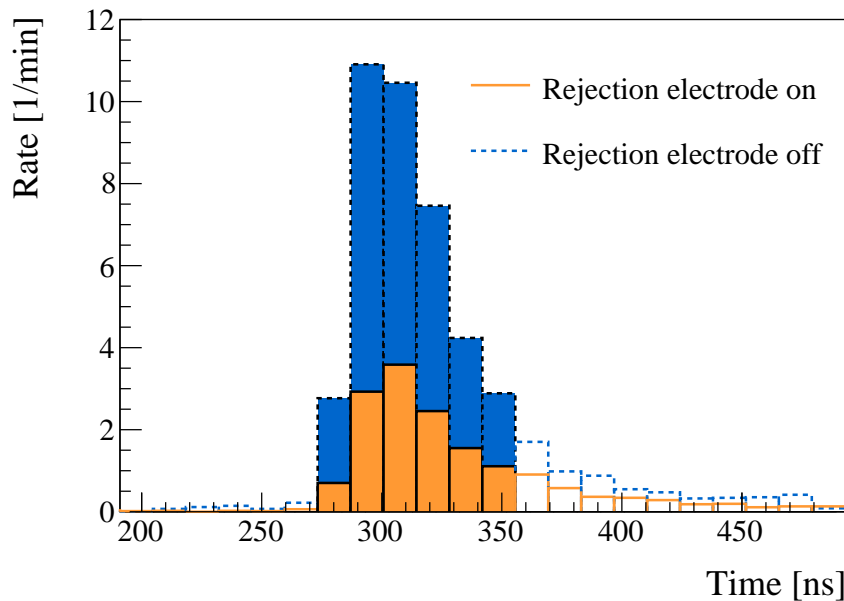


FIGURE 4.10: Histograms obtained from the dataset of 10 keV incident energy after background subtraction. The orange data is with rejection electrode on and corresponds to pure M signal. The blue data is with rejection electrode off and corresponds to M and  $\mu^+$  signals. The filled bins were used to extract M fractions, whereas the hollow bins were ignored due to large statistical uncertainty and additional background.

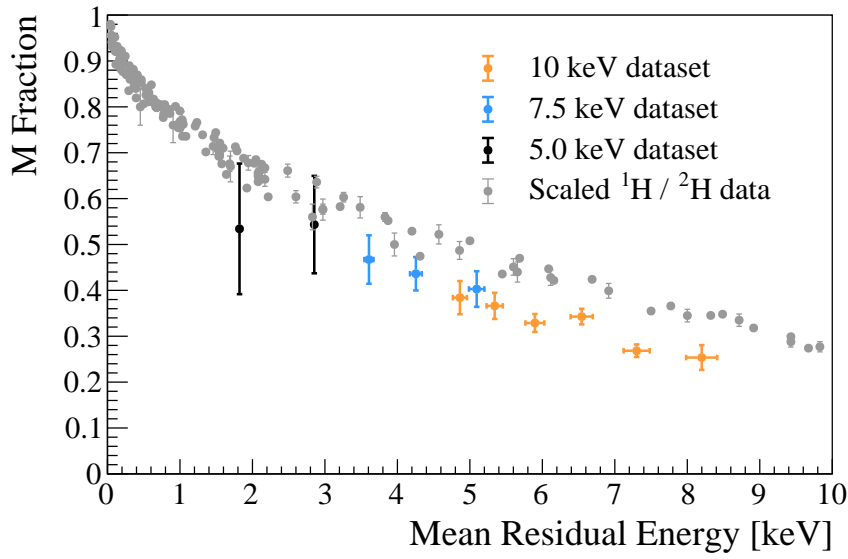


FIGURE 4.11: M fraction measured as a function of residual energy after the foil. The hydrogen and deuterium were taken from (194; 195; 196; 197; 198; 199; 200; 149) and their energies mass-scaled to obtain the case for M.

#### 4.2.4 M(2S) formation fraction

For the M(2S) measurement, the Ly- $\alpha$  setup was used. The goal was to see a Ly- $\alpha$  signature by demanding a triple coincidence signal. Additional to the Start- and Stop-MCP, also one of the Ly- $\alpha$  detectors needed to have a signal in their specified TOF windows. This specific signal signature corresponds to a  $\mu^+$  that released secondary electrons, picked up an electron to become M(2S), which continued its flight through the Ly- $\alpha$  setup, got quenched under emission of a Ly- $\alpha$  photon, and eventually ended up on the Stop-MCP. For this measurement, the rejection electrode stayed on for the entire time, but the quenching electrodes were for some runs ramped up to positive and negative 2.5 kV, respectively, or turned off completely.

In Fig. 4.12 an excess of signal is visible when the quenching field is on, indicating a successful detection of Ly- $\alpha$  photons. The area of the excess is giving the total rate of Ly- $\alpha$  photons detected  $R_{\text{Ly}\alpha}$ .

As normalization, similar as for the M formation fraction, the rate of M detected by the Stop-MCP  $R_{\text{M}}$  is used. The rate of Ly- $\alpha$  photons detected is calculable via:

$$R_{\text{Ly}\alpha} = R_{\text{M}} \cdot f_{2\text{S}/\text{M}} \cdot \epsilon_{\text{Det}} \quad (4.4)$$

where  $f_{2\text{S}/\text{M}}$  is the fraction of M(2S) out of the total M formed and  $\epsilon_{\text{Det}}$  the efficiency for the Ly- $\alpha$  photon detection. This efficiency was identified to be a convolution of the detection efficiency of the Ly- $\alpha$  MCPs, the quenching efficiency as well as the solid angle covered by the MCPs. Rearranging Eq. 4.4 to extract  $f_{2\text{S}/\text{M}}$  and introducing the two efficiencies  $\epsilon_{\text{QG}}$  (combination of quenching and geometry) and  $\epsilon_{\text{MCP}}$  (MCP detection), we obtain:

$$f_{2\text{S}/\text{M}} = \frac{R_{\text{Ly}\alpha}}{R_{\text{M}} \cdot \epsilon_{\text{QG}} \cdot \epsilon_{\text{MCP}}} \quad (4.5)$$

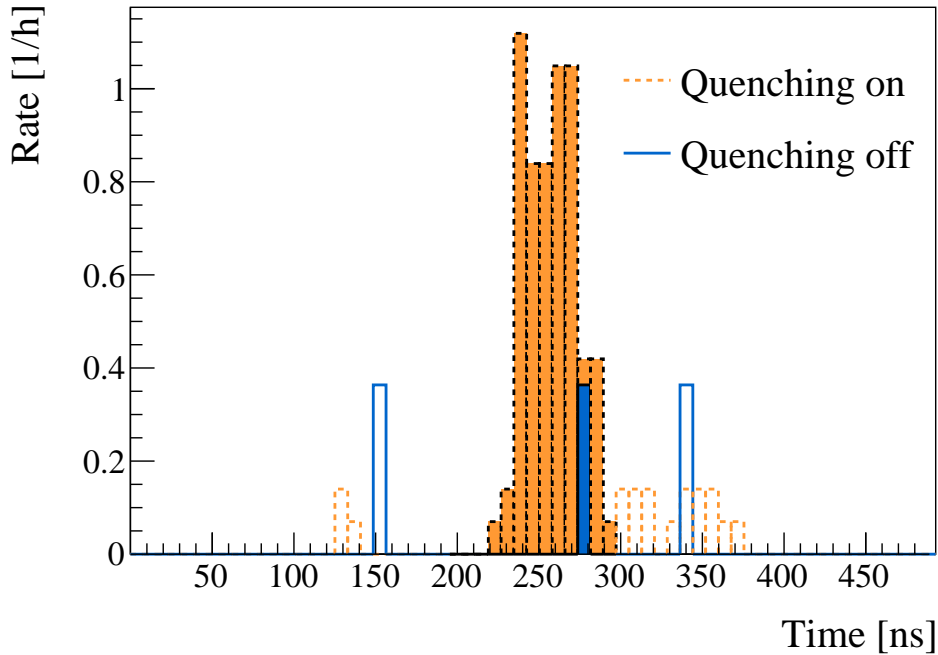


FIGURE 4.12: Time-of-flight distributions of the counts in the Ly- $\alpha$  MCPs, obtained from the triple coincidence dataset of 10 keV incident energy. The orange data is with quenching electrodes turned on, the blue data is with quenching off. The coloured area is the time window of interest, where the Ly- $\alpha$  signal is to be expected

The MCP detection efficiency was estimated by  $\epsilon_{\text{MCP}} = \text{OAR} \cdot \epsilon_{\text{CSI}}$ , where OAR stands for Open Area Ratio of the MCP and was in our case 0.45. The  $\epsilon_{\text{CSI}}$  is the conversion efficiency from a single photon to electron, called quantum efficiency, and is taken from (201; 190) to be in the range of 0.45-0.55. The quenching and solid angle efficiency  $\epsilon_{\text{QG}}$  was simulated in SIMION and is around 0.37. The therefrom calculated M(2S) formation fractions are summarized in Tab. 4.1. Unfortunately, for the dataset of 5 keV incident beam, no Ly- $\alpha$  photons above background could be detected due to too low statistics.

#### 4.2.5 Summary

The rate of the M(2S) beam is estimated by:

$$R_{2S} = R_{\mu} \cdot f_M \cdot f_{2S/M} \quad (4.6)$$

and results energy-dependent between 80 Hz to 100 Hz. These rates are around four orders of magnitude larger than what was obtained in the previous M Lamb shift experiments. Our result not only shows the successful commissioning of the GBAR Lamb shift setup, but also indicates that there would be the opportunity to improve upon the best determination of the M Lamb shift at LEM as reported in Chap. 5.

TABLE 4.1: Summary of values extracted from different incident energies  $E_{\text{inc}}$ . MPE is the Most Probable Energy for M that traversed the foil and reached the Stop-MCP.

$E_{\text{inc}}$ (keV)	MPE (keV)	$f_{M/\mu^+}$ (%)	$f_{2S/M}$ (%)	$R_{\mu^+}$ (kHz)	$R_{2S}$ (Hz)
5.0	$2.7 \pm 0.1$	$56.8 \pm 9.0$	-	1.45	$83^* \pm 21$
7.5	$4.7 \pm 0.2$	$43.2 \pm 2.4$	$11 \pm 4$	2.07	$100 \pm 30$
10.0	$7.0 \pm 0.3$	$31.8 \pm 0.8$	$10 \pm 3$	2.84	$90 \pm 30$

\* For  $R_{2S}$  at 5 keV,  $f_{2S/M} = 10(2)\%$  was assumed (see text).

### 4.3 Microwave

In this section, the complete microwave setup of the Lamb shift setup is presented. To have a simple but stable, high-power and broadband setup around a frequency of 1 GHz, the design of a transmission line (TL) was chosen. To run the TL in a well-predictable manner, the entire additional equipment and their specifications will be presented and different running modes explained. The predictability of the behaviour of the TL is an important feature, since the field inside needs to be modeled and included in the simulation to improve the analysis and study systematic effects. Therefore, also reproducible characterizations of the whole system needed to be done to study power losses and the working frequency ranges. Large parts of this section was not done by the author, but by B. Ohayon and students S. Bruno and N. Radevic.

#### 4.3.1 Design of Transmission Line

The design of the TL was inspired by Lundeen and Pipkin (202). The idea is to create an oscillating field between two plates by applying an RF frequency. Optimally, on both plates the RF frequency is applied, on one shifted by a  $\pi$  phase. In this case there will be a virtual ground plane in the center of the TL, and thus the complete TL will be symmetrical and easier to model.

To ensure the TL to be broadband, i.e. to have very little power loss over a large range of frequencies, a lot of trial and error needs to be done. For testing the system as efficiently as possible, outside of vacuum, and make its behaviour similar irrespective to the surrounding, a closed cube design made out of oxygen-free copper was chosen. The connectors are of SMA-type, whose pin is stuck into a groove on the plate. In the tests, the groove shape and dimension turned out to be one of the most sensitive element of the design to ensure optimal transmission. Non-conductive spacers made out of PEEK were chosen to be squeezed between plate and cube to assist with levelling the plates. A screw from the outside fixed the PEEK spacers in place. The cube design was held together by L-pieces made of stainless steel. The plates are eventually only held by the connector pins pressing against the plate grooves, therefore the L-pieces need to be tightly screwed.

The transmission and reflection of the specific TL was measured and optimized with a Vector Network Analyzer (VNA). After the optimization, the cube was placed into vacuum and the SMA-connectors with high-quality, commercially available SMA cables for UHV connected to the SMA-feedthroughs of the vacuum chamber. Further tests in vacuum showed that there is no significant measurable difference in

power transmission. The vacuum levels stayed stable at UHV of  $10^{-9}$  mbar level, after some short conditioning even at high powers of 30 W.

The length of the cube is around 42 mm, the plates are distanced from each other by 23.5 mm. The bore hole for the beam to pass through is 20 mm in diameter. The assembled cube is shown in Fig. 4.13.

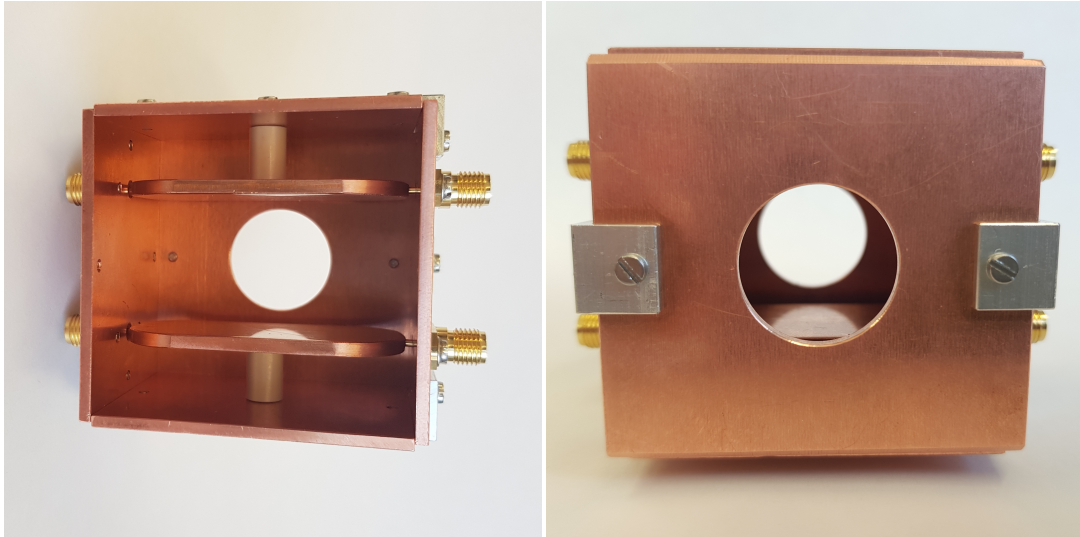


FIGURE 4.13: Picture of the HFS TL assembled. On the left, the view from the front without the front cover, and on the right the fully assembled TL from the front is shown.

### 4.3.2 Microwave Setup

The two TLs designed for the experiment need to fulfil two different sets of conditions. One TL will be used for scanning the specific transition (Scanner TL), whereas the other TL purpose (hyperfine state selector, HFS TL) is to drive other transitions to reduce background and influences on the line-shape. For the measurements, a Tektronix TSG-4102A (Scanner) and an AnaPico APSIN26G (HFS) were available as RF-generators. To measure the power, the Keysight USB Power Sensor U8481A was used. Different amplifiers and attenuators from MiniCircuits and splitters/combiners from TRM Microwave, depending on the frequency range and power needed, could be chosen from. These elements are described more detailed in Sec. 4.3.3.

#### Scanner TL

The field inside the Scanner TL should be as symmetric as possible. For this reason, on both plates the RF is applied, but on one plate shifted by a  $\pi$  phase. Like this is guaranteed that in the center of the TL, where most of the particles will fly through, is a virtual ground plane (see Fig. 5.1). The  $\pi$  shift can be established by introducing a splitter right after the RF-generator. After the splitter, both RF outputs are amplified with each a high-power amplifier (around 40 dB) and fed through the feedthroughs to the plates. On the other side of the TL, the two RF-lines are merged again with a combiner. The eventual power is measured with a power meter. To not saturate the power meter, the RF power is attenuated beforehand with a series of attenuators. Typically, the first attenuator in line is of around  $-3$  dB and only then stronger ones of  $-20$  dB are used, to avoid losing most of the power already at the first one, heating it up and possibly changing the characteristics of the setup.

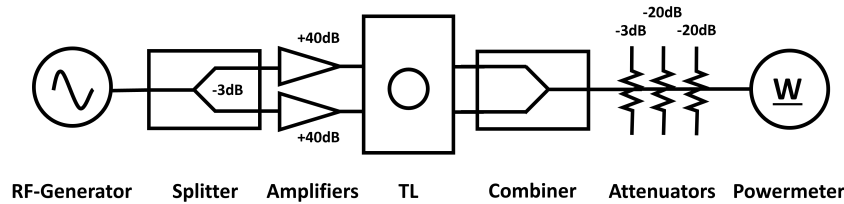


FIGURE 4.14: The MW setup sketch for the Scanner TL.

The downside of introducing splitters and combiner is that these elements are responsible for the majority of power loss. For the Scanner TL this is not a problem; the available power is more than sufficient for scanning since saturating the transition is not aspired and would complicate the analysis afterwards. The splitters as well as the amplifiers make it more difficult to have the TL at a high power over a large frequency band and therefore need to be chosen carefully for the frequency range to be scanned. The complete setup is sketched in Fig. 4.14.

### HFS TL

In case of the HFS TL, the field homogeneity or how well it can be modelled is less of importance. The task of this TL is to drive down as efficiently as possible unwanted transitions. Saturation of the line is beneficial, since the power broadening could possibly also drive states in the vicinity. Therefore, the splitter and combiner are removed. A single, strong amplifier at around 43 dB is used right after the RF-generator and the amplified signal fed directly to one of the plates. The other plate is kept grounded on both sides. A strong amplifier has the downside that the frequency-dependent amplification is less stable. This is not an issue for the HFS TL, since it does not have to be broadband anymore; the HFS TL will be fixed on a single frequency for the entire measurement. The power is read off the single plate with a power meter after being attenuated. The HFS TL setup is sketched in Fig. 4.15. A summary of available splitters and amplifiers can be found in Tab. 4.2, with working frequency range and minimum amplification listed. The actual characterization of these devices is shown in Sec. 4.3.3.

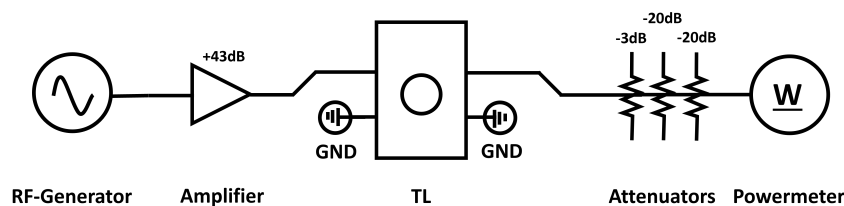


FIGURE 4.15: The MW setup sketch for the HFS TL.

### 4.3.3 Characterization

The characterization curves are measured by connecting the element directly to the RF-generator and to the power meter. For the power meter, the baseline is measured beforehand and subtracted from the measurements. In Fig. 4.16, the characterization curves for available amplifiers (right) and splitters/combiners (left) are shown. It is clearly visible that the response of these elements is strongly depending on the RF frequency and need to be chosen accordingly. For the Scanner TL, a reasonable



power in a range of at least  $\pm 250$  MHz from the resonance frequency is necessary to measure a line-shape. For the HFS TL, only the power at the resonance frequency is relevant.

From the characterizations, a combination of «ZHL-20W-202-S» amplifier and «RM Microwave HS101 fc1080» splitter is the most suitable for the muonium Lamb shift scan at 1140 MHz resonance. For hydrogen, less power is needed and therefore also the «ZHL-10W-2G+» amplifier and «TRM Microwave HS101 fc900» splitter can be used. To scan the isolated transition at 583 MHz in muonium, the choice of splitter and amplifier needs to be changed to «RM Microwave HS101 fc600» and «ZHL-20W-13SW+». Further characterizations can be done to study the losses in the TLs and also for each attenuator, see Fig. 4.17. These elements have much less influence on the overall power and have only to be taken into account for a correct power estimation in the analysis.

TABLE 4.2: List of available MW elements for the measurements.

Element	Model	Optimal Freq. (MHz)	Loss/Gain (dB)
Splitter/Comb.	TRM Microwave HS101 fc600	300 – 850	$> -0.8$
Splitter/Comb.	TRM Microwave HS101 fc1080	750 – 1350	$> -1.5$
Splitter/Comb.	TRM Microwave HS101 fc900	700 – 1150	$> -1.7$
Amplifier	ZHL-20W-13SW+	200 – 800	$> +43$
Amplifier	ZHL-20W-202-S+	200 – 1600	$> +44$
Amplifier	ZHL-10W-2G+	750 – 1400	$> +40$
Attenuator	BW-S3W20+	200 – 1600	$-3$
Attenuator	BW-S20W20+	200 – 1600	$-20$

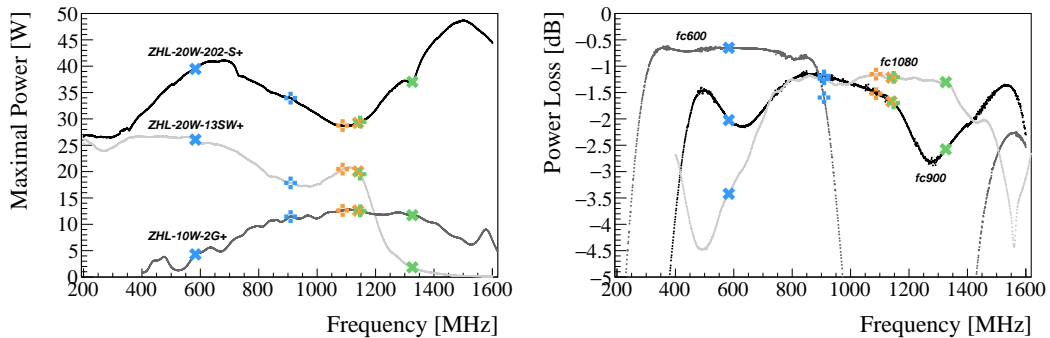


FIGURE 4.16: The characterization curves measured for the different amplifiers (left) and splitter-combiner combination (right). The crosses mark the resonances in muonium and pluses in hydrogen. The colors are chosen as used before in Chap. 3 for the different hyperfine levels.

#### 4.3.4 Power Determination inside TL

The knowledge of the frequency-dependent amplification is crucial to determine the maximal achievable power in the frequency range to be scanned, but is eventually not needed to calculate the power inside the TL. Only the transmitted power is measured, and characterization measurements showed a symmetric power loss behavior of the TL itself, so only the power losses after the center of the TL are of interest.



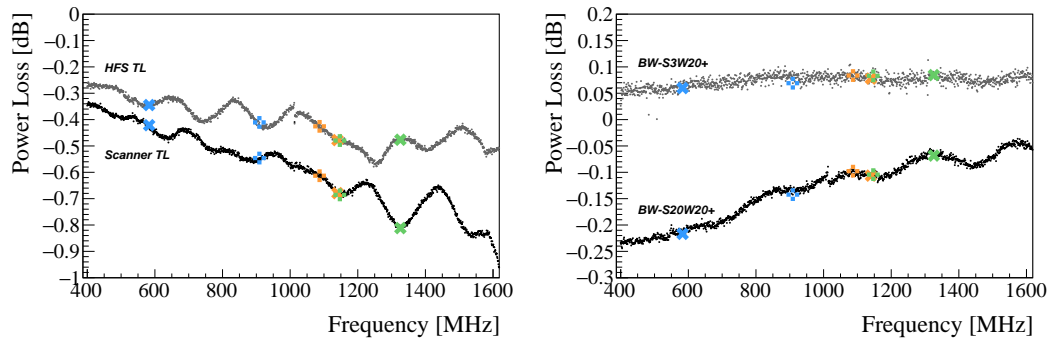


FIGURE 4.17: The characterization curves measured for the different TLs (left) and attenuators (right). The crosses mark the resonances in muonium and pluses in hydrogen. The colors are chosen as used before in Chap. 3 for the different hyperfine levels.

In the Scanner TL case, the characterization measurement to determine the power inside the TL can be set up as in Fig. 4.18. On the RF-generator, 0 dBm are typically set for convenience. The baseline consisting of a measurement of only RF-generator and power meter is used to correct the characterization to obtain only the case for the splitter-TL-combiner setup. The difference between the corrected measurement at the expected value of 0 dBm corresponds to the total power loss in dB. By taking half, the power loss after the center of the TL is obtained and can be used to correct the power measurements from the power meter, additional to the corrections of the series of attenuators. The power conversion from the units of dBm to the more intuitive one of watts is then done by:

$$P_W = 1W \times 10^{\frac{P_{\text{dBm}} - 30}{10}} \quad (4.7)$$

A similar approach can be done for the HFS TL shown in Fig. 4.19, although the power loss is much smaller and usually within the assumed uncertainties.

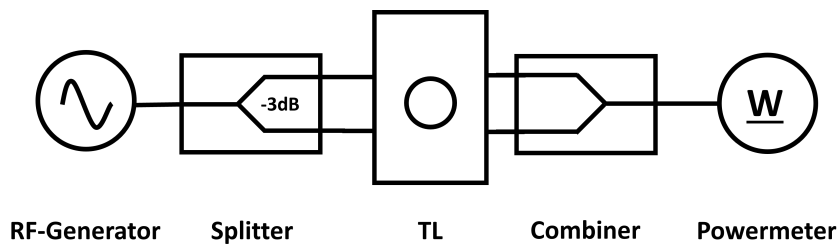


FIGURE 4.18: The setup to determine the power inside the Scanner TL.

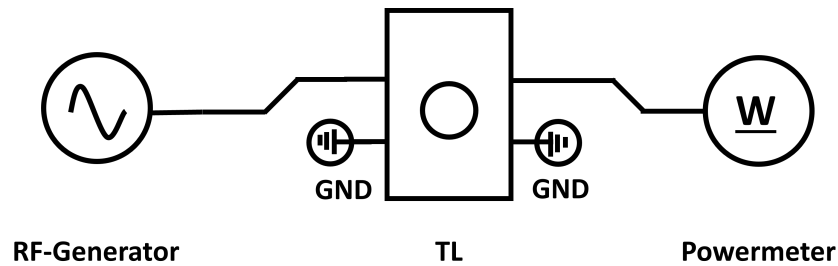


FIGURE 4.19: The setup to determine the power inside the HFS TL.

#### 4.4 Installation and commissioning at CERN

After the successful tests, the Lamb shift setup was installed in GBAR at CERN, as seen in Fig. 4.20. As a first step, the setup was tested with a pulsed proton beam at 10 keV energy firing onto a carbon foil, forming a hydrogen beam. By counting the Ly- $\alpha$  MCP signals with the TL at roughly 10 W, a clear excess of signals was counted when the TL frequency was off-resonance compared to on-resonance. Additionally, the background coming from  $\bar{p}$  annihilations when flying through the setup as well as gammas from the Ps decay was studied. Preliminary results indicate that the background can be distinguished from the Ly- $\alpha$  signal region by time-of-flight.

The next steps are to measure a line-shape of the hydrogen Lamb shift transitions, formed by either the beamfoil technique or the charge-exchange with Ps. In a second step, when antiprotons are available again in April 2022, the goals are to first detect a clear Ly- $\alpha$  signal from H(2S) and afterwards starting to scan the H Lamb shift transition.

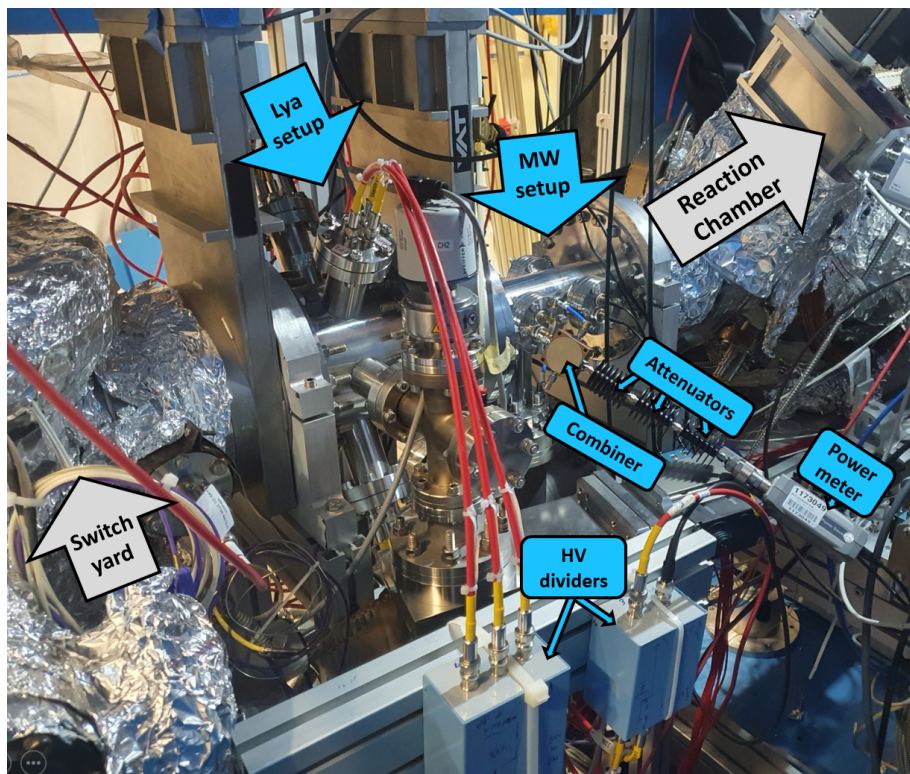


FIGURE 4.20: The GBAR Lamb shift setup installed in the GBAR beamline at CERN.

## Chapter 5

# Mu-MASS: Muonium Lamb Shift

As described in Chap. 4.2, due to the promising results obtained at PSI while commissioning the Ly- $\alpha$  setup for GBAR, the possibility opened up to measure and improve the muonium Lamb shift. A detailed Monte-Carlo simulation within the Geant4 framework, including the musrSIM simulation (203) of the LEM beamline, was written to study the expected line-shapes, which is described in Sec. 5.1. Equipped with the knowledge from simulation and from the measurements with the GBAR setup, a detection setup specifically for the muonium Lamb shift was designed.

The following sections are based on the published results in (204), adding more details and additional measurements. In Sec. 5.2, the differences in the setup compared to the one at GBAR is shown. The LEM beamline is not only capable of delivering an intense, monoenergetic  $\mu^+$  beam, but can also produce a proton beam. In the first stage, when no  $\mu^+$  beam was available yet, the setup was tested with hydrogen. This helped not only to commission the new setup for the muonium Lamb shift measurement, but also to benchmark the simulation. One of the findings with hydrogen was the evidence for the beam contamination from 4S states, which was essential for the further analysis with muonium. We eventually measured the  $2^2S_{1/2,F=1} \rightarrow 2^2P_{1/2,F=1}$  transition in muonium and determined the Lamb shift to be at 1047.2(25) MHz, which agrees well with our theoretical value within one standard deviation and comprises an order of magnitude of improvement upon the previously best value. With this improvement, we were able to set constraints on New Physics, such as CPT violation and new muonic forces.

Additionally, we scanned for a first time the isolated resonance  $2^2S_{1/2,F=0} \rightarrow 2^2P_{1/2,F=1}$  of muonium, whereof we were able to determine the muonium Lamb shift to 1045.3(72) MHz and the hyperfine splitting  $2S_{F=0} \rightarrow 2S_{F=1}$  to 559.6(72) MHz. This measurement comprises the first evidence for the detection of M(3S), which was determined to be 20(4) % of the muonium beam. These results are shown in greater detail in Sec. 5.6.

### 5.1 Simulation

To study the expected width and intensity of the Lamb shift line-shape as well as systematic effects such as the Doppler and Stark shift, a detailed Monte-Carlo simulation within the Geant4 framework was written. As a base we used the already existing musrSIM (203) and extended it with our own Lamb shift setup, shown in Fig. 5.2. The simulation was first run until just after the carbon foil to simulate the position and momentum distribution of the M(2S) right before entering the TLs. A dataset of  $10^8$  possible atom trajectories was saved. This dataset was then used to further simulate the transition probabilities in the TLs as well as the further trajectories until the Stop-MCP.

### 5.1.1 Simulating TL Fields

To extract the correct field strength inside the TL, the field maps were simulated with SIMION, following the procedure as used by S. R. Lundeen (202). The assumption is that the field inside the TL is made up completely by a TEM mode. The shape of this mode can be found by simulating a DC field, applying a voltage on the top and bottom plate. The actual oscillating field can then be obtained by multiplying it with a cosine:

$$V(y, z, t)_{\text{TEM}} = V(y, z)_{\text{SIMION}} \cdot S \cos(\omega t + \delta) \quad (5.1)$$

where  $S$  is a scaling factor,  $\omega$  the angular frequency applied on the TL,  $t$  the time and  $\delta$  the phase. The coordinate system is defined such as  $z$  is in the direction of beam propagation and  $y$  orthogonal to the TL plates. The scaling factor  $S$  is depending on what voltages have been applied for the DC field in SIMION. Two cases were tried:

- With the design shown in Fig. 4.14 with a splitter and combiner, both the top and bottom plate have the same voltage applied, but with opposite polarity. In this case, the top plate was simulated with 1 V and the bottom plate with  $-1$  V. The  $S$  factor in this case would be:

$$S = \sqrt{2} \sqrt{\frac{P}{2}} \cdot R \quad (5.2)$$

- For simplicity and less power loss through splitters, one plate can be put on voltage and the other plate remains grounded (the case in Fig. 4.15). This can be simulated by putting for example 1 V on the top plate and 0 V on the bottom. The  $S$  factor would then be:

$$S = \sqrt{2} \sqrt{P} \cdot R \quad (5.3)$$

In the scaling factor,  $P$  stands for the power inside the transmission line in watts.  $R$  is the resistance of the system, which is typically optimized to be  $50 \Omega$ . To get the peak value and not only the RMS, the scaling factor has to be multiplied with a  $\sqrt{2}$ .

The field  $E(y, z)_{\text{SIMION}}$  for the Scanner TL is shown in Fig. 5.1. When being on-axis ( $y=0$ ), the field component of  $E_z$  is approximately 0, which represents the virtual ground plane. Moving away from the center, e.g. at  $y=3\text{mm}$ , the  $E_z$  component becomes more influenced by fringe effects of the edges of the plates.

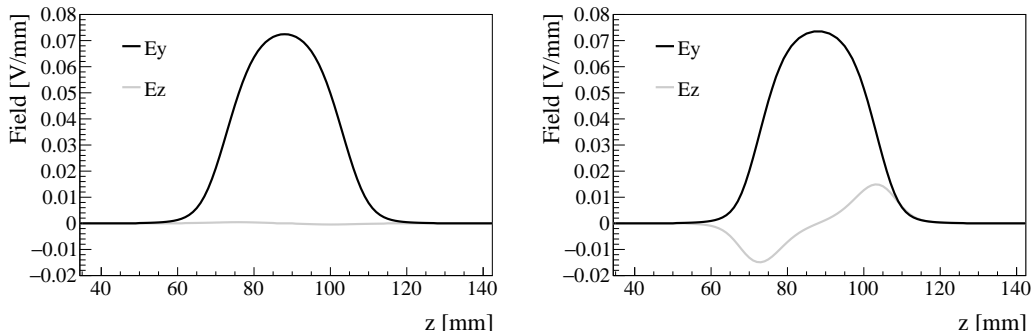


FIGURE 5.1: The SIMION simulation for the Scanner TL with  $\pm 1$  V applied on the plates is shown at the center ( $y=0$ , left) and off-center ( $y=3\text{mm}$ , right). The dark line shows the  $E_y$ -component, whereas the bright line the  $E_z$ -component.

### 5.1.2 Simulating Lamb Shift Transitions

In order to simulate the transition probabilities of the excited atom exposed to a specific frequency and power, the optical Bloch equations Eq. 3.53 to 3.55 were numerically solved via an adaptive stepsize RungeKutta integrator (205) while the atom was passing through the TL. To each atom, a specific initial hyperfine state population was assigned with corresponding resonance frequency (summarized in Tab. 5.1) and transition element (summarized in Tab. 3.2), which were used as an input to the optical Bloch equations. The power and scanning frequencies were set via macro file and were used to reproduce the microwave field expressed by Eq. 5.1, while the phase of the field was chosen for each atom randomly. Once leaving the TL, a random number in the range between 0 and 1 was generated. If the number was smaller than the transition probability calculated by the integrator, the M(2S) got excited to M(2P) and relaxed back to M(1S). This process was done for both the HFS TL and the Scanner TL. When the atom reached the Stop-MCP, the particle state and hit position was recorded.

By using the previously simulated dataset of possible atom trajectories, for each scanning frequency a large dataset was generated to average over different initial positions, momenta and phases. The ratio between the amount of M(1S) and the total amount of atoms reaching the Stop-MCP resulted in the average transition probability for the specific scanning frequency and initial hyperfine population. This procedure was used in the same way to simulate higher state transition probabilities such as 3S to 3P<sub>1/2</sub> or 4S to 4P<sub>3/2</sub>. Combining all hyperfine states of 2S, 3S and 4S contributions with their initial formation probabilities at the foil (see Sec. 3.2.2), a possible line-shape was simulated to be as in Fig. 3.7.

TABLE 5.1: Summary of transitions affecting the hydrogen and muonium Lamb shift.

Initial State		End State		Frequency (MHz)	
$n^2S_{1/2}$	$(F, m_F)$	$n^2S_{1/2}$	$(F, m_F)$	Hydrogen	Muonium
$2^2S_{1/2}$	(0,0)	$2^2P_{1/2}$	(1,0)	909.9	582.5
$2^2S_{1/2}$	(1,0)	$2^2P_{1/2}$	(0,0)	1146.6	1326.4
$2^2S_{1/2}$	(1,±1)	$2^2P_{1/2}$	(1,±1)	1087.4	1140.5
$3^2S_{1/2}$	(0,0)	$3^2P_{1/2}$	(1,0)	271.1	174.1
$3^2S_{1/2}$	(1,0)	$3^2P_{1/2}$	(0,0)	341.2	394.5
$3^2S_{1/2}$	(1,±1)	$3^2P_{1/2}$	(1,±1)	323.7	339.4
$4^2S_{1/2}$	(0,0)	$4^2P_{3/2}$	(1,0)	1252.9	1280.0
$4^2S_{1/2}$	(1,0)	$4^2P_{3/2}$	(2,0)	1233.6	1219.5
$4^2S_{1/2}$	(1,±1)	$4^2P_{3/2}$	(1,±1)	1230.7	1210.2



## 5.2 Experimental Setup

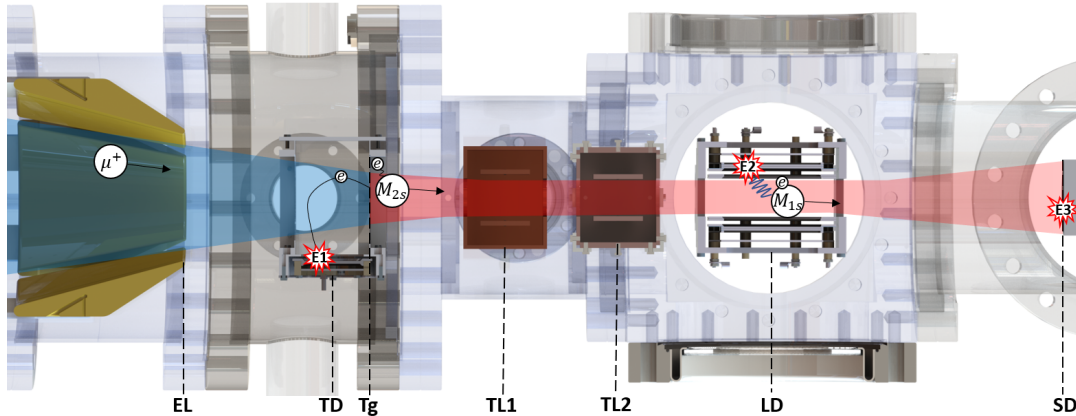


FIGURE 5.2: The experimental setup used with conical electrostatic lens (EL), tagging detector (TD), target (Tg), transmission lines (TL1, TL2), Lyman-alpha detectors (LD) and stop detector (SD). The signal signature explained in the text is marked with E1, E2 and E3. Figure from (204).

The experimental setup is shown in Fig. 5.2. It is similar to the setup used in Sec. 4.2, with a few differences. The former extension was replaced by the microwave setup, consisting of the two transmission lines (TL1 and TL2). The Ly- $\alpha$  detection setup only has two MCPs instead of four, at a closer distance to cover a similar solid angle. The MCP on the top is coated with CsI, whereas the MCP at the bottom with KBr. The quenching region is defined by grids in front of the MCPs instead of ring electrodes. Additionally, the rejection electrode was removed to keep the setup more compact. The signal signature stayed the same, though:

- **E1:** The  $\mu^+$  beam passes the carbon foil, where it releases secondary electrons. These are detected by the tagging detector (TD), giving the start signal. In another process, the muon can pick up an electron from the foil, forming muonium.
- **E2:** The muonium continues its path through the two transmission lines, where, depending on its state, a transition can be induced and its relaxation back to the ground state. It reaches afterwards the Ly- $\alpha$  detection region, where the electrical quenching field is applied. In case of the muonium still being in an excited state, it will relax to the ground state under the emission of a Ly- $\alpha$  photon. The photon will be detected by the Ly- $\alpha$  MCPs (LD) surrounding the region.
- **E3:** The now ground state muonium reaches the end of the beamline, where it leaves a signal in the stop MCP detector (SD).

### 5.3 DAQ and Trigger Logic

The signals from all detectors were guided with long BNC-cables from the experimental zone to the control room. In the control room, they were fed to a Constant Fraction Discriminator of type PSI CFD950, where the thresholds were set to the minimum ( $-5$  mV), just above noise level. The signals went afterwards from the CFD to a TDC unit (CAEN TDC 1190B). These parts were integrated in the LEM DAQ and slow control system based on MIDAS (206; 207), where the TDC values eventually were stored in ROOT files.

With the LEM slow-control system, most of the HV supplies could be controlled and the vacuum levels monitored. Additionally to the specific times of an event firing a specific detector, the specifications of the microwave setup such as frequency and power needed to be remotely controllable and logged. For this reason, a Raspberry Pi unit (RPI) was set up in the experimental zone, where all devices such as power meters and RF-generators were connected to. The RPI was accessible from the control room, so a specific measurement routine could be started. The power was logged every second to an external file, which MIDAS was reading from and integrated it in the slow control monitoring and saved in the ROOT file. Like this, for every event there was the information about which detector fired at which time, with what frequencies applied on the TLs and at what power. All the pathways for the DAQ are shown in Fig. 5.3.

The trigger logic for an event was set up as a coincidence signal between the TD and the SD. An event was allowed to last  $10\ \mu\text{s}$  and multiple hits on a single detector were accepted. As a live analysis, first histograms were created online; typically they consisted of a TOF between TD and SD as well as one of TD-LD and LD-SD.

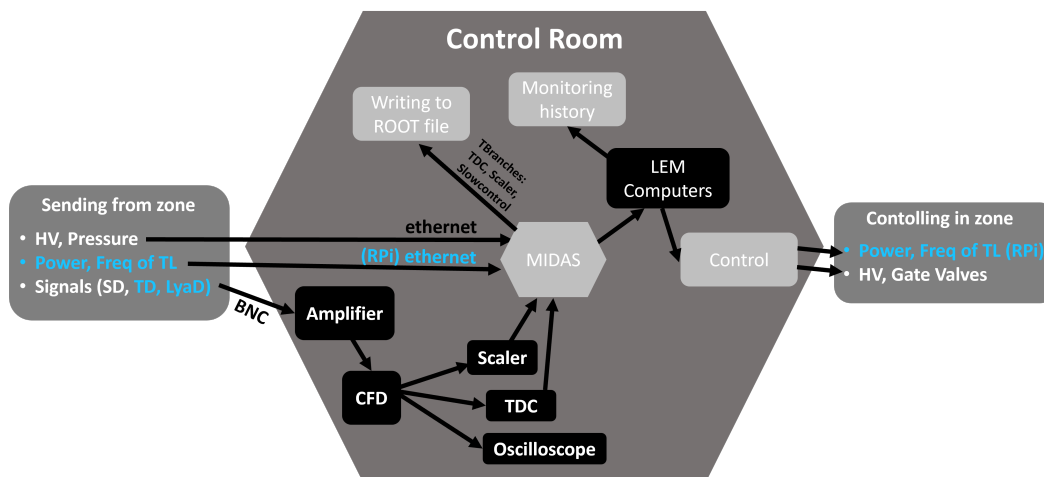


FIGURE 5.3: A sketch showing the pathways of the data acquisition and communication between control room and the zone.

## 5.4 Optimization and Data Taking

As soon as the setup was installed and reached vacuum levels at around  $10^{-7}$  mbar, the HV was turned on and the thresholds of the MCP signals set on the discriminator by looking at dark counts. As a first step, the rate of hydrogen and protons reaching the SD was optimized by scanning the lens voltages of the LEM beamline. Afterwards, the Ly- $\alpha$  rate on the LDs was studied. Both LDs were biased with 2.4 kV on the voltage divider, which means a grounded front plate and 2 kV across the plates. The quenching grids were set to the simulated optimum at 600 V on top and 100 V on the bottom. It showed that the LD signal needed amplifying, since the long cables from the zone to control room attenuated the signal significantly below the capability of the discriminators (around  $-5$  mV). By using amplifiers, independent if installed in the control room or in the zone, the rate was increased by a factor of 1.5.

With these settings, the TL1 was turned on to scan frequencies in the range between 840 and 1300 MHz with a power of around 10.6 W and one data point with no power applied. Before the measurement, the predefined frequencies were scanned with maximal input power to determine the maximal output power over all frequencies. All the other frequencies were then calibrated to this value by lowering their input power. The frequencies were scanned continuously in cycles, changing after every 30 min.

In a second step, we found that by biasing the LDs asymmetrically, for one of the LD the detection efficiency for Ly- $\alpha$  can be increased up to a factor of 4. The reason for that is that before, both LDs in combination with the quenching grids were biased to reject low energy electrons. By changing the HV divider for the bottom LD, the detector accepts electrons which are produced by Ly- $\alpha$  photons on the surface of the MCP. The bottom LD was biased afterwards with 2.8 kV on the divider box, keeping the voltage across the plates the same but increasing the voltage on the front plate, whereas the top LD and both quenching grids remained the same. With these settings, a second dataset was taken with protons with the same frequencies as before in cycles of 10 min, but lower power at 5.3 W. The optimized average Ly- $\alpha$  rate was measured to be 0.65 Hz.

When switching from protons to muons, the lenses needed first slight tweaking to optimize the transmission to the SD. Then, the frequencies in the range of 900 to 1400 MHz and a MW off point were chosen to be scanned with TL1. The TL2 was fixed on 580 MHz with an average power of 26.7 W to drive down the isolated  $F = 0$  resonance to reduce the background contribution. After half of the measuring time, the microwave field direction was swapped by exchanging the input with output in the attempt to average out the Doppler shift. The scanning frequency was changed every 20 min. A total of 60 000 Ly- $\alpha$  photons were detected in roughly 74 h.

As a last scan, the TL1 was set to constantly drive the frequency of 1140 MHz, where TL2 was set to scan the frequencies between 250 to 750 MHz and another data point with TL2 off. It would have been beneficial to measure at least another data point in the region between 275 and 350 MHz, but in this range the TL interfered with all the MCPs and created signal rates of  $>1$  MHz. Therefore, this frequency range had to be skipped. A total of 23 200 Ly- $\alpha$  photons were detected in 42.5 h. All the scans are summarized in Tab. 5.2.



TABLE 5.2: Statistics gathered during the beamtime June 2021

H, 10.6 W			H, 5.3 W			Mu, 1140 MHz			Mu, 583 MHz						
Freq (MHz)	Lya ( $10^3$ )	Norm ( $10^6$ )	time (h)	Freq (MHz)	Lya ( $10^3$ )	Norm ( $10^6$ )	time (h)	Freq (MHz)	Lya ( $10^3$ )	Norm ( $10^6$ )	time (h)	Freq (MHz)	Lya ( $10^3$ )	Norm ( $10^6$ )	time (h)
840	0.9	1.1	1.5	840	1.1	0.7	0.7	900	6.6	2.5	6.8	250	3.1	1.7	5.3
910	0.8	1.1	1.5	910	1.0	0.7	0.7	1030	6.3	2.6	7.1	400	2.8	1.6	5.2
1020	0.5	0.7	1.0	1020	0.7	0.5	0.5	1085	5.9	3.0	8.0	450	2.8	1.6	5.0
1050	0.5	1.1	1.5	1050	0.7	0.5	0.5	1150	3.9	2.5	6.7	535	2.7	1.8	5.7
1100	0.5	1.2	1.8	1100	0.5	0.5	0.5	1190	4.5	2.6	7.1	586	2.7	1.8	5.5
1160	0.5	1.1	1.5	1160	0.9	0.7	0.7	1235	4.9	2.5	6.7	660	2.8	1.7	5.3
1230	0.8	1.1	1.5	1230	0.8	0.5	0.5	1320	6.6	3.2	8.4	750	3.0	1.6	5.3
1300	0.6	0.7	1.0	1300	0.9	0.5	0.5	1360	6.1	2.7	7.3				
OFF	1.1	1.1	1.6	OFF	0.7	0.4	0.3	1400	7.0	2.8	7.4	OFF	3.3	1.6	5.2
Total	6.2	9.2	12.9		7.3	5.0	4.9		60.0	27.2	73.2		23.2	13.4	42.5
Rate (*)	0.19 Hz	200 Hz			0.65 Hz	280 Hz			0.37 Hz	100 Hz			0.33 Hz	88 Hz	

\* The rate mentioned in the table is the maximal rate, which is calculated by taking only the data with TL OFF and additionally corrected for a possible active HFS TL (M cases).

## 5.5 Data Analysis

This section explains the steps of how the raw data was processed to extract the Ly- $\alpha$  counts and normalization factors, and what corrections needed to be applied to eventually be able to plot a line-shape scan. In a further step, the fitting procedure is explained with which the parameters of interest such as resonance frequency or background levels were extracted.

### 5.5.1 Data Extraction

Following the clear signal signature described in Sec. 5.2, labeled with E1, E2 and E3, certain cuts on the data can be applied to reduce noise and background. The first step to clean the data was done by looking at the combined signature of E1 and E3, the start and stop signal of the  $\mu^+$  and M. The time difference between these two events can be estimated by knowing the most-probable energy of the beam, as well as the total path length. Signals outside of this time window will not be considered and cut from the data. This cut is shown in Fig. 5.4, for both the hydrogen and muonium case, both with incident energy before the foil of 7.5 keV. The colored area represents the amount of tagged muons and muonium which managed to reach the stop detector. This value  $S_{\text{norm}}$  will be used as normalization for the signal. The time in the TOF spectra is shown in units of TDC bins, which corresponds to around 0.195 ns per bin.

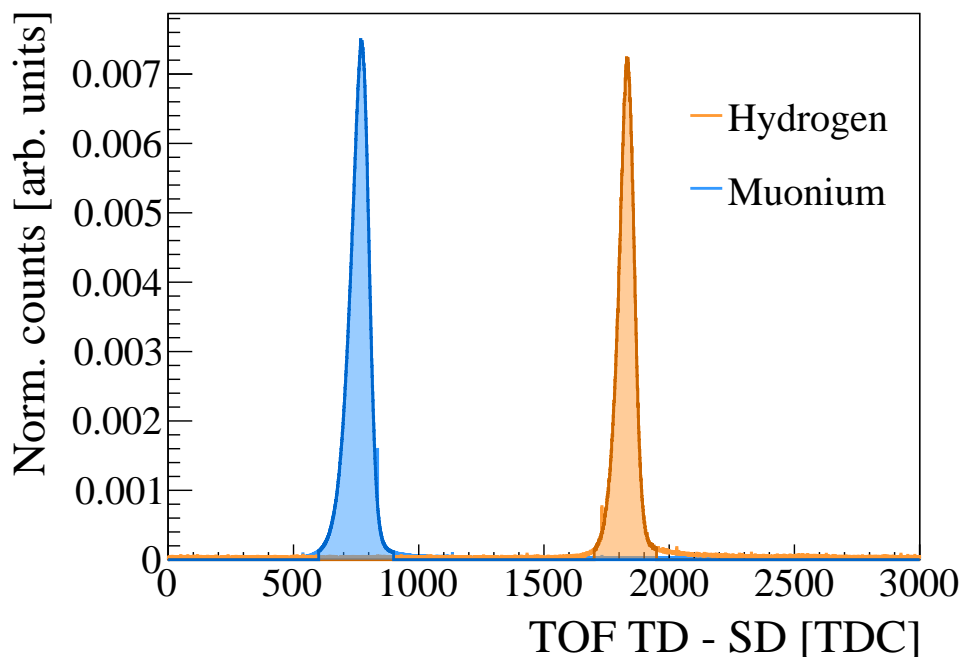


FIGURE 5.4: First cut applied on the datasets. The peaks in the TOF TD-SD of muonium (blue) or hydrogen (orange) were selected, and the other events lying outside discarded.

In a second step, the time difference between E1 and E2, namely the tagging detector and the Ly- $\alpha$  detection region, is constrained. With the same reasoning as in the cut above, only a certain time-of-flight would be allowed. This case is shown in Fig. 5.5 on the left side. In both the hydrogen and muonium case, only a small

fraction of the signal is accepted. The largest uncolored contribution is stemming from cross-talk between the LD and SD. The wiggles after the peaks are coming from ringing of the MCP, the amplitudes of which were large enough to pass the discriminator thresholds.

Due to hydrogen being much slower than muonium, the true signal for hydrogen and cross-talk peaks are well separated. Therefore, a third cut using the the time difference between E2 and E3 of the remaining signal (shown in Fig. 5.5 on the right side) is not necessary anymore. For the muonium case, the third cut rejects the remaining noise and background. The colored areas after the final cut represent the amount of Ly- $\alpha$  photons detected ( $S_{\text{Ly}\alpha}$ ).

Since for all datasets the frequency applied in the TL is known, both the normalization  $S_{\text{norm}}$  and the Ly- $\alpha$  signal  $S_{\text{Ly}\alpha}$  can be extracted frequency-dependent. Eventually, the normalized signal  $S_c = \frac{S_{\text{Ly}\alpha}}{S_{\text{norm}}}$  is calculated for each measured frequency point.

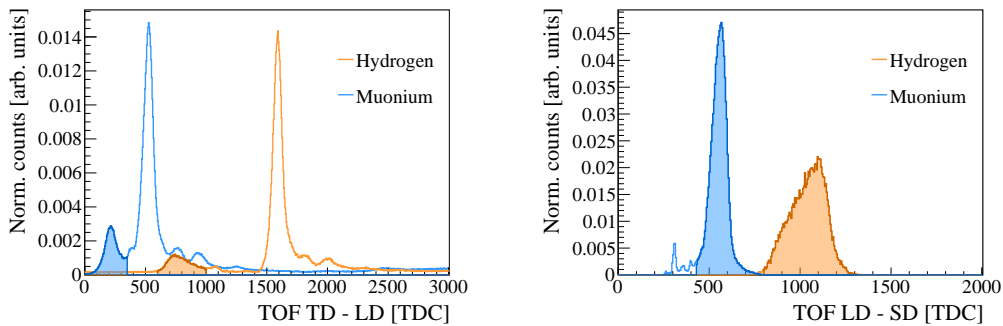


FIGURE 5.5: The second (left) and third cut (right) applied to the datasets. The second cut selects the correct timing for Ly- $\alpha$  to be detected, whereas the third cut chooses the TOF window from LD to SD for hydrogen (orange) and muonium (blue).

### 5.5.2 Power Corrections

As seen from the characterization measurements described in Sec. 4.3.4, calculating the power inside the TLs during the measurement is non-trivial and therefore also having the same power at all measured frequencies not viable. The goal of the analysis would be to be able to fit a line-shape through the extracted signals, which comes with the condition that all measured frequencies do have the same power applied. During the measurement, it was attempted to keep the output power constant, independent from the frequency. Therefore, the corrections that needed to be applied to the calculated powers inside the TL are smaller, with less uncertainty. For that, before the measurement started, the predefined frequencies were scanned with maximally allowed input power for the amplifiers to determine the frequency with the biggest losses. All other frequencies were tuned down to the same output power by adjusting the input power on the RF-generator.

The extracted signals are corrected by using the simulation. Knowing at what average power the data on a specific frequency was taken, one can define a global power where all the frequency points will be corrected to. The survival probability of the atoms in the TL at the average power measured and at the goal power is simulated and a frequency-dependent correction factor extracted. Since the power

can vary also within a single frequency due to drifts, the standard deviation needs to be taken along to estimate an uncertainty for the correction.

### 5.5.3 Fitting Procedure

From simulation, high-statistics survival probabilities  $P_i^n$  in a range of 200 MHz to 2000 MHz in steps of 1 MHz are generated, for each principal quantum state  $n$  and hyperfine state  $i$  the simulated particle can be in. For this, the theoretical resonance value of the specific transition as well as the average power in the TLs was given to the simulation as input parameter. A large dataset of possible paths the particle could take through the system starting from the carbon foil was simulated beforehand and eventually fed to the survival probability simulation, where for each event a random draw was taken from. Like this was ensured that the complete line-shape was simulated with a realistic position and momentum distribution. The final fitting function was constructed from the simulated survival probabilities:

$$S_c = S_{\text{BKG}} + \sum_n \left[ B_n \cdot \sum_i C_i^n \cdot P_i^n (f - f_{\text{offset}}) \right] \quad (5.4)$$

In this fitting equation,  $S_c$  represents our signal to be fitted.  $S_{\text{BKG}}$  is a fit parameter that describes the frequency-independent level of the background in the data.  $B_n$  is a general parameter to scale the line-shapes to the experimental dataset. This parameter contains detection efficiencies for the Ly- $\alpha$  photon, e.g. solid angle covered, quenching probability and wavelength dependent quantum efficiency of the coatings, and is therefore different for each principal quantum state  $n$ . The ratio between two  $B$  parameters of different  $n$  is giving the relative amount of this specific state in the beam when corrected for efficiency differences. The parameters  $C_i^n$  are the weights of the survival probabilities of a specific hyperfine state and are described by the relative population. As an example, the three  $2S-2P_{1/2}$  transitions possible for muonium would be at 583, 1140 and 1326 MHz, their relative populations are (0.25, 0.5, 0.25) due to the states statistics explained in Sec. 3.1.1. These weights are well-known and are fixed in the fit. The last parameter is  $f_{\text{offset}}$ , which describes the offset from the theoretical central value.

## 5.6 Results

In this section, the results of the beamtime in June 2021 are presented. First, the results of the first tests with the proton beam at two different powers are shown. Afterwards, the muonium data are presented, which comprises a dataset scanned in the region between 900 and 1400 MHz to be able to determine the resonance frequency of the  $2S_{1/2,F=1} \rightarrow 2P_{1/2,F=1}$  transition and from there extract the  $n=2$  Lamb shift of muonium. The second dataset was scanned in the range of 200 to 800 MHz to extract the  $2S_{1/2,F=0} \rightarrow 2P_{1/2,F=1}$  resonance frequency. With both results, the hyperfine splitting  $2S_{F=0} \rightarrow 2S_{F=1}$  was determined. A discussion of the major systematic effects is included and simulation studies of the Doppler and Stark shift shown. At the end, all results are summarized and their impact on constraining New Physics discussed.

### 5.6.1 Fitting Results for Hydrogen

The results for hydrogen are shown in Fig. 5.6, with all the fitting parameters summarized in a table on the top.

As an initial attempt, a fitting function was constructed with no H(4S) contribution. Especially in the case of higher power, the goodness of the fit was not convincing anymore towards higher frequencies, with the TL OFF point disagreeing with the fit the most. Additionally, the  $f_{\text{offset}}$  was in both cases larger than its uncertainty, in the high power case almost  $2\sigma$ , which means that the resonance frequency determined here is also by this amount off from the theoretical value.

Allowing for a H(4S) contribution, the goodness of the fit improved for the high power case, and also the resonance frequency lies well within  $1\sigma$  reach of the theoretical value. This result confirms the expectation that the beam contains higher n-state contamination, which needs to be taken into account as well for the muonium analysis. With hydrogen, we found a ratio between H(4S) and H(2S) of roughly 9(6)%, which agrees with the estimations done in Sec. 3.2.2, where we expected to have around 9% produced at the foil and half of it relaxed back to ground state until the Ly- $\alpha$  detection due to its lifetime. No precise prediction motivated by the experiment can be done for the muonium case though due to its large measurement uncertainty.

Power (W)	4S	$S_{\text{BKG}}$ ( $\times 10^{-4}$ )	$B_{2S}$ ( $\times 10^{-4}$ )	$B_{4S}$ ( $\times 10^{-4}$ )	$f_{\text{offset}}$ (MHz)	$\chi^2_{\nu}$
5.3	x	$1.0 \pm 1.1$	$15.8 \pm 1.3$	-	$5.4 \pm 4.9$	0.8
5.3	✓	$0.7 \pm 1.3$	$15.8 \pm 1.3$	$0.5 \pm 1.2$	$3.9 \pm 6.8$	0.9
10.6	x	$0.3 \pm 0.3$	$9.1 \pm 0.4$	-	$6.0 \pm 3.3$	1.6
10.6	✓	$0.0 \pm 0.2$	$8.6 \pm 0.4$	$1.2 \pm 0.5$	$-0.4 \pm 4.8$	0.9

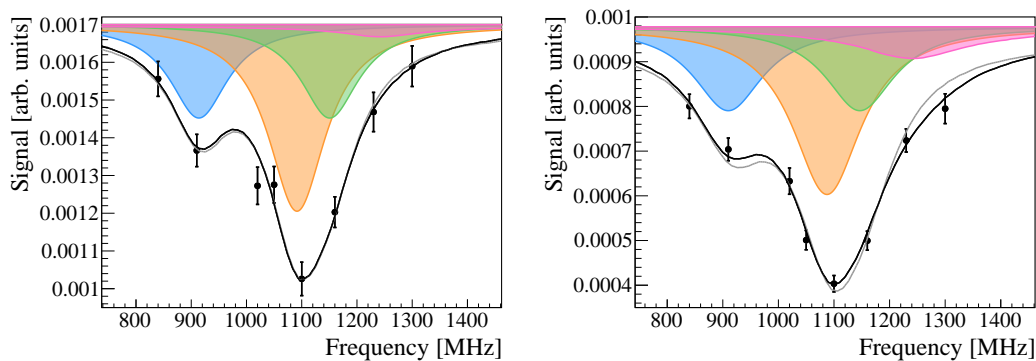


FIGURE 5.6: Hydrogen scan at 5.3 W (left) and 10.6 W (right). The fitted black line is with, the gray line without the 4S contribution. The colored areas represent the underlying contributions from  $2S - 2P_{1/2}$  transitions, namely 909 MHz (blue), 1087 MHz (orange), 1147 MHz (green), and the combined  $4S - 4P_{3/2}$  (pink). The data points with TL OFF are not displayed in the figures, but are included in the fits; they would lie at  $(17.3 \pm 0.6) \times 10^{-4}$  (left) and  $(9.7 \pm 0.3) \times 10^{-4}$  (right).

### 5.6.2 Fitting Results for Muonium

As mentioned in Sec. 5.4, the idea was to average out the Doppler shift by changing the Scanner TL field direction after half of the measuring time. During the analysis of both separate datasets, it was seen that a mistake had happened while switching direction and the combiner degraded for certain frequencies, giving a large uncertainty of the calculated power inside the TL. Fitting the first dataset lead to a  $\chi^2$  of 1.2, while the second dataset had a  $\chi^2$  of 4.5. Unfortunately, this was realized too late and no measurements had been done during beamtime to be able to compensate for such a change in power. This forced us to reject around 36 h of statistics and only accept the first dataset. The results for muonium are shown in Fig. 5.7, with the fitting parameters listed above.

In the analysis with muonium, the first attempt was as well to not include any beam contamination of higher n-states and only allow for M(2S). In the case of the 1140 MHz dataset, the fit goodness with a  $\chi^2$  of 1.2 was sound. Adding a M(4S) contribution, the fit tried to keep the  $B_{4S}$  parameter at 0 nonetheless and the goodness of the fit slightly worsened to a  $\chi^2$  of 1.4. This might not come as a surprise, since with the fitting procedure used, the hyperfine splitting between the resonances of 1140 and 1326 MHz is fixed. The main contribution of the M(4S) would lie just in between those two frequencies (see Fig. 3.4 or Tab. 5.1). By fixing the hyperfine splitting, this effect might have been absorbed and seemingly reduced to a level below our precision. In contrast for hydrogen, the H(4S) contribution is more isolated towards higher frequencies and would distort the shape of the fitting function. Nonetheless, the beam contamination needs to be included as a systematic uncertainty.

Dataset (MHz)	3S	4S	$S_{\text{BKG}}$ ( $\times 10^{-4}$ )	$B_{2S}$ ( $\times 10^{-4}$ )	$B_{3S}$ ( $\times 10^{-4}$ )	$B_{4S}$ ( $\times 10^{-4}$ )	$f_{\text{offset}}$ (MHz)	$\chi^2_{\nu}$
1140	x	x	$5.9 \pm 0.5$	$31.5 \pm 1.0$	-	-	$-0.6 \pm 2.3$	1.2
1140	x	✓	$5.9 \pm 0.6$	$31.5 \pm 1.9$	-	$0.0 \pm 1.8$	$-0.7 \pm 2.9$	1.4
583	x	x	$7.8 \pm 0.8$	$22.0 \pm 1.8$	-	-	$-24.8 \pm 7.4$	6.7
583	✓	x	$3.4 \pm 1.1$	$25.0 \pm 1.9$	$5.0 \pm 0.9$	-	$2.3 \pm 6.8$	2.0

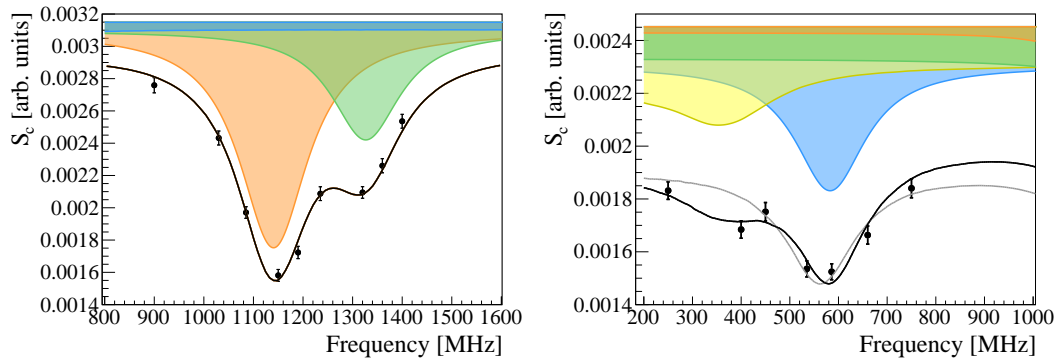


FIGURE 5.7: Muonium scan at 29 W in the range of 800 to 1600 MHz (left) and 22.5 W in the range of 200 to 800 MHz (right). The fitted black line is with, the gray line without the 3S contribution. The colored areas represent the underlying contributions from  $2S - 2P_{1/2}$  transitions, namely 583 MHz (blue), 1140 MHz (orange), 1326 MHz (green), and the combined  $3S - 3P_{1/2}$  (yellow). The data points with TL OFF are not displayed in the figures, but are included in the fits; they would lie at  $(29.6 \pm 0.5) \times 10^{-4}$  (left) and  $(20.4 \pm 0.4) \times 10^{-4}$  (right).

In the case of the 583 MHz dataset, when neglecting the M(3S) contribution the goodness of the fit is unacceptable with a reduced  $\chi^2$  of 6.7. By allowing for a M(3S) contribution, the fit improves significantly to a reduced  $\chi^2$  of 2.0. The ratio between M(3S) and M(2S) was determined to be 20(4) %. In the 68 ns from the foil to the Ly- $\alpha$  detection setup, 35 % of the M(3S) already relaxed to the 1S state. Taking this into account, the M(3S) contamination would be 31(6) % at the foil level. This result is slightly smaller than what we estimated in Sec. 3.2.2, where we expected to have around 44(4) % produced at the foil. Nonetheless, these results confirm the first detection of M(3S).

### 5.6.3 Systematics

Even though the results are statistically limited, we are close to the region where systematic effects might take the upper hand. Therefore, an analysis of the systematics is essential, especially in regards of planning future muonium Lamb shift experiments. In this section, several systematic effects will be presented and their impact on the result discussed.

#### Doppler Shift

A misalignment between the TL and the mean M(2S) beam direction, making it not perpendicular anymore, would lead to a significant frequency shift. To account for this effect, the misalignment angle  $\alpha$  was scanned with the simulation in the range between  $-100$  mrad to  $100$  mrad. The M(2S) was virtually rotated by calculating the rotated velocity  $v_{\text{rot}}$ :

$$v_{\text{rot}} = (\hat{p}_x \cos(\alpha) + \hat{p}_z \sin(\alpha)) v \quad (5.5)$$

where  $\hat{p}_x$  and  $\hat{p}_z$  describe the normalized momentum  $\hat{p}$  in a specific direction and  $v$  the original velocity. With the rotated velocity, the Doppler-shifted  $f_{\text{Doppler}}$  was calculated via:

$$f_{\text{Doppler}} = f \left( 1 + \frac{v_{\text{rot}}}{c} \right) \quad (5.6)$$

where  $f$  is the original frequency and  $c$  the speed of light. The Doppler-shifted frequency was then passed on as parameter for the optical Bloch equations to be solved and an entire line-shape was simulated. The resonance frequency was extracted by fitting a Lorentzian model. The results of the scan are summarized in Fig. 5.8, left side.

The Doppler shift is in the small-angle approximation proportional to the misalignment angle. Therefore, a linear fit was chosen. From mechanical tolerances in the TL construction, we estimate an upper limit for the misalignment to be 30 mrad. For the 1140 MHz scan this would lead to a systematic shift of around 320 kHz. For the 583 MHz scan, the Doppler shift would be expected to be roughly half as strong and was confirmed by simulation to be around 160 kHz.

#### Stark Shift

The M(2S) experience in the TL a time-varying electrical field and therefore another systematic frequency shift called Stark shift. By simulating the line-shape at different power and fitting it with a Lorentzian model, the shifted resonance frequency can be extracted. Since in simulation the rotating-wave approximation is not applied, also the Bloch-Siegert shift is automatically included. The Stark shift is proportional to the power in the regime where the resonance is not saturated yet. The powers

were therefore scanned in the range from 5 to 35 W and linearly fitted. The results are summarized in Fig. 5.8, right side.

In the case of the 1140 MHz scan at 29 W, a Stark shift of around 740 kHz was found. The 583 MHz scan was measured at a power of 22.5 W, which leads to a Stark shift of 1080 kHz.

With the fitting method chosen to extract the central values (see Eq. 5.4), these shifts are automatically included in the line-shapes  $P_i^n$ . By using only the equations of a two-level system, we neglected the contribution of the  $2P_{3/2}$  states, which will lead to overestimating the Stark shift by a factor of 0.34, as calculated and confirmed with a measurement by Andrews et al. (208; 209). Therefore, the 1140 MHz central value is corrected back by 0.26(2) MHz and the one of 583 MHz by 0.39(2) MHz.

Dataset (MHz)	Shift	Offset (MHz)	Slope ( $\times 10^{-3}$ )	$\chi^2_\nu$
1140	Doppler	0	$-10.6(3) \text{ MHz mrad}^{-1}$	1.1
583	Doppler	0	$-5.3(3) \text{ MHz mrad}^{-1}$	0.9
1140	Stark	0	$25.5(5) \text{ MHz W}^{-1}$	0.7
583	Stark	0	$48.1(8) \text{ MHz W}^{-1}$	0.8

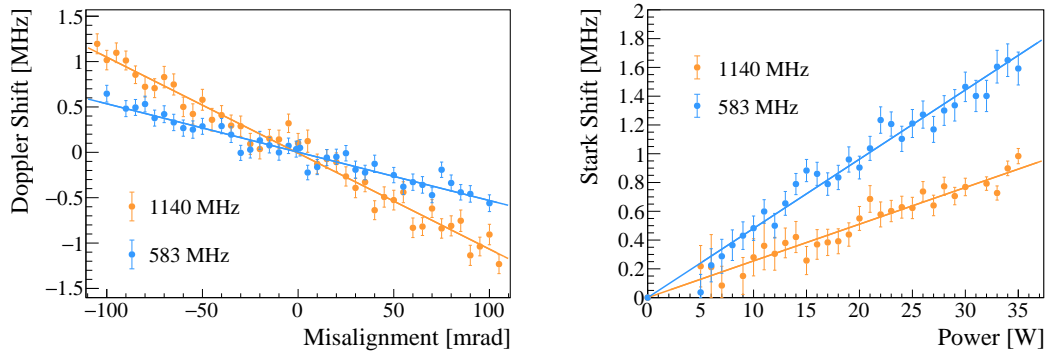


FIGURE 5.8: The scans for determining the Doppler shift (left) and the Stark shift contribution (right). The orange data points were simulated with the resonance frequency at 1140 MHz, whereas the blue ones at 583 MHz. The data was fitted in all cases with a linear model.

### Higher States Contamination

As seen from the hydrogen measurements in Fig. 5.6 and the 583 MHz scan in Fig. 5.7, higher  $n$ -states are present in the beam and reach the Ly- $\alpha$  detection region. In the case of the 583 MHz scan, the 3S contribution is modelled in the line-shape fit and the error is automatically absorbed in the fitting. This was also applied to the 1140 MHz dataset, but the fit preferred to have a zero  $B_{4S}$ . From the detected  $M(3S)/M(2S)$  population of 20(4) % and estimating in Sec. 3.2.2 a ratio between 4S and 3S of 0.2, a  $M(4S)/M(2S)$  population of 4 % would be expected. Therefore, a 5 %  $M(4S)$  population was fixed in the fit and the systematic uncertainty extracted to be smaller than 1 MHz.

### MW Field Intensity

From characterization measurements of the power meter and mechanical tolerances of the TL construction, we estimated to have a MW field intensity uncertainty of around 6 %. This would lead to a power uncertainty of  $\pm 1.8 \text{ W}$  in the 1140 MHz and



$\pm 1.4$  W in the 583 MHz scan, respectively. The line-shapes at these powers were simulated and taken to fit the experimental data. The systematic uncertainty was determined to be of less than 0.04 MHz in the 1140 MHz and less than 0.07 MHz in the 583 MHz case, mainly stemming from the uncertainty of the AC Stark shift.

### Velocity Distribution

With previous measurements at the LEM beamline, the `muSrSIM` simulation was benchmarked to reproduce the energy loss as well as angular scattering due to the carbon foil accurately with an uncertainty of only a few percent (153). This leads to a most-probable M energy after the foil of 5.7(2) keV. The energy uncertainty was simulated and the line-shapes fitted to the experimental data. For both datasets, no significant difference was visible and therefore the systematic uncertainty set to be  $<0.01$  MHz.

### Earth's Magnetic Field

The magnetic field measured around the setup was around 50  $\mu$ T, which corresponds to the Earth's magnetic field in that region. According to C. Fry (161), M(2S) travelling through a field of 100  $\mu$ T would experience a shift of less than 0.1 MHz. Since our field is only half the strength, we estimate a conservative 0.05 MHz systematic uncertainty.

### Quantum Interference

The resonance can be distorted by quantum-mechanical interference with another resonance when fulfilling a special condition. Let us assume the resonance of interest is described by the state transition from  $|a\rangle$  to  $|b\rangle$ , and the potentially interfering resonance from  $|c\rangle$  to  $|d\rangle$ . If  $|c\rangle$  has an allowed decay transition to  $|a\rangle$  and  $|d\rangle$  to  $|b\rangle$ , this condition is met.

A. Marsman et al. (210) studied the quantum interference in case of the  $n=2$  Lamb shift and the transition from  $3S$  to  $3P_{3/2}$ . They found an approximated formula to estimate the effect. In our simulation, this effect was not taken into account and therefore has to be added as a systematic uncertainty. From the 583 MHz scan, the effective  $3S/2S$  ratio found to be present in the beam is around 30%. With this population, a systematic uncertainty coming from quantum interference is estimated for both datasets to be smaller than 0.04 MHz.

## 5.6.4 Summary & Constraints on New Physics

The results found in the previous section are summarized in Tab. 5.3. By measuring the resonance frequency of the transition  $2S_{1/2,F=1} \rightarrow 2P_{1/2,F=1}$  in muonium to a value of 1140.2(25) MHz, the muonium  $n=2$  Lamb shift is calculated to be 1047.2(25) MHz. The result is well within one standard deviation from our calculated theoretical value of 1047.498(1) MHz and constitutes an improvement of an order of magnitude upon the last best measurements. The  $2S_{1/2,F=0} \rightarrow 2P_{1/2,F=1}$  transition in muonium was observed for the first time and the resonance frequency found to be at 580.6(68) MHz. From this transition, the M LS was determined to be at 1045.5(68) MHz. All the Lamb shift measurements for muonium are summarized in Fig. 5.9. Having measured both transitions, the 2S hyperfine splitting can be determined to a value of 559.6(72) MHz, which agrees well with the theoretical value

of 557.9(1) MHz. All the results are limited by statistics; systematic effects only play a secondary role.

	$2S_{1/2,F=1} \rightarrow 2P_{1/2,F=1}$		$2S_{1/2,F=0} \rightarrow 2P_{1/2,F=1}$	
	Value (MHz)	Uncertainty (MHz)	Value (MHz)	Uncertainty (MHz)
Fitting	1139.9	2.3	580.2	6.8
Beam contamination		< 1.0		-
MW-Beam alignment		< 0.32		< 0.16
MW field intensity		< 0.04		< 0.07
M velocity		< 0.01		< 0.01
AC Stark $2P_{3/2}$	+0.26	< 0.02	+0.39	< 0.02
2 <sup>nd</sup> -order Doppler	+0.06	< 0.01	+0.03	< 0.01
Earth's magnetic field		< 0.05		< 0.05
Quantum interference		< 0.04		< 0.04
Total	1140.2	2.5	580.6	6.8
Lamb Shift	1047.2	2.5	1045.5	6.8
HFS $2S_{F=0} \rightarrow 2S_{F=1}$			559.6	7.2
Theoretical value	1047.498	0.002	557.9(*)	< 0.1

\* The value was calculated by taking the most precise 1S HFS measurement in muonium (65) and dividing it by a factor of  $2^3$ . The uncertainty was estimated by calculating the QED  $D_{21}$  difference (211).

TABLE 5.3: The results of the measurements with muonium summarized.

Since our result for the muonium Lamb shift is agreeing well with the theoretical value, the constraints on the Lorentz- & CPT-violating coefficients explored in the context of the SME framework described in Sec. 3.4.1 can be updated with a 95% level of confidence to:

$$\left| \overset{\circ}{a}_4^{\text{NR}} + c_4^{\text{NR}} \right| < 1.7 \times 10^5 \text{ GeV}^{-3} \quad (5.7)$$

which corresponds to an improvement of roughly a factor of six.

Additionally, as prepared in Sec. 3.4.2, we can constrain the coupling strengths  $g_e g_\mu$  as a function of the mass of a new scalar or vector boson and compare it to the favoured region for the g-2 muon anomaly. The comparison is shown in Fig. 5.10. The overlap between the constraints coming from the M LS and the favoured region for the g-2 muon anomaly can be excluded for a new particle with indicated mass and coupling constants. However, this region could already be excluded from the constraints coming from the most precise muonium 1S – 2S measurement.

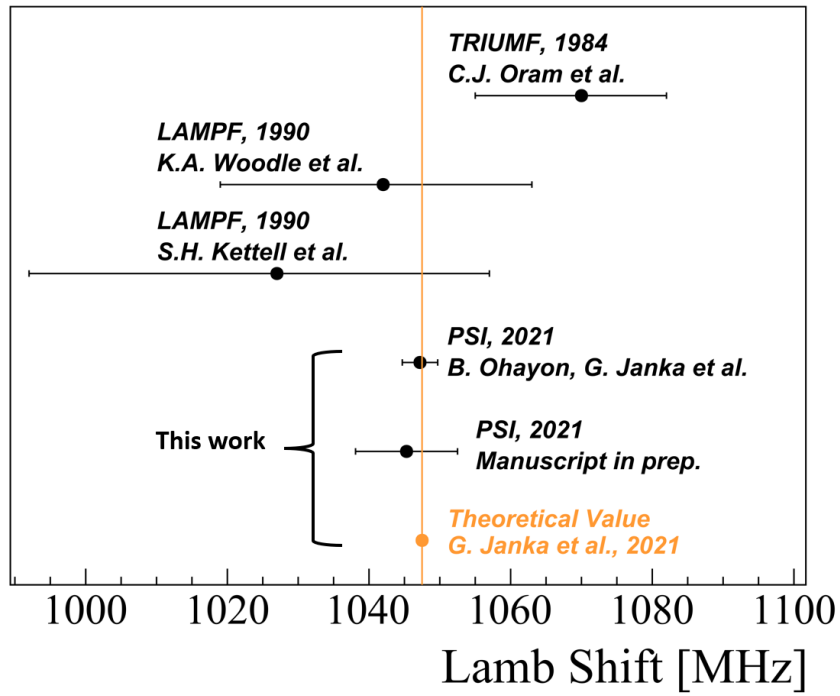


FIGURE 5.9: A summary of all measurements of the  $n=2$  muonium Lamb shift (black). The orange data point and band indicates the theoretical value including  $1\sigma$  uncertainty. The references are (69; 70; 71; 204) for the experimental and (170) for the theoretical value.

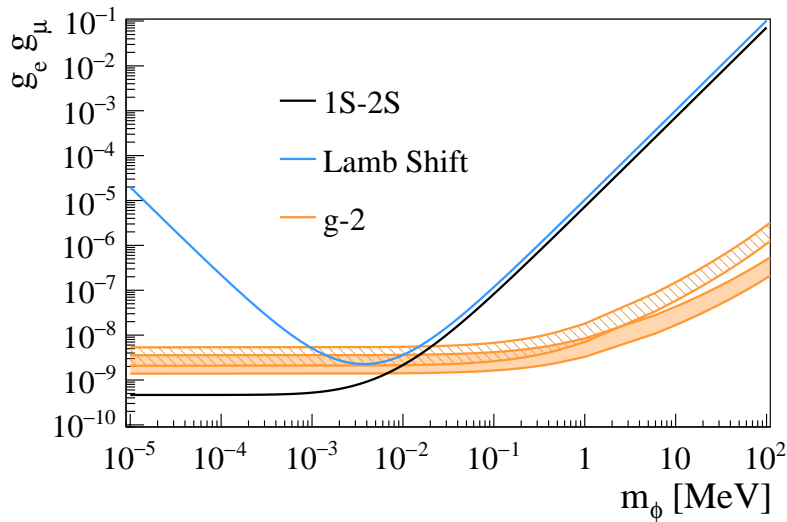


FIGURE 5.10: Constraints from  $M$  spectroscopy on  $g_e^s, g_\mu^s$  as a function of the scalar/vector mass. The blue line is the constraints set by the Lamb shift measurement presented here, while the solid black line is from the  $M$  1S–2S measurement (74). The orange band represents the region suggested by the  $g - 2$  muon anomaly considering the lower bound from the measurement of the electron gyromagnetic factor for the scalar and the hatched region for the vector case. Figure from (204).



## Chapter 6

# Conclusions and Future Prospects

In this final chapter we will review the obtained results and discuss the future prospects of GBAR (Sec. 6.1) and of Mu-MASS (Sec. 6.2).

## 6.1 GBAR

In Chap. 2, we presented the work on the GBAR Micromegas trackers, which will be used to reconstruct the annihilation vertex of the antihydrogen after the free fall. Additionally, we developed a novel approach to efficiently reconstruct multiple hits in the same Micromegas detector. We will summarize in Sec. 6.1.1 the status of the GBAR MMD detectors and in Sec. 6.1.2 the performance of the unfolding algorithm together with their future prospects.

In Chap. 4, we further explored the design of the GBAR Lamb shift setup and saw its commissioning with a M(2S) beam at PSI. Furthermore, the design of the microwave setup was shown, including all characterization measurements. In Sec. 6.1.3, we will summarize the results and give an outlook for the future of the antihydrogen Lamb shift.

### 6.1.1 Micromegas Detectors

In Chap. 2, the studies for optimizing the GBAR MMDs were presented. These studies motivated the reduction of the multiplexing factor from 17 to 12, which allowed us to decrease the ambiguities introduced by the multiplexing and increase the signal-to-noise ratio, while keeping a high detection efficiency and sufficient spatial resolution. The GBAR MMDs were given into production and were recently delivered to GBAR. They are in the final phase of being commissioned and characterized. The goal is to first determine the efficiency and resolution of each detector with cosmic radiation, and in a second step detect the first antiproton annihilations. The tracker support structure around the free fall chamber will be designed and the background in the GBAR zone studied. This measurement will be the experimental proof-of-principle of the trackers' ability to reject background stemming from cosmic rays. The trackers will then be used to optimize the two charge-exchange reaction to form as well as afterwards trap  $\bar{\text{H}}^+$ .

### 6.1.2 Multiple Hit Reconstruction

Additionally, we developed a novel unfolding algorithm that allows us to reconstruct events with multiple hits in the same Micromegas detector. This was required because a detailed simulation of the free fall showed that in more than 40% of the cases, multiple pions from a single  $\bar{\text{H}}$  annihilation would trigger the same MMD. By validating the algorithm with experimental data with detectors similar to the GBAR

MMD, we showed that the double hit reconstruction efficiency is around 87 % within an accuracy of 1 mm. The single hit reconstruction efficiency was shown to be competitive to the one obtained with conventional methods.

The algorithm has though the downside of residual oscillations, potentially being identified as a cluster and therefore making the tracking more difficult. Furthermore, since every plane needs to be minimized separately, and a minimization takes in average 20 s, it would take a lot of computing power to analyse one full annihilation event for GBAR with 36 planes involved. A simple estimation can be done by assuming a time window of 200 ms where one  $\bar{H}$  annihilation takes place. Due to the cosmic background ( $\sim 1 \text{ cm}^{-2} \text{ min}^{-1}$ ), we have to assume that all MMD will be triggered at least once in that time window and therefore all 36 planes need to be analyzed with the algorithm. Conservatively, we assume the MMD will only be triggered once in this time window. This would lead to a total computation time of 720 s with a single core. Since such an annihilation could take place every 110 s due to the AD cycle, the event reconstruction would have to be done with parallelising the algorithm, fully occupying a computer with a 8 core CPU.

A solution to that could be to move to an approach involving Neural Networks (NN). Since the unfolding algorithm is only needed when multiple hits are to be expected in the same plane, as a first step a NN could decide if in one of the MMD triplets multiple hits can be found. Only if the NN suggests that multiple hits are present, the unfolding algorithm will be used; in case of a single hit, the regular approach by looking for the largest cluster is more efficient. Another attempt would be to let a NN handle the entire hit reconstruction, learning from the results of the unfolding algorithm. For both approaches, some preliminary tests were done and explained in the following sections.

### Data Preparation

For simplicity, as input to the NN we feed simulated data for a MMD with multiplexing factor 5 and a total of 305 strips. The cluster width and total charge was taken from experimental data to make the toy data as realistic as possible. Only the weaker Y-coordinate was simulated, since this would be the most challenging one to reconstruct. Events were generated with the number of hits ranging from 1 to 4, and as solution all hit positions saved. For the tests, 500 000 events were simulated, from which half was thought for training and the other half for validating.

### Setting up the NN

A very simple, one-dimensional network was chosen to test such an approach. The design of the NN is shown in Tab. 6.1. Such a NN can be easily set up with the help of TensorFlow (212) and Keras (213) in Python. It consists of an input layer, which contains the information about the event in strip space, i.e. an array with 305 entries, one entry per strip. The value of the entry corresponds to the strip amplitude. These values are then passing through dense layers of different dimensions, connected in series. The dense layer operation is defined in Keras as:

$$\text{output} = \text{activation}(\text{input} \cdot \text{kernel}) \quad (6.1)$$

which is a matrix multiplication between the input array and the kernel matrix. The kernel contains the trained weights of the neural network. Activation is a function that shapes the result of the matrix multiplication into the correct form for the output

(214). Typically, the Rectified Linear Unit (ReLU) function is used in between layers:

$$\text{ReLU}(x) = \max(0, x) \quad (6.2)$$

For the eventual output, different functions can be used depending on the purpose. A typical choice for a categorizing problem is the softmax function returning a probability, whereas for a regression the linear function is more suitable:

$$\begin{aligned} \text{Linear}(x) &= x \\ \text{SoftMax}(x, i) &= \frac{e^{x_i}}{\sum_{j=1}^J e^{x_j}} \end{aligned} \quad (6.3)$$

where the index  $i$  describes the specific category label and  $J$  is the total amount of categories.

A NN starts its training by taking the training data and initializing random weights in the kernel. With comparing the predicted result on an event-by-event basis to the actual solution, or more accurately evaluating its loss function, the NN learns and adjusts the weights continuously. At the end of a training cycle (epoch), the validation data is evaluated with the current training. A goodness of the training, e.g. an accuracy or a residual is given. Based on that, the next epoch starts, trying to improve upon the last result, minimizing the loss function while keeping the validation accuracy high. The end of the training is defined before the start by setting the maximum amount of epochs.

TABLE 6.1: The design of a simple, one-dimensional Neural Network for testing multiple-hits identification and reconstruction in multiplexed Micromegas.

Layer Type	Output Dimensions	# Parameter	Activation
Input	305	0	-
Dense 1	605	185130	ReLU
Dense 2	500	303000	ReLU
Dense 3	400	200400	ReLU
Dense 4	300	120300	ReLU
Dense 5	200	60200	ReLU
Dense 6	100	20100	ReLU
Dense 7	50	5050	ReLU
Dense 8	20	1020	ReLU
Dense 9	4	105	linear \ softmax
Output	4	0	-

### Multiple Hits Identification

The multiplexed data in strip-space, for example shown in Fig. 2.3, was fed as an array of the dimension of 305. The solution for the NN to learn on is the amount of hits. The amount of hits is converted in different categories, from 1 to 4. The output layer is therefore activated by the softmax function, so a probability is assigned for every number of possible hits. With this design, one can not only tell the probability of multiple hits present, but also the more challenging probability of how many exactly. The loss function to be minimized was chosen to be the categorical cross-entropy, and as metric the accuracy of the prediction, i.e. how many events have

been guessed correctly. Both are typical for a categorization problem. 50 epochs were trained, which led to a computing time of around 2 h.

The validation at the end of the training showed that in 95 % of the cases, the NN predicted the correct amount of hits, and in 99 % of the cases correctly whether it is a single or multiple hits event. Going back to our time estimation, we would get a response from the NN within seconds, deciding on which plane there are multiple hits. The hits from cosmics could be ignored completely, since a shower ending up in a MMD and leaving multiple hits at the same time is unlikely. Therefore, only the 3 planes with multiple hits from the actual annihilation would have to be analyzed with the unfolding algorithm. This would lead to a computation time of 60s on a single CPU core. All the other planes can be analyzed with conventional methods that are not computationally intense and will be done within seconds.

Although being already highly efficient, this result can be improved with longer training or a more refined choice of the network design. In Fig. 6.1, the training curve is shown. The orange solid line corresponds to the minimization value of the loss function, whereas the black dashed line the validation check. After 10 epochs, the training becomes very unstable, indicating that no stable solution below current accuracy was found yet and longer training is needed. However, it is more likely that the design chosen is too simple to improve further and would need to be changed if a higher accuracy is aimed at.

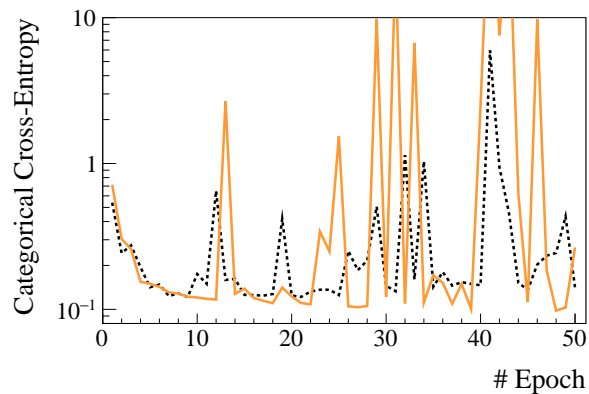


FIGURE 6.1: The training curve for the Multiple Hits Neural Network. The solid orange line describes the minimized value of the loss function, whereas the dashed black line is the validation.

### Hit reconstruction

Now knowing from the multi-hit NN how many hits are present, a second NN can be built to reconstruct the hit positions. We chose a similar design as discussed before in Tab. 6.1. We still feed the event as an array in strip-space, and the same dense layers are applied. The difference is in the output layer, which was activated by a linear function instead, not returning a probability but a strip position. The output layer is an array of dimension 5, where the position information for each hit is stored. In case there are less than 5 hits found, the assigned value is 0. This design was trained separately on data containing either 1, 2 or 3 hits. The Mean Absolute Error between true and predicted hits was used to be minimized as loss function and used as metric at the same time. As before, 50 epochs were trained.



The results of the training and validation are shown in Fig. 6.2. On the left side, the training progress is shown. It is clear that reconstructing a single hit is not a difficult problem for a NN, since the loss function was minimized in only a few epochs to a decent level. The double and triple hits are more difficult, visible in the rather large oscillations of the training curve. Eventually, also there a more stable solution was found. In all three cases, the validation (dashed) and training (solid) are still agreeing, and the tendency of the training curve is continuously decreasing. In Fig. 6.2 on the right side, the residual distributions for true and predicted hit are shown. Except for the well-trained single hit, the distributions are still rather broad. The other thing that has to be investigated is the relative offset; one would expect the distributions to be centered around 0.

The reconstruction efficiencies for single ( $99^{+1}_{-1}\%$ ), double ( $95^{+3}_{-18}\%$ ) and triple hits ( $93^{+4}_{-20}\%$ ) (following the convention of the residual cut at  $1\text{ mm} \pm 0.5\text{ mm}$  from Sec. 2.5.2), are very promising. The behaviour of the training curves is a clear indication that the training has not finished yet after 50 epochs and should be continued to improve the results. Additionally, the offset will get smaller through more training, but by choosing a more optimized loss function, this issue should be easier to tackle. With such a NN at hand, the unfolding algorithm would only be used to train the network. For the actual live reconstruction of the hit events, the NN would be sufficient and return an annihilation vertex position within a few seconds.

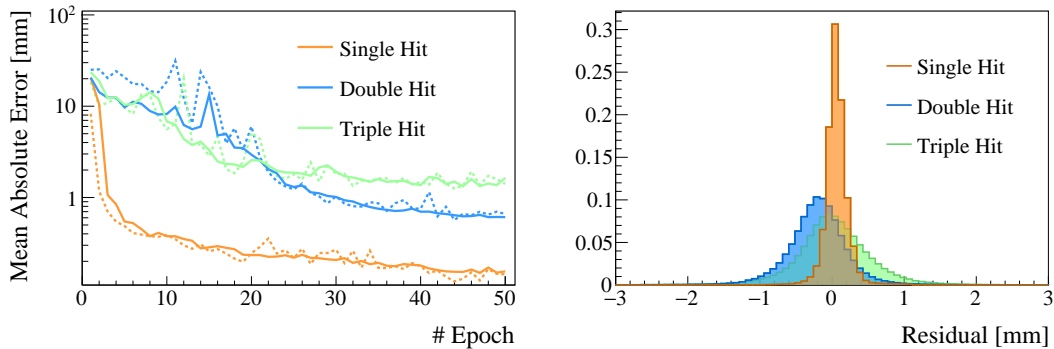


FIGURE 6.2: The training curve (left) and the residuals of the validation (right) of the multiple hit reconstruction with the Neural Network for single, double and triple hits.

Since these simple tests show already promising results, the next step to take would be to train a new network with experimental data. To extract the hit positions to feed as the true solutions, the unfolding algorithm could be used. One could also imagine to use an improved version of the network trained with simulated data, and re-train it with experimental data (transfer learning (215; 216)). This might end up to be the faster way, since the most fundamental features the network already knows from simulation and so it only needs to learn the details from experiment.

A more sophisticated, but computationally intense NN could be set up for a 2D hit reconstruction. In this case, the input would not be just a 1D-array in strip-space, but rather a matrix with for example the row being the X-coordinate and column the Y-coordinate. An example of such an image is shown in Fig. 6.3. With an image or pattern recognition NN such as a Convolutional Neural Network (CNN) (217), the hit position could be extracted. Such CNN were already successfully tested on 1D-Micromegas detectors (218), building a 2D image of hit position and time. For multiplexed XY signals, such an approach would be novel. In Keras, a variety of pre-defined 2D convolutional models are available, such as VGG (219), ResNet (220)

or Inception (221). By building an image of  $305 \times 305$  pixels for the MMD with multiplexing factor 5, the amount of input parameters becomes already extremely large (93 025 parameters) and therefore the training of such a network computationally very heavy. Also in this case, transfer learning might be the solution to reduce the complexity, if a trained open-source network with similar features can be found.

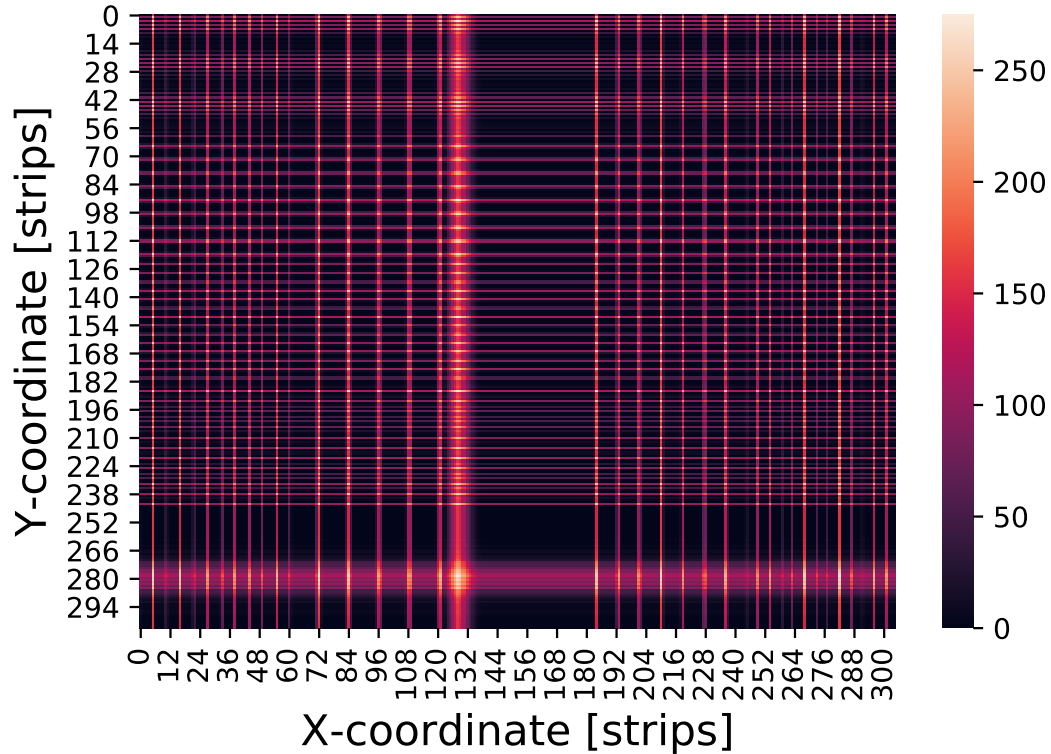


FIGURE 6.3: Example for an input image of a 2D hit from a multiplexing factor 5 MMD with 305 strips in X- and Y-coordinate. The true hit would be found at roughly  $(x,y) = (130,280)$  strip position where the image is the brightest.

### 6.1.3 Antihydrogen Lamb Shift

In Chap. 4, we further explored the design of the GBAR Lamb shift setup and saw its commissioning with a M(2S) beam at PSI. By detecting the  $Ly-\alpha$  rate we were able to characterize the intensity of the M(2S) beam, which was with incident  $\mu^+$  energies of 5 keV to 10 keV between 80 Hz to 100 Hz. Additionally, the design of the microwave setup was shown, including all characterization measurements.

After the successful tests, the GBAR Lamb shift setup was installed in the GBAR beamline and is currently being commissioned. The first goal is to measure the hydrogen Lamb shift by shooting 10 keV protons on a carbon foil located in the reaction chamber to form a pulsed H(2S) beam. Once the system is commissioned, the second step would be to reproduce the hydrogen Lamb shift measurement, but this time from hydrogen formed by protons picking up an electron from a positronium cloud via charge-exchange. This will be a crucial test to characterize the gamma background coming from the positronium decay in the reaction chamber. Additional shielding or gating the MCPs (e.g. (222)) can be looked at in case the gamma background covers the signal region for the  $Ly-\alpha$ . Another advantage of studying

the Lamb shift first with hydrogen is to learn about the systematics of the measurement and how to reduce them. Once the antiprotons are back in the AD hall, the first attempts of detecting Ly- $\alpha$  coming from antihydrogen will be done. The system will first be used to further optimize the charge-exchange reaction. When a stable and intense antihydrogen is routinely produced, the first attempt of scanning the antihydrogen Lamb shift directly will be done.

## 6.2 Muonium Lamb Shift

By seeing that an intense M(2S) beam is available at PSI, the opportunity opened up to improve upon the muonium Lamb shift. In Chap. 5, we saw a revised design of the Lamb Shift setup for muonium and a detailed explanation of the data taking and the analysis. During the beamtime in June 2021, we measured the Lamb shift of muonium to be 1047.2(25) MHz, the muonium 2S hyperfine splitting (559.6(72) MHz) and detected for a first time M(3S). Currently, these results are limited by statistics.

To further probe QED, we identified in Chap. 3 the contributions of the Barker-Glover correction and the nucleus self-energy to be most promising, since they are enhanced in muonium and currently out of reach of the hydrogen Lamb shift accuracy. Their contributions lie at 160 kHz (Barker-Glover) and 40 kHz (nucleus self-energy), respectively. To reach such levels, not only the statistical, but also systematic uncertainty will have to be lowered. Especially the beam contaminations of either 3S or 4S states need to be controlled and the first order Doppler shift accounted for. Furthermore, the microwave setup needs to be improved to lower the uncertainty of the power estimation inside the TLs. All other systematic effects contribute to the uncertainty with less than totally 50 kHz in both determinations with either measuring the 583 MHz or 1140 MHz transition. In the following sections, the approaches on how to reach these goals are explored.

### 6.2.1 Statistics

In Sec. 3.2 we discussed that due to the straggling at the foil, the muonium beam will become diffuse. So far, a 10 nm foil was used, which is well-tested and a lot of know-how present at PSI on how to produce them. From the measurements at the LEM beamline was clear that a thinner foil with less straggling would be beneficial for transporting the beam efficiently to the stop detector at the end of the beamline. Recently, ultra-thin graphene foils of just a few atomic layers have successfully been produced and tested (200; 223). From angular scattering measurements with such foils, at low energies of a few keV, the scattering half angle was found to be proportional to the foil thickness (224). Since the ultra-thin graphene foils are between 5 to 10 times thinner (minimum three layers,  $\sim 1$  nm), a substantial increase of M(2S) rate of between 15 to 25 is expected (204). Such foils have already been ordered to PSI and transferred by Z. Salman and H. P. Weber onto the target holders with ease. Currently, a technique needs to be identified to dissolve the protective layer on top without destroying the foil. Once this problem is overcome, first tests in a beamline can be done.

Another option to reduce straggling would be to let the muon beam interact with a gas target instead of the carbon foil. The currently most precise determination of the hydrogen Lamb shift was done with protons on a H<sub>2</sub> target (225). The gas would be located in a cell with two tiny holes, one for the entrance of the beam and one for the exit. The holes are tiny so the gas will not leak out too fast into vacuum,

interfering with the moderator. For that reason, the muon beam would have to be focused very tightly, which will not be possible with the LEM beamline alone.

A promising technique to cool and compress a muon beam is muCool (226) at PSI. Longitudinal (227) as well as transverse phase-space (228) compression were already shown separately. The goal of muCool is to deliver a keV beam of roughly  $2 \cdot 10^4$  Hz rate and a small phase space (40 mm mrad at 10 keV) (229). Another advancement at PSI is the High Intensity Muon Beam (HiMB) project, which aims at increasing the surface muons rate by a factor 100 to  $10^{10}$  Hz by improving target and beamlines (230). In combination with muCool, a keV  $\mu^+$  beam could be produced with a rate of around  $5 \cdot 10^5$  Hz (229), already being an improvement of an order of magnitude in rate compared to LEM, but having a much smaller phase space and therefore leading to a much better transportation efficiency through the beamline. The project is currently in the planning and preparation phase, with the implementation starting in 2027 when accepted. The operation would be planned for 2028 (231).

### 6.2.2 Beam Contamination

From our current best measurement of the muonium Lamb shift, the 4S beam contamination was accounted for with a systematic uncertainty of 1 MHz. There is no way around reducing the contamination for a precision measurement. Additionally, by reducing the 3S beam contamination, the systematic uncertainty coming from quantum interference would be reduced as well. In the following, three approaches are looked at:

- Increasing the length of the beamline to have the higher  $n$  states relaxing to the ground state
- Adding another transmission line to depopulate states similar as to the HFS selector
- Adding a weak electrical field to quench states

#### Increasing Length of Beamline

With the help of the Grotrian diagram in Fig. 3.6 and the Eq. 3.6, the depopulation of 3S and 4S states by having longer time-of-flight can be estimated. Currently, the distance from the foil to the entrance of the Ly- $\alpha$  detection setup is roughly 19 cm. For the average muonium atom with an energy of 5.7 keV, the time-of-flight would be 60 ns and hence, only 32 % of the 3S and 24 % of the 4S states relaxed back. The length would have to be increased significantly, as shown in Fig. 6.4, to reduce the beam contamination only by time-of-flight. The total length between foil and stop detector is currently at 0.37 m. By doubling the length, the contamination would be reduced for both cases roughly only by half, but would also mean a significant loss in statistics due to the divergence of the beam. Therefore, relying on the states relaxing to the ground state is only to be taken as a beneficial side effect.

#### Adding Transmission Line

Similar to the HFS selector, another transmission line optimized for the frequency around 350 MHz to depopulate 3S states could be added. For the 4S states, such an approach is more difficult to realize, since the 4S contribution lies between the

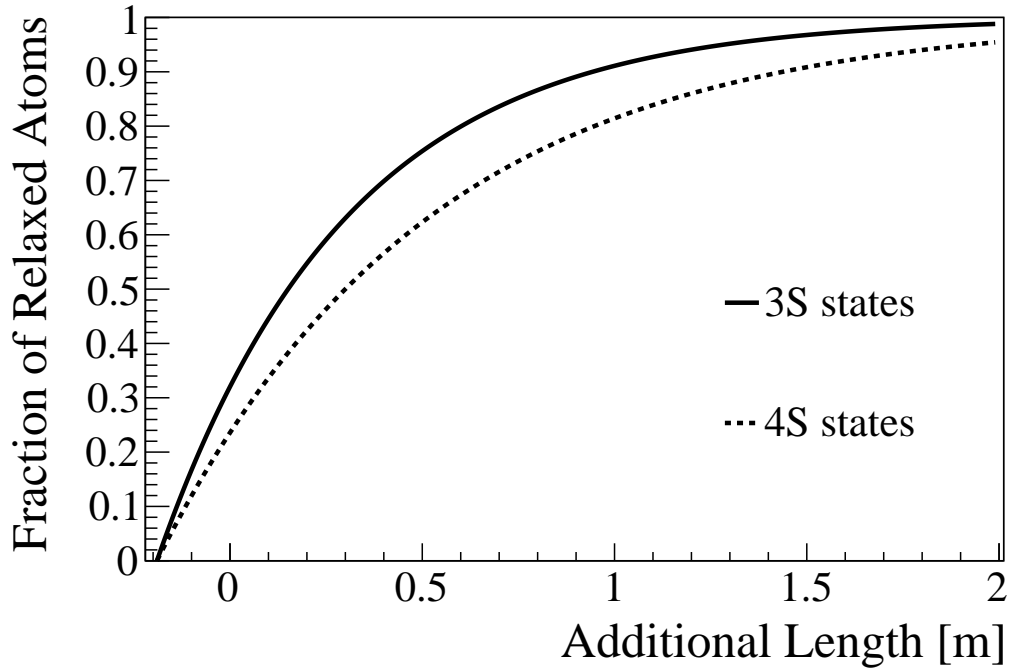


FIGURE 6.4: Scan of depopulating 3S (solid) and 4S (dashed) states by extending the beamline length.

1140 MHz and 1326 MHz resonance. The TL was estimated to add 5 cm to the beamline, depopulating already 20 % more of the 3S states.

The allowed 3S transitions are:

$$3^2S_{1/2}(F = 0, m_F = 0) \rightarrow 3^2P_{1/2}(F = 1, m_F = 0) \quad (6.4)$$

$$3^2S_{1/2}(F = 1, m_F = 0) \rightarrow 3^2P_{1/2}(F = 0, m_F = 0) \quad (6.5)$$

$$3^2S_{1/2}(F = 1, m_F = \pm 1) \rightarrow 3^2P_{1/2}(F = 1, m_F = \pm 1) \quad (6.6)$$

with the resonance frequencies of  $\nu_{(6.4)} = 174$  MHz,  $\nu_{(6.5)} = 394$  MHz and  $\nu_{(6.6)} = 339$  MHz, respectively.

The optimum frequency for depopulating the 3S states, minimizing the effect on the 583 MHz transition, was found by simulation to be at 360 MHz. With a reasonable power of 30 W applied, the 394 MHz transition can be depopulated by 84 % and the twice as intense transition of 339 MHz by 90 %. The transition at 174 MHz is only driven down by 29 %, but is also furthest away from the 2S resonance and has therefore the least influence. From the 2S transition, only 10 % would be lost.

The comparison without and with additional TL is shown in Fig. 6.5. For this estimation, the amount of detected 3S states was fixed to 20 % as previously determined by experiment. It is clear that the remaining 3S states still distort the left tail of the 2S resonance and would still have to be modeled in the analysis. Since the contribution is lower, it will be more difficult to accurately determine the fraction and hence still leave a significant uncertainty. Adding only a single additional TL will not be the optimal solution.

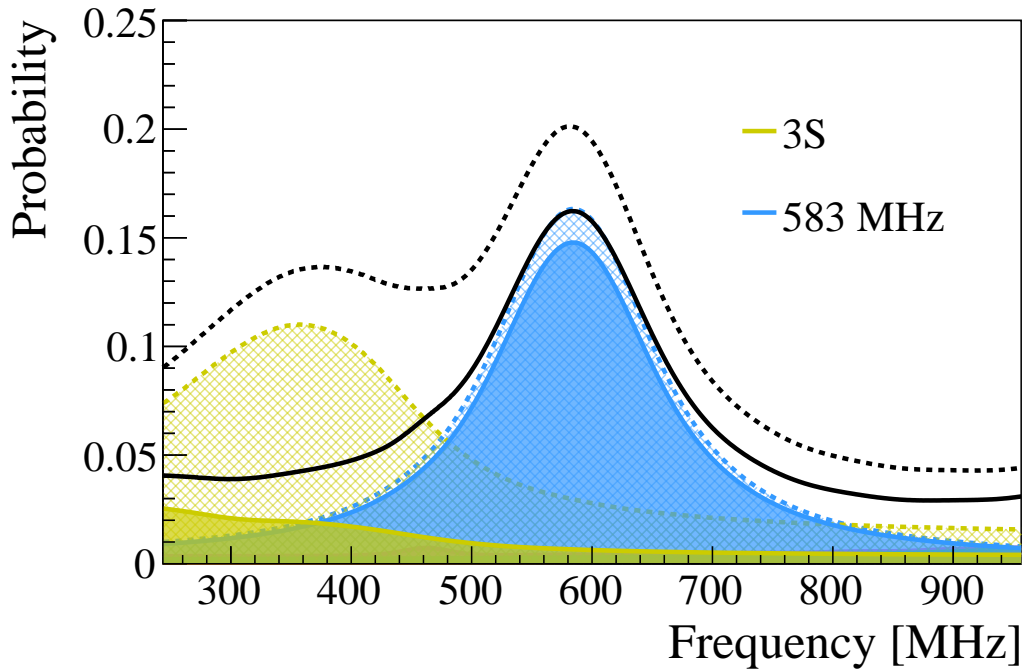


FIGURE 6.5: Example of the line-shape for the 583 MHz transition scan without (hatched area and dashed lines) and with (colored area and solid lines) an additional transmission line depopulating the 3S states. In this case, the frequency was set to 360 MHz at 30 W. The colored areas in yellow represent the 3S contribution, whereas the blue areas are the 583 MHz transition.

### Adding Electrical Field

By looking at the quenching equation Eq. 3.68, a dependence on the transition frequency as well as the transition matrix element is seen. This can be exploited to drive some transitions efficiently, where for others still a large fraction is surviving. This approach can be done by either for example adding 5 cm to the beamline to accommodate a well-defined electrical field (583 MHz case) or simply replacing the HFS selector with the electrical field (1140 MHz case). A 5 cm long electrical field would correspond for an average beam energy of 5.7 keV to a transit time of 15 ns. With such an exposure, the Fig. 6.6 was simulated for different field strengths, taking the transition elements from Tab. 3.2. In this simulation, only the  $nS-nP_{1/2}$  transitions were looked at, the D- and F-states were neglected for the mixing. To determine a more accurate optimal voltage, the system would have to be simulated by for example using the density-matrix approach (e.g. for 3S (232)).

It can nicely be seen that for example all the 3S states can be quenched with a field of roughly  $75 \text{ V cm}^{-1}$ , but still keeping 50% of the 583 MHz resonance atoms. This takes also into account that due to the additional 5 cm, 20% more of the 3S states will relax just by time-of-flight. With this approach, the contribution of the 3S states becomes insignificant and the leaking of the 1326 MHz transition more important to model (since the 1140 MHz will still be depopulated with the HFS selector). The comparison for without and with additional electric field is shown in a scan in Fig. 6.7 on the left side.

Another option would be to apply a field of only  $40 \text{ V cm}^{-1}$  to drive down all 4S and around 70% of the 3S states. 80% of the 583 MHz states would survive, and 95% of the 1140 MHz and 1326 MHz. An estimated line-shape is shown in Fig. 6.7 on



the right side. The option of scanning the 1140 MHz line-shape seems to be the most promising. The disadvantage of the 583 MHz approach is that it does not only get rid of the 3S states, but also 50 % of the 2S F=0 states, making it much more difficult to acquire high statistics, while the signal would already be only half of the one from the 1140 MHz transition.

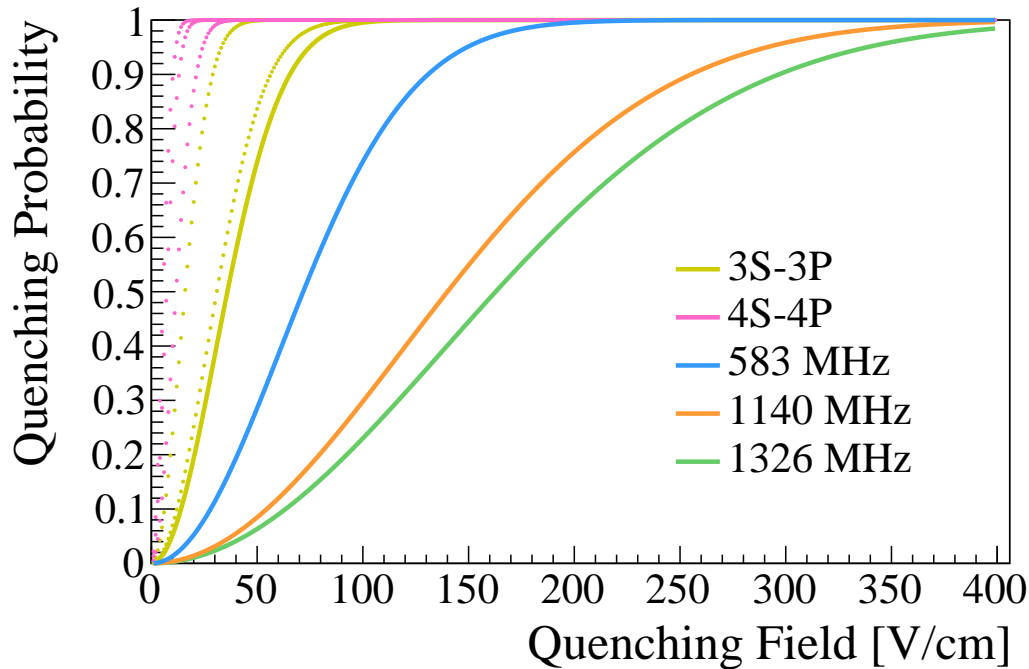


FIGURE 6.6: A scan for the quenching probability of muonium atoms experiencing an electrical field for 15 ns. The yellow lines are the three hyperfine states involved in the 3S quenching, with the solid yellow line being closest to the 583 MHz Lamb shift line. The pink lines are associated to the 4S quenching, all affecting both the 1140 MHz and 1326 MHz transitions. The three hyperfine transitions of the 2S are shown in blue, orange and green.

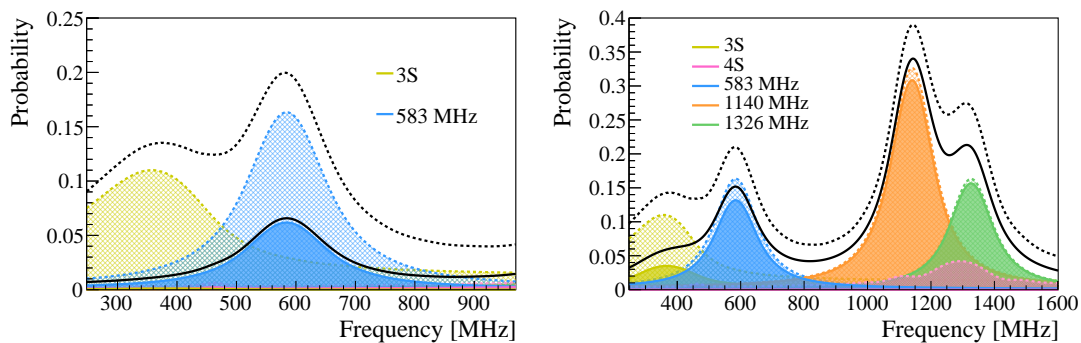


FIGURE 6.7: Line-shape scans with (solid lines and colored areas) and without (dashed lines and hatched areas) additional electrical quenching field for both 583 MHz (left) and 1140 MHz (right) transitions.

### 6.2.3 Beamtime Estimations

The promising line-shape simulated in Sec. 6.2.2 was taken to estimate the achievable statistical uncertainty in an upcoming beamtime. The statistics value refers to how many  $M(2S,3S,4S)$  atoms were entering the Lamb shift setup, before interacting with any fields. The line-shape was built at the same frequencies as used in the previous beamtime, summarized in Tab. 5.2. The line-shapes were built with different amount of statistics, eventually fitting a simple Lorentzian model, since most of the background is quenched and can therefore be neglected. This process was repeated 10 000 times to get an average distribution of the extracted central frequency. The standard deviation on the central frequency value was eventually plotted versus the amount of statistics used. In Fig. 6.8, the function  $\propto \frac{1}{\sqrt{x}}$  fitted to the simulation data is shown for the 1140 MHz approach.

To translate from statistics to a time, the  $M(2S,3S,4S)$  rate summarized in Tab. 5.2 is used, which corresponds to the amount of excited muonium being tagged, quenched in the  $Ly-\alpha$  setup and eventually reaching the stop detector if no TL would be active. By using the value of roughly 0.3 Hz of  $M(2S,3S,4S)$ , the results shown in Chap. 5 had around 100 000 statistics for the 1140 MHz line-shape in 3 d.

When using the entire beamtime of 10 d to scan the Lamb shift, at least a factor of 3 more statistics can be collected. By installing a 5 to 10 times thinner carbon foil, as explained in Sec. 6.2.1, a 15 to 25 times higher flux reaching the stop detector can be achieved. With these improvements, the 200 kHz level can be reached with the 1140 MHz approach. Adding another TL to depopulate the  $2S F = 0$  states, reducing the background, would bring another improvement in uncertainty of roughly a factor 1.25 (e.g. from 200 kHz to 160 kHz statistical uncertainty).

The goal of reaching 40 kHz level and going beyond seems still to be out of reach and further improvements such as using muCool or the acceptance of constructing the HiMB at PSI would be needed. Additionally, some systematic effects such as the motional Stark created by the Earth's magnetic field should be reviewed, which has been given at the moment a rather large upper bound.

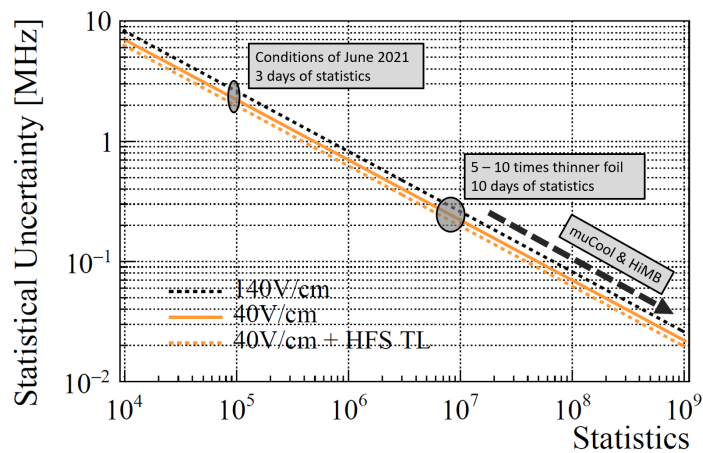


FIGURE 6.8: The uncertainty estimation depending on how much statistics needs to be gathered. The black dashed line corresponds to the estimation for a 1140 MHz line-shape scan with a field applied of  $140 \text{ V cm}^{-1}$ , the orange solid line with the optimal field of  $40 \text{ V cm}^{-1}$  (see Sec. 6.2.2). The dashed orange line corresponds to a measurement with an additional TL, depopulating the  $2S F=0$  states and hence reducing background.



### 6.2.4 Doppler Shift & Monitoring Power

Seeing that a statistical uncertainty of a few hundred kHz is not out of reach, and the main systematic uncertainty of the beam contamination can be handled, the next systematic effect in line to be controlled would be the Doppler shift. By using a thinner foil, also the transversal velocity due to straggling will be reduced and therefore also the Doppler shift. Furthermore, a way to average out the Doppler shift would be to collect half the statistics with the Scanner TL in the original mode, and the other half of the statistics with reversing the field by changing the MW input with the output. From simulations we saw that such an attempt would compensate the Doppler shift by at least a factor of 20, with the current setup reducing it to less than 16 kHz uncertainty.

This approach was already tried in the beamtime of June 2021, but unfortunately while reversing the MW field a combiner degraded, which was only noticed after a detailed analysis of the data. To avoid having to discard data and therefore not being able to compensate for the Doppler shift due to such an incident, the MW equipment should be reduced to a minimum.

The most optimal solution would be to use a frequency generator with two outputs to get rid of the need of a splitter but still being able to have a  $\pi$ -phase shift. For each channel, a separate amplifier should be used, directly fed to the transmission line. To avoid the combiner, on each output channel a power meter should be installed to monitor the power on each plate continuously. A sketch of the setup is shown in Fig. 6.9. With this setup, not only the power monitoring would become more straightforward, but also determining the power inside the TL as well as frequency-dependent power corrections.

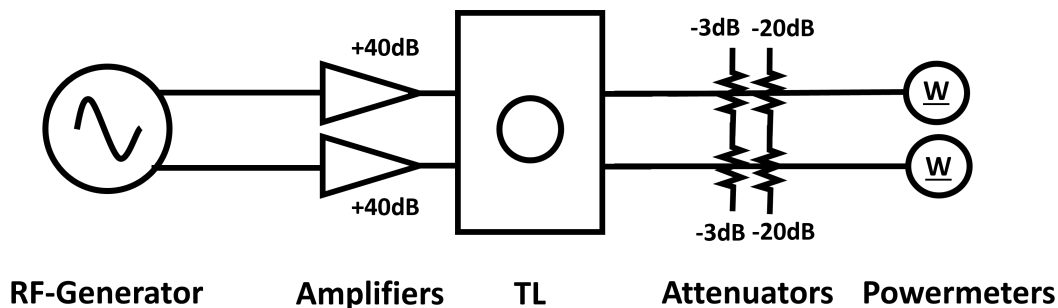


FIGURE 6.9: The sketch of the proposed MW setup for a future muonium Lamb shift measurement.

### 6.2.5 Summary

With the improvements mentioned before, the Barker-Glover correction could be probed with M already in the next years. With the acceptance of the HiMB project, the systematics could be studied more thoroughly during beamtime and therefore the M LS measurements become competitive to the one of the hydrogen. A summary of the possible upgrades is given in Tab. 6.2.

TABLE 6.2: Summary of possible upgrades to the Mu-MASS setup and which contributions of the M LS could be probed.

Beamline	Target	Timeline	M(2S) (Hz)	LS Uncertainty (kHz / 10 d)	Contributions
muE4/LEM	C-Foil	2021	5	1000	$E_{SE}, E_{VP}, E_{rec,S}$
muE4/LEM	Graphene	2023	100	200	$E_{BKG}$
PiE1/muCool	Graphene	2025	1000	70	$E_{2ph}$
PiE1/muCool	Gas	2026	5000	30	$E_{SEN}$
HiMB/muCool	Gas	2029	100 000	10	$E_{RR}, E_{HFS}, E_{rec,R}$

## Appendix A

# Additional Figures

### A.1 Updated Sensitivity Plot for CPT-violation

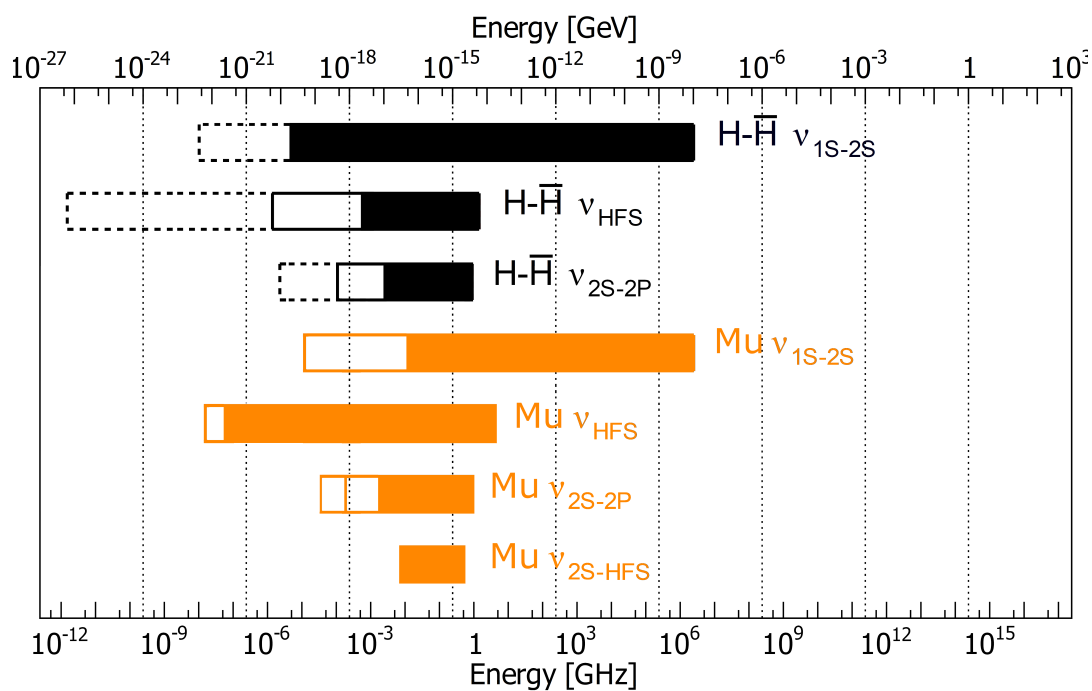


FIGURE A.1: Sensitivity for CPT-violation in antihydrogen and muonium. The right edge represents the absolute value, whereas the left edge is the absolute accuracy of the measurement. Filled bars are the to-date most precise determination and the solid empty bars the expected accuracies of ongoing measurements, the references given in the text. The dashed bars indicate the most precise measurement of the hydrogen equivalent.

## A.2 Complete Efficiency Scan for all MMD

Mission	Resistivity (M $\Omega$ /sq)	Double Hit Efficiency [%]		
		X-Plane	Y-Plane	XY-Plane
Einstein 1-4	3.5 to 4	94 <sup>+1</sup> <sub>-4</sub>	92 <sup>+1</sup> <sub>-5</sub>	86 <sup>+3</sup> <sub>-6</sub>
Fert 1	$\sim$ 4	96 <sup>+1</sup> <sub>-1</sub>	92 <sup>+1</sup> <sub>-5</sub>	89 <sup>+2</sup> <sub>-6</sub>
Fert 2	$\sim$ 3	95 <sup>+1</sup> <sub>-3</sub>	90 <sup>+2</sup> <sub>-5</sub>	86 <sup>+2</sup> <sub>-7</sub>
Fert 3	$\geq$ 5	94 <sup>+1</sup> <sub>-2</sub>	92 <sup>+1</sup> <sub>-5</sub>	87 <sup>+2</sup> <sub>-8</sub>
Fert 4	$\sim$ 4	96 <sup>+1</sup> <sub>-2</sub>	92 <sup>+1</sup> <sub>-4</sub>	89 <sup>+2</sup> <sub>-5</sub>
Alhazen 1-4	$\sim$ 0.4	91 <sup>+0</sup> <sub>-4</sub>	89 <sup>+1</sup> <sub>-5</sub>	81 <sup>+1</sup> <sub>-8</sub>

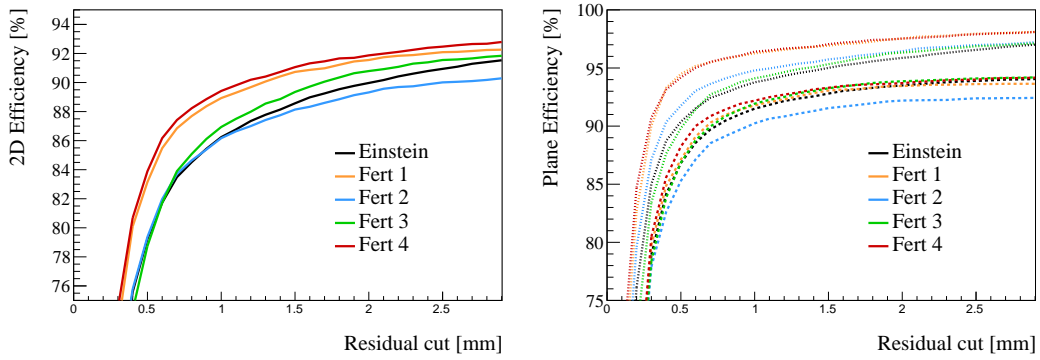


FIGURE A.2: Summary of the results for double hit reconstruction with different MMDs, analysed with the unfolding algorithm. On the left side is the 2D hit reconstruction efficiency displayed, whereas on the right side the separated efficiencies for X (dotted) and Y (dashed). The efficiency quoted in the table is for a 1 mm residual cut. The super- and subscripts are within  $\pm 0.5$  mm.

## Appendix B

# Algorithms for Micromegas

## B.1 Creating Multiplexing Map

```

1 int main(){
2
3     int p=61; int Nstrip_MG=1037;
4     int MultiplexSeries[]={
5         30,10,15,19,5,20,27,22,11,24,
6         18,12,9,6,3,4,1,16,8,2,23,21,
7         7,25,14,28,17,26,13,29};
8     int Detector[Nstrip_MG]; // strip to channel correspondance
9     for(int i=0;i<(p-1)/2;i++)
10    {
11        for(int j=0;j<p;j++)
12        {
13            if(i*p+j<Nstrip_MG)
14            {
15                Detector[i*p+j]=(0+MultiplexSeries[i]*j)%p;
16            }
17        }
18    }
19
20 // create map
21
22 ofstream myfile;
23 myfile.open ("multiplexing_p61_m17.txt");
24 double entry=0.0;
25 for(int ch=0; ch<61; ch++)
26 {
27     for(int strip=0; strip<1037; strip++)
28     {
29         if(Detector[strip] == ch){entry = 1.0;}
30         else{entry = 0.0;}
31         myfile << ch << "\t" << strip << "\t" << entry << "\n";
32     }
33 }
34 myfile.close();
35 }

```

## B.2 Building Minimization Function

```

1 double LogLikelihood(const double *pars )
2 {
3     // evaluate model
4     for(int i = 0; i < Ns; i++){vstrips(i, 0) = pars[i];}
5
6     // multiplex
7     //mmultiplex: multiplexing matrix
8     vmultiplex = mmultiplex * vstrips;
9
10    Double_t logl = 0;
11    for(int i = 0; i < data_v.size(); i++)
12        {
13        if(data_v[i] > 0)
14            {
15            logl += ( vmultiplex(i, 0) - data_v[i] )*( vmultiplex(i, 0) -
16            data_v[i] );
17            }
18        }
19
20    // Additional constraint - Smoothness
21    // mreg: Regularization Matrix, 2nd Derivative
22    mQ2 = mreg * vstrips;
23    mQ2T = mQ2.transpose();
24    ms = mQ2T * mQ2;
25
26    //lambda as runtime input
27    logl += pow(lambda,2)*ms(0,0);
28
29    return logl;
30 }

```

## B.3 Unfolding Algorithm

```

1 std::vector<double> NumericalMinimization(std::vector<double> parini)
2 {
3     Eigen::setNbThreads(8);
4     int n = Eigen::nbThreads();
5
6     ROOT::Math::Minimizer* min = NULL;
7     min = ROOT::Math::Factory::CreateMinimizer("Minuit2", "Migrad"
8     );
9     min->SetPrintLevel(0);
10    min->SetMaxIterations(50);
11    min->SetMaxFunctionCalls(5e+04);
12
13    ROOT::Math::Functor f(&LogLikelihood,Ns);
14    double step[Ns];
15    for(int i = 0; i < Ns; i++){step[i] = 100;}
16
17    double variable[Ns];
18    for(int i = 0; i < Ns; i++){variable[i] = parini[i];}
19
20    min->SetFunction(f);
21
22    // Set the free variables to be minimized
23    for(int i = 0; i < Ns; i++)
24        {
25        std::string name = "x" + std::to_string(i);

```

```
25     min->SetVariable(i,name.c_str(),variable[i], step[i]);
26     min->SetVariableLimits(i, 0, 1e+04);
27     }
28
29     for(int i = 0; i < Ns; i++)
30     {
31         if(parini[i] == 0){min->FixVariable(i);}
32     }
33
34     min->Minimize();
35     solution_v.clear();
36     const double *pars = min->X();
37     for(int i = 0; i < Ns; i++){solution_v.push_back(pars[i]);}
38
39     delete min;
40     return solution_v;
41 }
```





## Appendix C

# Mathematica Code for Lamb Shift Theory

### C.1 Calculating Transition Elements

```

1 a0 = 1;
2
3 (*Radial wavefunction*)
4 Rnl[n_, l_, r_] :=
5 Sqrt[(2/(n*a0))^3*Factorial[n - l - 1]/(2*n*((Factorial[n + 1])^3))]*
6 Exp[-(r/(n*a0))] ((2*r)/(n*a0))^l*Factorial[n + 1]*
7 LaguerreL[n - l - 1, 2*l + 1, (2*r)/(n*a0)]
8
9 (*Initial Parameters*)
10 n = 2;
11 L = 0;
12 J = 0.5;
13 F = 1;
14 M = 1;
15
16 n2 = 2;
17 L2 = 1;
18 J2 = 0.5;
19 F2 = 1;
20 M2 = 1;
21
22 S = 0.5;
23 i = 0.5;
24 Q = M2 - M;
25
26 (*Transition Element for specific states*)
27 Integrate[Rnl[n2, L2, r]*Rnl[n, L, r]*r*r*r, {r, 0, Infinity}]*
28 Sqrt[(2 J + 1)*(2 J2 + 1)*(2 F + 1)*(2 F2 + 1)]*
29 SixJSymbol[{L2, J2, S}, {J, L, 1}]*
30 SixJSymbol[{J2, F2, i}, {F, J, 1}] *
31 ThreeJSymbol[{F, M}, {1, Q}, {F2, -M2}]

```

### C.2 Calculating Theoretical 2S Lamb Shift Contributions

# Hydrogen & Muonium LS

Formulas taken from CODATA 2018, adapted from Thomas Udem's notebook

<https://doi.org/10.1103/RevModPhys.93.025010>

```
In[ ]:= ClearAll["Global`*"];  
Pfad=NotebookDirectory[];  
WorkingPrecision->1000;
```

## Constants

```
In[ ]:= c=299792458; (* speed of light *)  
  
M[mn_, me_] = me + mn; (*total mass*)  
mr[mn_, me_] = me mn / M[mn, me]; (*reduced mass*)  
  
(* electron to muon mass ratio *)  
mem $\mu$ =4.83633169`128 $\times 10^{-3}$ ;  
 $\delta$ mem $\mu$ =0.00000011`128 $\times 10^{-3}$ ;  
  
(* fine structure constant *)  
 $\alpha$ CODATA=7.2973525693`128 $\times 10^{-3}$ ;  
 $\delta\alpha$ CODATA=0.000000011`128 $\times 10^{-3}$ ;  
  
(* proton charge radius *)  
RpCODATA=0.8414`128 $\times 10^{-15}$ ;  
 $\delta$ RpCODATA=0.0019`128 $\times 10^{-15}$ ;  
  
(* Friar radius of the proton eqn.(29) for nuclear size correction E(5) *)  
rpF=1.947`128 $\times 10^{-15}$ ;  
 $\delta$ rpF=0.075`128 $\times 10^{-15}$ ;  
  
Z=1;  
h = 6.62607015 $\times 10^{-34}$ ; (*plank constant*)
```

## Dirac Energy

```
(*Functions used to evaluate Dirac Energy, Eq 8*)
δ[i_,j_]=KroneckerDelta[i,j];
δδ[J_,α_]=J+ $\frac{1}{2}$ -Sqrt[ $\left(J+\frac{1}{2}\right)^2-(Z\alpha)^2$ ];
ff[n_,J_,α_]= $\left(1+\frac{(Z\alpha)^2}{(n-\delta\delta[J,\alpha])^2}\right)^{-1/2}$ ;

(*Dirac and some recoil corrections; eqns (9) *)
eM[n_,J_,α_, mn_, me_]= M[mn, me] c2 +
  (ff[n,J,α]-1) mr[mn, me] c2 -
  (ff[n,J,α]-1)2  $\frac{mr[mn, me]^2 c^2}{2 M[mn, me]}$ ;

(* Barker-Glover correction considered to be part of the Lamb shift;
  last terms in eqns (9) *)
EBG[n_,L_,J_,α_, mn_, me_]= $\frac{1-\delta[L,0]}{(-1)^{J-L+1/2} (J+1/2) (2 L+1)}$   $\frac{(Z\alpha)^4 mr[mn, me]^3 c^2}{2 n^3 mn^2}$ ;
```

## Relativistic Recoil

```
(*functions used to compute relativistic recoil*)

(* some Bethe logarithms lnk0[n,L] for S states from Drake PRA 41, 1243 (1990) *)
lnk0[2,0]=2.811769893120563`128;
lnk0[2,1]=-0.030016708630213`128;

a[n_,L_]=If[L==0,-2 (Log[2/n]+Sum[1/i,{i,1,n}]+1-1/(2 n)), 1/(L (L+1) (2L+1))];

(* table III of CODATA 2018 and Yerokhin PRA 93, 062514 (2016)
and PRL 115,233002 (2015) *)
GREC[2,0,1/2]=14.899`128/π;
δGREC[2,0,1/2]=10.003`128/π;
GREC[2,1,1/2]=1.5097`128/π;
δGREC[2,1,1/2]=0.0002`128/π;

(*leading relativistic recoil correction, Eq. 11*)
ES[n_,L_,α_, mn_, me_]=
  (mr[mn, me]^3 (Z α)^5)/(me^2 mn π n^3) me c^2 (
    (1/3)δ[L,0] Log[(Z α)^-2]-
    (8/3) lnk0[n,L]- (1/9)δ[L,0]- (7/3) a[n,L]-
    (2δ[L,0]/(mn^2-me^2)) (mn^2 Log[me/mr[mn, me]]-
    me^2 Log[mn/mr[mn, me]]);

(*higher order recoil correction, Eq. 12*)
ER[n_,L_,J_,α_, mn_, me_]=
  (me (Z α)^6)/(mn n^3) me c^2 (
    (δ[L,0] (4 Log[2]-7/2) +
    (1-δ[L,0]) (3-L(L+1)/n^2)) (2/(4 L^2-1) (2 L+3)) +
    (Z α) GREC[n,L,J]);

(* type u0 correlated uncertainty *)
δER[n_,L_,J_,α_, mn_, me_]=If[δGREC[n,L,J]<0,
  (ER[n,L,J,α,mn,me])/100,
  (me (Z α)^6)/(mn n^3) me c^2 (Z α) δGREC[n,L,J]];

```

## Self Energy

(\* functions used to compute self energy \*)

(\* table IV of CODATA 2018

and <https://physics.nist.gov/PhysRefData/HDEL/PDF/selfen.pdf> \*)

GSE[2,0,1/2]=-31.18515`128;

δGSE[2,0,1/2]=0.00009`128;

(\*Functions within F(x), Eq. 15\*)

(\*"Following convention", last line of self energy section\*)

$$A41[L_, mn_, me_] = \frac{4}{3} \delta[L, \theta] \frac{mr[mn, me]^3}{me^3};$$

$$A40[n_, L_, J_, mn_, me_] = \left( -\frac{4}{3} \ln k\theta[n, L] + \frac{10}{9} \delta[L, \theta] \right) \frac{mr[mn, me]^3}{me^3} - \frac{1 - \delta[L, \theta]}{2 (-1)^{J-L+1/2} (J+1/2) (2L+1)} \frac{mr[mn, me]^2}{me^2};$$

$$A50[L_, mn_, me_] = \left( \frac{139}{32} - 2 \operatorname{Log}[2] \right) \pi \delta[L, \theta] \frac{mr[mn, me]^3}{me^3};$$

$$A62[L_, mn_, me_] = -\delta[L, \theta] \frac{mr[mn, me]^3}{me^3};$$

$$A61[n_, L_, J_, mn_, me_] = \operatorname{If}[L == 0, \left( 4 \sum_{i=1}^n \frac{1}{i} + \frac{28}{3} \operatorname{Log}[2] - 4 \operatorname{Log}[n] - \frac{601}{180} - \frac{77}{45 n^2} \right) \frac{mr[mn, me]^3}{me^3}, \left( 1 - \frac{1}{n^2} \right) \left( \frac{2}{15} + \frac{1}{3} \delta[2J, 1] \right) \frac{mr[mn, me]^3 \delta[L, 1]}{me^3} + \frac{96 n^2 - 32 L (L+1)}{3 n^2 (2L-1) (2L) (2L+1) (2L+2) (2L+3)} \frac{(1 - \delta[L, \theta]) mr[mn, me]^3}{me^3}];$$

(\* self energy contribution, Eq. 14 \*)

$$E2SE[n_, L_, J_, \alpha_, mn_, me_] = \frac{\alpha (Z \alpha)^4}{\pi n^3} me c^2 \left( A41[L, mn, me] \operatorname{Log} \left[ \frac{me/mr[mn, me]}{(Z \alpha)^2} \right] + A40[n, L, J, mn, me] + A50[L, mn, me] (Z \alpha) + A62[L, mn, me] (Z \alpha)^2 \operatorname{Log} \left[ \frac{me/mr[mn, me]}{(Z \alpha)^2} \right]^2 + A61[n, L, J, mn, me] (Z \alpha)^2 \operatorname{Log} \left[ \frac{me/mr[mn, me]}{(Z \alpha)^2} \right] + GSE[n, L, J] (Z \alpha)^2 \frac{mr[mn, me]^3}{me^3} \right);$$

(\* type un uncorrelated uncertainty \*)

$$\delta E2SE[n_, L_, J_, \alpha_, mn_, me_] = \frac{\alpha (Z \alpha)^4}{\pi n^3} me c^2 \delta GSE[n, L, J] (Z \alpha)^2 \frac{mr[mn, me]^3}{me^3};$$

## Vacuum Polarization

```
(* vacuum polarization Uhling potential G1VP[n,L,J] ONLY FOR Z=1 *)
(* table V of CODATA 2018 and physicsRefData/HDEL/PDF/vac_pol.pdf *)

G1VP[2,0,1/2]=-0.808872`128;

(* functions used to compute vacuum polarization *)
V40[L_]=- $\frac{4}{15}\delta[L,0]$ ;
V50[L_]= $\frac{5}{48}\pi\delta[L,0]$ ;
V61[L_]=- $\frac{2}{15}\delta[L,0]$ ;
GRVP[L_, $\alpha$ ]= $\left(\frac{19}{45}-\frac{\pi^2}{27}\right)\delta[L,0]+\left(\frac{1}{16}-\frac{31\pi^2}{2880}\right)\pi(Z\alpha)\delta[L,0]$ ;

(* The stationary point nucleus second-order vacuum polarization Eq16*)
E2VP[n_,L_,J_, $\alpha$ _, mn_, me_]= $\frac{\alpha(Z\alpha)^4}{\pi}\frac{mr[mn,me]^3}{n^3 me^3} me c^2$ 
 $\left(V40[L]+V50[L](Z\alpha)+V61[L](Z\alpha)^2\text{Log}\left[\frac{mr[mn,me]/me}{(Z\alpha)^2}\right]+G1VP[n,L,J](Z\alpha)^2+GRVP[L,\alpha](Z\alpha)^2\right)$ ;

(* vacuum polarization for mu+mu- pairs Eq18 *)
E2 $\mu$ VP[n_,L_, $\alpha$ _, mn_, me_]= $\frac{\alpha}{\pi}\frac{(Z\alpha)^4}{n^3} me c^2\left(-\frac{4}{15}mem\mu^2\left(\frac{mr[mn,me]}{me}\right)^3\right)\delta[L,0]$ ;

(* hadronic vacuum polarization Eq19*)
E2hadVP[n_,L_, $\alpha$ _, mn_, me_]= $\frac{671}{1000}E2\mu VP[n,L,\alpha,mn,me]$ ;
(* type u0 correlated uncertainty *)
 $\delta E2hadVP[n_,L_,\alpha_,mn_,me_]=\frac{15}{1000}E2\mu VP[n,L,\alpha,mn,me]$ ;

```

## Two Photon Corrections

```
(* coefficients for the two photon corrections NS[n] and NP[n] *)
(* table VI of CODATA 2018 and Jentschura JPhysA 36,L229 (2003)
   and http://physics.nist.gov/PhysRefData/HDEL/PDF/two_photon.pdf *)
NS[2]=12.03214158`128;
δNS[2]=0.00000001`128;

(* B60[n,L,J] coefficient from table VII, u0=correlated uncertainty,
   un=uncorrelated uncertainty *)
(* S-states *)
B60[2,0,1/2]=-63.6`128;
δB60un[2,0,1/2]=0.3`128;
δB60u0[2,0,1/2]=9.3`128;
(* P_1/2 states *)
B60[2,1,1/2]=-1.8`128;
δB60un[2,1,1/2]=0;
δB60u0[2,1,1/2]=0.3`128;

(* functions used to compute two photon corrections *)
B40[L_,J_, mn_, me_]=
  ( ( 3 π^2 Log[2] - 10 π^2 - 2179 - 9 Zeta[3] ) δ[L,0] mr[mn, me]^3 +
    ( π^2 Log[2] - π^2 - 197 - 3 Zeta[3] ) (1-δ[L,0]) mr[mn, me]^2 ) /
  ( 2 27 648 4 (-1)^(J-L+1/2) (J+1/2) (2 L+1) me^3 );

b50=-21.554470`128;
δb50=0.00013`128;
B50[L_,J_, mn_, me_]=
  ( b50 δ[L,0] mr[mn, me]^3 ) / me^3 ;
δB50[L_,J_, mn_, me_]=
  ( δb50 δ[L,0] mr[mn, me]^3 ) / me^3 ;
B63[L_, mn_, me_]=
  ( 8 δ[L,0] mr[mn, me]^3 ) / ( 27 me^3 );

ψ[n_]=PolyGamma[n];
γ=EulerGamma;
B62[n_,L_, mn_, me_]=
  ( 16 ( 71/60 - Log[2] + γ + ψ[n] - Log[n] - 1/n + 1/(4 n^2) ) δ[L,0] mr[mn, me]^3 +
    4 (n^2-1) δ[L,1] mr[mn, me]^3 ) / ( 27 n^2 me^3 );

B61[n_,L_,J_, mn_, me_]=
  ( 413581/64800 + 4 NS[n]/3 + 2027 π^2/864 - 616 Log[2]/135 - 2 π^2 Log[2]/3 + 40 Log[2]^2/9 + Zeta[3] +
    ( 304/135 - 32 Log[2]/9 ) ( 3/4 + γ + ψ[n] - Log[n] - 1/n + 1/(4 n^2) ) ) δ[L,0] mr[mn, me]^3 +
  ( 4/3 NP[n] + (n^2-1)/n^2 ( ( 166/405 - 8/27 Log[2] ) δ[2 J,1] +
    ( 31/405 - 8/27 Log[2] ) δ[2 J,3] ) ) δ[L,1] mr[mn, me]^3 ) / me^3 ;

B711S=-116;
δB711S=12;
```

$$B71[n_, L_, mn_, me_] = \left( \pi \left( \frac{427}{36} - \frac{16}{3} \text{Log}[2] \right) \left( \frac{3}{4} - \frac{1}{n} + \frac{1}{4n^2} + \psi[n] + \gamma - \text{Log}[n] \right) + B711S \right) \frac{\delta[L, \theta] mr[mn, me]^3}{me^3} +$$

$$\pi \left( \frac{139}{144} - \frac{4 \text{Log}[2]}{9} + \frac{5}{216} \right) \left( 1 - \frac{1}{n^2} \right) \frac{\delta[L, 1] mr[mn, me]^3}{me^3};$$

$$B72[n_, L_, mn_, me_] = \left( -\frac{139}{48} + \frac{4 \text{Log}[2]}{3} - \frac{5}{72} \right) \pi \frac{\delta[L, \theta] mr[mn, me]^3}{me^3};$$

(\*Two photon correction Eq20\*)

$$E4[n_, L_, J_, \alpha_, mn_, me_] = \left( \frac{\alpha}{\pi} \right)^2 \frac{(Z \alpha)^4}{n^3} me c^2 \left( B40[L, J, mn, me] + B50[L, J, mn, me] (Z \alpha) + \right.$$

$$B63[L, mn, me] (Z \alpha)^2 \text{Log} \left[ \frac{me/mr[mn, me]}{(Z \alpha)^2} \right]^3 +$$

$$B62[n, L, mn, me] (Z \alpha)^2 \text{Log} \left[ \frac{me/mr[mn, me]}{(Z \alpha)^2} \right]^2 +$$

$$B61[n, L, J, mn, me] (Z \alpha)^2 \text{Log} \left[ \frac{me/mr[mn, me]}{(Z \alpha)^2} \right] +$$

$$B60[n, L, J] \frac{(Z \alpha)^2 mr[mn, me]^3}{me^3} +$$

$$B71[n, L, mn, me] (Z \alpha)^3 \text{Log} \left[ \frac{me/mr[mn, me]}{(Z \alpha)^2} \right] +$$

$$B72[n, L, mn, me] (Z \alpha)^3 \text{Log} \left[ \frac{me/mr[mn, me]}{(Z \alpha)^2} \right]^2 \Big);$$

(\* type u0 correlated part of  $\delta E4$  \*)

$$\delta E4a[n_, L_, J_, \alpha_, mn_, me_] = \left( \frac{\alpha}{\pi} \right)^2 \frac{(Z \alpha)^4}{n^3} me c^2 \delta B50[L, J, mn, me] (Z \alpha);$$

(\* type un uncorrelated part of  $\delta E4$ , drops out for the fine structure transitions \*)

$$\delta E4b[n_, L_, \alpha_, mn_, me_] = \left( \frac{\alpha}{\pi} \right)^2 \frac{(Z \alpha)^4}{n^3} me c^2 \frac{4 (Z \alpha)^2 mr[mn, me]^3}{3 me^3}$$

$$(\delta NS[n] \times \delta[L, \theta] + \delta NP[n] \times \delta[L, 1]) \text{Log} \left[ \frac{me/mr[mn, me]}{(Z \alpha)^2} \right];$$

(\* type u0 correlated part of  $\delta E4$ , for the fine structure this part is treated as uncor

$$\delta E4c[n_, L_, J_, \alpha_, mn_, me_] = \left( \frac{\alpha}{\pi} \right)^2 \frac{(Z \alpha)^4}{n^3} me c^2 \delta B60u0[n, L, J] \frac{(Z \alpha)^2 mr[mn, me]^3}{me^3};$$

(\* type un uncorrelated part of  $\delta E4$  \*)

$$\delta E4d[n_, L_, J_, \alpha_, mn_, me_] = \left( \frac{\alpha}{\pi} \right)^2 \frac{(Z \alpha)^4}{n^3} me c^2 \delta B60un[n, L, J] \frac{(Z \alpha)^2 mr[mn, me]^3}{me^3};$$

(\* type u0 correlated part of  $\delta E4$  \*)

$$\delta E4e[n_, L_, J_, \alpha_, mn_, me_] = \left( \frac{\alpha}{\pi} \right)^2 \frac{(Z \alpha)^4}{n^3} me c^2 \pi \left( \frac{427}{36} - \frac{16}{3} \text{Log}[2] \right) \delta B711S$$

$$\frac{\delta[L, \theta] mr[mn, me]^3}{me^3} (Z \alpha)^3 \text{Log} \left[ \frac{me/mr[mn, me]}{(Z \alpha)^2} \right];$$

$$\delta E4[n_, L_, J_, \alpha_, mn_, me_] = \text{Sqrt} \left[ \delta E4a[n, L, J, \alpha, mn, me]^2 + \delta E4b[n, L, \alpha, mn, me]^2 + \right.$$

$$\delta E4c[n, L, J, \alpha, mn, me]^2 + \delta E4d[n, L, J, \alpha, mn, me]^2 + \delta E4e[n, L, J, \alpha, mn, me]^2 \Big];$$



## Three Photon Correction

```
(* functions used to compute three photon corrections*)

(* function for C40 coefficient *)
a4 = Sum[1/(2^i i^4), {i, 1, Infinity}];

C40[L_, J_, mn_, me_] = (
  -568 a4/9 + 85 Zeta[5]/24 - 121 pi^2 Zeta[3]/72 - 84071 Zeta[3]/2304 -
  71 Log[2]^4/27 - 239 pi^2 Log[2]^2/135 + 4787 pi^2 Log[2]/108 +
  (1591 pi^4/3240 - 252251 pi^2/9720 + 679441/93312) delta[L, 0] mr[mn, me]^3/me^3 +
  (
    -100 a4/3 + 215 Zeta[5]/24 - 83 pi^2 Zeta[3]/72 - 139 Zeta[3]/18 -
    25 Log[2]^4/18 + 25 pi^2 Log[2]^2/18 + 298 pi^2 Log[2]/9 + 239 pi^4/2160 -
    17101 pi^2/810 - 28259/5184
  ) (1 - delta[L, 0]) mr[mn, me]^2/((-1)^(J-L+1/2) (J+1/2) (2L+1) me^2);

C61[n_, L_, mn_, me_] = 2/n^2 (
  -1523/648 - 10 pi^2/27 + 3/2 pi^2 Log[2] - 9/4 Zeta[3] - 82/81
) delta[L, 1] mr[mn, me]^3/me^3;

C62[L_, mn_, me_] = -2/3 (
  -1523/648 - 10 pi^2/27 + 3/2 pi^2 Log[2] - 9/4 Zeta[3] - 82/81
) delta[L, 0] mr[mn, me]^3/me^3;

(* three photon corrections Eq24 *)
E6[n_, L_, J_, alpha_, mn_, me_] = (alpha/pi)^3 (Z alpha)^4/me^3 c^2 (
  C40[L, J, mn, me] +
  C61[n, L, mn, me] (Z alpha)^2 Log[me/mr[mn, me]/(Z alpha)^2] +
  C62[L, mn, me] (Z alpha)^2 Log[me/mr[mn, me]]^2);

(* type u0 correlated uncertainty contribution of C50 to delta E6 *)
deltaE6a[n_, L_, alpha_, mn_, me_] = (alpha/pi)^3 (Z alpha)^4/me^3 c^2 (Z alpha) 30 delta[L, 0];

(* type un correlated part of delta E6 *)
deltaE6b[n_, L_, alpha_, mn_, me_] = (alpha/pi)^3 (Z alpha)^4/me^3 c^2 10 delta[L, 0] (Z alpha)^2 Log[me/mr[mn, me]/(Z alpha)^2];

deltaE6c[n_, L_, alpha_, mn_, me_] = (alpha/pi)^3 (Z alpha)^4/me^3 c^2 (1 - delta[L, 0]) (Z alpha)^2;

deltaE6[n_, L_, alpha_, mn_, me_] = Sqrt[deltaE6a[n, L, alpha, mn, me]^2 + deltaE6b[n, L, alpha, mn, me]^2 + deltaE6c[n, L, alpha, mn, me]^2];
```

## Nuclear Size Effect

$$\lambda C = \frac{h}{2 \pi m_e c}$$

(\* nuclear size effects, Eq27, 28, 33, 38, 39 \*)

$$E4nucl[n_, L_, \alpha_, mn_, me_, Rn_] = \frac{2}{3} m_e c^2 \frac{(Z \alpha)^4}{n^3} \frac{mr[mn, me]^3}{me^3} \left(\frac{Rn}{\lambda C}\right)^2 \delta[L, \theta];$$

$$E5nucl[n_, L_, \alpha_, mn_, me_, Rn_] = -\frac{1}{3} m_e c^2 \left(\frac{mr[mn, me]}{me}\right)^3 \frac{(Z \alpha)^5}{n^3} \left(\frac{rpF}{\lambda C}\right)^3 \delta[L, \theta];$$

$$E6nucl[n_, L_, J_, \alpha_, mn_, me_, Rn_] = \left(\frac{mr[mn, me]}{me}\right)^3 \frac{(Z \alpha)^6}{n^3} m_e c^2 \left(\frac{Rn}{\lambda C}\right)^2$$

$$\left(-\frac{2}{3} \left(\frac{9}{4 n^2} - 3 - \frac{1}{n} + 2 \gamma - \text{Log}[n/2] + \psi[n] + \text{Log}\left[\frac{mr[mn, me]}{me} \frac{1.068497 \cdot 128 Rn}{\lambda C} (Z \alpha)\right]\right) \delta[L, \theta] +$$

$$\frac{1}{6} \left(1 - \frac{1}{n^2}\right) \delta[(-1)^{J-L+1/2} (J+1/2), 1] + \frac{h \cdot 0.393 \cdot 128 \cdot 10^3}{n^3} \delta[L, \theta] +$$

$$\frac{2}{3} \left(\frac{mr[mn, me]}{me}\right)^3 \frac{\alpha (Z \alpha)^5}{n^3} m_e c^2 \left(\frac{Rn}{\lambda C}\right)^2 (4 \text{Log}[2] - 5) \delta[L, \theta];$$

$$E7nucl[n_, L_, J_, \alpha_, mn_, me_, Rn_] = \frac{2}{3} \left(\frac{mr[mn, me]}{me}\right)^3 \frac{\alpha (Z \alpha)^6}{\pi n^3} m_e c^2 \left(\frac{Rn}{\lambda C}\right)^2$$

$$\left(-\frac{2}{3} \text{Log}[(Z \alpha)^{-2}]^2 + \text{Log}\left[\frac{mr[mn, me]}{me} \frac{Rn}{\lambda C}\right]^2\right) \delta[L, \theta] +$$

$$\frac{1}{6} \left(\frac{mr[mn, me]}{me}\right)^3 \frac{\alpha (Z \alpha)^6}{\pi n^3} m_e c^2 \left(\frac{Rn}{\lambda C}\right)^2$$

$$\left(\left(\left(1 - \frac{1}{n^2}\right) \frac{8}{9} \text{Log}[(Z \alpha)^{-2}] - \frac{8}{9} \text{Log}[2] + \frac{11}{27} + \delta[(-1)^{J-L+1/2} (J+1/2), 1] + 4NP[n]\right) \delta[L, 1];$$

$$Enucl[n_, L_, J_, \alpha_, mn_, me_, Rn_] = E4nucl[n, L, \alpha, mn, me, Rn] + E5nucl[n, L, \alpha, mn, me, Rn] + E6nucl[n, L, J, \alpha, mn, me, Rn] + E7nucl[n, L, J, \alpha, mn, me, Rn];$$

(\* type u0 correlated uncertainty for Enucl \*)

$$\delta E5nucl[n_, L_, \alpha_, mn_, me_, Rn_] = \frac{1}{3} \left(\frac{mr[mn, me]}{me}\right)^3 \frac{(Z \alpha)^5}{n^3} m_e c^2 \left(\frac{1}{\lambda C}\right)^3 rpF^2 \delta rpF \delta[L, \theta];$$

$$\delta E6nucl[n_, L_, J_, \alpha_, mn_, me_, Rn_] = \frac{h \cdot 0.393 \cdot 128 \cdot 10^3}{n^3} \delta[L, \theta];$$

$$\delta E7nucl[n_, L_, J_, \alpha_, mn_, me_, Rn_] = \frac{2}{3} \left(\frac{mr[mn, me]}{me}\right)^3 \frac{\alpha (Z \alpha)^6}{\pi n^3} m_e c^2 \left(\frac{Rn}{\lambda C}\right)^2 \text{Log}[(Z \alpha)^{-2}] \delta[L, \theta] +$$

$$\frac{1}{6} \left(\frac{mr[mn, me]}{me}\right)^3 \frac{\alpha (Z \alpha)^6}{\pi n^3} m_e c^2 \left(\frac{Rn}{\lambda C}\right)^2 \left(1 - \frac{1}{n^2}\right) (Z \alpha) \delta[L, 1];$$

$$\delta Enucl[n_, L_, J_, \alpha_, mn_, me_, Rn_] = \text{Sqrt}[\delta E5nucl[n, L, \alpha, mn, me, Rn]^2 + \delta E6nucl[n, L, J, \alpha, mn, me, Rn]^2 + \delta E7nucl[n, L, J, \alpha, mn, me, Rn]^2];$$

## Radiative Recoil Corrections

```
(*radiative recoil Eq.40*)
ERR[n_,L_,α_, mn_, me_] =  $\frac{mr[mn, me]^3}{me^2 mn} \frac{\alpha (Z \alpha)^5}{\pi^2 n^3} me c^2 \delta[L, \theta] \left( 6 \text{Zeta}[3] - 2 \pi^2 \text{Log}[2] + \frac{35 \pi^2}{36} - \frac{448}{27} + \frac{2}{3} \pi (Z \alpha) \text{Log}[(Z \alpha)^{-2}] \right);$ 

(* type u0 correlated uncertainty of δERR *)
δERRa[n_,L_,α_, mn_, me_] =  $10 \frac{mr[mn, me]^3}{me^2 mn} \frac{\alpha (Z \alpha)^5}{\pi^2 n^3} me c^2 \delta[L, \theta] (Z \alpha) \text{Log}[(Z \alpha)^{-2}];$ 

(* type un uncorrelated uncertainty of δERR *)
δERRb[n_,L_,α_, mn_, me_] =  $\frac{mr[mn, me]^3}{me^2 mn} \frac{\alpha (Z \alpha)^5}{\pi^2 n^3} me c^2 \delta[L, \theta] (Z \alpha) \text{Log}[(Z \alpha)^{-2}];$ 
δERR[n_,L_,α_, mn_, me_] =  $\text{Sqrt}[\deltaERRa[n, L, \alpha, mn, me]^2 + \deltaERRb[n, L, \alpha, mn, me]^2];$ 
```

## Nucleus Self Energy

```
(*nucleus self energy Eq.42*)
(*added 5/6 from https://doi.org/10.1103/PhysRevA.52.1079, Eq. 61, but ONLY FOR MUONIUM!*)
ESEN[n_,L_,J_,α_, mn_, me_] =  $\frac{mr[mn, me]^3}{mn^2} \frac{4 Z^2 \alpha (Z \alpha)^4}{3 \pi n^3} c^2 \left( \left( \frac{5}{6} + \text{Log}\left[ \frac{mn}{mr[mn, me] (Z \alpha)^2} \right] \right) \delta[L, \theta] - \text{Ink0}[n, L] \right);$ 

(* type u0 correlated uncertainty of δESEN from CODATA*)
δESEN[n_,L_,α_, mn_, me_] =  $\frac{mr[mn, me]^3}{mn^2} \frac{4 Z^2 \alpha (Z \alpha)^4}{3 \pi n^3} c^2 \left( \frac{1}{2} \delta[L, \theta] \right);$ 
```

## Off-Diagonal HFS shift

```
(*taken from https://doi.org/10.1002/andp.201800324*)
e = 1.602176634 × 10-19;
mp = 1.67262192369 × 10-27;

mun = e / (2*mp);
mue[muX_] = muX * mun;

ERECHFS[n_,L_,J_,F_,α_,mn_, me_, muX_] =
 $me c^2 \frac{me^2}{mp^2} \frac{\alpha^2 (Z \alpha)^2}{n^3} \frac{mue[muX]^2}{mun^2} \frac{2 F(F+1)}{81} (-1)^{J+1/2} \delta[L, 1];$ 
```

## Results

```

(* Electron *)
mele = 9.1093837015 * 10-31 ;
δmele = 0; (*0.0000000028 * 10-31*);

(* Proton *)
mp = 1.67262192369 * 10-27;
δmp = 0.0000000051 * 10-27;

(* Muon*)
mu = 1.883531627 * 10-28;
δmu = 0.000000042 * 10-28;

mX = mu;
δmX = δmu;

mXe = mele;
δmXe = δmele;

RX = RpCODATA;
δRX = 0; (*δRpCODATA*);

muProtonCODATA = 1.41060679736 * 10-26; (*proton magnetic moment*)
δmuProtonCODATA = 0.0000000060 * 10-26;

muMuonCODATA = -4.49044830 * 10-26; (*muon magnetic moment*)
δmuMuonCODATA = 0.00000010 * 10-26;

muMagnetonCODATA = 5.0507837461 * 10-27; (*nuclear magneton*)
δmuMagnetonCODATA = 0.000000015 * 10-27;

momentX = muMuonCODATA / muMagnetonCODATA;
δmomentX = momentX * Sqrt[(δmuMuonCODATA/muMuonCODATA)2 +
                          (δmuMagnetonCODATA/muMagnetonCODATA)2];

(*adding up terms*)
EE[n_,L_,J_,α_, mn_, me_, Rn_, F_, muX_] =
eM[n,J,α,mn,me] + EBG[n,L,J,α,mn,me] + ES[n,L,α,mn,me] + ER[n,L,J,α,mn,me] +
E2SE[n,L,J,α,mn,me] + E2VP[n,L,J,α,mn,me] + E2μVP[n,L,α,mn,me] + E2hadVP[n,L,α,mn,me] +
E4[n,L,J,α,mn,me] + E6[n,L,J,α,mn,me] + ERR[n,L,α,mn,me] + ESEN[n,L,J,α,mn,me] +
ERECHFS[n,L,J,F,α,mn,me, muX];

(*off-diag HFS not included in error yet*)
δEE[n_,L_,J_,α_,mn_, me_, Rn_, δα_,δmn_,δme_,δRn_, F_, muX_] =
Sqrt[δER[n,L,J,α,mn,me]2 + δE2SE[n,L,J,α,mn,me]2 + δE2hadVP[n,L,α,mn,me]2 +
      δE4[n,L,J,α,mn,me]2 + δE6[n,L,α,mn,me]2 + δEnucl[n,L,J,α,mn,me,Rn]2 +
      δERR[n,L,α,mn,me,Rn]2 + δESEN[n,L,J,α,mn,me,Rn]2 +
      (Derivative[0,0,0,1,0,0,0,0][EE][n,L,J,α,mn,me,Rn,muX] δα)2 +
      (Derivative[0,0,0,0,1,0,0,0,0][EE][n,L,J,α,mn,me,Rn,F,muX] δmn)2 +
      (Derivative[0,0,0,0,0,1,0,0,0][EE][n,L,J,α,mn,me,Rn,F,muX] δme)2 +
      (Derivative[0,0,0,0,0,0,1,0,0][EE][n,L,J,α,mn,me,Rn,F,muX] δRn)2];

```

```

(*EE[n_,L_,J_,α_]= +Enucl[n,L,J,α,mn,me,Rn]*)

(* transition frequencies *)

FF[n1_,L1_,J1_,n2_,L2_,J2_,α_, mn_, me_,Rn_, F_, muX_]=
EE[n2,L2,J2,α,mn,me,Rn,F,muX]-EE[n1,L1,J1,α,mn,me,Rn,F,muX];

(*off-diag HFS not included in error yet*)
δFF[n1_,L1_,J1_,n2_,L2_,J2_,α_, mn_, me_,Rn_,δα_,δmn_,δme_,δRn_, F_, muX_]=
If[L1≠L2 ∨ J1≠ J2 ,Sqrt[δER[n2,L2,J2,α,mn,me]^2+δER[n1,L1,J1,α,mn,me]^2+
δE2SE[n2,L2,J2,α,mn,me]^2+δE2SE[n1,L1,J1,α,mn,me]^2+δE2hadVP[n2,L2,α,mn,me]^2+
δE2hadVP[n1,L1,α,mn,me]^2+δE4[n2,L2,J2,α,mn,me]^2+δE4[n1,L1,J1,α,mn,me]^2+
δE6[n2,L2,α,mn,me]^2+δE6[n1,L1,α,mn,me]^2+δEnucl[n2,L2,J2,α,mn,me,Rn]^2+
δEnucl[n1,L1,J1,α,mn,me,Rn]^2+δERR[n2,L2,α,mn,me]^2+δERR[n1,L1,α,mn,me]^2+
δESEN[n2,L2,α,mn,me]^2+δESEN[n1,L1,α,mn,me]^2 +
(Derivative[0,0,0,1,0,0,0,0][EE][n2,L2,J2,α,mn,me,Rn,F,muX] δα-
Derivative[0,0,0,1,0,0,0,0][EE][n1,L1,J1,α,mn,me,Rn,F,muX] δα)^2+
(Derivative[0,0,0,0,1,0,0,0,0][EE][n2,L2,J2,α,mn,me,Rn,F,muX] δmn-
Derivative[0,0,0,0,1,0,0,0,0][EE][n1,L1,J1,α,mn,me,Rn,F,muX] δmn)^2+
(Derivative[0,0,0,0,0,1,0,0,0][EE][n2,L2,J2,α,mn,me,Rn,F,muX] δme-
Derivative[0,0,0,0,0,1,0,0,0][EE][n1,L1,J1,α,mn,me,Rn,F,muX] δme)^2+
(Derivative[0,0,0,0,0,0,1,0,0][EE][n2,L2,J2,α,mn,me,Rn,F,muX] δRn-
Derivative[0,0,0,0,0,0,1,0,0][EE][n1,L1,J1,α,mn,me,Rn,F,muX] δRn)^2],
Sqrt[(δER[n2,L2,J2,α,mn,me]-δER[n1,L1,J1,α,mn,me])^2+δE2SE[n2,L2,J2,α,mn,me]^2+
δE2SE[n1,L1,J1,α,mn,me]^2+(δE2hadVP[n2,L2,α,mn,me]-δE2hadVP[n1,L1,α,mn,me])^2+
(δE4a[n2,L2,J2,α,mn,me]-δE4a[n1,L1,J1,α,mn,me])^2+δE4b[n2,L2,α,r]^2+
δE4b[n1,L1,α,mn,me]^2+(δE4c[n2,L2,J2,α,mn,me]-δE4c[n1,L1,J1,α,mn,me])^2+
δE4d[n2,L2,J2,α,mn,me]^2+δE4d[n1,L1,J1,α,mn,me]^2+δE4e[n2,L2,J2,α,mn,me]^2+
δE4e[n1,L1,J1,α,mn,me]^2+(δE6a[n2,L2,α,mn,me]-δE6a[n1,L1,α,mn,me])^2+
δE6b[n2,L2,α,mn,me]^2+δE6b[n1,L1,α,mn,me]^2+(δEnucl[n2,L2,J2,α,mn,me,Rn]-
δEnucl[n1,L1,J1,α,mn,me,Rn])^2+(δERRa[n2,L2,α,mn,me]-δERRa[n1,L1,α,mn,me])^2+
δERRb[n2,L2,α,mn,me]^2+δERRb[n1,L1,α,mn,me]^2+
(δESEN[n2,L2,α,mn,me]-δESEN[n1,L1,α,mn,me])^2+
(Derivative[0,0,0,1,0,0,0,0][EE][n2,L2,J2,α,mn,me,Rn,F,muX] δα-
Derivative[0,0,0,1,0,0,0,0][EE][n1,L1,J1,α,mn,me,Rn,F,muX] δα)^2+
(Derivative[0,0,0,0,1,0,0,0,0][EE][n2,L2,J2,α,mn,me,Rn,F,muX] δmn-
Derivative[0,0,0,0,1,0,0,0,0][EE][n1,L1,J1,α,mn,me,Rn,F,muX] δmn)^2+
Derivative[0,0,0,0,0,1,0,0,0][EE][n2,L2,J2,α,mn,me,Rn,F,muX] δme-
Derivative[0,0,0,0,0,1,0,0,0][EE][n1,L1,J1,α,mn,me,Rn,F,muX] δme)^2+
(Derivative[0,0,0,0,0,0,1,0,0][EE][n2,L2,J2,α,mn,me,Rn,F,muX] δRn-
Derivative[0,0,0,0,0,0,1,0,0][EE][n1,L1,J1,α,mn,me,Rn,F,muX] δRn)^2];

(* transition frequency H 2P_1/2-2S_1/2 *)
Print[IntegerPart[FF[2,1,1/2,2,0,1/2,αCODATA,mX,mXe,RX,1/2,momentX]/(h)]," Hz"]
Print[IntegerPart[δFF[2,0,1/2,2,1,3/2,αCODATA,mX,mXe,RX,δαCODATA,δmX,δmXe,δRX,1/2,momentX]
/(h)]," Hz"] (*prints LS uncertainty*)

```

1 047 497 966 Hz

1811 Hz



# Bibliography

- [1] S. Weinberg. A model of leptons. *Phys. Rev. Lett.*, 19:1264–1266, 1967. doi:10.1103/PhysRevLett.19.1264.
- [2] A. Salam. Weak and Electromagnetic Interactions. *Conf. Proc. C*, 680519:367–377, 1968. doi:10.1142/9789812795915\_0034.
- [3] S. L. Glashow. The renormalizability of vector meson interactions. *Nuclear Physics*, 10:107–117, 1959. ISSN 0029-5582. doi:https://doi.org/10.1016/0029-5582(59)90196-8.
- [4] G. Arnison, A. Astbury, et al. Experimental observation of isolated large transverse energy electrons with associated missing energy at  $s=540$  GeV. *Physics Letters B*, 122(1):103–116, 1983. ISSN 0370-2693. doi:https://doi.org/10.1016/0370-2693(83)91177-2.
- [5] M. Banner, R. Battiston, et al. Observation of single isolated electrons of high transverse momentum in events with missing transverse energy at the CERN pp collider. *Physics Letters B*, 122(5):476–485, 1983. ISSN 0370-2693. doi:https://doi.org/10.1016/0370-2693(83)91605-2.
- [6] F. Abe, H. Akimoto, et al. Observation of top quark production in  $\bar{p}p$  collisions with the collider detector at Fermilab. *Phys. Rev. Lett.*, 74:2626–2631, 1995. doi:10.1103/PhysRevLett.74.2626.
- [7] K. Kodama, N. Ushida, et al. Observation of tau neutrino interactions. *Physics Letters B*, 504(3):218–224, 2001. ISSN 0370-2693. doi:https://doi.org/10.1016/S0370-2693(01)00307-0.
- [8] G. Aad, T. Abajyan, and B. Abbott. Observation of a new particle in the search for the Standard Model Higgs boson with the ATLAS detector at the LHC. *Physics Letters B*, 716(1):1–29, 2012. ISSN 0370-2693. doi:https://doi.org/10.1016/j.physletb.2012.08.020.
- [9] D. J. Griffiths. Introduction to elementary particles; 2nd rev. version. Physics textbook. Wiley, New York, NY, 2008.
- [10] V. Trimble. Existence and nature of dark matter in the Universe. *Annual Review of Astronomy and Astrophysics*, 25(1):425–472, 1987. doi:10.1146/annurev.aa.25.090187.002233.
- [11] B. Schwarzschild. Very distant supernovae suggest that the cosmic expansion is speeding up. *Physics Today*, 51(6):17–19, 1998. doi:10.1063/1.882267.
- [12] Y. Fukuda, T. Hayakawa, et al. Evidence for oscillation of atmospheric neutrinos. *Phys. Rev. Lett.*, 81:1562–1567, 1998. doi:10.1103/PhysRevLett.81.1562.

- [13] G. Lemaitre. A Homogeneous Universe of Constant Mass and Growing Radius Accounting for the Radial Velocity of Extragalactic Nebulae. *Annales Soc. Sci. Bruxelles A*, 47:49–59, 1927. doi:10.1007/s10714-013-1548-3.
- [14] L. Canetti, M. Drewes, and M. Shaposhnikov. Matter and antimatter in the Universe. *New Journal of Physics*, 14(9):095012, 2012. doi:10.1088/1367-2630/14/9/095012.
- [15] A. D. Sakharov. Violation of CP invariance, C asymmetry, and baryon asymmetry of the Universe. *Soviet Physics Uspekhi*, 34(5):392–393, 1991. doi:10.1070/pu1991v034n05abeh002497.
- [16] J. H. Christenson, J. W. Cronin, V. L. Fitch, and R. Turlay. Evidence for the  $2\pi$  decay of the  $K_2^0$  meson. *Phys. Rev. Lett.*, 13:138–140, 1964. doi:10.1103/PhysRevLett.13.138.
- [17] V. Fanti, A. Lai, et al. A new measurement of direct CP violation in two pion decays of the neutral kaon. *Physics Letters B*, 465(1):335–348, 1999. ISSN 0370-2693. doi:https://doi.org/10.1016/S0370-2693(99)01030-8.
- [18] A. Alavi-Harati, I. F. Albuquerque, et al. Observation of direct CP violation in  $K_{S,L} \rightarrow \pi\pi$  decays. *Phys. Rev. Lett.*, 83:22–27, 1999. doi:10.1103/PhysRevLett.83.22.
- [19] R. Aaij, C. Abellan Beteta, et al. First observation of CP violation in the decays of  $B_s^0$  mesons. *Phys. Rev. Lett.*, 110:221601, 2013. doi:10.1103/PhysRevLett.110.221601.
- [20] R. Aaij, C. Abellán Beteta, et al. Observation of CP violation in charm decays. *Phys. Rev. Lett.*, 122:211803, 2019. doi:10.1103/PhysRevLett.122.211803.
- [21] G. R. Farrar and M. E. Shaposhnikov. Baryon asymmetry of the Universe in the minimal standard model. *Phys. Rev. Lett.*, 70:2833–2836, 1993. doi:10.1103/PhysRevLett.70.2833.
- [22] O. W. Greenberg. CPT violation implies violation of Lorentz invariance. *Phys. Rev. Lett.*, 89:231602, 2002. doi:10.1103/PhysRevLett.89.231602.
- [23] R. Lehnert. CPT- and Lorentz-symmetry breaking: a review. <https://arxiv.org/abs/hep-ph/0611177>, 12 2006.
- [24] D. Colladay and V. A. Kostelecký. CPT violation and the standard model. *Phys. Rev. D*, 55:6760–6774, 1997. doi:10.1103/PhysRevD.55.6760.
- [25] D. Colladay and V. A. Kostelecký. Lorentz-violating extension of the standard model. *Phys. Rev. D*, 58:116002, 1998. doi:10.1103/PhysRevD.58.116002.
- [26] V. A. Kostelecký. Gravity, Lorentz violation, and the standard model. *Phys. Rev. D*, 69:105009, 2004. doi:10.1103/PhysRevD.69.105009.
- [27] V. A. Kostelecký and N. Russell. Data tables for Lorentz and CPT violation. *Rev. Mod. Phys.*, 83:11–31, 2011. doi:10.1103/RevModPhys.83.11.
- [28] D. Hanneke, S. Fogwell Hoogerheide, and G. Gabrielse. Cavity control of a single-electron quantum cyclotron: Measuring the electron magnetic moment. *Phys. Rev. A*, 83:052122, 2011. doi:10.1103/PhysRevA.83.052122.



- [29] T. Aoyama, M. Hayakawa, T. Kinoshita, and M. Nio. Tenth-order QED contribution to the electron  $g-2$  and an improved value of the fine structure constant. *Phys. Rev. Lett.*, 109:111807, 2012. doi:10.1103/PhysRevLett.109.111807.
- [30] L. Morel, Z. Yao, P. Cladé, and S. Guellati-Khélifa. Determination of the fine-structure constant with an accuracy of 81 parts per trillion. *Nature*, 588(7836):61–65, 2020. doi:10.1038/s41586-020-2964-7.
- [31] R. H. Parker, C. Yu, et al. Measurement of the fine-structure constant as a test of the standard model. *Science*, 360(6385):191–195, 2018. doi:10.1126/science.aap7706.
- [32] J. Bailey, W. Bartl, et al. Precision measurement of the anomalous magnetic moment of the muon. *Physics Letters B*, 28(4):287–290, 1968. ISSN 0370-2693. doi:https://doi.org/10.1016/0370-2693(68)90261-X.
- [33] J. Bailey, K. Borer, et al. Final report on the CERN muon storage ring including the anomalous magnetic moment and the electric dipole moment of the muon, and a direct test of relativistic time dilation. *Nuclear Physics B*, 150:1–75, 1979. ISSN 0550-3213. doi:https://doi.org/10.1016/0550-3213(79)90292-X.
- [34] G. W. Bennett, B. Bousquet, et al. Final report of the E821 muon anomalous magnetic moment measurement at BNL. *Phys. Rev. D*, 73:072003, 2006. doi:10.1103/PhysRevD.73.072003.
- [35] B. Abi, T. Albahri, et al. Measurement of the positive muon anomalous magnetic moment to 0.46 ppm. *Phys. Rev. Lett.*, 126:141801, 2021. doi:10.1103/PhysRevLett.126.141801.
- [36] J. Kawamura, S. Okawa, and Y. Omura. Current status and muon  $g - 2$  explanation of lepton portal dark matter. *JHEP*, 08:042, 2020. doi:10.1007/JHEP08(2020)042.
- [37] G. Arcadi, L. Calibbi, M. Fedele, and F. Mescia. Muon  $g - 2$  and B anomalies from dark matter. *Phys. Rev. Lett.*, 127:061802, 2021. doi:10.1103/PhysRevLett.127.061802.
- [38] G. Baur et al. Production of anti-hydrogen. *Phys. Lett. B*, 368:251–258, 1996. doi:10.1016/0370-2693(96)00005-6.
- [39] G. Blanford, D. C. Christian, et al. Observation of atomic anti-hydrogen. *Phys. Rev. Lett.*, 80:3037–3040, 1998. doi:10.1103/PhysRevLett.80.3037.
- [40] P. Belochitskii, J. Bossler, et al. Commissioning and first operation of the Antiproton Decelerator (AD). volume 1, pages 580 – 584 vol.1. 2001. doi:10.1109/PAC.2001.987574.
- [41] M. Amoretti et al. Production and detection of cold anti-hydrogen atoms. *Nature*, 419:456–459, 2002. doi:10.1038/nature01096.
- [42] G. Gabrielse et al. Background-Free Observation of Cold Antihydrogen with Field-Ionization Analysis of Its States. *Phys. Rev. Lett.*, 89:213401, 2002. doi:10.1103/PhysRevLett.89.213401.
- [43] G. B. Andresen et al. Trapped antihydrogen. *Nature*, 468:673–676, 2010. doi:10.1038/nature09610.

- [44] G. B. Andresen et al. Confinement of antihydrogen for 1000 seconds. *Nature Phys.*, 7:558–564, 2011. doi:10.1038/nphys2025.
- [45] C. Carli, W. Bartmann, et al. Extra Low ENergy Antiproton ring ELENA: From the Conception to the Implementation Phase. In 5th International Particle Accelerator Conference, page TUOAA03. 2014. doi:10.18429/JACoW-IPAC2014-TUOAA03.
- [46] M. Ahmadi et al. Observation of the 1S-2S transition in trapped antihydrogen. *Nature*, 541:506–510, 2016. doi:10.1038/nature21040.
- [47] M. Ahmadi et al. Observation of the hyperfine spectrum of antihydrogen. *Nature*, 548(7665):66–69, 2017. doi:10.1038/nature23446.
- [48] M. Ahmadi et al. Observation of the 1S–2P Lyman- $\alpha$  transition in antihydrogen. *Nature*, 561(7722):211–215, 2018. doi:10.1038/s41586-018-0435-1.
- [49] M. Ahmadi et al. Investigation of the fine structure of antihydrogen. *Nature*, 578(7795):375–380, 2020. doi:10.1038/s41586-020-2006-5. [Erratum: *Nature* 594, E5 (2021)].
- [50] C. J. Baker et al. Laser cooling of antihydrogen atoms. *Nature*, 592(7852):35–52, 2021. doi:10.1038/s41586-021-03289-6.
- [51] E. Widmann et al. Measurement of the hyperfine structure of antihydrogen in a beam. *Hyperfine Interact.*, 215(1-3):1–8, 2013. doi:10.1007/s10751-013-0809-6.
- [52] W. Bartmann, P. Belochitskii, et al. The ELENA facility. *Phil. Trans. Roy. Soc. Lond. A*, 376(2116):20170266, 2018. doi:10.1098/rsta.2017.0266.
- [53] A. Einstein. Die Grundlage der allgemeinen Relativitätstheorie. *Annalen der Physik*, 354(7):769–822, 1916. doi:https://doi.org/10.1002/andp.19163540702.
- [54] M. M. Nieto and T. Goldman. The arguments against antigravity and the gravitational acceleration of antimatter. *Physics Reports*, 205(5):221–281, 1991. ISSN 0370-1573. doi:https://doi.org/10.1016/0370-1573(91)90138-C.
- [55] C. Amole et al. Description and first application of a new technique to measure the gravitational mass of antihydrogen. *Nature Commun.*, 4:1785, 2013. doi:10.1038/ncomms2787.
- [56] M. Doser et al. Exploring the WEP with a pulsed cold beam of antihydrogen. *Class. Quant. Grav.*, 29:184009, 2012. doi:10.1088/0264-9381/29/18/184009.
- [57] C. Amsler et al. Pulsed production of antihydrogen. *Commun. Phys.*, 4(1):19, 2021. doi:10.1038/s42005-020-00494-z.
- [58] W. A. Bertsche. Prospects for comparison of matter and antimatter gravitation with ALPHA-g. *Philosophical Transactions of the Royal Society A: Mathematical, Physical and Engineering Sciences*, 376(2116):20170265, 2018. doi:10.1098/rsta.2017.0265.
- [59] G. Chardin et al. Proposal to measure the Gravitational Behaviour of Antihydrogen at Rest. <http://cds.cern.ch/record/1386684>, 2011.
- [60] P. Crivelli, D. Cooke, and M. W. Heiss. Antiproton charge radius. *Phys. Rev. D*, 94:052008, 2016. doi:10.1103/PhysRevD.94.052008.

- [61] V. W. Hughes, D. W. McColm, K. Ziock, and R. Prepost. Formation of muonium and observation of its Larmor precession. *Phys. Rev. Lett.*, 5:63–65, 1960. doi:10.1103/PhysRevLett.5.63.
- [62] P. R. Bolton, A. Badertscher, et al. Observation of muonium in vacuum. *Phys. Rev. Lett.*, 47:1441–1444, 1981. doi:10.1103/PhysRevLett.47.1441.
- [63] A. C. Janissen, G. A. Beer, et al. Muonium production from fine silica powder. *Phys. Rev. A*, 42:161–169, 1990. doi:10.1103/PhysRevA.42.161.
- [64] W. Schwarz, V. Ebert, et al. Thermal muonium in vacuo from silica aerogels. *Journal of Non-Crystalline Solids*, 145:244–249, 1992. ISSN 0022-3093. doi:https://doi.org/10.1016/S0022-3093(05)80465-X.
- [65] W. Liu, M. G. Boshier, et al. High precision measurements of the ground state hyperfine structure interval of muonium and of the muon magnetic moment. *Phys. Rev. Lett.*, 82:711–714, 1999. doi:10.1103/PhysRevLett.82.711.
- [66] S. Nishimura et al. Rabi-oscillation spectroscopy of the hyperfine structure of muonium atoms. *Phys. Rev. A*, 104(2):L020801, 2021. doi:10.1103/PhysRevA.104.L020801.
- [67] K. S. Tanaka, M. Iwasaki, et al. Development of microwave cavities for measurement of muonium hyperfine structure at J-PARC. *Progress of Theoretical and Experimental Physics*, 2021(5), 04 2021. ISSN 2050-3911. doi:10.1093/ptep/ptab047.
- [68] A. Badertscher, S. Dhawan, et al. Formation of muonium in the  $2s$  state and observation of the Lamb shift transition. *Phys. Rev. Lett.*, 52:914–917, Mar 1984. doi:10.1103/PhysRevLett.52.914.
- [69] C. J. Oram, J. M. Bailey, et al. Measurement of the Lamb shift in muonium. *Phys. Rev. Lett.*, 52:910–913, 1984. doi:10.1103/PhysRevLett.52.910.
- [70] K. A. Woodle, A. Badertscher, et al. Measurement of the Lamb shift in the  $n = 2$  state of muonium. *Phys. Rev. A*, 41:93–105, 1990. doi:10.1103/PhysRevA.41.93.
- [71] S. H. Kettell. Measurement of the  $2s_{1/2} - 2p_{3/2}$  fine structure interval in muonium. Ph.D. thesis, Yale University, 1990. doi:10.2172/6849854.
- [72] S. Chu, A. P. Mills, et al. Laser excitation of the muonium  $1s - 2s$  transition. *Phys. Rev. Lett.*, 60:101–104, 1988. doi:10.1103/PhysRevLett.60.101.
- [73] F. Maas, B. Braun, et al. A measurement of the  $1s - 2s$  transition frequency in muonium. *Physics Letters A*, 187(3):247–254, 1994. ISSN 0375-9601. doi:https://doi.org/10.1016/0375-9601(94)90903-2.
- [74] V. Meyer, S. N. Bagayev, et al. Measurement of the  $1s - 2s$  energy interval in muonium. *Phys. Rev. Lett.*, 84:1136–1139, 2000. doi:10.1103/PhysRevLett.84.1136.
- [75] P. Crivelli. The Mu-MASS (muonium laser spectroscopy) experiment. *Hyperfine Interactions*, 239(1), 2018. ISSN 1572-9540. doi:10.1007/s10751-018-1525-z.
- [76] C. G. Parthey, A. Matveev, et al. Improved measurement of the hydrogen  $1s - 2s$  transition frequency. *Phys. Rev. Lett.*, 107:203001, 2011. doi:10.1103/PhysRevLett.107.203001.

- [77] S. Liu, X. Wu, et al. Frequency–temperature effect of hydrogen maser: Theoretical analysis and temperature control optimization. *Review of Scientific Instruments*, 91(7):073201, 2020. doi:10.1063/5.0008072.
- [78] N. Bezginov, T. Valdez, et al. A measurement of the atomic hydrogen Lamb shift and the proton charge radius. *Science*, 365(6457):1007–1012, 2019. doi:10.1126/science.aau7807.
- [79] E. Widmann, M. Diermaier, et al. Measurement of the hyperfine structure of antihydrogen in a beam. *Hyperfine Interactions*, 215(1-3):18, 2013. ISSN 1572-9540. doi:10.1007/s10751-013-0809-6.
- [80] J. Walz and T. W. Hansch. A proposal to measure antimatter gravity using ultracold antihydrogen atoms. *Gen. Rel. Grav.*, 36:561–570, 2004. doi:10.1023/B:GERG.0000010730.93408.87.
- [81] A. Husson, B. Kim, et al. A pulsed high-voltage decelerator system to deliver low-energy antiprotons. *Nuclear Instruments and Methods in Physics Research Section A: Accelerators, Spectrometers, Detectors and Associated Equipment*, 1002:165245, 2021. ISSN 0168-9002. doi:https://doi.org/10.1016/j.nima.2021.165245.
- [82] S. Niang et al. Accumulation of Positrons from a LINAC Based Source. *Acta Phys. Polon. A*, 137:164–166, 2020. doi:10.12693/APhysPolA.137.164.
- [83] B. Kim, J. Choi, et al. Performance of the time-of-flight detector for a measurement of free fall of antihydrogen at the GBAR experiment. *Nuclear Instruments and Methods in Physics Research Section A: Accelerators, Spectrometers, Detectors and Associated Equipment*, 973:164162, 2020. ISSN 0168-9002. doi:https://doi.org/10.1016/j.nima.2020.164162.
- [84] D. Banerjee. Resistive Multiplexed Micromegas Detectors to Search for Dark Sector Physics and Test the Weak Equivalence Principle for Anti-Matter at CERN. Ph.D. thesis, Sussex U., 2017. doi:10.3929/ethz-b-000231250.
- [85] O. Rousselle, P. Cladé, et al. Analysis of the timing of freely falling antihydrogen. <https://arxiv.org/abs/2111.02815>, 2021.
- [86] O. Rousselle, P. Cladé, et al. Improving the statistical analysis of anti-hydrogen free fall by using near edge events. <https://arxiv.org/abs/2111.06722>, 2021.
- [87] G. Dufour, R. Guérout, et al. Quantum reflection of antihydrogen in the GBAR experiment. *International Journal of Modern Physics: Conference Series*, 30:1460265, 2014. doi:10.1142/S2010194514602658.
- [88] P.-P. Crépin, C. Christen, et al. Quantum interference test of the equivalence principle on antihydrogen. *Phys. Rev. A*, 99:042119, 2019. doi:10.1103/PhysRevA.99.042119.
- [89] C. Delaunay, B. Ohayon, and Y. Soreq. Towards an independent determination of muon  $g - 2$  from muonium spectroscopy. *Phys. Rev. Lett.*, 127:251801, Dec 2021. doi:10.1103/PhysRevLett.127.251801.

- [90] T. Prokscha, E. Morenzoni, et al. The new muE4 beam at PSI: A hybrid-type large acceptance channel for the generation of a high intensity surface-muon beam. *Nucl. Instrum. Meth. A*, 595:317–331, 2008. doi:10.1016/j.nima.2008.07.081.
- [91] E. Morenzoni, T. Prokscha, et al. Characteristics of condensed gas moderators for the generation of very slow polarized muons. *Journal of Applied Physics*, 81(8):3340–3347, 1997. doi:10.1063/1.365027.
- [92] M. W. Heiss. Precision Spectroscopy of Positronium Using a Pulsed Slow Positron Beam. Ph.D. thesis, Zurich, ETH, 2021. doi:10.3929/ethz-b-000477081.
- [93] Z. Burkley, L. de Sousa Borges, et al. Stable high power deep-UV enhancement cavity in ultra-high vacuum with fluoride coatings. *Opt. Express*, 29(17):27450–27459, 2021. doi:10.1364/OE.432552.
- [94] B. Radics, G. Janka, et al. Double hit reconstruction in large area multiplexed detectors. *Review of Scientific Instruments*, 90(9):093305, 2019. doi:10.1063/1.5109315.
- [95] Y. Giomataris, P. Rebourgeard, J. Robert, and G. Charpak. Micromegas: a high-granularity position-sensitive gaseous detector for high particle-flux environments. *Nuclear Instruments and Methods in Physics Research Section A: Accelerators, Spectrometers, Detectors and Associated Equipment*, 376(1):29–35, 1996. ISSN 0168-9002. doi:https://doi.org/10.1016/0168-9002(96)00175-1.
- [96] B. Radics, Y. Nagata, et al. The ASACUSA Micromegas tracker: A cylindrical, bulk Micromegas detector for antimatter research. *Review of Scientific Instruments*, 86(8):083304, 2015. doi:10.1063/1.4927685.
- [97] D. Banerjee, V. Burtsev, et al. Performance of multiplexed XY resistive Micromegas detectors in a high intensity beam. *Nuclear Instruments and Methods in Physics Research Section A: Accelerators, Spectrometers, Detectors and Associated Equipment*, 881:72–81, 2018. ISSN 0168-9002. doi:https://doi.org/10.1016/j.nima.2017.10.067.
- [98] S. Bouteille, D. Attié, et al. A Micromegas-based telescope for muon tomography: The WatTo experiment. *Nuclear Instruments and Methods in Physics Research Section A: Accelerators, Spectrometers, Detectors and Associated Equipment*, 834:223–228, 2016. ISSN 0168-9002. doi:https://doi.org/10.1016/j.nima.2016.08.002.
- [99] A. Koulouris. ATLAS New Small Wheel Micromegas production and performance. *Nuclear Instruments and Methods in Physics Research Section A: Accelerators, Spectrometers, Detectors and Associated Equipment*, 958:162757, 2020. ISSN 0168-9002. doi:https://doi.org/10.1016/j.nima.2019.162757. Proceedings of the Vienna Conference on Instrumentation 2019.
- [100] S. Procureur et al. The M-Cube project: Large area Micromegas for homeland security. In MPGD 2015 and RD51 Collaboration meeting. 2015.
- [101] K. Nikolopoulos, P. Bhattacharya, V. Chernyatin, and R. Veenhof. Electron transparency of a Micromegas mesh. *Journal of Instrumentation*, 6(06):P06011–P06011, 2011. doi:10.1088/1748-0221/6/06/p06011.

- [102] T. Alexopoulos, J. Burnens, et al. A spark-resistant bulk-Micromegas chamber for high-rate applications. *Nuclear Instruments and Methods in Physics Research Section A: Accelerators, Spectrometers, Detectors and Associated Equipment*, 640(1):110–118, 2011. ISSN 0168-9002. doi:<https://doi.org/10.1016/j.nima.2011.03.025>.
- [103] O. Şahin, İ. Tapan, E. N. Oezmutlu, and R. Veenhof. Penning transfer in argon-based gas mixtures. 5(05):P05002–P05002, 2010. doi:[10.1088/1748-0221/5/05/p05002](https://doi.org/10.1088/1748-0221/5/05/p05002).
- [104] F. Kuger. Signal formation processes in Micromegas detectors and quality control for large size detector construction for the ATLAS New Small Wheel. <https://arxiv.org/abs/1708.01624>, 2017.
- [105] M. P. Titov. Gaseous Detectors: Recent developments and applications. <https://arxiv.org/abs/1008.3736>, 2010.
- [106] J. Bortfeldt. Development of floating strip Micromegas detectors. Ph.D. thesis, 2014. doi:[10.5282/edoc.16972](https://doi.org/10.5282/edoc.16972).
- [107] F. Iguaz, S. Andriamonje, et al. New developments in Micromegas microbulk detectors. *Physics Procedia*, 37:448–455, 2012. ISSN 1875-3892. doi:<https://doi.org/10.1016/j.phpro.2012.02.392>. Proceedings of the 2nd International Conference on Technology and Instrumentation in Particle Physics (TIPP 2011).
- [108] M. Vandenbroucke. Optimisation of gas composition for Micromegas of the ATLAS experiment. 2019. doi:[10.13140/RG.2.2.16706.09926](https://doi.org/10.13140/RG.2.2.16706.09926).
- [109] S. Procureur, R. Dupré, and S. Aune. Genetic multiplexing and first results with a 50x50 cm<sup>2</sup> Micromegas. *Nuclear Instruments and Methods in Physics Research Section A: Accelerators, Spectrometers, Detectors and Associated Equipment*, 729:888–894, 2013. ISSN 0168-9002. doi:<https://doi.org/10.1016/j.nima.2013.08.071>.
- [110] S. Agostinelli, J. Allison, et al. Geant4—a simulation toolkit. *Nuclear Instruments and Methods in Physics Research Section A Accelerators Spectrometers Detectors and Associated Equipment*, 506:250, 2003. doi:[10.1016/S0168-9002\(03\)01368-8](https://doi.org/10.1016/S0168-9002(03)01368-8).
- [111] S. Procureur and D. Attié. Development of high-definition muon telescopes and muography of the great pyramid. *Comptes Rendus Physique*, 20(6):521–528, 2019. ISSN 1631-0705. doi:<https://doi.org/10.1016/j.crhy.2019.09.003>.
- [112] S. Procureur. Micromegas detectors for the GBAR tracker. GBAR internal note, manuscript in preparation.
- [113] C. Flouzat et al. Dream: a 64-channel Front-end Chip with Analogue Trigger Latency Buffer for the Micromegas Tracker of the Clas12 Experiment. In TWEPP conference. 2014.
- [114] D. Calvetti, S. Morigi, L. Reichel, and F. Sgallari. Tikhonov regularization and the L-curve for large discrete ill-posed problems. *Journal of Computational and Applied Mathematics*, 123(1):423–446, 2000. ISSN 0377-0427. doi:[https://doi.org/10.1016/S0377-0427\(00\)00414-3](https://doi.org/10.1016/S0377-0427(00)00414-3). Numerical Analysis 2000. Vol. III: Linear Algebra.

- [115] A. Doicu, T. Trautmann, and F. Schreier. Tikhonov regularization for linear problems, pages 39–106. Springer Berlin Heidelberg, Berlin, Heidelberg, 2010. ISBN 978-3-642-05439-6. doi:10.1007/978-3-642-05439-6\_3.
- [116] M. Hatlo, F. James, et al. Developments of mathematical software libraries for the LHC experiments. *IEEE Transactions on Nuclear Science*, 52(6):2818–2822, 2005. doi:10.1109/TNS.2005.860152.
- [117] G. Guennebaud, B. Jacob, et al. Eigen v3. <http://eigen.tuxfamily.org>, 2010.
- [118] J. R. Sapirstein and D. R. Yennie. THEORY OF HYDROGENIC BOUND STATES. *Adv. Ser. Direct. High Energy Phys.*, 7:560–672, 1990. doi:10.1142/9789814503273\_0012.
- [119] J. J. Thomson. XI. Cathode rays. *The London, Edinburgh, and Dublin Philosophical Magazine and Journal of Science*, 44(269):293–316, 1897. doi:10.1080/14786449708621070.
- [120] E. Rutherford. LXXIX. The scattering of  $\alpha$  and  $\beta$  particles by matter and the structure of the atom. *The London, Edinburgh, and Dublin Philosophical Magazine and Journal of Science*, 21(125):669–688, 1911. doi:10.1080/14786440508637080.
- [121] N. Bohr. I. On the constitution of atoms and molecules. *The London, Edinburgh, and Dublin Philosophical Magazine and Journal of Science*, 26(151):1–25, 1913. doi:10.1080/14786441308634955.
- [122] J. R. Rydberg. XXXIV. On the structure of the line-spectra of the chemical elements. *The London, Edinburgh, and Dublin Philosophical Magazine and Journal of Science*, 29(179):331–337, 1890. doi:10.1080/14786449008619945.
- [123] A. Sommerfeld. Zur Quantentheorie der Spektrallinien. *Annalen der Physik*, 356(17):1–94, 1916. doi:https://doi.org/10.1002/andp.19163561702.
- [124] W. Gerlach and O. Stern. Über die Richtungsquantelung im Magnetfeld. *Annalen der Physik*, 379(16):673–699, 1924. doi:https://doi.org/10.1002/andp.19243791602.
- [125] F. Weinert. Wrong theory – right experiment: The significance of the Stern-Gerlach experiments. *Studies in History and Philosophy of Science Part B: Studies in History and Philosophy of Modern Physics*, 26(1):75–86, 1995. ISSN 1355-2198. doi:https://doi.org/10.1016/1355-2198(95)00002-B.
- [126] S. A. Goudschmidt and G. H. Uhlenbeck. Spinning electrons and the structure of spectra. *Nature*, 117:264–265, 1926. doi:10.1038/117264a0.
- [127] E. Schrödinger. An undulatory theory of the mechanics of atoms and molecules. *Phys. Rev.*, 28:1049–1070, 1926. doi:10.1103/PhysRev.28.1049.
- [128] P. A. M. Dirac and R. H. Fowler. The quantum theory of the electron. *Proceedings of the Royal Society of London. Series A, Containing Papers of a Mathematical and Physical Character*, 117(778):610–624, 1928. doi:10.1098/rspa.1928.0023.
- [129] W. V. Houston. A new method of analysis of the structure of  $H_{\alpha}$  and  $D_{\alpha}$ . *Phys. Rev.*, 51:446–449, Mar 1937. doi:10.1103/PhysRev.51.446.
- [130] R. C. Williams. The fine structures of  $H_{\alpha}$  and  $D_{\alpha}$  under varying discharge conditions. *Phys. Rev.*, 54:558–567, Oct 1938. doi:10.1103/PhysRev.54.558.

- [131] W. E. Lamb and R. C. Retherford. Fine structure of the hydrogen atom by a microwave method. *Phys. Rev.*, 72:241–243, 1947. doi:10.1103/PhysRev.72.241.
- [132] W. E. Lamb. Fine structure of the hydrogen atom. *Science*, 123(3194):439–442, 1956. doi:10.1126/science.123.3194.439.
- [133] S. Tomonaga. On a Relativistically Invariant Formulation of the Quantum Theory of Wave Fields\*. *Progress of Theoretical Physics*, 1(2):27–42, 1946. ISSN 0033-068X. doi:10.1143/PTP.1.27.
- [134] R. T. Robiscoe and B. L. Cosens. Remeasurement of the Lamb shift in H,  $n = 2$ . *Phys. Rev. Lett.*, 17:69–72, 1966. doi:10.1103/PhysRevLett.17.69.
- [135] G. Newton, D. A. Andrews, P. J. Unsworth, and R. J. Blin-Stoyle. A precision determination of the Lamb shift in hydrogen. *Philosophical Transactions of the Royal Society of London. Series A, Mathematical and Physical Sciences*, 290(1373):373–404, 1979. doi:10.1098/rsta.1979.0004.
- [136] N. F. Ramsey. Experiments with separated oscillatory fields and hydrogen masers. *Rev. Mod. Phys.*, 62:541–552, 1990. doi:10.1103/RevModPhys.62.541.
- [137] S. R. Lundeen and F. M. Pipkin. Measurement of the Lamb shift in hydrogen,  $n = 2$ . *Phys. Rev. Lett.*, 46:232–235, 1981. doi:10.1103/PhysRevLett.46.232.
- [138] I. Angeli. The quest for the proton charge radius. <https://arxiv.org/abs/2103.17101>, 2021.
- [139] R. Pohl et al. The size of the proton. *Nature*, 466:213–216, 2010. doi:10.1038/nature09250.
- [140] A. Antognini, F. Nez, et al. Proton structure from the measurement of 2s-2p transition frequencies of muonic hydrogen. *Science*, 339(6118):417–420, 2013. doi:10.1126/science.1230016.
- [141] A. C. Vutha and E. A. Hessels. Frequency-offset separated oscillatory fields. *Phys. Rev. A*, 92:052504, 2015. doi:10.1103/PhysRevA.92.052504.
- [142] A. Marsman, M. Horbatsch, Z. A. Coriveau, and E. A. Hessels. Systematic effects important to separated-oscillatory-field measurements of the  $n = 2$  Lamb shift in atomic hydrogen. *Phys. Rev. A*, 98:012509, 2018. doi:10.1103/PhysRevA.98.012509.
- [143] W. Xiong, A. Gasparian, et al. A small proton charge radius from an electronproton scattering experiment. *Nature (London)*, 575(7781), 11 2019. doi:10.1038/s41586-019-1721-2.
- [144] A. Beyer, L. Maisenbacher, et al. The Rydberg constant and proton size from atomic hydrogen. *Science*, 358(6359):79–85, 2017. doi:10.1126/science.aah6677.
- [145] A. D. Brandt, S. F. Cooper, et al. Measurement of the  $2s_{1/2} - 8d_{5/2}$  transition in hydrogen. *Phys. Rev. Lett.*, 128:023001, Jan 2022. doi:10.1103/PhysRevLett.128.023001.
- [146] A. Grinin, A. Matveev, et al. Two-photon frequency comb spectroscopy of atomic hydrogen. *Science*, 370(6520):1061–1066, 2020. doi:10.1126/science.abc7776.



- [147] H. Fleurbaey, S. Galtier, et al. New measurement of the  $1s - 3s$  transition frequency of hydrogen: Contribution to the proton charge radius puzzle. *Phys. Rev. Lett.*, 120:183001, 2018. doi:10.1103/PhysRevLett.120.183001.
- [148] J.-P. Karr, D. Marchand, and E. Voutier. The proton size. *Nature Reviews Physics*, pages 1–14, 2020. doi:https://doi.org/10.1038/s42254-020-0229-x.
- [149] F. Allegrini, R. W. Ebert, and H. O. Funsten. Carbon foils for space plasma instrumentation. *Journal of Geophysical Research: Space Physics*, 121(5):3931–3950, 2016. doi:https://doi.org/10.1002/2016JA022570.
- [150] H. Rothard, C. Caraby, et al. Target-thickness-dependent electron emission from carbon foils bombarded with swift highly charged heavy ions. *Phys. Rev. A*, 51:3066–3078, 1995. doi:10.1103/PhysRevA.51.3066.
- [151] F. Allegrini, R. W. Ebert, G. Nicolaou, and G. Grubbs. Semi-empirical relationships for the energy loss and straggling of 1–50keV hydrogen ions passing through thin carbon foils. *Nuclear Instruments and Methods in Physics Research Section B: Beam Interactions with Materials and Atoms*, 359:115–119, 2015. ISSN 0168-583X. doi:https://doi.org/10.1016/j.nimb.2015.07.098.
- [152] M. Gonin, R. Kallenbach, and P. Bochler. Charge exchange of hydrogen atoms in carbon foils at 0.4–120 keV. *Review of Scientific Instruments*, 65(3):648–652, 1994. doi:10.1063/1.1145132.
- [153] K. Khaw, A. Antognini, et al. Geant4 simulation of the PSI LEM beam line: energy loss and muonium formation in thin foils and the impact of unmoderated muons on the  $\mu$ SR spectrometer. *Journal of Instrumentation*, 10(10):P10025–P10025, 2015. doi:10.1088/1748-0221/10/10/p10025.
- [154] M. J. Alguard and C. W. Drake. Stark beats in Lyman-series emission. *Phys. Rev. A*, 8:27–36, 1973. doi:10.1103/PhysRevA.8.27.
- [155] G. Gabrielse. Measurement of the  $n = 2$  density operator for hydrogen atoms produced by passing protons through thin carbon targets. *Phys. Rev. A*, 23:775–784, 1981. doi:10.1103/PhysRevA.23.775.
- [156] H. Garnir, Y. Baudinet-Robinet, P. Dumont, and A. Himdy. Measurement of the ratio of the  $2s$  to the  $2p$  populations for beam-foil excited hydrogen. *Zeitschrift für Physik D Atoms, Molecules and Clusters*, 14:45–49, 1989. doi:10.1007/BF01401342.
- [157] R. Tielert, H. H. Bukow, et al. Ionenstrahlspektroskopie mit Wasserstoffionen als Primärteilchen. *Zeitschrift für Physik*, 264(2):129–138, 1973. doi:10.1007/BF01398938.
- [158] P. H. Heckmann, H. H. Bukow, and R. Tielert. Relative Anfangsbesetzungszahlen der Zustände  $2p$  und  $3d$  folienangeregter Wasserstoffatome. *Zeitschrift für Physik*, 264(2):109–117, 1973. doi:10.1007/BF01398936.
- [159] B. Andresen, S. Hultberg, et al. A study of molecular effects in beam-foil spectroscopy. *Physica Scripta*, 19(4):335–338, 1979. doi:10.1088/0031-8949/19/4/007.
- [160] P. B. Kramer. RF spectroscopy on coherent populations using quantum beats. *Phys. Rev. Lett.*, 38:1021–1024, 1977. doi:10.1103/PhysRevLett.38.1021.

- [161] C. A. Fry. Measurement of the Lamb shift in muonium. Ph.D. thesis, University of British Columbia, 1985. doi:10.14288/1.0085236.
- [162] J. Bozek, J. Furst, et al. Production of excited atomic hydrogen and deuterium from  $H_2$  and  $D_2$  photodissociation. *Journal of Physics B: Atomic, Molecular and Optical Physics*, 39:4871, 2006. doi:10.1088/0953-4075/39/23/006.
- [163] M. M. Duncan and M. G. Menendez. Measurements of beam-foil electrons emitted near  $0^\circ$  from  $H^+$  and  $H_2^+$  on carbon in the energy range 0.175–1.0 MeV/amu. *Phys. Rev. A*, 13:566–571, 1976. doi:10.1103/PhysRevA.13.566.
- [164] W. Meckbach, N. Arista, and W. Brandt. Analysis of experimental velocity distributions of convoy electrons. *Physics Letters A*, 65(2):113–116, 1978. ISSN 0375-9601. doi:https://doi.org/10.1016/0375-9601(78)90588-1.
- [165] P. Focke, W. Meckbach, I. Nemirovsky, and G. Bernardi. Beam-foil convoy electron double differential distributions for 60–300 keV protons incident on carbon foils. *Nuclear Instruments and Methods in Physics Research Section B: Beam Interactions with Materials and Atoms*, 17(4):314–320, 1986. ISSN 0168-583X. doi:https://doi.org/10.1016/0168-583X(86)90118-7.
- [166] P. Indelicato and P. Mohr. Introduction to bound-state quantum electrodynamics. 2017. doi:10.1007/978-3-642-40766-6\_36.
- [167] G. Drake. Springer handbook of atomic, molecular, and optical physics. 2006. ISBN 978-0-387-20802-2. doi:10.1007/978-0-387-26308-3.
- [168] U. D. Jentschura. Quantum electrodynamic bound state calculations and large order perturbation theory. <https://arxiv.org/abs/hep-ph/0306153>, 2003.
- [169] E. Tiesinga, P. J. Mohr, D. B. Newell, and B. N. Taylor. CODATA recommended values of the fundamental physical constants: 2018. *Journal of Physical and Chemical Reference Data*, 50(3):033105, 2021. doi:10.1063/5.0064853.
- [170] G. Janka, B. Ohayon, and P. Crivelli. Muonium Lamb shift: theory update and experimental prospects. <https://arxiv.org/abs/2111.13951>, 2021.
- [171] K. Pachucki. Radiative recoil correction to the Lamb shift. *Phys. Rev. A*, 52:1079–1085, 1995. doi:10.1103/PhysRevA.52.1079.
- [172] I. Blokland, A. Czarnecki, and K. Melnikov. Expansion of bound-state energies in powers of  $m/M$  and  $(1 - m/M)$ . *Phys. Rev. D*, 65:073015, 2002. doi:10.1103/PhysRevD.65.073015.
- [173] M. I. Eides and H. Grotch. Corrections of order  $\alpha^6$  to S levels of two-body systems. *Phys. Rev. A*, 52:1757–1760, 1995. doi:10.1103/PhysRevA.52.1757.
- [174] M. I. Eides and V. A. Shelyuto. Three-loop corrections to the Lamb shift in muonium and positronium. *Phys. Rev. A*, 105:012803, Jan 2022. doi:10.1103/PhysRevA.105.012803.
- [175] V. A. Yerokhin, K. Pachucki, and V. Patkó. Theory of the Lamb shift in hydrogen and light hydrogen-like ions. *Annalen der Physik*, 531(5):1800324, 2019. doi:https://doi.org/10.1002/andp.201800324.

- [176] C. Frugiuele, J. Pérez-Ríos, and C. Peset. Current and future perspectives of positronium and muonium spectroscopy as dark sectors probe. *Phys. Rev. D*, 100:015010, 2019. doi:10.1103/PhysRevD.100.015010.
- [177] A. H. Gomes, V. A. Kostelecký, and A. J. Vargas. Laboratory tests of Lorentz and *CPT* symmetry with muons. *Phys. Rev. D*, 90:076009, 2014. doi:10.1103/PhysRevD.90.076009.
- [178] P. Fadeev, Y. V. Stadnik, et al. Revisiting spin-dependent forces mediated by new bosons: Potentials in the coordinate-space representation for macroscopic- and atomic-scale experiments. *Phys. Rev. A*, 99:022113, 2019. doi:10.1103/PhysRevA.99.022113.
- [179] Y. M. Andreev, D. Banerjee, et al. Constraints on new physics in electron  $g - 2$  from a search for invisible decays of a scalar, pseudoscalar, vector, and axial vector. *Phys. Rev. Lett.*, 126:211802, 2021. doi:10.1103/PhysRevLett.126.211802.
- [180] D. V. Kirpichnikov, V. E. Lyubovitskij, and A. S. Zhevlakov. Implication of hidden sub-GeV bosons for the  $(g - 2)_{\mu}$ ,  ${}^8\text{Be} - {}^4\text{He}$  anomaly, proton charge radius, EDM of fermions, and dark axion portal. *Phys. Rev. D*, 102:095024, 2020. doi:10.1103/PhysRevD.102.095024.
- [181] D. Hanneke, S. Fogwell, and G. Gabrielse. New measurement of the electron magnetic moment and the fine structure constant. *Phys. Rev. Lett.*, 100:120801, Mar 2008. doi:10.1103/PhysRevLett.100.120801.
- [182] M. O. Scully and M. S. Zubairy. Quantum optics. Cambridge University Press, 1997. doi:10.1017/CBO9780511813993.
- [183] J. Walraven. Atomic physics lectures. [https://staff.fnwi.uva.nl/j.t.m.walraven/walraven/Publications\\_files/2021-AtomicPhysics.pdf](https://staff.fnwi.uva.nl/j.t.m.walraven/walraven/Publications_files/2021-AtomicPhysics.pdf), 2021.
- [184] M. Haas, U. D. Jentschura, et al. Two-photon excitation dynamics in bound two-body Coulomb systems including AC Stark shift and ionization. *Phys. Rev. A*, 73:052501, 2006. doi:10.1103/PhysRevA.73.052501.
- [185] L. Chérigier-Kovacic, P. Ström, A. Lejeune, and F. Doveil. Electric field induced Lyman- $\alpha$  emission of a hydrogen beam for electric field measurements. *Review of Scientific Instruments*, 86(6):063504, 2015. doi:10.1063/1.4922856.
- [186] P. Ström. Measurements of electric fields in a plasma by stark mixing induced Lyman- $\alpha$  radiation. Master's thesis, Uppsala University, 2013.
- [187] G. Janka, B. Ohayon, et al. Intense beam of metastable muonium. *Eur. Phys. J. C*, 80(9):804, 2020. doi:10.1140/epjc/s10052-020-8400-1.
- [188] A. Pozos, E. Castillo, M. Chávez, and L. Trujillo. Modeling micro-channel plates as astronomical detectors of UV radiation. In 2016 13th International Conference on Electrical Engineering, Computing Science and Automatic Control (CCE), pages 1–6. 2016. doi:10.1109/ICEEE.2016.7751230.
- [189] J. Ladislav Wiza. Microchannel plate detectors. *Nuclear Instruments and Methods*, 162(1):587–601, 1979. ISSN 0029-554X. doi:[https://doi.org/10.1016/0029-554X\(79\)90734-1](https://doi.org/10.1016/0029-554X(79)90734-1).

- [190] O. H. W. Siegmund, C. Ertley, et al. Microchannel plate detector technology potential for LUVOIR and HabEx. In O. H. Siegmund, editor, *UV, X-Ray, and Gamma-Ray Space Instrumentation for Astronomy XX*, volume 10397, pages 282 – 295. International Society for Optics and Photonics, SPIE, 2017. doi:10.1117/12.2274281.
- [191] O. Siegmund, J. Vallerga, and A. Tremsin. Characterization of microchannel plate quantum efficiency. In O. H. W. Siegmund, editor, *UV, X-Ray, and Gamma-Ray Space Instrumentation for Astronomy XIV*, volume 5898, pages 113 – 123. International Society for Optics and Photonics, SPIE, 2005. doi:10.1117/12.621708.
- [192] S. R. Jelinsky, O. H. W. Siegmund, and J. A. Mir. Progress in soft x-ray and UV photocathodes. In O. H. W. Siegmund and M. A. Gummin, editors, *EUV, X-Ray, and Gamma-Ray Instrumentation for Astronomy VII*, volume 2808, pages 617 – 625. International Society for Optics and Photonics, SPIE, 1996. doi:https://doi.org/10.1117/12.256036.
- [193] M. Whiteley, J. Pearson, G. Fraser, and M. Barstow. The stability of CsI-coated microchannel plate X-ray detectors. *Nuclear Instruments and Methods in Physics Research*, 224(1):287–297, 1984. ISSN 0167-5087. doi:https://doi.org/10.1016/0167-5087(84)90477-0.
- [194] K. Berkner, I. Bornstein, R. Pyle, and J. Stearns. Charge fractions and excited-atom populations of 8-100 keV deuterium beams emerging from solid films of C, Mg, Nb, and Au. *Phys. Rev. A*, 6, 1972. doi:10.1103/PhysRevA.6.278.
- [195] B. T. Meggitt, K. G. Harrison, and M. W. Lucas. Equilibrium charge-fractions for H<sup>+</sup> and H<sub>2</sub><sup>+</sup> ions transmitted through carbon foils at 60-300 keV. 6(12):L362–L364, 1973. doi:10.1088/0022-3700/6/12/005.
- [196] S. Kreussler and R. Sizmann. Neutralization of 50-230-keV hydrogen ions which have penetrated Al, Au, C, and Cs films. *Phys. Rev. B*, 26:520–529, 1982. doi:10.1103/PhysRevB.26.520.
- [197] B. Mazuy, A. Belkacem, et al. Foil dissociation of 40–120 keV/p hydrogen clusters. *Nuclear Instruments and Methods in Physics Research Section B: Beam Interactions with Materials and Atoms*, 28(4):497–501, 1987. doi:https://doi.org/10.1016/0168-583X(87)90494-0.
- [198] R. Kallenbach, M. Gonin, A. Bürgi, and P. Bochsler. Charge exchange of hydrogen ions in carbon foils. *Nuclear Instruments and Methods in Physics Research Section B: Beam Interactions with Materials and Atoms*, 83(1):68–72, 1993. ISSN 0168-583X. doi:https://doi.org/10.1016/0168-583X(93)95909-O.
- [199] H. O. Funsten, D. J. McComas, and B. L. Barraclough. Application of thin foils in low-energy neutral-atom detection. In S. Chakrabarti, editor, *Instrumentation for Magnetospheric Imagery*, volume 1744, pages 62 – 69. International Society for Optics and Photonics, SPIE, 1992. doi:10.1117/12.60580.
- [200] F. Allegrini, R. W. Ebert, et al. Charge state of 1 to 50 keV ions after passing through graphene and ultrathin carbon foils. *Optical Engineering*, 53(2):1 – 7, 2014. doi:10.1117/1.OE.53.2.024101.

- [201] A. S. Tremsin and O. H. W. Siegmund. Dependence of quantum efficiency of alkali halide photocathodes on the radiation incidence angle. In O. H. W. Siegmund and K. A. Flanagan, editors, *EUV, X-Ray, and Gamma-Ray Instrumentation for Astronomy X*, volume 3765, pages 441 – 451. International Society for Optics and Photonics, SPIE, 1999. doi:<https://doi.org/10.1117/12.366524>.
- [202] S. R. Lundeen and F. M. Pipkin. Separated oscillatory field measurement of the Lamb shift in  $H, n = 2$ . *Metrologia*, 22(1):9–54, 1986. doi:10.1088/0026-1394/22/1/003.
- [203] K. Sedlak, R. Scheuermann, et al. MusrSim and MusrSimAna - simulation tools for  $\mu$ SR instruments. *Physics Procedia*, 30:61–64, 2012. ISSN 1875-3892. doi:<https://doi.org/10.1016/j.phpro.2012.04.040>. 12th International Conference on Muon Spin Rotation, Relaxation and Resonance (SR2011).
- [204] B. Ohayon, G. Janka, et al. Precision measurement of the Lamb shift in muonium. *Phys. Rev. Lett.*, 128:011802, 2022. doi:10.1103/PhysRevLett.128.011802.
- [205] W. H. Press and S. A. Teukolsky. Adaptive stepsize Runge–Kutta integration. *Computers in Physics*, 6(2):188–191, 1992. doi:10.1063/1.4823060.
- [206] L. for Muon Spin Spectroscopy (LMU). Low-energy muon (LEM) experiment. <http://lmu.web.psi.ch/docu/nemu/html/>.
- [207] T. Prokscha, R. Scheuermann, et al. A novel VME based  $\mu$ SR data acquisition system at PSI. *Physica B: Condensed Matter*, 404(5):1007–1009, 2009. ISSN 0921-4526. doi:<https://doi.org/10.1016/j.physb.2008.11.206>.
- [208] D. A. Andrews and G. Newton. Bloch-Siegert shifts in resonances between excited states. *Journal of Physics B: Atomic and Molecular Physics*, 9(9):1453–1460, 1976. doi:10.1088/0022-3700/9/9/010.
- [209] D. A. Andrews and G. Newton. Observation of Bloch-Siegert shifts in the  $2^2s_{1/2} - 2^2p_{1/2}$  microwave resonance in atomic hydrogen. *Journal of Physics B: Atomic and Molecular Physics*, 8(9):1415–1419, 1975. doi:10.1088/0022-3700/8/9/008.
- [210] A. Marsman, M. Horbatsch, and E. A. Hessels. Interference between two resonant transitions with distinct initial and final states connected by radiative decay. *Phys. Rev. A*, 96:062111, 2017. doi:10.1103/PhysRevA.96.062111.
- [211] S. Karshenboim and V. Ivanov. Hyperfine structure of the ground and first excited states in light hydrogen-like atoms and high-precision tests of QED. *The European Physical Journal D*, 19:13–23, 2002. doi:10.1140/epjd/e20020050.
- [212] M. Abadi, P. Barham, et al. Tensorflow: A system for large-scale machine learning. <https://arxiv.org/abs/1605.08695>, 2016.
- [213] T. O'Malley, E. Bursztein, et al. Keras Tuner. <https://github.com/keras-team/keras-tuner>, 2019.
- [214] R. Parhi and R. D. Nowak. The role of neural network activation functions. *IEEE Signal Processing Letters*, 27:1779–1783, 2020. doi:10.1109/LSP.2020.3027517.

- [215] K. Wang, X. Gao, et al. Pay attention to features, transfer learn faster CNNs. <https://openreview.net/forum?id=ryxyCeHtPB>, 2020.
- [216] C. Tan, F. Sun, et al. A survey on deep transfer learning. <https://arxiv.org/abs/1808.01974>, 2018.
- [217] S. Albawi, T. A. Mohammed, and S. Al-Zawi. Understanding of a convolutional neural network. In 2017 International Conference on Engineering and Technology (ICET), pages 1–6. 2017. doi:10.1109/ICEngTechnol.2017.8308186.
- [218] L. Flekova and M. Schott. Reconstruction of micropattern detector signals using convolutional neural networks. *Journal of Physics: Conference Series*, 898:032054, 2017. doi:10.1088/1742-6596/898/3/032054.
- [219] K. Simonyan and A. Zisserman. Very deep convolutional networks for large-scale image recognition. <https://arxiv.org/abs/1409.1556>, 2015.
- [220] K. He, X. Zhang, S. Ren, and J. Sun. Deep residual learning for image recognition. <https://arxiv.org/abs/1512.03385>, 2015.
- [221] C. Szegedy, V. Vanhoucke, et al. Rethinking the inception architecture for computer vision. <https://arxiv.org/abs/1512.00567>, 2015.
- [222] T. Sokollik. Gated MCPs, pages 113–116. Springer Berlin Heidelberg, Berlin, Heidelberg, 2011. ISBN 978-3-642-15040-1. doi:10.1007/978-3-642-15040-1\_15.
- [223] R. W. Ebert, F. Allegrini, et al. Angular scattering of 150 keV ions through graphene and thin carbon foils: Potential applications for space plasma instrumentation. *Review of Scientific Instruments*, 85(3):033302, 2014. doi:10.1063/1.4866850.
- [224] A. D. Vira, P. A. Fernandes, et al. Angular scattering of protons through ultrathin graphene foils: Application for time-of-flight instrumentation. *Review of Scientific Instruments*, 91(3):033302, 2020. doi:10.1063/1.5134768.
- [225] N. Bezginov. Measurement of the  $2S_{1/2}, f = 0 \rightarrow 2P_{1/2}, f = 1$  Transition in Atomic Hydrogen. Ph.D. thesis, York U., Canada, 2020.
- [226] D. Taqqu. Compression and extraction of stopped muons. *Phys. Rev. Lett.*, 97:194801, 2006. doi:10.1103/PhysRevLett.97.194801.
- [227] Y. Bao, A. Antognini, et al. Muon cooling: Longitudinal compression. *Phys. Rev. Lett.*, 112:224801, 2014. doi:10.1103/PhysRevLett.112.224801.
- [228] A. Antognini et al. Demonstration of Muon-Beam Transverse Phase-Space Compression. *Phys. Rev. Lett.*, 125(16):164802, 2020. doi:10.1103/PhysRevLett.125.164802.
- [229] A. Antognini and D. Taqqu. muCool: muon cooling for high-brightness  $\mu^+$  beams. *SciPost Phys. Proc.*, 5:030, 2021. doi:10.21468/SciPostPhysProc.5.030.
- [230] M. Aiba, A. Amato, et al. Science case for the new high-intensity muon beams HIMB at PSI. <https://arxiv.org/abs/2111.05788>, 2021.
- [231] A. Knecht. Status of HIMB. <https://indico.psi.ch/event/10547/>, 2021.
- [232] N. Rouze, C. C. Havener, W. B. Westerveld, and J. S. Risley. Branching ratios for the decay of  $n=3$  hydrogen atoms in axial and transverse electric fields. *Phys. Rev. A*, 33:294–300, 1986. doi:10.1103/PhysRevA.33.294.

# Gianluca Janka | Curriculum Vitae

Hirzenbachstrasse 66, 8051 Zürich, CH

☎ +41 79 530 39 08 • ✉ jankag@phys.ethz.ch

Date of birth: 29.11.1992

## Education

---

- **PhD candidate** **ETH Zürich**  
since Oct. 2017  
○ Main projects: GBAR and Mu-MASS
- **M.Sc. in Interdisciplinary Science** **ETH Zürich**  
2016–2017  
○ Focus: Experimental Particle Physics
- **B.Sc. in Interdisciplinary Science** **ETH Zürich**  
2012–2016  
○ Focus: Physics and Physical Chemistry
- **High School** **Kantonsschule Chur**  
2007–2011  
○ Focus: Physics and Mathematics, Second: Chemistry

## Research Projects

---

- **Master's thesis under supervision of Prof. A. Rubbia** **ETH Zürich**  
Spring 2017  
○ Development of a Ly- $\alpha$  Detector for Measuring the Anti-Hydrogen Lamb Shift
- **Research Project under supervision of Dr. P. Crivelli** **ETH Zürich**  
Autumn 2016  
○ Building a Ly- $\alpha$  Micromegas Detector Prototype
- **Bachelor's thesis under supervision of Prof. K. Kirch** **ETH Zürich**  
Autumn 2015  
○ Programming Remote Magnetometers on Raspberry Pis and Testing their Sense HAT Sensors for the nEDM Experiment at PSI
- **Research Project under supervision of Prof. R. Signorell** **ETH Zürich**  
Spring 2015  
○ Characterization of Optically Trapped Particles using Raman and Broadband Mie Scattering

## Publications

---

- G. Janka, B. Ohayon, and P. Crivelli. Muonium lamb shift: theory update and experimental prospects, 2021
- B. Ohayon, G. Janka, et al. Precision Measurement of the Lamb Shift in Muonium. *Phys. Rev. Lett.*, 128(1):011802, 2022
- G. Janka et al. Intense beam of metastable Muonium. *Eur. Phys. J. C*, 80(9):804, 2020
- B. Radics, G. Janka, D. A. Cooke, S. Procureur, and P. Crivelli. Double hit reconstruction in large area multiplexed detectors. *Review of Scientific Instruments*, 90(9):093305, 2019